

The University of Nottingham

UNITED KINGDOM · CHINA · MALAYSIA

Hybrid Photonic-Plasmonic Structures for Optical Trapping of Nanoparticles

Mina Mossayebi, MEng(Hons)

Thesis submitted to The University of Nottingham

for the degree of Doctor of Philosophy, July 2018

To my parents, with love.

Abstract

There is a need for compact, easy to use devices that allow high-throughput, single-molecule experiments including optical trapping and manipulation to be conducted in real time. These devices have the potential of being widely used in laboratories and hospitals, resulting in a significant impact on patient care.

This thesis concerns the numerical design of a hybrid photonic-plasmonic cavity as a building-block for such technology. The hybrid cavity takes advantage of a photonic crystal resonator for energy storage and a plasmonic nanoantenna for sub-wavelength localization of light to create a cavity which benefits from the best of both worlds. The energy efficiency of the photonic crystal allows integration with photonic integrated circuits and parallelization of optical experiments as well as ensuring high optical density in the experiment site. The nanoplasmonic antenna creates a nanosized hot-spot with a high intensity gradient enabling optical trapping and manipulation of nanoparticles. The separation between the photonic crystal and the plasmonic nanoantenna elements of the hybrid cavity controls the flow of energy between them. It is optimized by the introduction of a new figure of merit which maximises the brightness of the externally accessible nano-sized "hot-spot" for a given input power to the device. The integrability of the hybrid device is also demonstrated by coupling it to a photonic crystal waveguide.

The numerical design of devices in this project has resulted in the successful fabrication of bowtie-shaped plasmonic nanoantennas as well as ongoing fabrication efforts

of photonic crystal cavities at the University of Nottingham. This thesis presents a comparison between conventional optical traps created at the focus of a laser beam and nanoplasmonic tweezers created by the illumination of plasmonic nanoantennas fabricated at the University of Nottingham. The novel technique developed during this PhD to increase the speed of nanoplasmonic trapping experiments for micron-sized particles is also described in this thesis. Using this technique, the effect of aspect ratio and size variation in the plasmonic nanoantennas on the trap strength is evaluated and reported for 2μm and 200nm beads, matching the predictions made from their simulated resonant behaviour. Stable trapping of 6nm dielectric quantum dots using nanoplasmonic traps created during this project is also demonstrated. Finally, this thesis presents preliminary results which demonstrate the ability to control the rotation of a rod-shaped particle, trapped at the near-field of a cross-shaped plasmonic nanoantenna, by changing the polarization of the illumination beam.

Acknowledgements

I would like to thank my supervisors Prof. Eric C. Larkins and Dr. Amanda J. Wright for their support and encouragement throughout this project. Professor Larkins, thank you for many exciting and challenging discussions about solid state physics, photonic crystals and nonlinear optics, for encouraging me to apply for a research project and for always supporting me. Dr. Wright, thank you for introducing me to the exciting world of optical trapping and manipulation, for trusting me and encouraging me to work independently and for providing me with a chance to work in an interdisciplinary environment. I would also like to express my gratitude to the University of Nottingham for giving me the opportunity to pursue a fully funded PhD under the Dean's scholarship.

I am grateful for many fruitful discussions with Prof. Mike G. Somekh. Thank you for your collaboration in this project, for teaching me about optical sensors and the field of plasmonics. I would also like to thank Dr. Gaetano Bellanca and Prof. Stefano Trillo at the University of Ferrara, Italy. Thank you Dr. Bellanca for teaching me about FDTD, for countless skype calls and frequent correspondence over the past five years. I also would like to thank the internal collaborators of this project, Dr. Christopher Mellor and Dr. Richard Cousins for the fabrication of devices without

which the completion of this project would not have been possible.

I would like to thank Prof. Clivia Sotomayor Torres and her group at ICN2, Barcelona, for hosting me, and teaching me about phononics. I am grateful to Prof. Romain Quidant and Dr. Pau Mestres Junque at ICFO, Barcelona for giving me a tour of their laboratories and sharing their method of sample preparation with me. I am thankful to Dr. Andrew Hudson and Dr. Natalie Garton of the University of Leicester for enabling a day visit to their laboratories and providing the mycobacterium used in this project.

I am grateful to my friends and colleagues Dr. Stephen Bull, Dr. Anas Helal, Aishah Mustapha, Pieter Smid, Dr. Sidahmed Abayazeed, Dr. Emilia Moradi, Harriet Boyd and all the other members of the optics and photonics group for their help and support and for many interesting conversations during our breaks. This experience would not have been the same without you.

I would like to thank my friends and family for supporting me throughout this time. A special thanks to my siblings Matthew and Elahe for always being on my side. Many thanks to Samuel for always being there and for reading many parts of this thesis. Finally, I would like to thank my parents whom this thesis is dedicated to, for their constant love and support.

Publications

Peer reviewed journal articles:

[J1] **M. Mossayebi**, A. J. Wright, A. Parini, M. G. Somekh, G. Bellanca and E. C. Larkins, "Investigating the use of a hybrid plasmonic-photonic nanoresonator for optical trapping using finite-difference time-domain method," Optical and Quantum Electronics 48: 275 (2016).

Journal articles in preparation:

[PJ1] **M. Mossayebi**, A. J. Wright, A. Parini, M. G. Somekh, G. Bellanca and E. C. Larkins, "A hybrid photonic-plasmonic platform for high-throughput single-molecule studies".

[PJ2] **M. Mossayebi**, R. Cousins, G. Bellanca, C. Mellor, E. C. Larkins, A. J. Wright, "Nanoplasmonic trapping, from micron- to nanoscale".

Book chapters:

[B1] **Mina Mossayebi**, Gaetano Bellanca, Alberto Parini, Amanda J. Wright and Eric C. Larkins, "Engineering of Hybrid Photonic-Plasmonic Devices for Enhanced Light-Matter Interactions," Springer, Recent Trends in Computational Photonics (2017).

Conferences with abstract:

[A1] **Mina Mossayebi**, Amanda J. Wright and Eric C. Larkins, "Use of Plasmonic and Photonic Structures to Enhance Optical Trapping," poster presentation,

Photonex (2014), Coventry, UK.

[A2] **Mina Mossayebi**, Alberto Parini, Amanda J. Wright, Mike G. Somekh, Gaetano Bellanca and Eric C. Larkins, "Vertical emission properties of a hybrid nanophotonic-plasmonic resonator," oral presentation, Semiconductor and Integrated Optoelectronics (SIOE), 31st March - 2nd April (2015), Cardiff, UK.

[A3] **Mina Mossayebi**, Alberto Parini, Mike G. Somekh, Gaetano Bellanca, Amanda J. Wright, and Eric C. Larkins, "Coupling mechanisms and field confinement in a hybrid plasmonic-photonic crystal resonator for enhanced optical trapping," Poster presentation, Optical wave and waveguide theory and numerical modelling workshop (OWTNM), 17th - 18th April (2015), City University London, UK. (prize)

[A4] **M. Mossayebi**, A. Parini , A. J. Wright , M. Somekh, E. C. Larkins, G. Bellanca, "Coupling mechanisms and field confinement in a hybrid plasmonic-photonic crystal resonator for enhanced optical trapping," Poster presentation,Photonex (2015), Coventry, UK. (prize)

[A5] **M. Mossayebi**, A. Parini, A. J. Wright, G. Bellanca, E. C. Larkins, "A realizable hybrid photonic-plasmonic nanocavity with high quality factor and confinement of light," Oral presentation, Photon16, 5 - 8 September (2016), University of Leeds, UK.

Fundings

[F1] **Dean of Engineering scholarship for international excellence**, University of Nottingham, Jun 2013 .

Amount: £60,000.

Description: Competitive scholarship for international students fully funding a PhD project.

[F2] **The Building Experience and Skills Scholarship (BESTS)**, The Graduate School, University of Nottingham, Jul 2015.

Amount: £3,000.

Application led by: Mina Mossayebi

Description: Competitive scholarship for staff and postgraduate students that allows fully funded travel to visit and work in other organizations to develop search skills, knowledge and networks.

Visits funded under this scholarship:

1) Four week visit to meet Professor Sotomayor at the Photonic and Phononic Nanostructures group (P2N), Catalan Institute of Nanotechnology (ICN2), Campus de Bellaterra, Barcelona, Spain (Oct-Nov 2015).

2) One day visit to Plasmon nanooptics group at The Institute of Photonic Sciences (ICFO), meeting with Dr. Pau Mestres (Prof. Quidant's post-doc) and visiting the phononics and optical trapping laboratories.

3) Four weeks collaborative visit to the University of Ferrara, Ferrara, Italy for collaboration with Dr. Bellanca (Mar-Apr 2016).

[F3] **University of Nottingham Interdisciplinary Centre for Analytical Science (UNICAS) funding**, University of Nottingham, Mar 2015.

Amount: £3,700.

Application led by: Mina Mossayebi

Applicants: Mina Mossayebi (School of Electrical and Electronic Engineering (EEE)) and Richard Cousins (Physics).

Description: A competitive cross-faculty initiative providing funding for collaborative projects, focused on research equipment, and analytical science.

Project led by this funding: Design and fabrication of plasmonic nanoantennas. This project combined the design and application expertise within EEE and Institute of Biophysics, Imaging and Optical Science (IBIOS) with the fabrication capabilities of the School of Physics and Astronomy (SPA) to design, fabricate and evaluate high quality plasmonic devices on top of a glass substrate. The design and fabrication of plasmonic nanoantennas presented in sections 4.5.2 and 6.2 are results of this funding which allowed us to collaborate with Dr. Richard Cousins and his PhD supervisor Dr. Christopher Mellor.

Contents

Abstract ii

Acknowledgements iv

List of Publications vi

Fundings viii

List of Symbols xv

List of Abbreviations xvii

1 Introduction 1

1.1 Overview and objectives . . . 3

1.2 Synopsis . . . 6

2 Optical tweezers: principles and applications 8

2.1 A brief history . . . 8

2.2 Overview of optical trapping force . . . 9

2.3 Optical trapping in ray optics regime . . . 10

2.3.1 Gradient force . . . 12

2.3.2 Equilibrium position . . . 15

2.4 Optical trapping in Mie regime . . . 16

2.5 Optical trapping in Rayleigh regime . . . 18

2.6 Measuring the optical trapping force . . . 19

2.6.1 Equipartition of energy . . . 22

2.6.2 Frequency-spectrum method . . . 23

2.6.3 Viscous drag force . . . 24

2.7 Applications and advances of optical trapping . . . 24

2.7.1 Far-field optical trapping . . . 24

2.7.2 Near-field optical trapping . . . 25
2.8 Summary . . . 29

3 Numerical modelling tool, FDTD **30**
3.1 Electromagnetics background . . . 30
3.1.1 Maxwell's equations . . . 30
3.1.2 Constitutive relations . . . 32
3.1.3 Refractive index and material impedance . . . 33
3.1.4 The wave equation . . . 34
3.1.5 Boundary conditions at interfaces . . . 35
3.2 Numerical solutions to Maxwell's equations . . . 36
3.3 Finite-difference time-domain method . . . 38
3.3.1 Finite difference approximation and its error . . . 38
3.3.2 The Yee cell . . . 39
3.3.3 The FDTD algorithm . . . 40
3.3.4 Meshing . . . 42
3.3.5 Sources in FDTD . . . 45
3.3.6 Time-space stability condition . . . 46
3.3.7 Numerical boundary conditions, PML . . . 47
3.4 FDTD simulation procedure . . . 48
3.4.1 Comparing two simulations . . . 52
3.5 Numerical tools used during this project . . . 53
3.5.1 Meep and MPB . . . 53
3.5.2 Lumerical . . . 53
3.5.3 Paraview . . . 53
3.6 Summary . . . 54

4 Building blocks of the hybrid device **55**
4.1 Figures of merit for photonic resonators . . . 56
4.2 Photonic crystals . . . 57

4.2.1 2D photonic crystals . . . 60
4.2.2 2D photonic crystal cavities . . . 64
4.2.3 2D photonic crystal waveguides . . . 65
4.3 Plasmonic nanoantennas . . . 66
4.3.1 Popular designs of gap nanoantennas, design choice . . . 69
4.4 FDTD Simulation results for PhCs . . . 71
4.4.1 L3 cavity design for the hybrid device . . . 71
4.4.2 Designed L3 cavity in water . . . 73
4.4.3 L3 cavity tolerances for fabrication purposes . . . 75
4.5 FDTD Simulation results for BNAs . . . 78
4.5.1 BNA for the hybrid device . . . 78
4.5.2 BNA simulation results for fabrication and experimental purposes . . . 83
4.6 Summary . . . 84
5 Design of a hybrid photonic-plasmonic cavity for applications in high-throughput single-molecule experiments 86
5.1 Existing hybrid photonic-plasmonic devices . . . 88
5.2 The proposed hybrid device . . . 89
5.3 Figure of Merit . . . 92
5.4 Optimisation of the spacer layer . . . 95
5.5 Characteristics of the optimised hybrid device . . . 98
5.5.1 Spectral response . . . 98
5.5.2 Intensity profiles . . . 99
5.5.3 Coupling the hybrid device to a waveguide . . . 101
5.5.4 The hybrid device in water . . . 106
5.5.5 Overall comparison . . . 107
5.6 K-space and far-field pattern analysis . . . 108
5.7 Discussion . . . 111
5.8 Summary . . . 113

6 Fabrication of devices **115**

6.1 Basic principles of electron-beam lithography . . . 116

6.2 Fabrication of nanoplasmonic antennas . . . 119

6.3 Fabrication of the hybrid device . . . 124

6.3.1 Fabrication method . . . 125

6.3.2 Results . . . 127

6.3.3 Future work . . . 130

6.4 Summary . . . 130

7 Design and characterization of nanoplasmonic tweezers **131**

7.1 Experimental setup . . . 132

7.1.1 Imaging of the sample . . . 136

7.2 Characterisation of the experimental setup . . . 137

7.2.1 Image pixel size . . . 137

7.2.2 Numerical aperture of the objective lens and the focus of the beam . . . 138

7.2.3 Polarisation of the beam . . . 143

7.2.4 Laser power . . . 145

7.3 Measuring the trap stiffness . . . 149

8 Optical trapping using nanoplasmonic tweezers **153**

8.1 Sample preparation . . . 154

8.1.1 Sample solution . . . 154

8.1.2 Sample chamber and cleaning the coverslip . . . 154

8.1.3 Calculation of the thickness of the sample chamber and the depth of focus . . . 156

8.2 Method of nanoplasmonic trapping . . . 157

8.3 Numerical prediction of trap strength as a function of BNA length . . 160

8.4 Trapping 2μm particles . . . 162

8.4.1 Conventional trapping . . . 165

8.4.2 Nanoplasmonic trapping . . . 170
8.5 Trapping 200nm particles . . . 178
8.5.1 Conventional trapping . . . 178
8.5.2 Nanoplasmonic trapping . . . 179
8.6 Trapping 6nm particles . . . 181
8.6.1 Conventional trapping . . . 181
8.6.2 Nanoplasmonic trapping . . . 181
8.7 Alignment and rotation of Mycobacteria . . . 183
8.8 Summary . . . 186

9 Conclusion **188**
9.1 Summary and discussions . . . 188
9.2 Ongoing work . . . 191
9.3 Recommendations for future work . . . 191

Bibliography **193**
Appendices **222**

A Models for representing material used in simulations **222**

B Labview program for live imaging and calculating the trap stiffness using the Dalsa camera **224**

C Labview program for calculating the trap stiffness using the Optimos camera **226**

List of Symbols

This list includes symbols that are frequently used in this thesis.

Symbol	Description	Units
a	Periodicity	
B	Magnetic flux density	T
c	speed of light	$\frac{m}{s}$
D	Electric flux density	$\frac{C}{m^2}$
E	Electric field	$\frac{N}{C}$
E_x	The x component of the electric field	$\frac{N}{C}$
E_y	The y component of the electric field	$\frac{N}{C}$
E_z	The z component of the electric field	$\frac{N}{C}$
H	Magnetic field	T
H_x	The x component of the magnetic field	$\frac{A}{m}$
H_y	The y component of the magnetic field	$\frac{A}{m}$
H_z	The z component of the magnetic field	$\frac{A}{m}$
J	Electric current density	$\frac{A}{m^2}$
h	Planck's constant	Js
λ	Wavelength	m
λ_0	Wavelength in vacuum	m
λ_0	Fundamental resonant wavelength	m
n	Refractive index	
n^2	Dielectric constant	
ω	Angular frequency	$\frac{rad}{s}$
W	Width	m
f	Frequency	Hz

f	Force density	$\frac{N}{m^3}$
F	Force	N
F_{scat}	Scattering force	N
F_{grad}	Gradient force	N
Q	Quality factor	
k	Trap stiffness	$\frac{pN}{\mu m}$
k_B	Boltzmann constant	$\frac{J}{K}$
U	Energy	J
U_{tot}	Total energy	J
v	Frequency	Hz
P_{loss}	Power lost per cycle	Watt
P	Polarization	$\frac{C}{m}$
M	Magnetization denisty	T
p	Momentum	$\frac{kg\ m}{s}$
ρ	Charge density	$\frac{C}{m^3}$
T	Temperature	K
d	Diameter	m
r	Radius	m
L	Length	m
ϵ_0	Permittivity of vacuum	$\frac{F}{m}$
ϵ_r	Relative permittivity	
ϵ	Permittivity	$\frac{F}{m}$
μ_0	Permeability of vacuum	$\frac{H}{m}$
μ_r	Relative permeability	
μ	Permeability	$\frac{H}{m}$
α	Polarisability	$\frac{Cm^2}{V}$
σ	Electric conductivity	$\frac{S}{m}$
η	Material impedance	Ω

List of Abbreviations

AFM	Atomic-force microscope
BNA	Bowtie nanoantenna
BR	Bragg reflection
EBL	Electron-beam lithography
EM	Electromagnetic
FDTD	Finite-difference time-domain method
FOM	Figure of merit
fps	Frames per second
FT	Fourier transform
GaAs	Gallium arsenide
HCl	Hydrochloric acid
ICP	Inductive coupled plasma
IPA	Isopropyl alcohol
LSP	Localised surface plasmon
MST	Maxwell stress tensor
NA	Numerical aperture
OT	Optical trapping
PhC	Photonic crystal
PML	Perfectly matched layers
PMMA	Poly(methyl methacrylate)
Q-factor	Quality factor
SDS	Sodium dodecyl sulfate
SNOM	Scanning near-field optical microscope
SEM	Scanning electron microscope

SiO_2	Silicon dioxide
SP	Surface plasmon
TE	Transverse electric
TIR	Total internal reflection
ROI	Region of interest
FT	Fourier transform

1

Introduction

The study and manipulation of nanostructures has become a common theme in many disciplines. This is because understanding atomic and molecular interactions and the ability to control them can lead to significant advances in science and technology. In electronics, nanostructures are being deployed to reduce the size and increase the speed and memory of devices. This means that single molecules could potentially take on basic digital electronic roles, creating novel processing architectures [1]. In biology, research is moving away from studying biological processes using crude methods that look into the average behaviour of collections of molecules. The integration of techniques that allow detection, characterization and manipulation of single molecules are providing insight into the fundamental mechanisms and machines that run the cell. This holds promise for providing insight into the chemistry of molecules and the development of new generations of drugs, composites and medical devices [2–4].

Optical imaging in the nanoscale and beyond the diffraction limit is usually done either in the far field by the collection of light from nanosized fluorescent beads or in the near field by the use of nanosized metallic and dielectric tips [5,6]. A dominant example of the former technique is super-resolution fluorescent microscopy [7]. Scanning near-field optical microscopy (SNOM) [8] isan example of the latter. When

it comes to single-cell/molecule investigation and manipulation, however, magnetic and optical tweezers are two of the key tools used [9]. These techniques can be used alongside other sensing and spectroscopic techniques to gain more information about the molecule/cell of interest in real time, while having active control over its position. Magnetic tweezers with forces ranging from pico- to nano-Newtons usually use a set of magnets as well as a micron-sized magnetic bead attached to the molecule of interest. The bead is trapped in the magnetic field created between the two magnets and is used to exert torque on the molecule of interest and study its mechanical properties or manipulate it. [10]. Optical tweezers typically use a focused beam of light to directly trap and manipulate micron-sized objects with forces in the pico-Newton range [11]. They are minimally invasive and often label free. They can also be used in single-molecule experiments by attaching a micron-sized bead to the molecule of interest [12,13].

Whilst tools such as optical tweezers can manipulate single cells and molecules, they are not high throughput and require lengthy experiments on many individual molecules/cells before reliable conclusions can be made [14]. There is a need for tools that allow a large number of single-molecule experiments to run in a small time window. This will generate a large enough sample number to make statistical analysis possible [15]. These techniques also usually operate on the micrometre scale studying single cells. They are not typically label-free while studying single molecules. Therefore there is also a need to push such techniques to the nanoscale where label-free single-molecule experiments are possible.

Although tools such as optical tweezers have been available for the past few decades, they have had limited clinical uptake. This is because they require highly trained users and large, high-cost optical systems. There is a need for techniques that are low-cost and easy to use, which are also able to perform high-throughput, single-molecule measurements in real time. Such devices have the potential of being widely used in laboratories and hospitals, where they are having a big impact on patient

care.

In this thesis, I will provide an account of my development of plasmonic and hybrid photonic-plasmonic technologies as routes for enabling high throughput, label-free, user-friendly optical trapping of micro- and nanoparticles.

1.1 Overview and objectives

The work presented in this thesis covers three main topics concerning the design, fabrication and testing of devices that can be used for optical trapping and manipulation in the nanoscales. The first aim in this project is the design of a hybrid photonic-plasmonic device that can be a building block of a multicomponent platform for single-molecule, high-throughput optical trapping experiments. The second aim is the fabrication of some of the designed devices so that they can be tested in the laboratory and the final aim of this project is the design of nanoplasmonic tweezer systems based on the fabricated devices, and performing optical trapping measurements and experiments to calibrate them.

Design of the hybrid device: When designing a hybrid photonic-plasmonic device, the aim was to create a building block for a multi-component platform capable of running multiple single-molecule experiments simultaneously. The platform itself is imagined to be inexpensive and hand-held with a planar surface only allowing light to be focused on the surface in multiple nanosized hot-spots that allow label-free optical trapping and the investigation of single-molecules. The optical behaviour of the surface of the platform would be tailored depending on the application and controlled centrally. For instance, in a blood sample, it could guide specific molecules to specific experiment sites either by optical or microfluidic means. The envisaged platform is integrated to a central control and analysis hub via an optical fibre, removing the need for highly trained users and bulky and expensive optics at each

experiment site. The building block of such a platform should therefore be energy efficient to allow the distribution of light to multiple single-molecule experiment sites. It should have an externally accessible, nanosized hot-spot with a high photon density and it should be integratable. Figure 1.1 illustrates the concept for the envisaged platform.

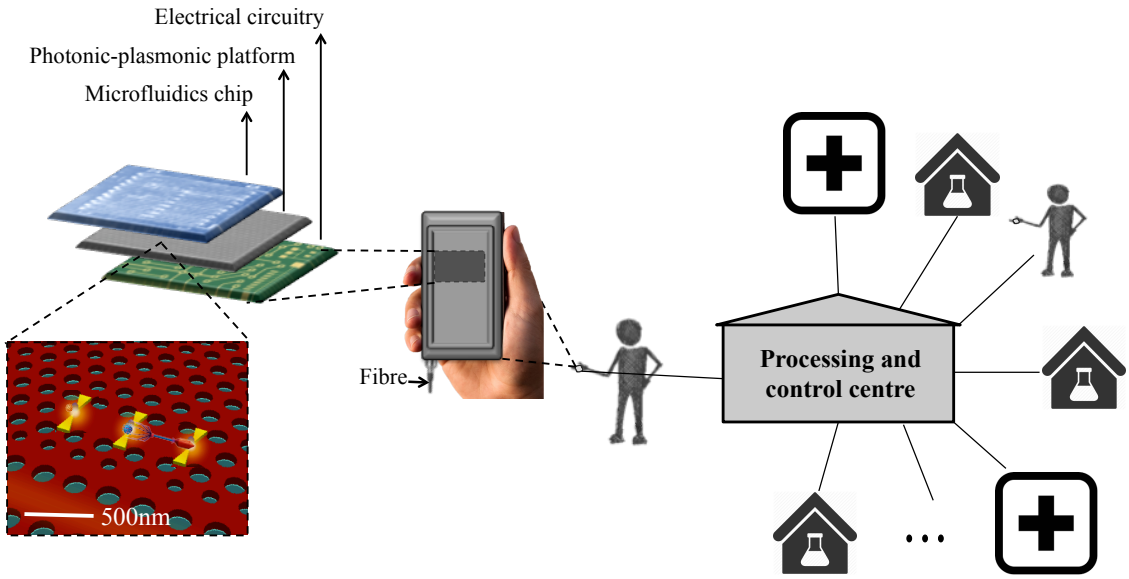


Figure 1.1: Illustration of the device concept.

Two dimensional (2D) photonic crystals (PhC) were chosen as a base for the building block, to allow for control over flow of light within a planar device, integration and compatibility with fibre optics and high optical efficiency. Photonic crystals are microscopic media in which different dielectric constants are repeated periodically. This periodicity can result in a wavelength window wherein the propagation of light is forbidden, namely a photonic bandgap. Engineering defects in these photonic crystals can allow for light to locallise in the defect and form hugely energy efficient resonators and waveguides [16]. The resonators and waveguides created in a 2D PhC are commonly created by removing holes from a regular slab of high refractive index material with low refractive-index holes etched into it. The light localises in the high refractive index material. This localisation is however limited by the

diffraction limit. However, the light is usually confined within the slab and cannot be accessed externally without special designs.

To address these issues, plasmonic gap antennas are combined with a 2D PhC resonator. Plasmonic gap antennas are created by placing two metallic structures next to each other with a nanosized gap between them [17]. Plasmonic gap antennas are lossy compared to most photonic devices and have a broad excitation spectrum. When plasmonic gap antennas are excited with an electric field component normal to the gap, oscillating electrons of the metal resonantly gather at the sharp corners of the antenna, creating an electric field hot-spot in the gap. This is because the oscillating electrons must fullfil the electromagnetic boundary conditions enforcing continuity of the normal vector component of the electric flux at the metal/dielectric interface [18]. When plasmonic gap antennas are combined with the 2D PhCs, they can funnel the light that is trapped within the PhC to a nanozised hot-spot on the surface. This hot-spot can be used to perform single-molecule, optical trapping, manipulation and investigation experiments. Combining the plasmonic gap antennas and 2D PhC devices, makes it possible to have devices with high optical efficiencies as well as externally accessible nanoscale hot-spots for single-molecule experiments.

The device design begins by studying the individual components of the hybrid photonic-plasmonic building block. This is followed by the optimization of the hybrid device, to determine the spacing between the plasmonic and photonic components that results in the brightest nanosized hot-spot on the surface, for a fixed input power.

Fabrication of devices: The objective of this part of the project was to design the fabrication process for plasmonic nanoantennas for use in plasmonic tweezers, 2D PhC devices and hybrid photonic-plasmonic devices.

The fabrication of the designed plasmonic structures was possible due to the success

of an internal, cross-faculty grant application, which I led. I performed numerical analysis and design of the structures and Dr. Richard Cousins was responsible for the fabrication of the plasmonic devices. The fabrication of the PhC devices was possible due to the success of another internal cross-faculty grant application led by Dr. Amanda J. Wright. Dr. Christopher Mellor was responsible for the fabrication and characterization of the PhC devices. These fabrication efforts and results are also briefly presented in this thesis.

Nanoplasmonic tweezers: This part of the project aimed to design, implement and characterize a nanoplasmonic tweezer system based on the existing conventional optical tweezer setup in the laboratory. The nanoplasmonic tweezers increase the strength of the trap for a given input power and enable trapping nano-sized particles. An objective here was to increase the speed of the typical nanoplasmonic trapping experiments and compare the nanoplasmonic tweezer with the typical optical tweezer system which it was based on. Another objective here was to rotate a rod-shaped microparticle using plasmonic tweezers.

1.2 Synopsis

Chapter 2 briefly describes the physical principles of optical trapping and manipulation as well as describing the main characterization techniques for typical optical trapping systems. This is followed by looking at the applications and advances of optical trapping systems over the past forty years.

Chapter 3 introduces the finite-difference time-domain method, which was the main tool for the numerical design of the devices used throughout this project.

Chapter 4 gives an overview of photonic and plasmonic resonators. It also describes the relevant working principles of photonic crystals, photonic crystal cavities

and waveguides. This is followed by a description of the plasmonic gap antennas and their operating principles. The results of the numerical investigations of individual plasmonic nanoantennas and photonic crystal cavities and waveguides are then presented in this chapter.

Chapter 5 presents the numerical design and characterization of the hybrid photonic-plasmonic device. The device is optimized with respect to a new figure of merit. This figure of merit is introduced in order to maximise the brightness of the externally accessible, nanosized hot-spot for a fixed input power.

Chapter 6 gives a brief overview of the key principles of electron beam lithography. This is followed by a description of the fabrication process used to make the nanoplasmonic antennas. This includes the steps taken to fabricate the designed photonic devices, the issues tackled and the results obtained. The fabrication process envisaged for the hybrid photonic-plasmonic device concludes this chapter.

Chapter 7 begins by describing the plasmonic tweezer and imaging setup. This is followed by the characterization of the experimental setup. Finally, the method used for measuring the strengths of the optical traps is described.

Chapter 8 describes the sample preparation method followed by the results obtained from optical and nanoplasmonic trapping experiments, comparing the two when possible. The results obtained for rotating a rod-shaped microbacterium concludes this chapter.

Chapter 9 provides a summary of the results and data presented in this thesis. The thesis concludes with a brief description of the future work to be carried out in this project.

2

Optical tweezers: principles and applications

This chapter begins by giving a brief history of optical trapping. It then describes the optical trapping force in the ray optics, Mie and Rayleigh regimes. This is followed by a short description of the common calibration methods used to measure the optical trapping force. The chapter concludes by giving a short overview of the applications and advances of far-field and near-field optical trapping schemes.

2.1 A brief history

German Astronomer Johannes Kepler first reported that the tail of a comet always points away from the sun in 1619 [19]. The general conception at the time was that there is a solar wind, causing this effect, and it can be harvested to allow transport in space [20] much like the sail of a boat on the sea. In the 1860s, James Clerk Maxwell, published the theory of electromagnetism in which he showed that light itself carries momentum (i.e. moving mass) and can exert pressure on objects [21]. This is the reason for the comet tail always pointing away from the sun [20]. Nicholas, Hull and Lebedev first experimentally demonstrated radiation pressure on absorbing glasses

in 1901 [22]. Although this was considered very interesting science, it was not put to practice. After the invention of the laser in 1960 [23], radiation pressure began to be put into real use. In the early 1970s Arthur Ashkin first demonstrated the ability to change the acceleration of a neutral micron-sized particle using a laser beam [24]. He observed two types of forces imparted on the particle from the laser beam, one that "pushed" the particle along the laser beam propagation direction; and one that "pulled" the particle in the direction of the positive intensity gradient of the beam. Controlling these two forces enables acceleration, deceleration and immobilization of particles, establishing the field of optical trapping [11,24–29].

2.2 Overview of optical trapping force

Optical trapping force arises from the interaction of light and matter at an intensity gradient. A dielectric particle of any size in a medium of lower refractive index is at its lowest energy state (equilibrium), when placed at a position with the highest optical intensity [30]. When removed from this position, it experiences an intensity gradient and hence a restoring force referred to as the **gradient force**. Small regions with high intensities resulting in high gradient forces can be created using various techniques. The most conventional method, resulting in a 3D trap is to tightly focus a single beam of light, using a high numerical aperture (NA) objective lens. The traps created using this technique are normally diffraction limited and hence best suited to micron-sized particles. In this case the optical trap is created by balancing the effects of scattering and gradient forces. The gradient force is the force pulling the particle towards the highest intensity region of the beam and the scattering force is the force pushing the particle in the direction of propagation.

Optical trapping can be discussed in three different regimes:

1. **Ray optics regime** where the size of the particle, d, is much larger than the

wavelength, λ, of light ($\lambda << d$). Here the optical force can be described using ray optics.

2. **Mie regime** where the size of the particle is of the order of the wavelength of light ($\lambda \approx d$). Here the light-matter interactions are described using electromagnetic field models.

3. **Rayleigh regime** where the size of the particle is much smaller than the wavelength of light ($\lambda >> d$). Here the particle can be modelled as a dipole experiencing a constant electromagnetic field.

2.3 Optical trapping in ray optics regime

In this regime, since the object is much larger than the wavelength of light, the optical trapping mechanism can be simplified to conservation of linear momentum in forward scattered light [31,32]. A beam of light incident on a particle can be decomposed into multiple rays propagating in straight lines, carrying streams of photons with energy, $E = hv$ [J], and linear momentum, $\mathbf{p}= \frac{h}{\lambda}$ in $[\frac{kg.m}{s}]$, where h is Planck's constant ($h \approx 6.62e^{-34}[\frac{m^2.kg}{s}]$), v is the frequency of light [Hz] and λ is wavelength [m]. From the impulse equation, the force exerted on the particle from a single photon is equal in magnitude to the rate of change of momentum of the photon. Substituting energy, E from Einstein's formula ($E=mc^2 = \mathbf{p}c$, where c is the speed of light and m is mass [kg]) [33]:

$$\mathbf{F} = -\frac{\mathrm{d}\mathbf{p}}{\mathrm{d}t} = \frac{1}{c}\frac{\mathrm{d}E}{\mathrm{d}t}. \tag{2.3.1}$$

The force exerted on the particle has the same magnitude and opposite direction to the photon momentum change as dictated by the conservation of momentum. The magnitude of the force exerted on a particle from a beam of light with power,

X [Watts], traveling in a medium of refractive index, n, can be calculated from equation 2.3.1 using the relation $X = -\frac{dE}{dt}$,

$$|F| = Q_{transfer}\frac{n}{c}X. \tag{2.3.2}$$

where $Q_{transfer}$ is a dimensionless quantity between 0 and 1 denoting the efficiency of the transfer of momentum from light to the particle resulting in force. For example, $Q_{transfer}$ depends on the size and geometry of the particle, mass and the refractive index difference between the particle and the surrounding medium [34,35]. For dielectric and metallic particles, $Q_{transfer}$ usually ranges between 0.03 and 0.1 [36].

The most conventional method for creating a 3D optical trap is to focus a laser beam with a Gaussian intensity profile using a high NA objective lens. In this section, this configuration is used to explain the optical forces acting on a trapped particle with a refractive index greater than that of the surrounding medium.

Consider a particle with refractive index higher than that of its medium illuminated by a laser beam focused using a high NA objective lens. The particle experiences two forces: the **scattering force** and the **gradient force**. The scattering force pushes the particle along the propagation direction of the beam and is the result of absorption of momentum of light by the particle or transfer of momentum from light to the particle in non-forward scattering. The gradient force pulls the particle towards the high intensity region of the beam and is the result of transfer of momentum from light to the particle when it diffracts through it (i.e. forward scattering). For the particle to be stably trapped, the net force exerted on the particle needs to be zero. In the optical trapping community, the gradient force or the trapping force is decomposed into the lateral and axial components. In a stable trap, the axial gradient force is used to counter the scattering force and should have the same magnitude, but act in the opposite direction to the scattering force. The net lateral gradient force should be zero. This is shown in Fig. 2.1.

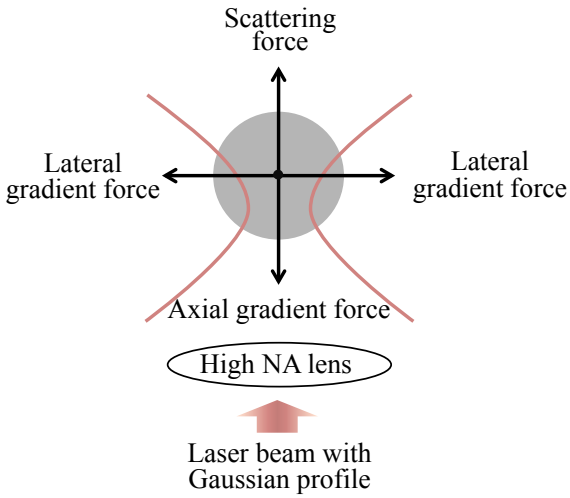


Figure 2.1: Illustration of lateral and axial forces in a 3D optical trap created at the tight focus of a beam with a Gaussian intensity profile. The trapped particle is larger than the wavelength of light.

2.3.1 Gradient force

2.3.1.1 Lateral gradient force

Figure 2.2 illustrates a scenario where a laser beam, with a Gaussian optical intensity profile (TEM mode), is incident on a solid dielectric sphere ($n_{sphere} > n_{medium}$). The dielectric sphere is placed off-axis, away from the highest intensity region of the Gaussian beam. Rays a and b represent two rays of different momentum (intensity), traveling in the same direction. The principles behind the lateral gradient force can be illustrated by considering the transfer of momentum from these two rays.

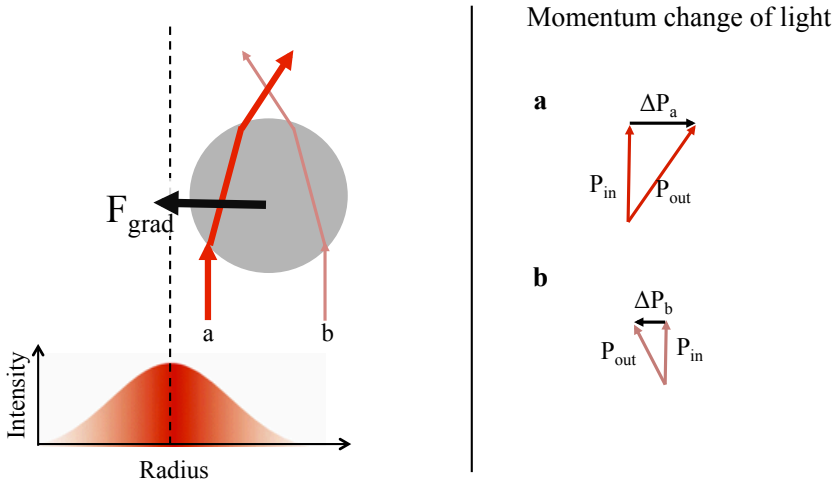


Figure 2.2: Illustration of the lateral gradient force. The change in the momentum of light after passing through the dielectric sphere produces a net restoring force, pulling the sphere towards the region of highest intensity. The scattering force is not represented in this illustration.

When light travels through the particle, the individual rays experience a change in their momentum. This is shown in the right hand size of Fig. 2.2. This momentum change between an incoming and outgoing ray ($\Delta\mathbf{P}$), is transferred to the particle resulting in a force in the opposite direction to abide by the law of conservation of momentum. In Fig. 2.2, ray a has a higher intensity compared to ray b and induces a larger momentum change. This results in the net force, F_{grad}, with magnitude equal to the total momentum change, and in the opposite direction pulling the particle towards the region of highest intensity of the beam.

2.3.1.2 Axial gradient force

When a beam of light is focused into a small high-intensity region, an intensity gradient is created near the focus of the beam in both lateral and axial directions. The magnitude of the axial gradient force is dictated by the gradient of the optical

intensity in the axial direction. In a trap created at the focus of a laser beam, this is determined by the NA of the objective lens. The principles behind the axial gradient force can be illustrated by considering the transfer of momentum to the particle from two rays showing the focusing of light using a high NA objective lens. This is shown in Fig 2.3.

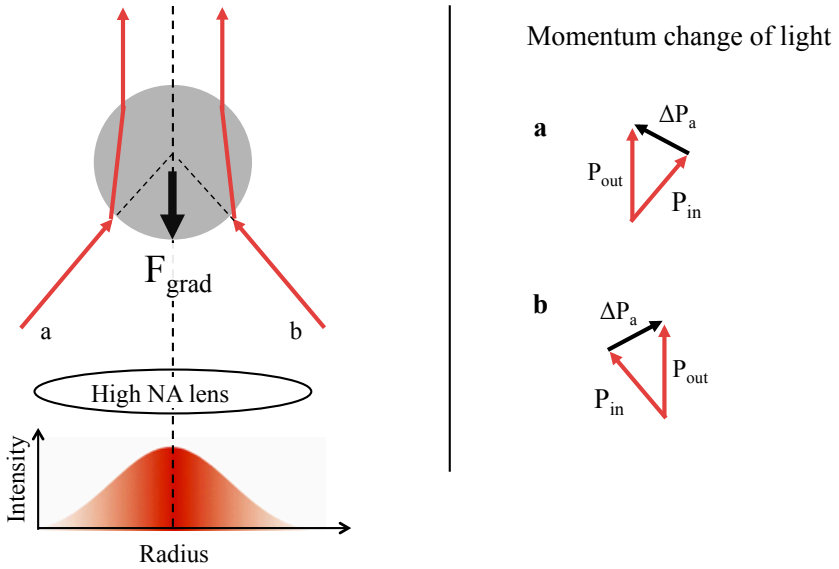


Figure 2.3: Origins of axial gradient force. The scattering force is not represented in this figure.

Increasing the NA of the objective lens increases the angle of incidence of the light rays on the trapped particle and therefore increases the gradient force in the axial direction. Increasing the beam power, increases the intensity gradient linearly. Therefore in a stable optical trap created at the focus of a laser beam, increasing the NA of the objective lens and the power of the beam both increase the strength of the trap.

2.3.2 Equilibrium position

A solid dielectric particle in a stable trap is at equilibrium slightly upstream of the focus of the laser beam. Figure 2.4 illustrates the forces leading to this equilibrium position. In this figure the particle is positioned at the centre of a beam with a Gaussian profile and does not experience a lateral gradient force. Arrows a, b, c and d represent light rays whose change in momentum results in forces exerted on the particle.

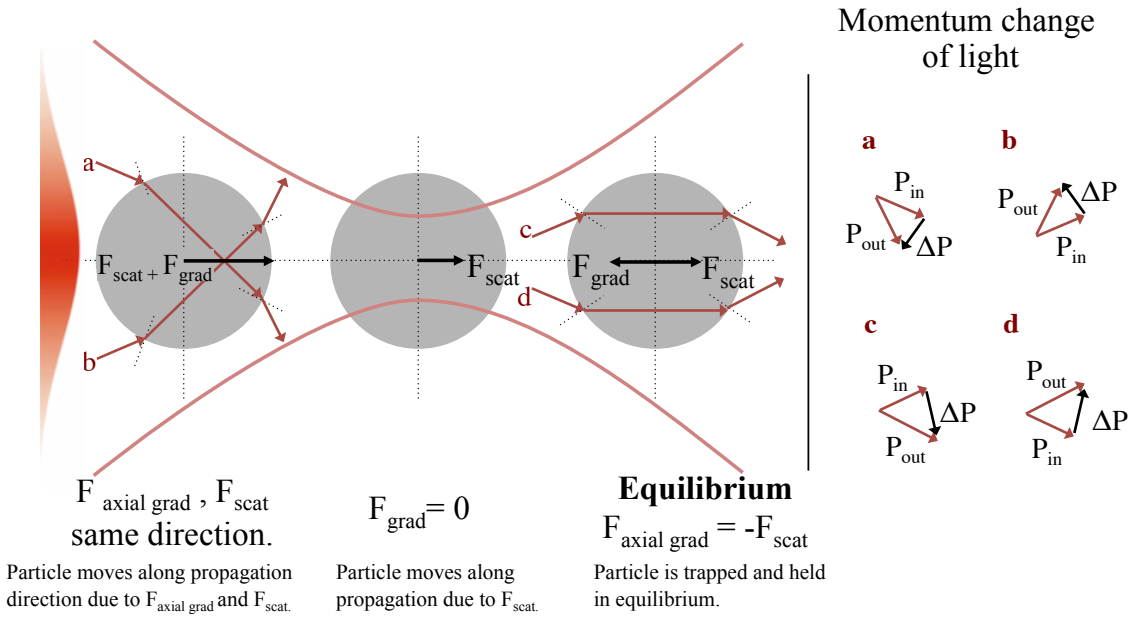


Figure 2.4: The equilibrium position in a stable optical trap. The particle is positioned at the centre of the beam (laterally) and does not experience a lateral gradient force.

If the scattering force is reduced, the equilibrium position shifts closer to the focal point of the laser beam. One way of achieving this is to illuminate the back aperture of a high NA objective lens in a way that only the large cone angles are illuminated (i.e. illuminating a ring). This removes the on-axis rays which are responsible for the

majority of the scattering force since the on-axis rays have higher intensities.

2.4 Optical trapping in Mie regime

In this regime, the particle size is comparable to the wavelength of light. The optical force exerted on a particle depends on the electromagnetic field distribution in the vicinity of the particle and the charge distribution across it. As the particle is of similar size to the wavelength of light, the charge distribution across the particle is a result of the electromagnetic field and is dependent on the shape, size and material properties of the particle. A simple approximation cannot be made to analytically calculate the forces for all particles in this regime. Instead, numerical calculations (i.e. calculating the fields across the domain) are made to evaluate the net force exerted on the particle from the electromagnetic field in each case. Note that this method of calculating the forces is accurate for all particle sizes and is not limited to the calculation of forces on particles in the Mie regime. It is interesting to also note that most optical trapping experiments are performed in the Mie regime, but in the optical trapping community, usually the forces are discussed in either the Rayleigh regime or the ray optics regime for simplicity.

The calculation of optical force on a particle in an electromagnetic field simulation, is generally based on the Lorentz force law and Maxwell's equations (please refer to section 3.1.1 for a brief explanation of Maxwell's equations). Lorentz force law describes force density, $\mathbf{f}$, as a result of an electromagnetic field as [37]:

$$\mathbf{f} = \rho\mathbf{E} + \mathbf{J} \times \mathbf{B}, \tag{2.4.1}$$

where ρ is charge density $[\frac{C}{m^3}]$, $\mathbf{E}$ is the electric field $[\frac{N}{C}]$, $\mathbf{J}$ is current density $[\frac{A}{m^2}]$ and $\mathbf{B}$ is the magnetic flux density [T]. From Gauss's law (refer to equation 3.1.1c), $\rho = \nabla \cdot \mathbf{D}$ and from Ampère-Maxwell's law (refer to equation 3.1.1b), $\mathrm{J} = \nabla \times \mathbf{H} - \frac{d\mathbf{D}}{dt}$, where $\mathbf{D}$ is electric flux density $[\frac{C}{m^2}]$ and $\mathbf{H}$ is the magnetic field $[\frac{A}{m}]$ [38,39]. Therefore

equation 2.4.1 can be written as:

$$\mathbf{f} = (\nabla \cdot \mathbf{D})\mathbf{E} + \left(\nabla \times \mathbf{H} - \frac{\partial \mathbf{D}}{\partial t}\right) \times \mathbf{B} \tag{2.4.2}$$

Assuming a linear, isotropic and nondispersive material (i.e. $\mathbf{D}$=$\epsilon\mathbf{E}$ and $\mathbf{B}$=$\mu\mathbf{H}$) where ϵ is permittivity of the medium $[\frac{F}{m}]$ and μ is permeability of the medium $[\frac{H}{m}]$), equation 2.4.2 can be written as:

$$\mathbf{f} = \epsilon(\nabla \cdot \mathbf{E})\mathbf{E} + \frac{1}{\mu}(\nabla \times \mathbf{B}) \times \mathbf{B} - \frac{1}{\epsilon}\frac{d\mathbf{E}}{dt} \times \mathbf{B}. \tag{2.4.3}$$

Using Faraday's Law of induction (refer to equation 3.1.1a) and the product rule,

$$\frac{\partial \mathbf{E}}{\partial t} \times \mathbf{B} = \frac{\partial}{\partial t}(\mathbf{E} \times \mathbf{B}) + \mathbf{E} \times (\nabla \times \mathbf{E}). \tag{2.4.4}$$

Substituting the left term of equation 2.4.4 in equation 2.4.3 and using the identity $(\mathbf{E}.\nabla)\mathbf{E} = \frac{\nabla(\mathbf{E}\cdot\mathbf{E})}{2} - \mathbf{E}(\mathbf{E} \times \mathbf{E})$ [40] yields:

$$\begin{aligned}\mathbf{f} \; &= \epsilon[(\nabla \cdot \mathbf{E})\mathbf{E} + (\mathbf{E} \cdot \nabla)\mathbf{E})] + \frac{1}{\mu}[(\nabla \cdot \mathbf{B})\mathbf{B} + (\mathbf{B} \cdot \nabla)\mathbf{B})] \\ &- \frac{1}{2}\nabla\left(\epsilon E^2 + \frac{1}{\mu}B^2\right) - \epsilon\frac{\partial}{\partial t}(\mathbf{E} \times \mathbf{B})\end{aligned} \tag{2.4.5}$$

Equation 2.4.5 describes the force density in terms of the electric and magnetic fields. It can be more compactly written using **Maxwell's stress tensor (MST)**, describing the momentum flux density, defined as [39]:

$$\sigma_{ij} \equiv \epsilon(E_i E_j - \frac{1}{2}\delta_{ij}E^2) + \frac{1}{\mu}(B_i B_j - \frac{1}{2}\delta_{ij}B^2), \tag{2.4.6}$$

where E_i and E_j are the ith and jth components of the electric field given in $[\frac{V}{m}]$, B_i and B_j are the ith and jth components of the magnetic flux density $[\frac{Vs}{m^2}]$ and δ_{ik} is the Kronecker delta (a function with two possible outcomes: if i=k the outcome is 1, otherwise it is 0) [41,42].

Taking the tensor divergence of MST (equation 2.4.6) reveals:

$$\nabla \cdot \boldsymbol{\sigma} = \mathbf{f} + \epsilon\mu\frac{\partial \mathbf{S}}{\partial t}, \tag{2.4.7}$$

where $\mathbf{S} \equiv \mathbf{E} \times \mathbf{H}$, is the Poynting vector $[\frac{W}{m^2}]$, describing the energy flux of the electromagnetic field. Therefore, total force over volume, V, can be calculated by:

$$\mathbf{F} = \iiint_V \nabla \cdot \boldsymbol{\sigma} \; dV - \epsilon\mu \frac{\partial}{\partial t} \iiint_V \mathbf{S} \; dV. \tag{2.4.8}$$

The first term of equation 2.4.8 reveals the total electromagnetic force acting on an object contained in volume, V (i.e the gradient force), and the second term of equation 2.4.8 reveals the rate of change of momentum in that volume (i.e. the scattering force). Therefore for a time-harmonic incident field (i.e. time-averaged scattering force=0) the time-averaged force can be calculated from:

$$\boxed{\langle \mathbf{F(t)} \rangle = \iiint_V \nabla \cdot \langle \boldsymbol{\sigma} \rangle \; dV = \iint_S \langle \boldsymbol{\sigma} \rangle \; dV,} \tag{2.4.9}$$

where S is the surface at the boundary of V. In other words, taking the surface integral of the time-averaged MST over the surface enclosing the particle of interest gives the time-averaged force acting on the particle.

2.5 Optical trapping in Rayleigh regime

In this regime, since the particle is much smaller than the wavelength of light ($< 20\lambda$), the electromagnetic field can be assumed to be uniform across the particle and the distribution of charges on the particle can be approximated with a dipole. For a particle with volume, V, the force exerted on the particle by the electromagnetic field is

$$\mathbf{F} = \mathbf{f}V, \tag{2.5.1}$$

where force density, $\mathbf{f}$ is given by equation 2.4.5. For a particle with polarisability, α, the optical force simplifies to [40]:

$$\boxed{\mathbf{F} = \alpha\big(\frac{1}{2}\nabla(\mathbf{E}\cdot\mathbf{E}) + \frac{\partial}{\partial t}(\mathbf{E}\times\mathbf{B})\big).} \tag{2.5.2}$$

The first term in equation 2.5.2 described the gradient force and is proportional to the intensity gradient and the second term is the scattering force, proportional to the Poynting vector. For a time-harmonic field (i.e. time-averaged scattering force = 0), the time averaged force becomes [40,43]:

$$\langle\mathbf{F(t)}\rangle = \frac{\alpha}{2}\nabla\langle\mathbf{E}\cdot\mathbf{E}\rangle. \tag{2.5.3}$$

Equation 2.5.3 reveals that the gradient force on a Rayleigh particle is proportional to the intensity gradient and the polarisability of the particle.

When trapping with a standard high NA objective lens, the system is limited by diffraction and the gradient changes over a micron-sized focal region. Therefore trapping in the Rayleigh regime is only possible for nanoparticles with high α. During this project the aim was to design structures that can provide nanometre scale high-intensity "hot-spots". These hot-spots create high intensity gradients on the nanoscale and are therefore capable of trapping nanoparticles.

2.6 Measuring the optical trapping force

Trap stiffness:

In a stable trap, the optical trapping force follows a linear trend with displacement from equilibrium, $\mathbf{x}$, when $\mathbf{x}$ is small (typically less than half of the size of the trapped object) [14,44]. In this case, the strength of the optical trapping force can be modelled by Hooke's law, using a spring of stiffness, k, so that:

$$\mathbf{F} = -k\mathbf{x}, \tag{2.6.1}$$

where $\mathbf{x}$ is the displacement from the equilibrium position. The trapping potential energy, U_{trap} is given by:

$$U_{trap} = \frac{1}{2}k\mathbf{x}^2. \tag{2.6.2}$$

The strength of an optical trap is usually characterised using the trap stiffness, k, given in equation 2.6.2. This section briefly describes a few methods used for measuring k of an optically trapped particle.

Trap potential:

Normally, the potential distribution created by a 3D optical trap is represented using a potential well. Figure 2.5 illustrates a 2D projection of a potential well for a 3D optical trap. The depth of the potential well is determined by the optical trapping (gradient) force. This means that by increasing the optical trapping force, the corresponding potential well deepens. The depth of the potential well corresponds to the energy required to remove the particle from the trap . Ashkin established a rule of thumb to achieve a stable trap stating that the depth of the potential well of a trap should be 10 times the thermal energy to compensate for the stochastic kicks in the particle motion. i.e. [45].

$$U_{opt} > 10k_BT, \tag{2.6.3}$$

where k_B is Boltzmann's constant ($\approx 1.38 \times 10^{-23}$ $[\frac{m^2kg}{s^2K}]$) and T is the absolute temperature in [K] [46].

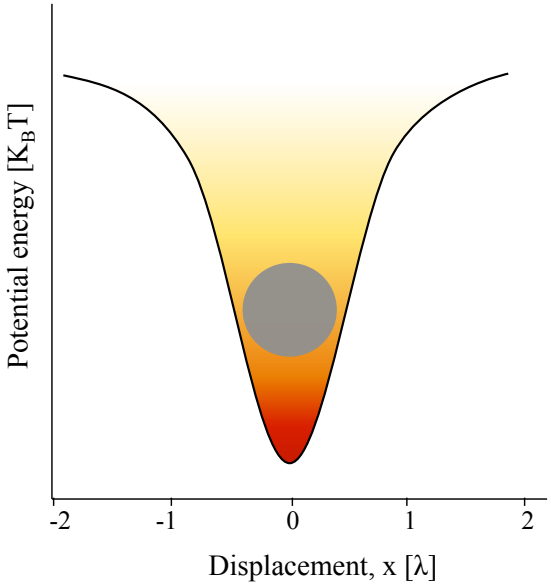


Figure 2.5: A typical potential well associated with the gradient force. For small x, U_{trap} follows the equation 2.6.2.

The physical size of this potential well is determined by the field distribution. In a 3D trap created at the focus of a laser beam, this size is limited by diffraction.

As the particle size decreases, the depth of the optical potential well decreases. This is because of two effects: firstly, reducing the size of the particle in the trap reduces the gradient force on the particle and secondly, reducing the particle size reduces the viscous drag force (or fluid resistance) exerted on the particle [46] against its motion. Please refer to section 2.6.3 for information of viscous drag force.

In order to determine the motion of the particle in the trap, inertial, viscous and optical forces on the particle should be taken into account. Measuring the trap motion and knowing the inertial and viscous drag force acting upon the particle in trap can reveal the trap strength.

Viscous drag force is the force exerted on a stationary sphere in a fluid flow. It is given by Stoke's law for fluids with laminar flow (i.e. low Reynolds number)

as [30,47]:

$$|F_{drag}| = 6\pi\eta r\mathbf{S}, \tag{2.6.4}$$

where $\mathbf{S}$ is the velocity of the fluid $[\frac{m}{s}]$, η is the viscosity of the fluid [PI] and r is the radius of the sphere.

Motion of the particle in the trap:

The motion of a trapped particle is governed by the sum of inertial, viscous and elastic forces [47,48]:

$$m\frac{\partial^2 x}{\partial t^2} + \beta\frac{\partial x}{\partial t} + kx = 0, \tag{2.6.5}$$

where m is the mass of the object [kg], $\beta = 6\pi\eta r$ is the viscous damping given by Stoke's law, and k is the trap stiffness.

2.6.1 Equipartition of energy

A particle in a solution has Brownian motion (random movement) due to heat. If it is in an optical trap, the potential energy of the trapped particle should be the same as the thermal energy of the particle from the equipartition theorem:

$$\frac{1}{2}k_B T = \frac{1}{2}k\langle x\rangle^2, \tag{2.6.6}$$

where k_B is the Boltzmann's constant, T is the absolute temperature [K], $\langle x\rangle^2$ is the variance of the position fluctuations $[m^2]$ and k is the trap stiffness (spring constant of the trap). Therefore, by measuring the variance of the position of the trapped particle and knowing the absolute temperature of the system, the trap stiffness can be calculated [49].

This method is very popular, since it can provide an accurate calculation of the trap stiffness without needing to know parameters such as the viscosity of the medium

and size and shape of the trapped particle. This method is used for the calibration of the optical trapping forces throughout this project.

2.6.2 Frequency-spectrum method

When a particle is trapped in a fluid with laminar flow (i.e. low Reynolds number) [30,47], viscosity is the dominant effect in equation and inertial effects in the liquid can be neglected. Therefore, equation 2.6.5 can be re-written using the overdamped Langevin equation:

$$kx + \beta\dot{x} = \xi(t), \tag{2.6.7}$$

where $\xi(t)$ is the Langevin force obeying:

$$\xi(t) = 0, \tag{2.6.8a}$$

$$\langle \xi(t)\xi(t+\tau)\rangle = 2\eta k_B T\delta(\tau), \tag{2.6.8b}$$

where k_B is Boltzmann's constant and T is the temperature [K]. Taking the Fourier transform of equation 2.6.7 with respect to time gives the frequency spectrum of the position fluctuations of the particle:

$$G(f) = \frac{2|\hat{x}(f)|^2}{t_{int}} = \frac{k_B T}{\pi^2\Gamma(f_c^2 + f^2)}, \tag{2.6.9}$$

where t_{int} is the interval between two position measurements and f_c is the cut-off frequency. Assuming that the laser light does not contribute to sample heating, the trap stiffness, k, can be calculated from the frequency spectrum:

$$k = 2\pi\beta f_c. \tag{2.6.10}$$

Although this method is considered one of the most reliable methods for calculating k, this method is not used in this project. This is because the assumption that the laser not contributing to the sample temperature may not be accurate in nanoplaasmonic trapping experiments, the need for the particle to be spherical and of known size and the need for viscosity of fluid to be known [49,50].

2.6.3 Viscous drag force

The total optical trapping force required to remove the object from the trap can be calculated directly from the drag force exerted on a bead when under liquid flow. Fluid flow of constant velocity can be created using a programmable microscope stage. Moving the stage at a constant speed without changing the direction of movement, creates a liquid flow with a constant velocity. At the critical speed of the fluid flow, v_c at which the drag force removes the particle from the trapping well, the drag force given by Stoke's Law is equal to the optical trapping force so that [44,48,51,52]:

$$F_{trap} = 6\pi\eta r v_c.$$

Here the inertial force on the particle is much smaller than the drag force and is therefore neglected [53].

2.7 Applications and advances of optical trapping

2.7.1 Far-field optical trapping

Since its introduction in the 1970's, optical tweezers, with forces in the pico-Newton scale have become an established optical technique. In their simplest, most conventional setting, they use an objective lens with a high numerical aperture (NA) to focus a laser beam to a diffraction limited spot at which micron sized particles are easily trapped and manipulated [54]. This scheme of trapping is known as "far-field" optical trapping because the optical trap is created at the propagating far-field of the focused laser beam. They are employed in a broad range of disciplines including life-sciences [55], physics [56,57] and chemistry [58,59].

In life sciences, examples of application of optical tweezers include deforming human red blood cells to study their mechanical properties providing insight in the diagnostics of diseases such as Leukaemia and malaria [60–62], stretching DNA to understand their fundamental mechanical behaviour leading to folding, packaging and replication [63], trapping bacteria and viruses [11], cell sorting [64] and internal cell manipulation [65]. Direct far-field trapping of transparent nano-sized objects, such as viruses and DNA, is not possible due to the diffraction limit and requirement for high polarisability of the particle. To trap them, the nano-particles of interest are usually fixed to a micron sized bead. Trapping and moving micron sized beads, allows the study and manipulation of nano-particles in far-field traps. Direct trapping of metallic nanoparticles (>50 nm in diameter) is possible for short durations in well designed far-field traps using high optical powers [66]. This is due to the high polarisability of the metallic particles, resulting in much higher forces compared to dielectric particles of similar size [31,67].

Advances in far-field tweezers include using spatial light modulators (SLMs) [64], projecting optical images [68] and computer generated holograms [69] to produce beams with complex electromagnetic field distributions at the focal plane such as the creation of a donut shaped illumination (removing the on-axis rays, reducing the scattering force in a conventional optical trap) [70] and multiple focal points. This can be used to increase the throughput of the optical trapping experiment and near-field imaging using a trapped particle [71].

2.7.2 Near-field optical trapping

To extend optical trapping beyond the diffraction limit, the use of evanescent fields has been investigated [72–85] and experimentally demonstrated [46,73,86–92]. Such optical traps are created by the non-propagating component of the field decaying rapidly with distance, leading to the term “near-field” optical traps.

Near-field optical traps are created using several methods including: creation of evanescent standing waves, interference patterns and focused light by total internal reflection (illumination) [72,73,87], by illumination of metallic nanostructures including metallic tips [74,82,88–90,93] and, illumination of metallic nanoapertures [77,79,80,90,94] and the use of the evanescent field from photonic cavities such as ring resonators and photonic crystal (PhC) cavities [84,85,92]

Near-field optical traps created at the vicinity of metallic nanostructures (including nanoapertures and nanoantennas) are referred to as "nanoplasmonic tweezers" [91,95]. They take advantage of the localised surface plasmon (LSP) for producing nano-scale high-intensity "hot-spots" (please refer to section 4.3.1.1 for an explanation of LSP) which enable trapping and manipulations of sub-micron particles [96]. The most popular designs of nanoplasmonic tweezers include arrays of pairs of nanoantennas with a nanometre-sized gap between them. Inclusion of the gap increases the light confinement by up to three orders of magnitude (please refer to section 4.3.1.1 for more explanation).

The first nanoplasmonic tweezer based on the illumination of nanostructured substrates was demonstrated by Grigorenko *et al.* in 2008 [88]. This was done by illuminating electromagnetically coupled pairs of gold nanodots using a conventional optical trapping set-up to trap 200nm dielectric beads. Figure 2.6(a) demonstrates the set-up used to create nanoplasmonic traps in this case. In 2009 Righini *et al.* demonstrated high-throughput optical trapping of particles in the range of 1μm to 200nm and aligning of Ecoli using arrays of rod-nanoantennas illuminated under total internal reflection using a hemispherical glass lens [89,97]. Figure 2.6(b) illustrates this set-up. In 2011, Pang *et al.* demonstrated optical trapping and unfolding of a single protein with radius of 3.4nm using a double-nanohole aperture illuminated using a conventional optical tweezer set-up [94]. They also demonstrated that by monitoring the shifts in the spectra of the nanoaperture, trapping and folding events can be detected. This is shown in Fig. 2.6(c). In 2016, a similar set-up was

used by Mestres *et al.*, to study the optomechanical nature of plasmonic trapping by trapping 50nm gold particles at the gap of bowtie-shaped apertures of different size in a gold film [98]. Their set-up is shown in Fig. 2.6(d).

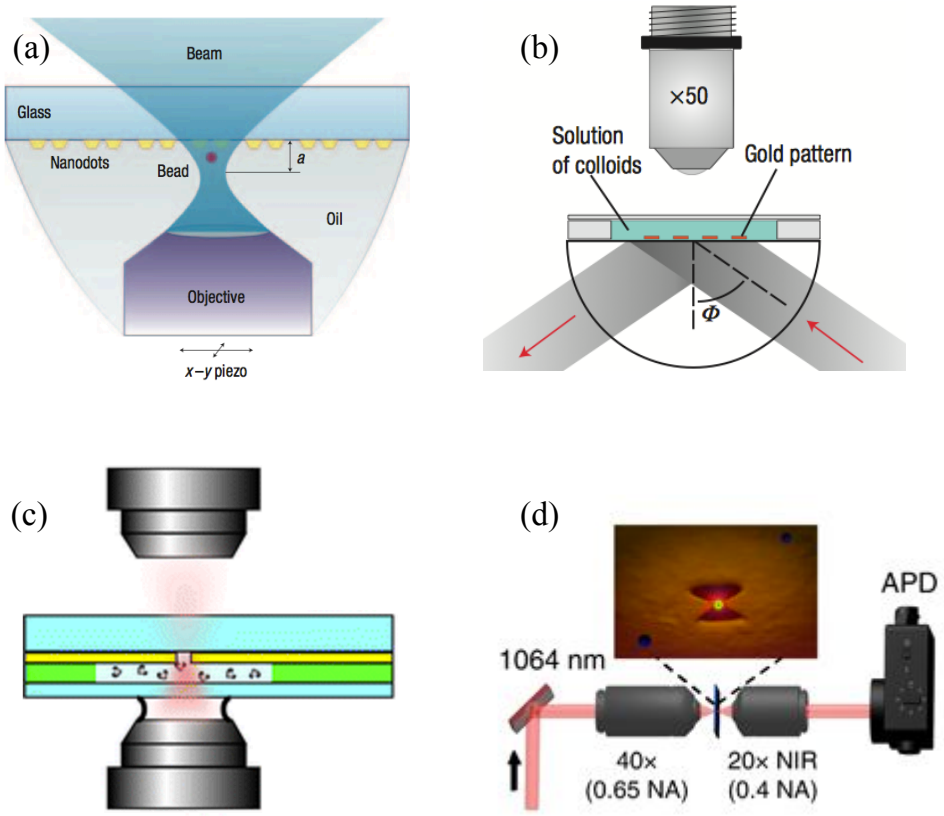


Figure 2.6: Illustration of nanoplasmonic tweezer setups created by (a) illumination of nanoplasmonic antennas in a conventional optical trapping set-up [88] (reproduced from Grigorenko *et al.*), (b) by illumination of the nanoantennas under total internal reflection using a hemispherical glass lens (courtesy of Righini *et al.*) [97] and (c, d) by illumination of an aperture using a focused laser beam [94,98]. Courtesy of Pang *et al.* and Mestres *et al.* respectively.

Using illuminated metalic nanostructured surfaces instead of conventional traps has its downfalls. Optical trapping forces are only felt at the near-field of the nanopatterned surfaces, the location of the trapping sites are predetermined and 3D trapping is difficult. Recently, some efforts have been made to combine photonic and plas-

monic devices, creating less bulky and more energy-efficient optical tweezers capable of nano-manipulation [99–101]. For example Berthelot *et al*. demonstrated optical trapping of 50nm dielectric particles at the tip of a fibre with a bowtie-shaped nanoaperture in 2014 [99]. This is shown in Fig. 2.7. This set-up allows more control over the 3D position of the trapped particle. Recently, some efforts have been made to use the trapped particle itself to play an active role in enhancing the restoring force, this effect is referred to as "self-induced back-action" (SIBA) and can be utilized for creating a more stable nanoplasmonic trap. [102,103].

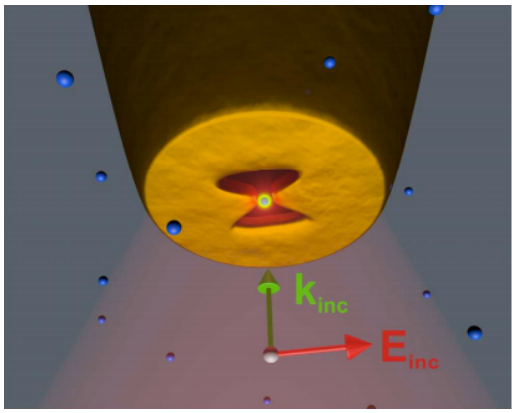


Figure 2.7: Illustration of nanoplasmonic tweezer created at the gold coated tip of an optical fibre with a bowtie-shaped nanoaperture [99].

Nanoplasmonic trapping using hybrid photonic-plasmonic devices has great potential for creating tailored devices that suit specific applications. These devices are less bulky compared to conventional traps, are more energy efficient and can be made user-friendly. The design of a hybrid photonic-plasmonic device will be presented in this thesis as well as a nanoplasmonic trap created by the illumination of an array of gold nanoantennas.

2.8 Summary

This chapter began by presenting a brief history of optical trapping. The mechanism behind optical trapping was then described in the ray-optics, Mie and Rayleigh regimes, showing that both the gradient force and the scattering forces are increased by increasing the optical intensity of the beam (power) and that the gradient force also increases by increasing the gradient of the optical field. Some methods of characterization of optical traps including the equipartition were then described. This was followed by describing the advances and applications of far-fied and near-field optical tweezers. It was discussed that far-field optical tweezers are created by the propagating component of the electromagnetic field whereas near-filed optical tweezers are created by the non-propagating, evanescent field. Far-field optical tweezers are diffraction limited and are normally used to trap micron-sized dielectric particles, whereas near-field tweezers can create nanometer-sized hot-spots that can be used to trap nanoparticles. The rise of hybrid photonic-plasmonic devices was discussed mentioning that they could potentially be used widely to trap nanoparticles due to their energy efficiency and the removal of bulky optics used in conventional and nanoplasmonic tweezers.

3

Numerical modelling tool, FDTD

This chapter describes the modelling tool used for the design and investigation of the devices presented in Chapters 4 and 5. The chapter begins by presenting a brief explanation of electromagnetics, including Maxwell's equations. This is followed by a brief introduction of some of the commonly used numerical methods for solving Maxwell's equations. The technique used in this work, the finite-difference time-domain (FDTD) method is then studied in more detail, looking at the meshing, time-step, sources, boundary conditions and convergence. A description of the common steps taken for setting-up a FDTD simulation and producing meaningful results follows this. A short summary concludes this chapter.

3.1 Electromagnetics background

3.1.1 Maxwell's equations

In the 1860's, James Clerk Maxwell presented a series of 20 equations for describing the electromagnetic phenomena. Around twenty years after his death, Oliver Heaviside and Heinrich Hertz reduced these equations to four coupled first-order

differential equations and presented the Maxwell's equations as we know them today [39,104–106]. Maxwell's equations consist of Faraday's law of induction, Ampère-Maxwell's law and Gauss' laws for electric and magnetic fields. Together, these equations mathematically relate electric charges with static electric fields and induced electric and magnetic fields. Faraday's law states that a magnetic field, changing with time, induces an electric current around a circuit: Ampère's law states that a flowing electric current induces a magnetic field around it and Maxwell's addition to this law is that a changing electric field behaves just like an electric current. These two laws together describe the propagation of electromagnetic waves. Gauss' law for electric fields states that the flux of the electric field exciting normal to a closed surface is equivalent to the electric charge enclosed by the surface. Gauss' law for magnetic fields states that magnetic charges (or magnetic monolpoles) do not exist. In differential form, Maxwell's equations can be expressed as:

$$\text{Faraday's law} \qquad \nabla \times \mathbf{E} = -\frac{\partial \mathbf{B}}{\partial t}, \tag{3.1.1a}$$

$$\text{Ampère-Maxwell's law} \qquad \nabla \times \mathbf{H} = \mathbf{J} + \frac{\partial \mathbf{D}}{\partial t}, \tag{3.1.1b}$$

$$\text{Gauss's law (electric field)} \qquad \nabla \cdot \mathbf{D} = \rho, \tag{3.1.1c}$$

$$\text{(magnetic field)} \qquad \nabla \cdot \mathbf{B} = 0, \tag{3.1.1d}$$

where $\mathbf{E}$ is the electric field $[\frac{N}{C}]$, $\mathbf{H}$ is the magnetic field $[\frac{A}{m}]$, $\mathbf{D}$ is the electric flux density $[\frac{C}{m^2}]$, $\mathbf{B}$ is the magnetic flux density $[T]$, ρ is the charge density given in $[\frac{C}{m^3}]$ and $\mathbf{J}$ is the electric current density $[\frac{A}{m^2}]$. $\mathbf{E}$, $\mathbf{H}$, $\mathbf{D}$, $\mathbf{B}$ and $\mathbf{J}$ are all vectors and functions of space and time [107]. Maxwell's equations in differential form hold for field vectors when they are continuous. At the boundaries between two media however, some extra conditions have to be applied to ensure continuity.

In integral form Maxwell's equations are given by the integration of equations (3.2.1a) and (3.2.1b) through an arbitrary surface, A, and the integration of equations (3.2.1c) and (3.2.1d) over an arbitrary volume, V, using Stoke's theorem and

divergence theorem respectively, yielding:

$$\oint_{\partial A} \mathbf{E} \cdot d\mathbf{s} = -\frac{\partial}{\partial t} \iint_{A} \mathbf{B} \cdot d\mathbf{A}, \tag{3.1.2a}$$

$$\oint_{\partial A} \mathbf{H} \cdot d\mathbf{s} = \iint_{A} \mathbf{J} \cdot d\mathbf{A} + \frac{\partial}{\partial t} \iint_{A} \mathbf{D} \cdot d\mathbf{A}, \tag{3.1.2b}$$

$$\oiint_{\partial V} \mathbf{D} \cdot d\mathbf{A} = \iiint_{V} \rho \, dV = Q, \tag{3.1.2c}$$

$$\oiint_{\partial V} \mathbf{B} \cdot d\mathbf{A} = 0, \tag{3.1.2d}$$

where ∂A and ∂V stand for the borders of domain A and V respectively, and Q stands for the electric charge enclosed in volume V, given in $[C]$. The integral form of Maxwell's equations is particularly useful when propagating the electromagnetic wave at curved interfaces between two materials when solving Maxwell's equations to reduce errors [108]. Other than this, the differential form of Maxwell's equations will be used throughout this thesis.

3.1.2 Constitutive relations

In dielectric materials, Maxwell's equations alone are not sufficient. They describe the relation between charges, currents and fields, but they do not describe the macroscopic field inside materials. To do this, the material properties need to be related to $\mathbf{E}$ and $\mathbf{H}$ (the constitutive relations). These properties are expressed using the polarization density, $\mathbf{P}$, and the magnetization density, $\mathbf{M}$. They describe the behaviour of matter under electric and magnetic fields as $\mathbf{D} = \epsilon_0\mathbf{E} + \mathbf{P}$ and $\mathbf{B} = \mu_0\mathbf{H} + \mathbf{M}$, where ϵ_0 and μ_0 are the electric permittivity $[\frac{F}{m}]$ and magnetic permeability of vacuum $[\frac{H}{m}]$ respectively. Generally, $\mathbf{P}$ is a function of $\mathbf{E}$, space and time, while, $\mathbf{M}$ is a function of $\mathbf{H}$, space and time. In linear, isotropic and non-dispersive materials,

with linear electric loss, the constitutive relations simplify to:

$$\mathbf{D} = \epsilon \mathbf{E}, \tag{3.1.3a}$$

$$\mathbf{B} = \mu \mathbf{H}, \tag{3.1.3b}$$

$$\mathbf{J} = \sigma \mathbf{E}, \tag{3.1.3c}$$

where ϵ is the electric permittivity (or the electrical dielectric constant) of the medium $[\frac{F}{m}]$, μ is the magnetic permeability of the medium $[\frac{H}{m}]$and σ is the electrical conductivity of the medium given in $[\frac{S}{m}]$.

3.1.3 Refractive index and material impedance

Refractive index, n, is a more tangible property in materials compared to ϵ and μ. It is a measure of the phase velocity, v, of the electromagnetic wave passing through a material and is defined as:

$$n \equiv \frac{c}{v}, \tag{3.1.4}$$

where c is the speed of light. Note that the wavelength of a material relates to its phase velocity by $f = \frac{v}{\lambda} = \frac{c}{n\lambda_0}$. That is the frequency of the electromagnetic wave, does not change while traveling through a material, just its phase velocity and wavelength. Refractive index is related to the complex relative permittivity and permeability of a material ϵ_r and μ_r by:

$$n = \sqrt{\epsilon_r \mu_r}. \tag{3.1.5}$$

This is derived by calculating the speed (phase velocity) of light in the material from the wave equation (refer to section 3.1.4). Since most materials used in photonics

are not magnetic (i.e. μ=μ_0, $\mu_r = 1$),

$$n \approx \sqrt{\epsilon_r}. \tag{3.1.6}$$

The relative permittivity (ϵ_r) of a material is sometimes referred to as the **dielectric constant**. It is a complex number where the imaginary part relates to attenuation. In metals for example, the imaginary part of the dielectric constant is high, since metals are lossy due to their high polarisability. The real part of ϵ_r represents polarisability and is often larger than 1 for dielectrics, but it can be designed to be a negative value (metamaterials demonstrating exotic behaviours such as super lensing). The numerical fits and and experimental values for the dielectric constant used to represent each material in the simulations in this thesis are listed in AppendixA.

Material impedance is the relation between electric and magnetic fields when an electromagnetic wave travels through a material. It is the most fundamental quantity that causes reflections and scattering [39].

$$\eta = \frac{|\mathbf{E}|}{|\mathbf{H}|} = \eta_0 \sqrt{\frac{\mu_r}{\epsilon_r}}. \tag{3.1.7}$$

where, the impedance of vaccum, $\eta_0 \approx 377\Omega$, showing that the electric field is much larger than the magnetic field in vacuum. This holds for most materials. When introducing sources in FDTD, η is used to make sure the ratio of the electric and magnetic fields generated in the material is correct.

3.1.4 The wave equation

It is useful to also show the Helmholtz wave equation ("the wave equation") because it allows for a simple representation of the induced electromagnetic fields in terms of the electric field. It is derived from the time-varying terms of Maxwell's equations (Faraday's and Ampère-Maxwell's laws). Assuming an isotropic, nondispersive, and

source-free region (i.e. ρ=0 , J=0), taking the curl of both sides of equation (3.1.2a) and substituting it in the equation (3.1.2b) yields the wave equation:

$$\nabla^2\mathbf{E} - \epsilon\mu\frac{\partial^2\mathbf{E}}{\partial t^2} = 0, \tag{3.1.8}$$

where ∇^2 is the Laplacian of the vector field. For simplicity, we assume that the electric field is TE-polarized along the x-direction ($E_y = E_z = 0$) and is propagating in the z direction. This results in a simple wave equation of the form $\partial^2 E_x/\partial z^2 = \mu\epsilon\partial^2 E_x/\partial t^2$. This equation has a solution of the form $E_x = f(z - vt)$ and $v = \frac{1}{\sqrt{\mu\epsilon}}$, is the phase velocity. For the wave travelling in vacuum, the phase velocity is the speed of light, $c = \frac{1}{\sqrt{\mu_0\epsilon_0}}$

3.1.5 Boundary conditions at interfaces

At the interfaces between two materials, boundary conditions can be derived by applying Maxwell's equations in the integral form to small regions at the interface of the two media [109]. A derivation of boundary conditions for electromagnetic fields from the integral form of Maxwell's equations is given in reference [110]. In simple terms, there are three main conditions dictated by Maxwell's equations together with the constitutive relations that need to be fulfilled when an electromagnetic wave crosses an interface between two materials [109,111]. These are illustrated in Fig. 3.1 and are as follows:

- Tangential components of the electric and magnetic fields, E_T and H_T, are continuous across the interface.
- The normal components of electric displacement flux density and magnetic flux density, D_N and B_N, are continuous across the interface.
- The tangential component of the wave vector, k_T, is continuous across the interface. This is a consequence of the previous two conditions.

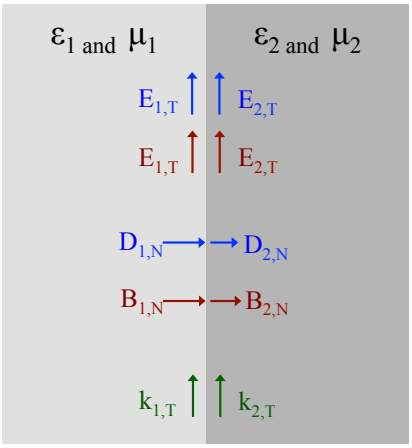


Figure 3.1: Simple representation of the boundary conditions imposed on the electromagnetic wave as it travels at the interface of two materials.

3.2 Numerical solutions to Maxwell's equations

Even though Maxwell's equations, together with the constitutive relations, form a self-consistent set of equations, non-uniform boundary conditions and complex geometries make them very difficult to solve in most real-life cases. The analytical solution is realistically possible only for simple geometries, such as infinite cylinders and spheres [112].

Various numerical techniques are used to solve Maxwell's equations for real-life applications involving complex materials and geometries. These techniques can be separated into two main classifications: time-domain and frequency-domain methods. Time-domain methods produce results over a large frequency window usually by propagating a wave of short duration (tens to hundreds of femto-seconds) through a discretized space. Recording the time varying field and taking its Fourier transform reveals the frequency response of the device. Time-domain methods are ideal for device design, where the features of the device are of the order of the wavelength of light (in free space) or smaller. This is because by propagating a small time-

signal, the response of the device can be studied over a large number of frequencies in the frequency domain (according to Fourier's theorem). Frequency-domain methods produce results over a large time-window, but each simulation only produces results at a single frequency. Here a few of the most popular methods for solving Maxwell's equations are briefly introduced [112–114].

Finite-difference time-domain (FDTD) method is used throughout this project for the design and numerical study of photonic, plasmonic and hybrid photonic-plasmonic devices. FDTD is a time-domain method that uses a time-difference approximation for spatial and temporal derivatives in the differential form of Maxwell's equations (equations (3.1.1)) on two stacked grids. A more extensive description of FDTD will be given in the subsequent sections.

Finite integration technique (FIT) is a time-domain method that solves the integral form of Maxwell's equations (equations (3.1.2)) across a grid. If a rectangular grid is used for the FIT method, FIT and FDTD produce almost identical results when the material properties are well defined in the two simulations [115].

Transmission line method (TLM) is a time-domain technique with similar capabilities compared to FDTD. In this technique, the simulations are performed across a single grid (as opposed to two stacked grids in FDTD). The nodes of grids in TLM are connected by virtual RLC transmission lines (where R is resistance, L is inductance and C is capacitance) . In other words instead of directly solving E and H, at each iteration (time step), voltages and currents are updated [116,117]. Krumpholz, *et al.* gives a good theoretical comparison between 3D TLM and 3D FDTD, wherein the advantages of FDTD are revealed (most importantly, the TLM method is unconditionally stable, but using the FDTD method the user needs to make sure that the time-space stability condition is met (refer to section 3.3.6) to achieve stable results) [118]. In this project the choice of FDTD over TLM was only due to the popular choice of FDTD for simulation of photonic crystals. This

enabled direct comparison of results obtained during this PhD with the majority of publications in the field.

Finite-element method (FEM) can operate in both time and frequency domains. It is mostly used in the field of optics in frequency-domain since achieving a stable model in time-domain is challenging [119]. It can loosely solve Maxwell's equations by breaking the domain into smaller non-overlapping elements and forming a set of linear partial differential equations using the mean weighted residual method. Since the meshing (creation of smaller domains) is unstructured, this method is more accurate than FDTD at the sharp corners and curved boundaries between materials. The disadvantage of FEM is that due to this unstructured mesh, solving 3D simulations (and large 2D simulations), requires excessive computation time and huge memory space for storing the matrix entries that limits its impractical use [120–122].

3.3 Finite-difference time-domain method

The FDTD algorithm for numerically solving Maxwell's equations in time domain for initial boundary value problems in isotropic media was pioneered by Kane S. Yee in 1966 [111,123]. The algorithm employs the finite difference approximation for both spatial and temporal derivatives to numerically solve the coupled Maxwell's curl equations (i.e. equations (3.1.1a) and (3.1.1b)).

3.3.1 Finite difference approximation and its error

The finite difference approximation to the derivative of a function is given in equation (3.3.1) and derived by expanding the function $f(x)$ over the point x_0 by $\pm\delta$ using the Taylor series expansion, subtracting the two series and dividing by δ [124]. This

is shown in Fig. 3.2.

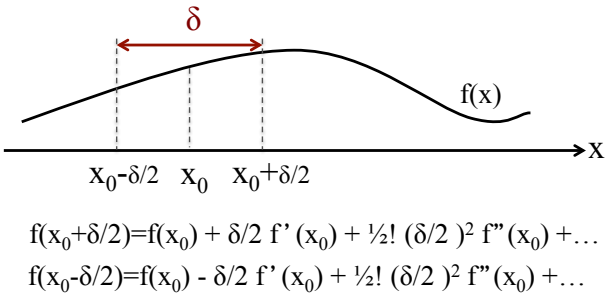


Figure 3.2: Taylor expansion of f(x) around x_0 by $\pm\frac{\delta}{2}$. f' denotes the derivative of function f.

$$\left.\frac{\partial f(x)}{\partial x}\right|_{x=x_0} = \frac{f(x_0+\frac{\delta}{2}) - f(x_0-\frac{\delta}{2})}{\delta} + O(\delta^2) \approx \frac{f(x_0+\frac{\delta}{2}) - f(x_0-\frac{\delta}{2})}{\delta}, \quad (3.3.1)$$

where $O(\delta^2)$ stands for the error in the approximation and denotes that it is of the order δ^2. As the largest power term ignored in the approximation is second order, the approximation is accurate to the second order. In other words, if δ is reduced by a factor of 2, the error is reduced by a factor of 4.

3.3.2 The Yee cell

Yee proposed a novel Cartesian grid, staggered in space and time where **E** and **H** are distanced by half a time step and positioned half a cell away from each other in a way that each E component is surrounded by four H components and each H component is surrounded by four E components (analogous to the Maxwell's curl equations). This means that in FDTD the electric and magnetic components are never calculated at the same position and time. The unit cell of this grid in space, the Yee cell, is shown in Fig. 3.3.

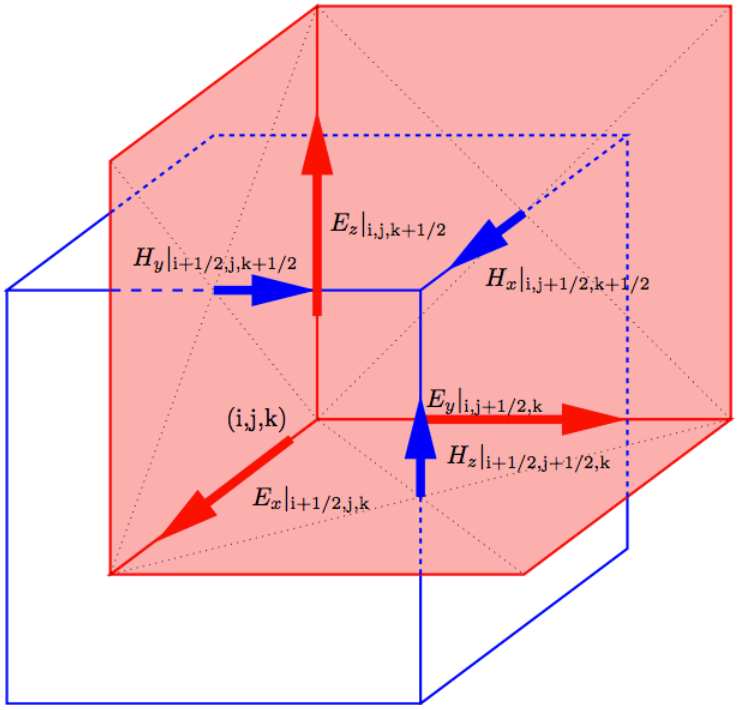


Figure 3.3: Illustration of the Yee cell staggered in space. Reproduced from Benkler [112].

3.3.3 The FDTD algorithm

In this algorithm, first the space (and time) is discretised, thenthe temporal and spatial derivatives of Maxwell's curl equations are replaced with finite difference terms, the space is discretized using the Yee-cell approach (E and H components are half a cell away from each other). The difference equations are then solved to obtain "update equations" at half a time step (δt) ahead, that expresses the future fields in terms of the known past fields (leap frog scheme). For example, E at time t is calculated in terms of E at time $t - \delta t$ and H at time $t - 0.5\delta t$. Note that the calculations for time t and time $t + 0.5\delta t$ are performed during a single iteration of the program to increase simulation speed. This process is repeated alternating between E and H components until the required time is reached [111,124]. Figure 3.4 shows an example of this iteration for a simple case of 1D FDTD. Note that in

FDTD, the E and H fields do not coexist in the same location and are calculated for different times. In real life, however, the electric and the induced magnetic fields coexist at the same points in space and time (and vice-versa).

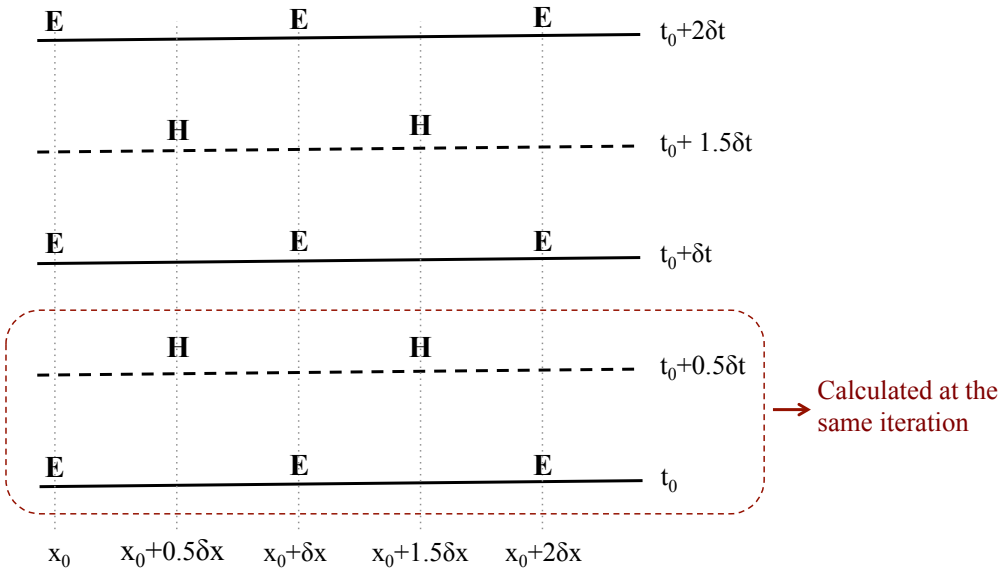


Figure 3.4: Illustration of the temporal iteration of the FDTD method in 1D. $\mathbf{E}|_{t_0}$ and $\mathbf{H}|_{t_0+0.5t_0}$ are calculated during the same computational iteration.

3.3.3.1 The update equations

The "update equations" used in FDTD are derived from substituting the material properties or the constitutive relations (equations (3.1.3a) and (3.1.3b)) in Maxwell's curl equations (equations (3.1.1a) and (3.1.1b)) and applying the finite-difference approximation to the derivatives in time and space. For a simple case of 1D FDTD, the "update equations" predicting "future fields" in terms of "past fields" read:

$$\mathbf{H}|_{t0+\frac{\delta t}{2}} = \mathbf{H}|_{t0-\frac{\delta t}{2}} - \frac{\delta t}{\mu}(\nabla \times \mathbf{E}|_{t0}), \tag{3.3.2a}$$

$$\mathbf{E}|_{t0+\delta t} = \mathbf{E}|_{t0} + \frac{\delta t}{\epsilon}(\nabla \times \mathbf{H}|_{t0+\frac{\delta t}{2}}). \tag{3.3.2b}$$

The same concept is applied in space, following the right hand rule on the grid.

3.3.4 Meshing

The discretization of space (computational domain) is called meshing. Meshing plays a critical role in FDTD simulations and, together with the domain size, determines the accuracy, speed and computational requirements (memory) for the simulation. In a uniform rectangular 3D grid, increasing the number of mesh points, improves the accuracy of the results (power of 2) at the cost of longer simulation time (power of 4) and memory requirements (power of 3) . The Nyquist-Shannon theorem dictates that the numbers of mesh points per wavelength to be higher than 4. This is often too small for modelling EM waves propagating through structures with features of the same order or smaller than the wavelength of light. A good analysis needs to be made for each structure, choosing the most suitable number of mesh points in each region. As a rule of thumb, the number of mesh points per wavelength should be kept higher than 10 (refer to section 3.3.6) giving at least 97.8% accuracy in the speed of light, given that the time-step constraints for stability are met (refer to section 3.3.6). In the simulations performed during this project, the number of mesh points in each wavelength was kept above 20.

3.3.4.1 Non-uniform meshing, conformal mesh CFDTD

Non-uniform rectangular grid

To reduce numerical and staircasing errors (due to discretization), usually the number of mesh points are increased when entering a material of higher refractive index to keep the number of mesh points per wavelength constant. This is because the speed of the wave in a material of refractive index n is $\frac{c}{n}$ and the frequency of the wave does not change. Its wavelength, therefore, reduces to $\frac{\lambda_0}{n}$ and the number of

mesh points should be multiplied by n to compensate for it. The mesh will become non-uniform in this case. Figure 3.5 shows an example of uniform and non-uniform meshing of the computational domain.

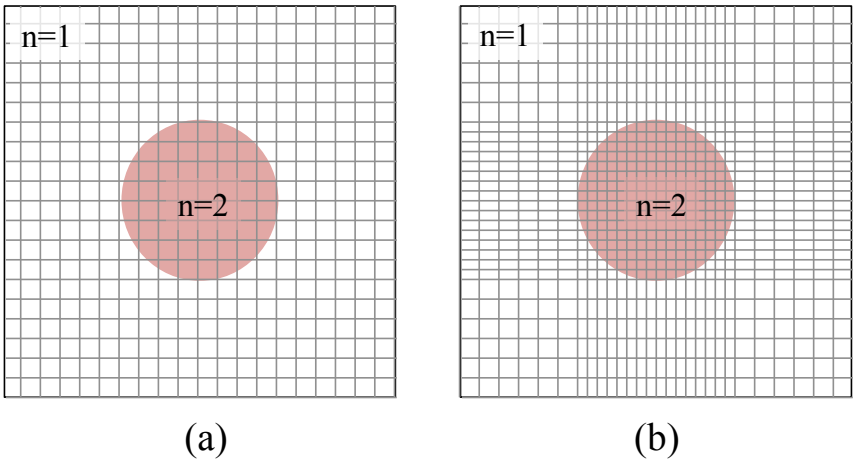


Figure 3.5: Illustration of (a) uniform (staircasing) and (b) non-uniform rectangular meshing of the simulation domain. The aim is to keep the number of mesh point per wavelength constant.

Conventional FDTD uses the Yee-cell approach on a uniform rectangular mesh resulting in higher staircasing errors compared to simulations with a non-uniform mesh. This can be reduced by increasing the number of mesh points for the whole computational domain. Increasing the number of mesh points reduces the errors by a power of two (refer to section 3.3.1), but usually increases the simulation time and memory requirements dramatically. Instead, smaller mesh sizes are often used across the boundaries and at smaller features in the simulation domain to reduce the staircasing errors caused by calculating the integration using the finite difference method at non-rectangular boundaries, this is referred to as "mesh override". Reducing the mesh size, even in a small region of the simulation domain, forces a smaller time step on the simulation (refer to section 3.3.6) and therefore increases the computational demands. Non-orthogonal FDTD methods allow for meshing with non-rectangular shapes, such as triangular and diamond meshes, which reduces this problem [125].

In this project, mesh overriding has been used only for a few final simulations.

Conformal mesh

Most of the results presented in this thesis are produced by employing some type of conformal mesh. FDTD simulations with a conformal mesh are sometimes referred to as conformal-FDTD (CFDTD). This meshing method uses a set of techniques to discretize space effectively to produce accurate results given a minimum mesh size. The discretization of space is non-uniform in a conformal mesh in a way that bigger grid sizes are used away from boundaries and smaller grid sizes are used at the boundaries between two materials. This improves the accuracy of the results at a smaller computational and simulation-time cost. Most conformal meshing techniques also use Maxwell's integral equations near the interfaces between two materials to improve performance [111]. If more than two materials are present in a single cell, the mesh applies a simple Yee-cell meshing instead. Most conformal meshing methods use a similar method to the Yu-Mittra method [108], where the integral form of Maxwell's equations (equations (3.1.2)) is applied at the boundary between two materials dealing with curved surfaces as well as perfectly conducting material. Figure 3.6 illustrates the improvement in the representation of an object when a conformal mesh is used (Fig. 3.6b) as opposed to a uniform rectangular mesh (Fig. 3.6a).

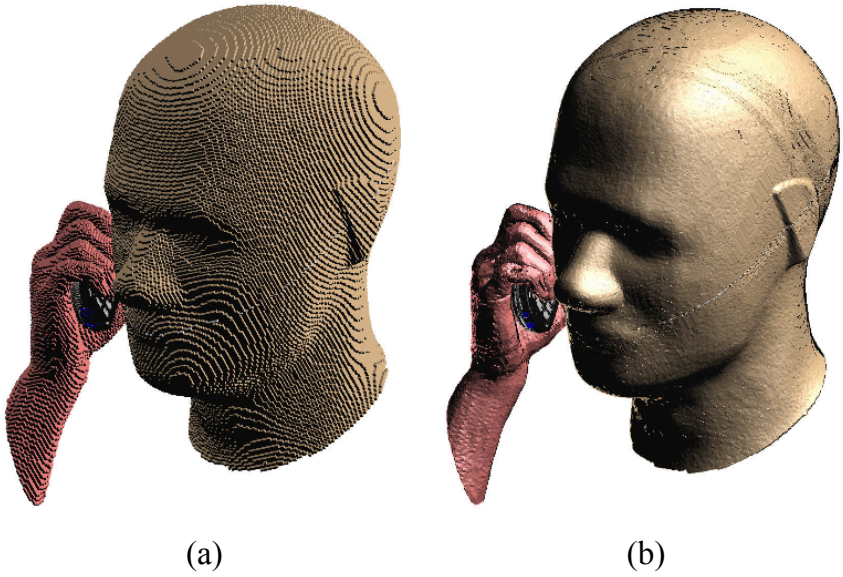


Figure 3.6: Illustration of (a) uniform rectangular and (b) conformal meshing of a 3D object. Courtesy of Stefen Benkler [126].

3.3.5 Sources in FDTD

Sources in FDTD are used to inject **E** and **H** fields in the simulation domain, by defining an electrical current, **J** in the Maxwell-Ampères equation (3.1.1b) using the constitutive relation in equation (3.1.3c).

A **point source** injects J at a single point on the Yee grid. It is used in some of the simulations presented in this thesis. It can have very large bandwidths in the frequency-domain depending on the time-step. The point sources propagate in all directions.

A **plane source** used in some of the simulations in this thesis is created by the injection of currents at several points in the computational domain forming the desired planar wavefront. Planar sources can be designed to propagate in a single direction, but in general propagate in two directions.

"Soft-sources" as opposed to "hard-sources" have been implemented for producing all the results presented in this thesis. This means that the source itself is implemented as an additional term in the "update equation" of the **E** and **H** fields at the point of definition. Therefore the other propagating fields (such as fields reflecting off adjacent cells) can pass through the source (i.e. the node that implements the source is still updated during the iteration of the algorithm). This removes numerical anomalies such as unwanted reflections from the source itself.

3.3.6 Time-space stability condition

Using the Fourier stability analysis (Von-Neumann stability analysis) on the leap frog integration of Maxwell's curl equations (equations (3.1.1a) and (3.1.1b)) on a uniform rectangular grid which expands to infinity, a stable time step is calculated as [111]:

$$\delta t < \sqrt{\frac{\epsilon\mu}{\frac{1}{\delta x^2} + \frac{1}{\delta y^2} + \frac{1}{\delta z^2}}}, \tag{3.3.3}$$

where δx, δy and δz are the mesh sizes in the x, y and z directions, ϵ is the permittivity and μ is the permeability of the material. In simulations with a non-uniform mesh, the smallest grid size would still determine the largest (stable) time step [112]. In a cubic grid (i.e. $\delta = \delta x{=}\delta y{=}\delta z$), equation (3.4.3) simplifies to:

$$\delta t < \frac{\delta}{c\sqrt{3}}, \tag{3.3.4}$$

where $c = \frac{1}{\sqrt{\epsilon_r \mu_r}}$ is the speed of light in the medium. Application of the upper limit on the largest time step of the simulation guarantees the stability of the simulation. In all simulations presented in this thesis, the stability condition (equation (3.3.4))

on the time step is met.

The above conditions arise from numerical dispersion in FDTD. That is, the speed (i.e. phase velocity) at which a wave travels through the computational domain depends on the time-step, the number of mesh points per wavelength and the direction of travel (since the grid is cubic, the speed in all directions is not the same). By reducing the size of the mesh, these errors reduce (refer to section 3.3.1 where the finite-difference approximation was discussed) so that if the mesh size is reduced by a factor of 10, the accuracy improves by a factor of 100. At the worse case (i.e. where the direction of the travel is at 45° compared to the grid), if the number of mesh points per wavelength is 10, the speed of the wave is 98.7% of its correct value [127].

3.3.7 Numerical boundary conditions, PML

At the boundaries of the simulation domain, the abrupt stop in the discretized space results in strong reflections. To avoid these reflections, some numerical boundary conditions must be applied. Absorbing boundary conditions (ABS), such as perfectly matched layers (PMLs) are very popular techniques to solve the problem of reflections at the boundaries of the computational domain. PML absorb incident electromagnetic waves [128–131].

Other methods such periodic boundary conditions and Bloch boundary conditions [132] effectively match the periodic boundaries to the grids adjacent to them and create a virtual infinite space in the direction that they are implemented. They should be used when modelling infinite systems (for example when interested in a wave travelling down a waveguide).

During this project, PMLs are used to meet the numerical boundary conditions in simulations. Usually multiple numbers of PML with various absorbing coefficients

and directions of absorption are used instead of one thick PML. Although in some of the simulations present in this thesis, waveguides are used to inject light into the cavity of interest, still PMLs are implemented for all boundaries of the simulation domain. This is due to the fact that the interest was the injection of light into the cavity, and not the field pattern at the boundaries where the waveguide meets the PML.

It is important to distance the PML far enough from the device of interest (e.g. cavity) to avoid the absorption of the energy stored in the device by the PML. Usually a convergence test is done to determine this distance (at least half a wavelength away from the device in all directions). In this project, a convergence test is done for each new structure to ensure that the PML does not affect the results of the simulation.

3.4 FDTD simulation procedure

The usual steps taken to achieve reliable simulation of a device are:

(1) Define the structure

Geometry and material properties are defined for the device.

(2) Define simulation domain

The size of the simulation domain is set in this step, as well as the size of the smallest mesh, the size of the largest time-step and the type and size of the boundary conditions applied. The size of the simulation domain is determined by the size of the device that is being modelled. It is usually set to be at least half a wavelength away from the device in all directions to avoid absorption and reflections from the boundaries.

For example, an eight-layered PML is used at the boundaries of the computational domain in most of the simulations presented in this thesis. An example of the computational domain including an example device is depicted in Fig. 3.7.

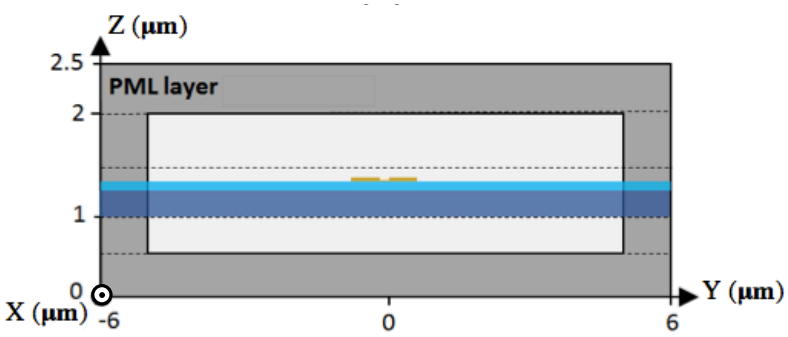


Figure 3.7: An example of the computational domain.

(3) Set source

Type, location, duration and shut-off (how the source current terminates in time) of the source are set.

The location of the source should be chosen with care. For example in a multi-mode cavity, care must be taken not to position a "point source" at the "zero" of any of the modes. If the source is placed at a "zero" of a mode, that mode is not excited which produces errors. Usually, a few simulations are run for a device, placing the source in different locations to make sure that the results are valid.

The duration and shut-off profile of the source determines the frequency-domain bandwidth of the results and the simulation duration (also depends on the meshing).

(4) Set monitors

Locations are chosen in which information about the fields are to be recorded. For instance, a point monitor refers to a monitor that saves the field information at a single node in space $(E_{i,j,k}, H_{i+\frac{1}{2},j+\frac{1}{2},k+\frac{1}{2}})$ for the duration of the simulation. A

plane monitor refers to a collection of point monitors across a plane in space.

(5) Test for accuracy and convergence

Multiple simulations are run to test the convergence of the required results with respect to simulation duration, mesh size, number of PML used and the size of the computational domain. Figure 3.8 shows an example of the convergence tests done throughout this project. Here the convergence of Q-factor (a figure of merit for optical cavities) as a function of the number of PML layers used in the simulation of the hybrid device presented in chapter 5. Based on this convergence test, 8 PML were implemented at the boundaries of simulations containing the hybrid device.

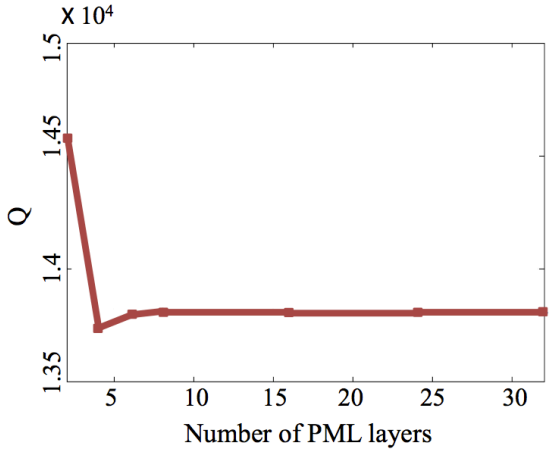


Figure 3.8: Q-factor as a function of number of PML layers.

(6) Run simulation

The simulation is run with optimized meshing, time-step, source settings and boundary conditions.

(7) Post-process data from monitors

Meaningful physical properties, such as field pattern, spectral response, Q, and effective mode volume, V_{eff} are produced using the data collected by the monitors in the simulation.

Mode plots: In order to capture the mode profiles and field patterns in all simulations, discrete Fourier transforms (DFT) of the electromagnetic field components at each resonant mode are computed on each mesh point while the simulations are running.

Spectral response: To study the resonant modes and their corresponding quality factors (Q-factor) of the PhC cavity and the hybrid device, a narrow temporal Gaussian pulse is used as the excitation field for both the point source and the waveguide excitation of the device. The spectral response is obtained by taking the Fourier transform of the data from a point probe collecting the E field close to the centre of the cavity of interest.

Q-factor: For low Q-factor cavities, the Q-factor can be calculated directly from the spectral response of the device, from the definition of Q-factor [39]:

$$Q = \frac{\Delta\omega}{\omega_0}, \tag{3.4.1}$$

where $\Delta\omega$ is the full width half maximum (FWHM) bandwidth at resonance and ω_0 is the angular frequency at resonance.

For devices with a high Q-factor, calculating the Q-factor directly from the spectral response means having very high simulation times and small time-steps. To avoid this, the Q-factor of the structure is determined numerically from the slope of the decaying field at the resonant frequency, such that [133]:

$$Q = \frac{-\omega_0 \log_{10} E}{2m} \tag{3.4.2}$$

where ω_0 is the angular frequency (rad) of the resonance, E is the electric field [N/C] and m is the gradient of the envelope of the decaying electrical field.

Mode volume: The evaluation of effective mode volume, V_{eff} is performed as

described in Kristensen *et al.* [134], where the total energy in the device is normalized to the maximum intensity in the device.

$$V_{eff} = \frac{\int \epsilon_r E^2 dv}{max(\epsilon_r E^2)}, \tag{3.4.3}$$

where ϵ_r is the relative permittivity and E^2 is the electric field intensity.

K-space plots: The k-space plots were produced by taking the FFT of the field pattern across a plane positioned 5nm above the surface of the device.

Far-field projections: The far-field projections were obtained by applying a simple near-field to far-field algorithm to the near field plots at a plane 5nm above the device and projecting it for sphere with a radius of 1m [135,136].

3.4.1 Comparing two simulations

Direct comparison between the values of $|E|$ and $|H|$ fields in simulations with identical sources but different structures is not good practice. This is because of the fact that even small changes in the device design and material properties, result in differences in meshing, which in turn changes the injected current, J, and the power propagated to the device from the source. A more meaningful comparison between two devices is comparing their figures of merit (FOM), such as Q-factors in cavities, field patterns and spectral response (refer to section 5.3 for description of FOMs in photonic, plasmonic and photonic-plasmonic devices). A valid way of comparing the fields propagated in two devices in two FDTD simulations, is to look at the field patterns in both simulations normalised to the value of the field at a shared maxima.

3.5 Numerical tools used during this project

Matlab was used during this project for post processing and plotting data.

3.5.1 Meep and MPB

Meep [137] implements rectangular, uniform mesh FDTD. It is an open source software and can couple to MIT photonic bands (MPB) for band diagram calculation. Meep is not very efficient for simulating the behaviour of metallic nanoantennas. This is because it requires a very fine mesh for subwavelength features across the whole simulation domain, making it very computationally expensive and time consuming. These two packages were used at the start of this PhD (2013-2015).

3.5.2 Lumerical

Lumerical [136] is a commercial FDTD solver, with non-uniform rectangular and conformal meshing capabilities. Most of the numerical results presented in this thesis were produced using Lumerical.

3.5.3 Paraview

Paraview [138] is a 3D visualisation and drawing program. It accepts input files from both Meep and Lumerical. Paraview was used for 3D visualisation of devices (and fields).

3.6 Summary

This chapter gave a brief overview of the fundamentals of electromagnetics. The FDTD method was then described discussing the meshing technique, time step and boundary conditions. The steps for running reliable FDTD simulations concluded the chapter.

4

Building blocks of the hybrid device

The results presented in this chapter are achieved in collaboration with Dr Bellanca and Dr. Parini of the Department of Engineering at the University of Ferrara. An initial model of the bowtie nanoantenna (BNA) was developed in Meep by Dr Parini. The results from this model are not used in this chapter, but provided initial insight to metallic nanoantennas at the beginning of this project. When modelling the PhC, the initial design was taken from a previous project of Dr. Bellanca (the Copernicus project) [139]. The results presented in this chapter are based on that original design but changed to suit the objectives of this PhD project.

One of the objectives of this PhD project was to design a hybrid device comprising of a photonic crystal cavity and a plasmonic nanoantenna. This device was conceived as the unit-cell of a multicomponent platform capable of running multiple single-molecule experiments. To achieve this, first the designs of the individual building blocks of the hybrid device was considered, namely the photonic crystal element and the plasmonic nanoantenna element.

This chapter begins by presenting the main figures of merit used for photonic resonators. Then photonic crystal are introduced, describing the principles of a "photonic band-gap" and how it can be used to control the flow of light by creating

photonic crystal cavities and waveguides. A section describing the working principles of plasmonic nanoantennas follows, explaining the concept of "localised surface plasmons" and creating sub-wavelength localisation of light. This is then followed by presenting finite-difference time-domain (FDTD) simulation results obtained for different designs of photonic crystal cavities and plasmonic nanoantennas, which will be used to form the building blocks of the hybrid device presented in this chapter. All simulation results presented in this chapter have been produced by running stable, convenregnt 3D FDTD simulations.

4.1 Figures of merit for photonic resonators

Photonic resonators often aim to increase the photon lifetime or energy storage in a device making it more efficient in terms of energy use. The **quality factor (Q-factor)** of a device is a measure of its ability to store optical energy and is defined as

$$Q \equiv 2\pi \frac{energy\ stored}{energy\ lost\ per\ cycle} = 2\pi f_r \frac{U_{stored}}{P_{loss}}, \tag{4.1.1}$$

where f_r stands for the resonant frequency in [Hz], U_{stored} is the energy stored in [J] and P_{loss} is power loss in [W].

Reducing the volume in which energy is stored in a resonator (i.e.spatial localization of light), results in higher photon densities inside the resonator, enabling miniaturization of the device and effects requiring high photon densities (for example nonlinear effects). **Effective mode volume (V_{eff})** in $[(\frac{\lambda}{n})^3]$ is a measure of the spatial localisation of the light in a device. It is commonly calculated at the resonant frequency using the following approximation:

$$V_{eff} = \frac{\iiint_{\partial V} \epsilon_r E^2 \, dV}{max(\epsilon_r E^2)}, \tag{4.1.2}$$

where ϵ_r is the relative permittivity, V is the computational domain and E^2 is the

electrical field intensity in $[(\frac{N}{C})^2]$. In other words V_{eff} is calculated by normalizing the energy in the computational domain with respect to its maximum energy density [134].

$\mathbf{Q/V}_{eff}$ is a well established figure of merit (FOM) for photonic resonators. It is used as a measure of energy localisation in photonic devices. Looking at single photonic resonators, it provides a good measure of energy localization. However, when looking at strongly coupled devices, specifically hybrid photonic-plasmonic cavities, it can produce misleading results (see section 5.3 for a more complete discussion and derivation of a more meaningful FOM for hybrid photonic-plasmonic devices).

4.2 Photonic crystals

In 1887, Lord Rayleigh published a paper in which he described the propagation of waves through a medium with a periodic structure [140]. After the observation of the reflection of x-rays from natural crystals by the Bragg brothers in 1913 [141], he described a similar effect for the "reflection of light from a regularly stratified medium" [142]. Rayleigh observed that for a periodic structure with modulation period, L, where the refractive index (optical density) of the material changes periodically between n_0 and n_1, there is a narrow band of wavelengths, λ, for which light propagation is prohibited [143]. The condition for this effect is:

$$\frac{\lambda^2}{4L^2} = \pm\frac{n_1}{2n_0}. \tag{4.2.1}$$

In other words, in a macroscopic periodic structure where two materials alternate with periodicity, L and the incident light, has a wavelength of approximately $4L$, constructive reflections of light from the boundaries between the two material prohibit light propagation. This is called a **photonic stop-band** resulting in near-perfect reflectivity of the periodic structures for a narrow wavelength window. This is the

basis of distributed Bragg reflectors or dielectric mirrors.

In the 1980's, Yablanovitch and others worked on making structures with photonic stop-bands in 2D and 3D as opposed to the 1D structures studied by Lord Rayleigh [144–146]. These structures were more complex, much like natural crystals and required a high refractive index contrast to produce stop-bands in 2D and 3D. The analogy to semiconductor crystals and their electronic band-gaps led to the use of the terms **photonic crystal** (PhC) and **photonic band-gap** [147]. This analogy is based on the similarities between the propagation of electron waves in a periodic electric potential (i.e. the time-dependent Schrödinger's equation) and the propagation of light in a periodic refractive index (i.e. the wave equation). Relative permittivity plays the same part in the wave equation that electric potential plays in Schrödinger's equation [148].

A **photonic band diagram**, or dispersion diagram, for a photonic crystal shows all the possible eigensolutions to the wave equation describing the energy and momentum states of photons in that crystal just as the electronic band diagram shows all the possible solutions to the time-dependent Schrödinger's equation describing the energy and momentum states of electrons in a natural crystal.

The **photonic band-gap** is the range of frequencies and k-vectors (angles) for which light is prohibited from propagating in the crystal. Figure 4.1 illustrates the electric band-diagram of a Gallium Arsenide (GaAs) zincblende crystal and compares this to the photonic band-diagram of a silicon woodpile PhC.

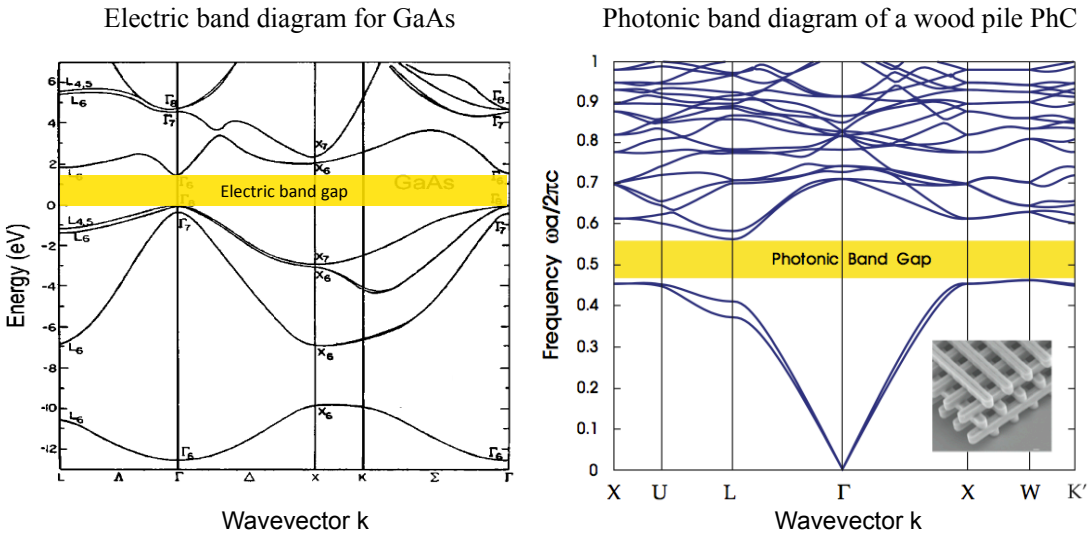


Figure 4.1: Examples of electric and photonic band diagrams. (a) The electrical band diagram for GaAs crystal (courtesy of Cohen *et al.* [149]). (b) The photonic band diagram for a unit-cell of a 3D silicon woodpile PhC in air (courtesy of Joannopoulos [113]). The inset of (b) shows the woodpile structure. The width of each beam is 1μm.

In Fig. 4.1, the yellow band in both graphs indicates the band in which electron states (for electric band diagram) or photon states (for the photonic band diagram) are not allowed to exist in.

Colour as a result of a photonic band-gap is commonly found in nature. The colour of peacock feathers and outer shells of jewel beetles [150], colour displays of birds of paradise and the ability of chameleons and octopuses to change their colour [151] can be named as a few examples of PhCs in nature. Fabricated PhCs sometimes take inspiration from these natural PhCs.

PhCs are attractive in the industry due to their wide range of applications. 1D PhCs are frequently used to create mirrors and reflection or anti-reflection coatings [152, 153]. 2D PhCs are used in low-loss hollow fibers, ultrafast lasers [154], waveguides, opto-electrical switches [155] and optical storage [156,157]. 3D PhC structures are

mostly fabricated and characterized in universities and research institutes and have not yet been commercialized. This is due to the complex fabrication processes required to create a structure with 3D periodicity [158].

Defects are introduced into a PhC to allow light to exist in parts of the photonic band-gap, enabling photon feedback and waveguiding of very specific ranges of frequencies and propagation angles. Engineering defects to create devices in a PhC with a photonic band-gap is sometimes referred to as band-gap engineering. The devices created using band-gap engineering can demonstrate interesting behaviour such as "slow light", where the group velocity of light is very low in a waveguide and second harmonic generation to high optical densities in a PhC cavity. Another group of PhC devices is designed by engineering dispersion effects to create exotic devices such as superlenses [159], super collimators [160] and negative refractors [161,162]; these do not necessarily all have band-gaps.

4.2.1 2D photonic crystals

2D PhCs are more widely used than 3D PhCs. This is because they are much easier to fabricate using common micro- and nanofabrication techniques such as electron-beam lithography, EBL, or photolithography (please refer to chapter 6 for a description of EBL). Since they are easier to fabricate compared to 3D PhCs, it is also much easier to create defects and features in 2D PhCs that result in localization and waveguiding of light, enabling more control over their functionality [147].

2D PhCs are usually created either as square lattices of high refractive index dielectric rods in a low refractive index medium (such as air) or as a triangular lattice of low refractive index holes in a high refractive index membrane. These two types of 2D PhC are named "rod slabs" and "hole slabs" respectively [16]. Figure 4.2 illustrates example designs of "rod" and "hole" slabs. The periodicity constant, a,

hole/rod radius, r, and thickness, d, are marked for both cases. Rod slabs usually produce band diagrams with TM band-gaps and hole slabs usually produce band diagram with TE band-gaps. This is because the electric fields are localised to regions of high refractive index at the fundamental mode. Membrane based 2D PhCs (hole slabs) with a triangular lattice of air holes can produce a complete band-gap. This is done by increasing the radius of the holes to the point that they are almost touching, creating periodic regions of high refractive index (much like a rod slab) and producing a band gap for TM and TE polarizations [163].

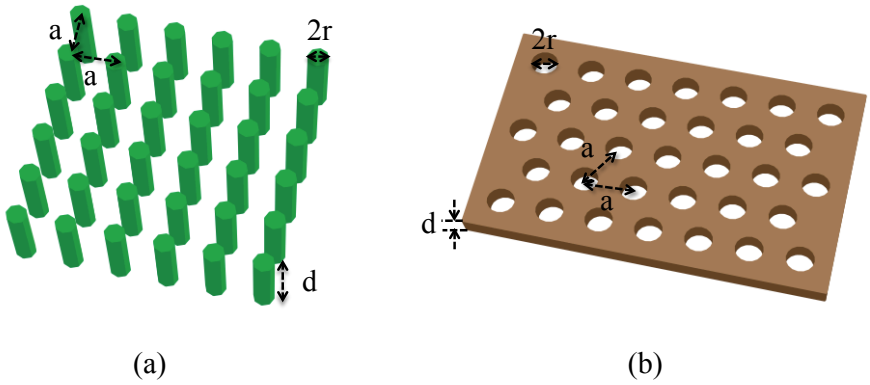


Figure 4.2: Examples of (a) rod and (b) hole slab designs for creating 2D PhCs. Reproduced from Joannopoulos [113].

4.2.1.1 Light cone

2D PhCs take advantage of the photonic band-gap in two dimensions. To trap light in the 3rd dimension, total internal reflection (TIR) is used. Therefore, light is effectively guided within a planar waveguide. The k-vectors that are allowed to escape and propagate outside the slab are determined by the light cone, which is defined by Snell's law as [158]:

$$\mathbf{k} \leq \frac{c\ \omega}{n_{eff}}, \tag{4.2.2}$$

where n_{eff} is the effective refractive index of the slab, ω is the angular frequency in $[\frac{rad}{s}]$, c is the speed of light in vacuum in $[\frac{m}{s}]$ and $\mathbf{k}$ is the k-vector $[\frac{1}{m}]$. This means that increasing the effective refractive index of the slab can reduce the amount of light lost vertically for the PhC in a low refractive index medium with periodicity in the x-y plane. Photons with k-vectors outside the light cone are not allowed to propagate outside the slab and result in evanescent fields. This is used extensively when designing high-Q PhC resonators and much of the effort is dedicated to perturbing the structures to move states outside the light cone.

Figure 4.3 illustrates the projection of a photonic band diagram for a 2D PhC consisting of a hexagonal (triangular unit cell) lattice of air holes in a dielectric slab with d=0.5a and ϵ_r=11.7 with the light cone also projected on the band diagram.

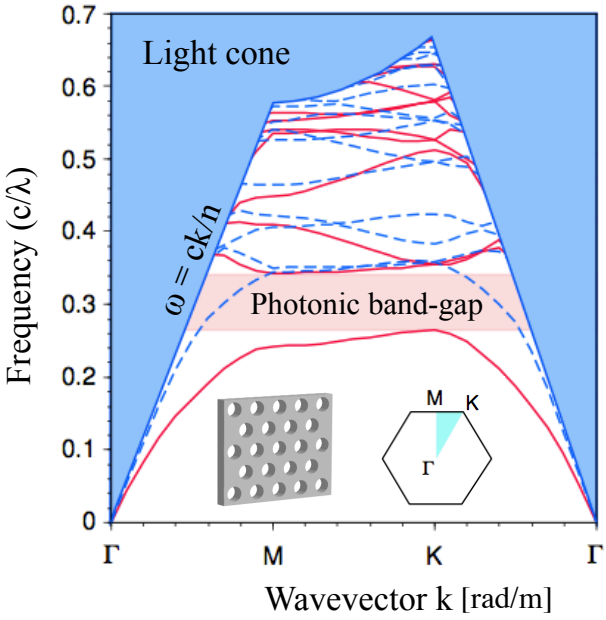


Figure 4.3: Illustration of the band diagram for a 2D hole-slab PhC structure. Modified courtesy of Johnson *et al.* [163]. The insets of the figure show the fundamental crystalline lattice (right) and the design of the PhC (left). The solid lines show the TE modes and the dotted line show the TM modes.

4.2.1.2 Refractive index contrast, hole/rod radius, periodicity and slab thickness

When creating PhCs, the higher the refractive index contrast between the alternating media, the wider the photonic-band gap [164]. For example, Gallium Arsenide (GaAs) and air have a refractive index contrast of 2.6 (at a wavelength of 1550 nm) which is one of the highest available [163].

The configuration of rods (in a rod slab) and holes (in a hole slab) are also very important for achieving a wide photonic band-gap. A wide band-gap is desirable because it allows the use of the device over a wide range of wavelengths as well as making it more energy efficient. One of the configurations resulting in the widest band-gaps is large holes of low refractive index material placed in a triangular lattice (honeycomb), wherein the optical path length in each material is close to $\frac{\lambda}{4}$. On the other hand, large air holes mean that light can diffract moving from the high n material to the low n material and cause loss of photons. To combat this effect, the hole size is reduced and the period is kept at approximately a = $\frac{\lambda}{2n_{eff}}$, where n_{eff} is the effective refractive index of the two media taking into account their thickness [165].

The slab thickness, d, determines the number of modes that can be supported by the PhC. It is usually kept at a fraction of λ (e.g. 0.2a-0.6a). This keeps the number of modes allowed to propagate low, resulting in a wide band-gap for high refractive index difference devices. If d is too small, the effective refractive index of the slab is small, the light cone is wide and a lot of k-vectors propagate outside the slab (in the normal direction to the periodicity). If it is too large, too many modes are allowed to exist, removing the band-gap [166,167].

2D PhCs with a triangular lattice of air holes (similar to Fig. 4.2) are used in this project. This is because membrane based 2D PhCs are more practical for

the envisaged device. They offer a planar surface that can be used in biological experiments.

When designing the PhC structure, the aim is to create a unit-cell that is symmetrical in all directions in the plane (i.e. 360 degrees of k-vector in the plane with 2D periodicity), the refractive index difference between the slab and the surrounding media needs to be high to avoid loss of energy due to refraction in the air holes, and for creating a narrow light-cone to limit the loss of energy outside the membrane.

4.2.2 2D photonic crystal cavities

Cavities are created by engineering defects in the PhC structure, this allows light to exist at a finite group of frequencies and k-vectors in the photonic band-gap at these defects. Because the photonic crystal acts like a near-perfect mirror in the adjacent regions, photons in the defect cavity cannot escape easily (i.e. have high photon lifetimes). This makes PhC cavities very good at retaining energy (i.e. PhC cavities have high Q-factors). This is why PhC cavites are chosen in this project as the energy reservoir component of the device.

Two of the most popular 2D PhC designs based on a hole slab are the L cavity and H cavity designs. L stands for line and H stands for hole describing the shape of cavity created. The L cavity design, removes a finite number of holes in a row from a PhC with a hexagonal (triangular unit cell) lattice of air holes, creating a mini-waveguide, and an H cavity design removes central holes in a hexagonal lattice. For example an L5 cavity removes 5 holes in a row and an H1 cavity removes a hole from the centre of the hexagonal lattice. During this project, the focus is on an **L3 cavity**, in which 3 holes are removed in a line from the PhC lattice, proving to have very high photon life-times in the near infrared regime [168]. Figure 4.4 shows

examples of H0 and L3 cavities fabricated in a silicon slab. Creating cavities can also be done by small shifts in the lattice, changing the hole dimension and shape as well. The H0 cavity is created by shifting the centre holes slightly without removing any holes [169,170].

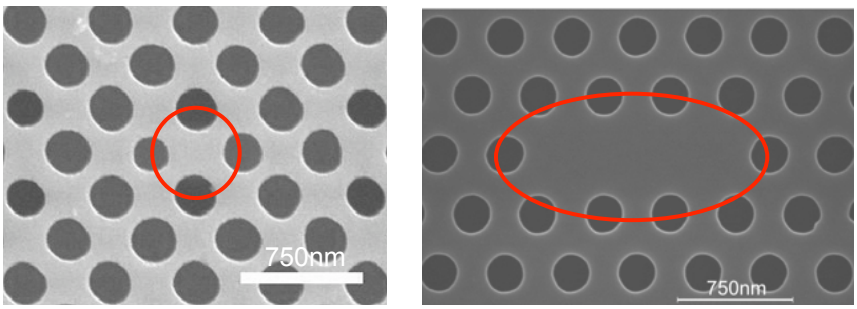


Figure 4.4: SEM Images of fabricated (a) H0 and (b) L3 cavities based on a silicon slab. Reproduced from Xu *et al.* and Ee *et al.* respectively [169,170]. Red ovals indicate the location of cavities.

Due to the band-gap of the PhC and TIR in the slab, PhC resonators have sharp spectral responses and can be designed to have Q-factors as high as 10^6 [171–173]. They usually have V_{eff} of the order of the cubic wavelength (similar V_{eff} to a diffraction limitted device). Note that the high intensity, confined light in membrane based PhC resonators is typically located within the slab and not accessible externally.

4.2.3 2D photonic crystal waveguides

In a hole slab, W1 waveguides are created by removing one row of holes, effectively creating a line in the dispersion diagram (band diagram), that allows light propagation in the photonic band-gap [174]. Unlike other optical waveguides, using PhCs allows the creation of sharp bends in the waveguides without loss of power. To do

this, usually the holes near the bend are increased in size to create a large, TIR-like reflection [175]. Figure 4.5 shows the designs of a silicon membrane based W1 waveguide as well as a W1 waveguide with sharp bends .

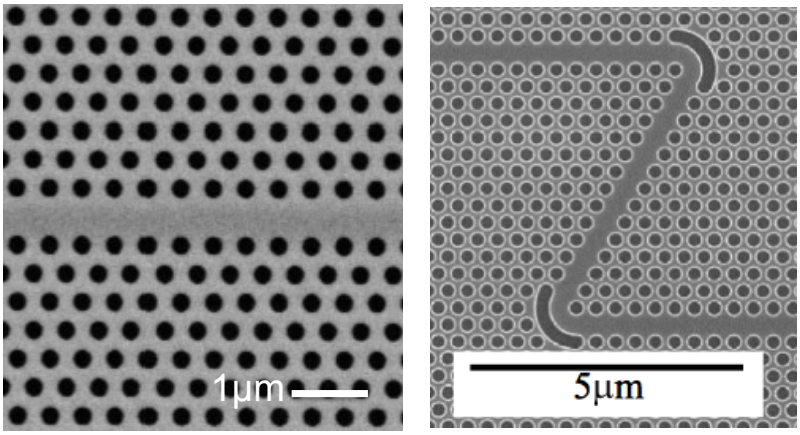


Figure 4.5: SEM images of a (a) W1 PhC waveguide and a (b) W1 waveguide with sharp bends, reproduced from Beggs *et al.* and Zhao *et al.* respectively [176,177].

In this project, a W1 waveguide was designed to deliver light to the hybrid device (refer to section 5.5.3).

Engineering a waveguide to reside near the bend of the line for fundamnetal propagating modes in the band diagram (i.e. the band-edge) of the PhC, results in "slow light", or light with very small group velocity. This concept is used to create cavities inside waveguides (or L cavities) with very high photon lifetimes [178–181].

4.3 Plasmonic nanoantennas

Dielectric particles that are much smaller than the wavelength of light behave like electric dipoles resonantly absorbing and scattering electromagnetic fields. Metallic

nanoparticles placed in an electric field, experience a force on the free electrons in the conduction band of the metal causing a collective oscillation of the free electrons. This phenomena is labelled "localised surface plasmons" (LSP) [182].

At a certain frequency, the oscillation of the free electrons is resonantly enhanced due to the antenna like-geometry of the structure. This creates larger charge displacements and confinement of light compared to LSP [83]. Resonantly enhanced LSP is referred to as "localised surface plasmon resonance" (LSPR). This effect is enhanced even further in gap nanoantennas where the antenna geometry incorporates a nano-sized gap in its design. Incorporation of the gap improves the light confinement dramatically [183]. This is because oscillating free electrons in the antenna are forced to fulfil the electromagnetic boundary conditions at the metal-insulator interface, so that the electric flux density is continuous across the gap [18]. Therefore, the surface charges of the metal are forced to accumulate at the gap, with opposite charges on the two sides of the gap, similar to a parallel plate capacitor. Also "lightning rod" effects at the sharp tips of metallic nanoantennas, force the surface charges to concentrate in very small volumes at the tips due to field continuity conditions [18]. Figure 4.6 shows the interaction of a metallic gap nanoantenna shaped like a bowtie, namely a bowtie nanoantenna (BNA), with an electromagnetic field with polarization along the longitudinal axis of the nanoantenna. Plasmonic gap nanoantennas can increase the intensity at the gap by 1- 3 orders of magnitude compared to the illumination. Reducing the gap and tip size results in an increase in the optical intensity in the gap (i.e. the optical intensity density increases since the gap volume has become smaller).

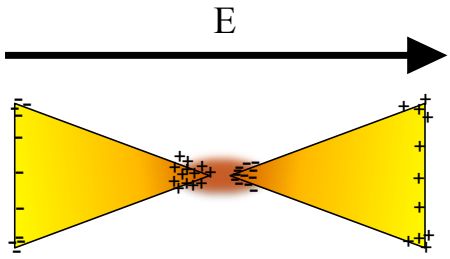


Figure 4.6: Illustration of a metallic BNA interacting with an EM wave propagating into the page with its polarization along its longitudinal axis. Note that this illustration demonstrates an single point in time.

If the size of the plasmonic nanoantenna is of the order of the wavelength of light, larger order LSPR modes (i.e. standing wave excitations of the nanoantenna with smaller wavelengths) can also be excited. The charge distribution across the device can be thought of as a multipolar antenna. Therefore, at larger modes, high intensity regions may form along the surface of the nanoantenna as well as at the edges [184,185].

Due to their nano-sized localization of light and ability to produce subwavelength "hot-spots" with broad resonance widths, plasmonic nanoantennas are used for an increasing range of applications, including the creation of nanolenses, optical trapping [46,93], surface enhanced Raman spectroscopy (SERS) [186], biosensing [187] and light bending [188].

Plasmonic nanoantennas can achieve V_{eff} much smaller than the cubic wavelength in vacuum (4 orders of magnitude smaller than the cubic wavelength is typical of gap nanoantennas [17]), but they have low Q-factors due to the dissipative losses in the metal and their broad spectral response with Q-factors usually smaller than 50 [17,189,190].

4.3.1 Popular designs of gap nanoantennas, design choice

Popular designs of metallic gap nanoantennas include nano-dimer pairs (also referred to as nano-dot and nano-disk pairs) consisting of two nano-dimers placed next to each other with a small gap, two-wire (or two-nanorod) designs consisting of two nanorods placed next to each other with a small gap in between them and the BNA design which consists of two triangles placed next to each other with a small gap to form a bowtie shape. These designs are shown in Fig. 4.7.

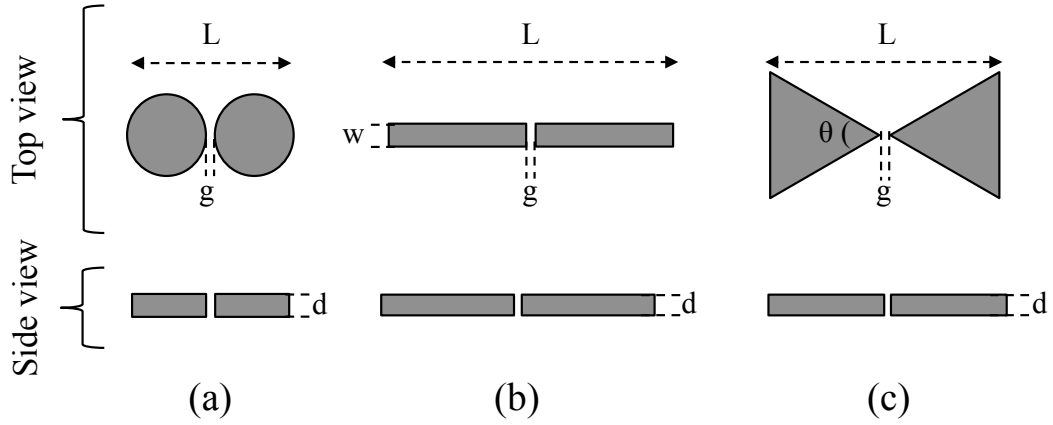


Figure 4.7: Illustration of (a) nano-dimer pair, (b) two-wire and (c) BNA nanoantenna designs.

4.3.1.1 Effect of material, shape and dimensions on spectral response

The **length**, L, of these nanoantennas determines their resonant wavelength (following a $\frac{\lambda}{2}$ rule of thumb). Their **effective refractive index,** n_{eff}, results in a shift of their spectral response so that increasing the effective refractive index of the nanoantenna compared to its surroundings constitutes reducing the length of the antenna. **Gap-size**, g, determines the strength and size of the localised field, so that reducing the gap-size increases the intensity in the gap. **Thickness**, d, determines the amount of losses in the metal, so that reducing the thickness of the nanoantennas increases the intensity enhancement at the gap.

In the two-wire design (Fig. 4.7(b)), the **width**, W, of the antenna determines their spectral width so that reducing W reduces the spectral width and sharpens the resonance. Increasing W also reduces the intensity in the gap. In the BNA design (Fig. 4.7(c)), increasing the **tip angle,** θ, has a similar result on the spectral behaviour of the antenna to increasing W in a two-wire nanoantenna, so that a larger θ corresponds to a broader resonance [191].

Figure 4.8 compares the spectral responses of the three designs discussed above. Resonances are presented for the nanoantenas based on silver with d=20nm and g=3nm. L of the nano-dimer pair, two-wire and BNA nanoantennas are 60nm, 90nm and 90nm respectively and θ in the BNA design is 60nm. The radius of the curvature at the BNA tips is 5nm and the radius of the curvature at the ends of the two-wire nanoantenna is 20nm. The resonances are numerically recorded at the gap of the nanoantennas by Pellegrini *et al.* [192].

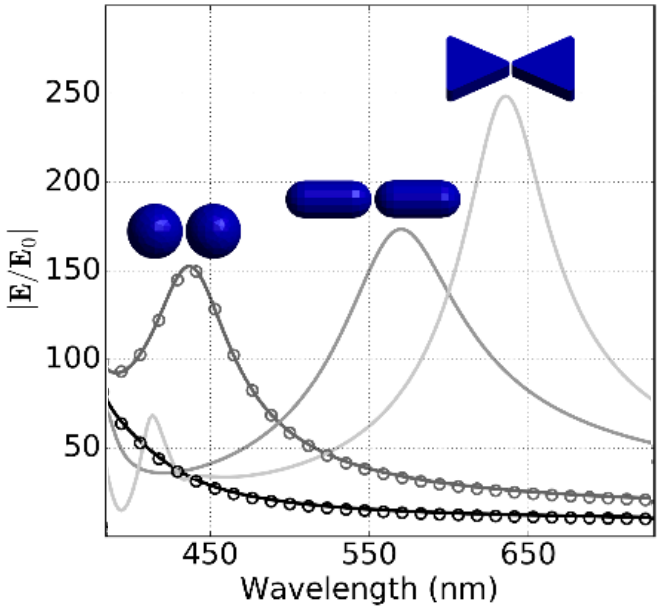


Figure 4.8: A comparison between numerical spectral responses of 3 designs of plasmonic gap nanoantennas of Pellegrini *et al.* [192]. Resonances are measured at the gap of nanoantennas.

In this project, BNAs are the choice for the nanoplasmonic component of the hybrid device. This is because the intensity enhancement of the BNA can still remain minimally reduced by increasing θ since it does not disturb the tip size dramatically. This is one of the main advantages of BNAs over the two-wire design. Even though two-wire nanoantennas are capable of producing sharper spectral responses compared to BNAs, BNAs remain a more popular choice. This is because with BNAs of similar sizes compared to two-wire nanoantennas, similar intensities can be achieved in the gap with the bonus of a more broad-band resonance, making it more practical experimentally (i.e. easier to couple light into). This is particularly beneficial for experiments such as Raman spectroscopy, where the operation of the device is required over a broad range of wavelengths.

4.4 FDTD Simulation results for PhCs

4.4.1 L3 cavity design for the hybrid device

The PhC cavity designed for the hybrid device is optimized to have a high Q-factor and operate in the C-band wavelength range (1.535μm - 1.565μm). The high Q-factor is desirable to ensure that the final device is energy efficient and working in the C-band is desirable to ensure compatibility with telecommunication components, such as sources, detectors and amplifiers and photonic integrated circuits. The PhC cavity is designed for a GaAs slab in air due to its high refractive index contrast. This results in better confinement of light in the vertical direction resulting in higher Q-factors. Other materials, such as silicon and indium phosphide, are also suitable materials for this PhC. The fundamental resonant wavelength of the cavity was tuned to 1.5μm through the choice of a suitable PhC lattice constant (a = 410nm), hole radius (r = 125nm) and membrane thickness (d = 275nm) [193,194] . The air holes at the ends of the cavity were shifted away from the cavity by 0.2a to increase

the quality factor [195]. With this arrangement, the Q-factor of the fundamental mode increases from ≈ 4,900 to ≈ 39,500 in air. Figure 4.9 illustrates the L3 cavity with the shift to the end holes.

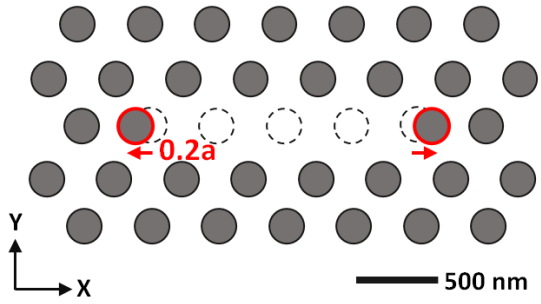


Figure 4.9: Illustration of the L3 resonator showing an outward shift of 0.2a in the end holes of the cavity resulting in an improvement of the quality factor of the fundamental mode from ≈4,900 to ≈37,000.

The L3 cavity has three major simulated resonances in the C-band. The wavelengths of these modes and the corresponding quality factors, effective mode volumes and $\frac{Q}{v_{eff}}$ are presented in Table 4.1.

Table 4.1: Major resonances of the L3 cavity and their corresponding Q-factor, V_{eff} and $\frac{Q}{V_{eff}}$

Resonance	$\lambda[\mu m]$	Q	V_{eff} $[(\frac{\lambda}{n})^3]$	$\frac{Q}{V_{eff}}$ $[(\frac{n}{\lambda})^3]$
Fundamental	1,54	37,333	0.77	50,800
Second	1.47	619	0.78	800
Third	1.36	1,141	0.77	1,460

Figure 4.10(a) shows the simulated spectrum of the L3 PhC cavity. As can be seen in this figure, the structure has a fundamental resonance at a wavelength of 1.54μm, a second resonance at 1.47μm and a third resonance at 1.36μm.

The mode patterns in Fig. 4.10(b-d) are plotted across the xy plane crossing the centre of the PhC cavity.

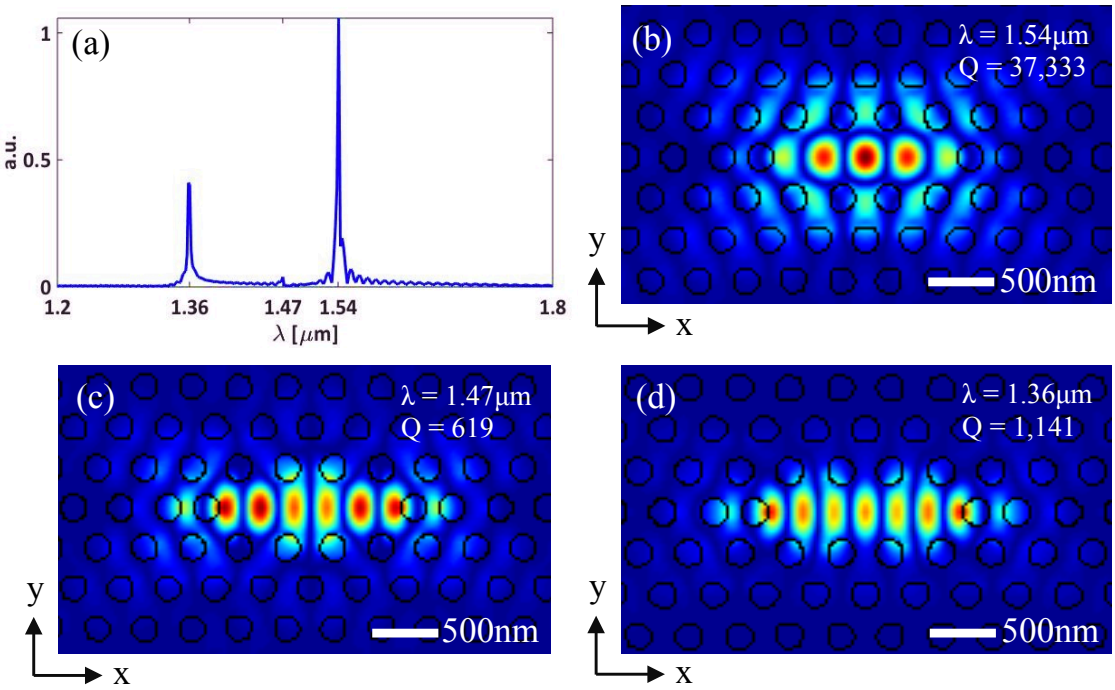


Figure 4.10: (a) Demonstration of the spectral response of the optimized L3 cavity with the field profiles for the fundamental, second and third resonant modes shown in (b-d) respectively.

The fundamental resonant mode and the third resonant mode both have a maximum at the centre of the PhC resonator, but the second resonant mode has a zero at the centre of the PhC cavity and maxima at the two outer missing holes of the L3 cavity. At the fundamental resonant mode, Q-factor is $\approx$ 37,000 V_{eff} is $\approx$ 0.77 $(\lambda/n)^3$ and Q/V_{eff} is $\approx$ 50,800.

4.4.2 Designed L3 cavity in water

It is also important to study the behaviour of the cavity in water since the hybrid device targets biological applications. Placing the L3 cavity designed in section

4.4.1 in water reduces the refractive index difference between the PhC and the surroundings. This increases the size of the light cone and the amount of energy lost in the vertical (z) direction (where the PhC plane is in the x-y direction). Reduction of the refractive index difference between the PhC and its surrounding (i.e. reducing n_{eff}) also induces a red-shift in the resonances due to the reduction of wavelength difference between the two materials (i.e. elongation of the PhC lengths with respect to the surrounding media). Table 4.2 shows the major resonant modes and their corresponding Q-factors, effective mode volumes and $\frac{Q}{V_{eff}}$ for the L3 cavity in water.

Table 4.2: Major resonances of the L3 cavity in water and their corresponding Q-factor, V_{eff} and $\frac{Q}{V_{eff}}$.

Resonance	$\lambda[\mu m]$	Q	V_{eff} $[(\frac{\lambda}{n})^3]$	$\frac{Q}{V_{eff}}$ $[(\frac{n}{\lambda})^3]$
Fundamental	1.593	11,900	0.81	14,700
Second	1.522	700	0.85	825
Third	1.408	1,470	0.79	1,860

Figure 4.11(a) shows the simulated spectrum of the L3 PhC cavity. The structure has a fundamental resonance at a wavelength of 1.54μm, a second resonance at 1.47μm and a third resonance at 1.36μm.

The mode patterns in Fig.4.11(b-d) are plotted across the xy plane crossing the centre of the PhC cavity.

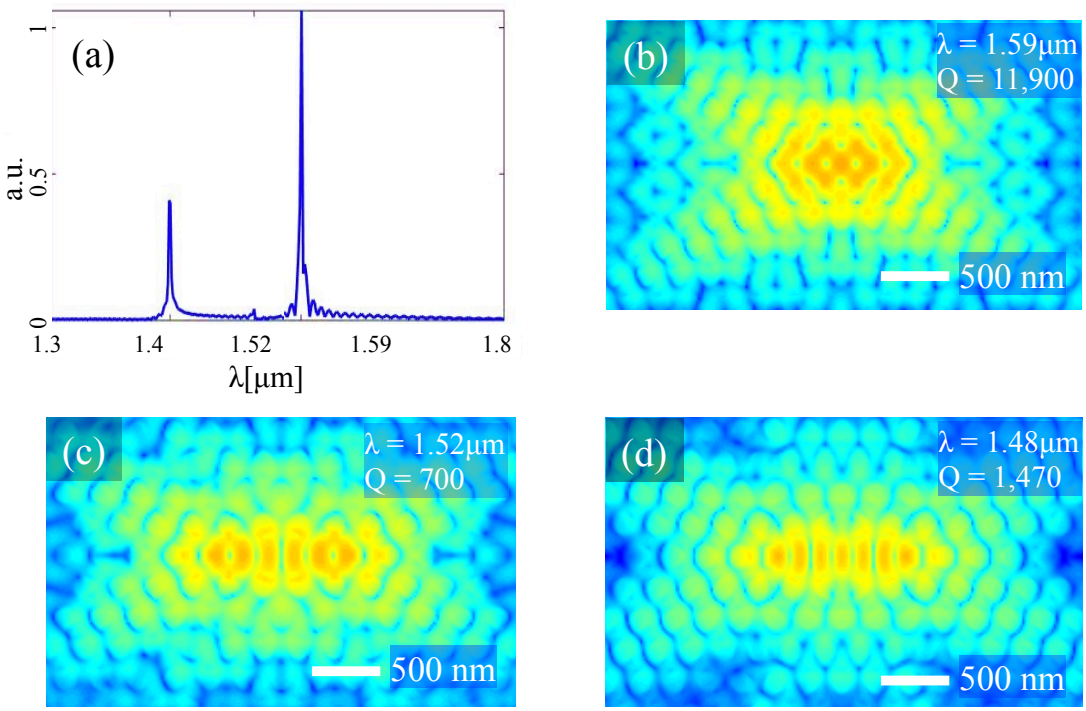


Figure 4.11: (a) Demonstration of the spectral response of the L3 cavity in water with the field profiles for the fundamental, second and third resonant modes shown in (b-d) respectively.

In water, the cavity has a lower Q-factor, larger V_{eff} and smaller $\frac{Q}{v_{eff}}$ compared to the case in air. This was expected due to widening of the light cone. Nevertheless, the device behaves similarly in water and in air.

4.4.3 L3 cavity tolerances for fabrication purposes

A 273nm thick GaAs slab was available to Dr. Chris Mellor of the School of Physics and Astronomy at the University of Nottingham for the first attempt to fabricate the L3 cavity (please refer to section 6.3 for the fabrication results of the L3 cavity). The desired device has a fundamental resonant mode at 1.55μm with a high Q. This section studies the tolerances on the design parameters a, r and shift to the end

holes of the cavity, $dx[a]$, suggesting the optimal values for a, r and dx as well as reporting the acceptable ranges for them.

4.4.3.1 Lattice constant, a, and hole radius, r

Figure 4.12(a) shows the 3D simulation results studying the effect of changing a, on the fundamental resonant mode, λ_0 of the L3 cavity. In all simulations, d = 273nm, r=125 nm and no shifts were introduced to the positions of the end holes of the cavity. Figure 4.12(b) illustrates the effect of changing r on the fundamental resonant mode, λ_0 of the L3 cavity. In all simulations, d = 273nm, a=415nm and no shifts were introduced to the positions of the end holes of the cavity.

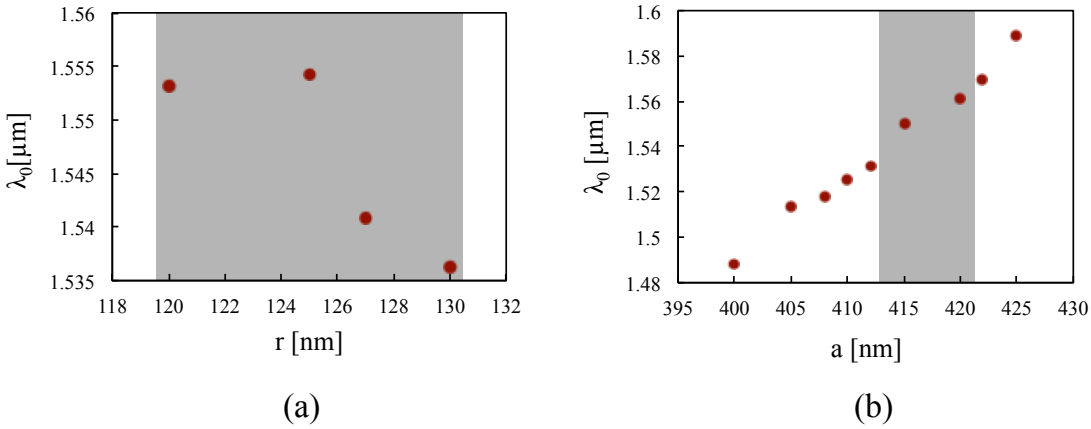


Figure 4.12: Demonstration of the effect of changing the (a) periodicity, a, and (b) hole radius, r, of the PhC on the fundamental resonant mode of the L3 cavity based on a 273nm GaAs slab. For simulations looking at the periodicity r = 125nm and for simulations looking at hole radius, a = 415nm. The grey box shows the acceptable range of values for a and r (less than 10% change in wavelength).

Figure 4.12(a) demonstrates a linear increase in the fundamental resonant mode of the PhC cavity with respect to a. At a = 415nm, the optimal wavelength, λ_0 of 1.55μm is achieved. For a in the range of 412nm - 422nm, λ_0 is in the acceptable

range (less than 10% change in wavelength) of 1.53μm-1.56μm.

Figure 4.12(b) shows a linear decrease in the fundamental resonance as a function of hole radius. The optimal λ_0=1.55μm is achieved at r = 125nm. Altering r, by 5nm results in fundamental resonances in the acceptable range (less than 10% change in wavelength) of 1.53μm-1.56μm.

4.4.3.2 Shift of end holes of L3, dx

Figure 4.13 demonstrates the effect of different shift values of the end holes of the L3 cavity, dx, on the Q factor of the fundamental mode, where d = 273nm and r=125nm.

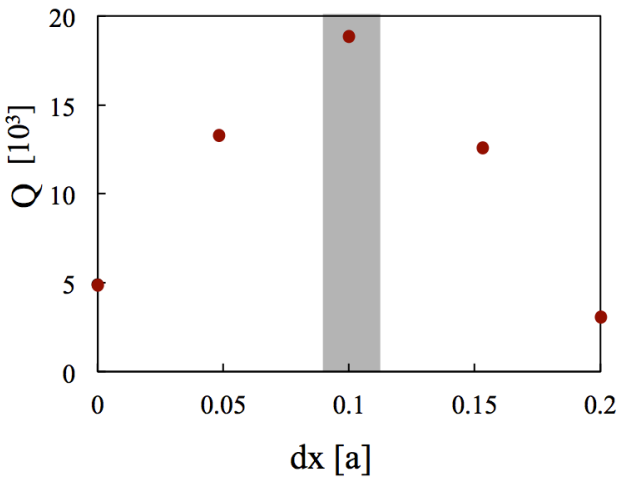


Figure 4.13: Demonstration of the effect of changing dx(a) on Q of the fundamental mode where d=273nm, r = 125nm and a = 415nm. The grey box shows the acceptable range of values of dx changing the Q by less than 10% .

Figure 4.13 shows that Q of the fundamental mode is extremely sensitive to the shift of the end holes.

4.5 FDTD Simulation results for BNAs

4.5.1 BNA for the hybrid device

In order to optimize the BNA for the hybrid device, its length, L, is tuned so that the resonant wavelength of the BNA coincides with the resonant wavelength of the PhC cavity (≈1.5 μm) to ensure the maximum coupling between the two. The BNA gap, g, is chosen to be 30nm, close to the limit of current fabrication processes in the University of Nottingham, offering a small volume for the spatial confinement of the optical field and making the device compatible with single molecule experiments. The tip angle, θ is chosen to be 30°, as it would ease the fabrication of the hybrid device (by avoiding areas of gold over PhC holes) as well as sharpening the spectrum of the BNA slightly. The BNA thickness, d, is kept constant at 40nm. The following sections, justify the choices of dimensions chosen for the BNA.

4.5.1.1 Length, L, and substrate

Figure 4.14 shows the spectral response of BNAs with g = 30nm, θ = 30° and L ranging from 500nm to 900nm. Results are produced in air and each spectrum is normalized with respect to its maximum. Figure 4.14 shows that BNAs with lengths in the range of 700nm to 800nm have broad responses close to the telecommunication wavelength range and are therefore suitable for coupling to the L3 PhC resonator.

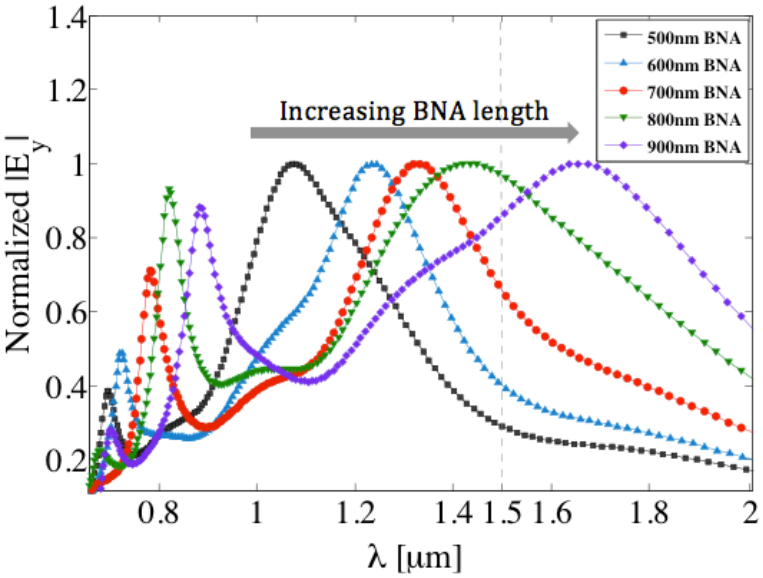


Figure 4.14: Spectra of a 40nm thick gold BNA with a tip angle of 30°, gap of 30nm and length of 500nm (black squares), 600nm (blue triangles), 700nm (red circles), 800nm (green inverted triangles) and 900nm (purple diamonds). Each spectrum is normalised with respect to its maximum.

The BNA with a length of ≈700nm is chosen as the nanoplasmonic element of the hybrid device, since placing the BNA on top of a substrate with higher refractive indexes, induces a red-shift in the spectral response making the ≈700nm long BNA in tune with the fundamental resonance of the L3 cavity (i.e. 1.54μm.). This is shown in the calculated spectra in Fig. 4.15.

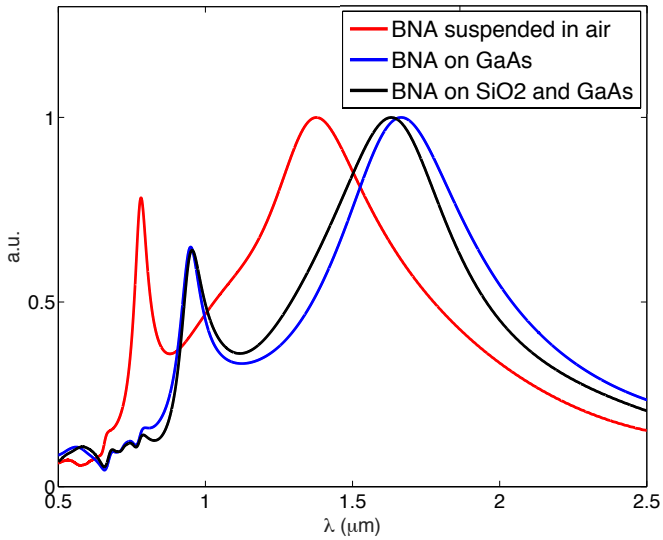


Figure 4.15: Spectra of the 700nm long BNA with no substrate (red), with a 100nm thick solid SiO_2 substrate (blue) and with a substrate comprising a 100nm thick SiO_2 layer on top of a 275nm thick solid GaAs layer (black). Each spectrum is normalised with respect to its maximum.

4.5.1.2 Tip angle, θ

The tip angle of 30° is primarily chosen so that the BNA can fit in between the holes of the L3 cavity, simplifying the fabrication process. Nevertheless, it is worth studying the effect of changing θ on the spectral response of the BNA. Figure 4.16 compares the spectral responses of BNAs with $\theta = 30°$, $\theta = 50°$ and $\theta = 90°$. All of the BNAs are 40nm thick, placed in air and have L = 700nm and g = 30nm. Each spectrum is normalised with respect to its maximum.

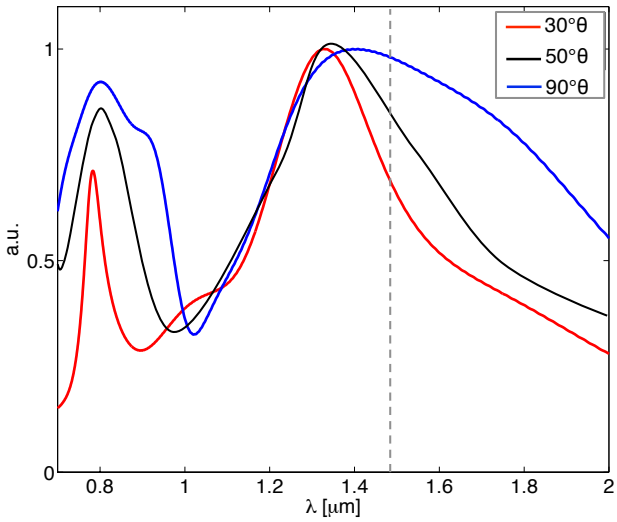


Figure 4.16: Spectra of 700nm long BNA with tip angles of 30° (red line), a 50°, (black line) and a 90° (blue line) showing the reduction in the bandwidth of the resonances when the tip angle decreases. Each spectrum is normalised with respect to its maximum.

Choosing the BNA with $\theta = 30°$ also reduces the width of the resonance resulting in a slight increase of Q-factor of the BNA.

4.5.1.3 Final BNA design for the hybrid device

The BNA designed as the nanoplasmonic component of the hybrid device has L = 700nm, $\theta = 30°$, d= 40nm and g = 30nm. Figure 4.17(a) shows the intensity pattern ($|E_y|^2$) at the XY plane passing the top surface of the designed BNA for the fundamental resonant mode. To produce this figure, the device is excited using a plane wave with a polarization along the longitudinal axis of the BNA. The BNA spectrum is presented in Fig. 4.17(b) and the fundamental and second resonances are marked. Note that although the second resonance is sharper, it is not used since it produces a zero at the BNA gap.

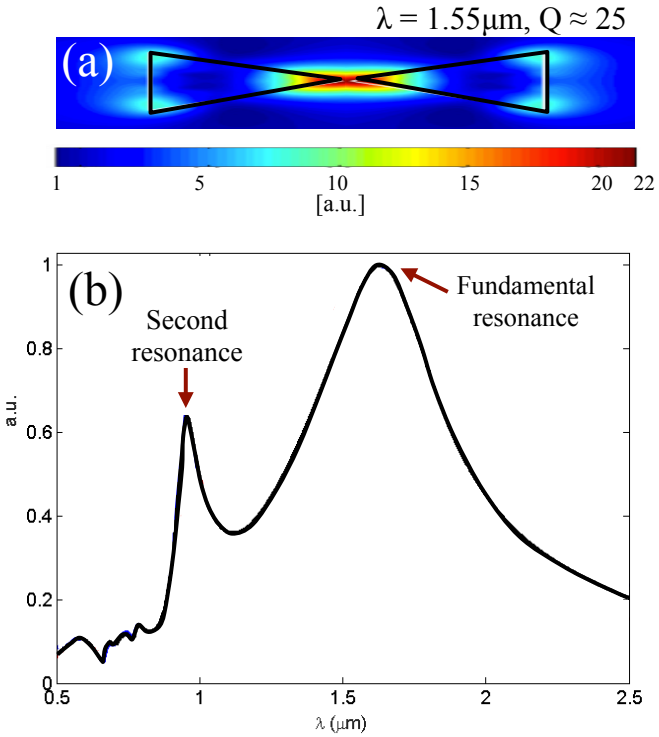


Figure 4.17: (a) Intensity pattern in an XY plane passing across the top surface of the BNA and (b) spectral response of the optimised BNA.

As can be seen in the intensity plot (Fig 4.17(a)), the beam has ≈ 20 times higher intensity in the gap of the BNA than on its surface. Optical intensity at the outer corners of the BNA also increases by ≈ 10 times compared to the surface of the BNA.

The designed BNA has a Q-factor of 25, a V_{eff} of $3.3\times10^{-3}(\lambda/n)^3$ and a Q/V_{eff} of ≈7,500.

4.5.2 BNA simulation results for fabrication and experimental purposes

BNAs of various dimensions were simulated for the fabrication of "plasmonic nanoantenna coverslips" (please refer to chapter 6 for information regarding the fabrication of BNAs) used for nanoplasmonic trapping experiments (please refer to chapter 8 for nanoplasmonic trapping results). Note that the trapping laser used for the nanoplasmonic trapping experiments has a wavelength of 1064nm.

The BNAs modelled in this section are made of gold and have d = 40nm. They are placed on top of a glass substrate and are immersed in water. Figure 4.18(a) shows the spectral responses of BNAs with g = 30nm and $\theta = 30°$ with L varying between 150nm and 1000nm. Figure 4.18(b) shows the spectral responses of BNAs with g = 50nm and $\theta = 30°$ with L varying between 150nm and 1000nm. Figure 4.18(c) shows the spectral responses of BNAs with g = 30nm and $\theta = 90°$ with L varying between 150nm and 1000nm. Figure 4.18(d) shows the spectral responses of BNAs with g = 50nm and $\theta = 90°$ with L varying between 150nm and 1000nm.

Looking at the position of each spectra with respect to the wavelength of the laser beam used during this PhD (λ = 1064nm) as well as width of the resonance (Q can be calculated from $\frac{\Delta\lambda}{\lambda}$), intensity enhancement at the gap of the BNA can be predicted and therefore the intensity gradient near the gap. This can be used to predict the trap strengths produced at the gap of each BNA. This is used in chapter 8 to compare the experimental and simulation results.

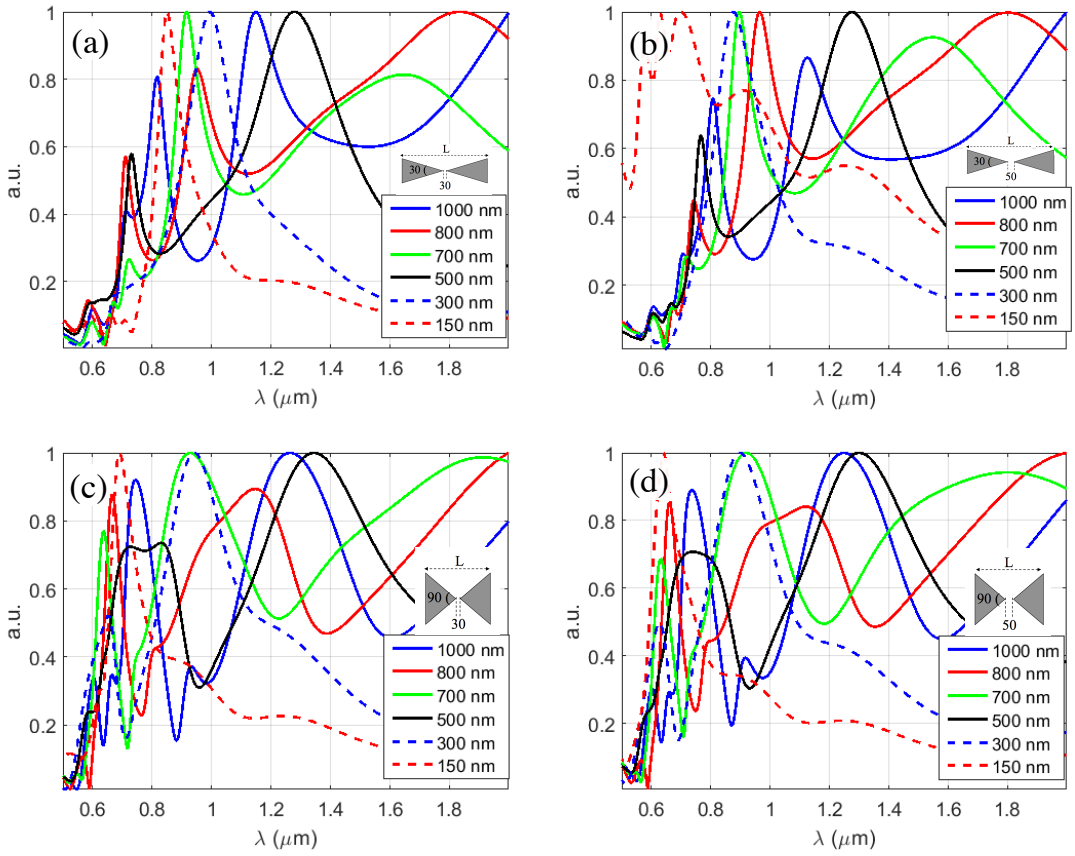


Figure 4.18: Spectral response of BNAs with variations in length for BNAs with (a) $\theta = 30°$ and g = 30nm, (b) $\theta = 30°$ and g = 50nm, (c) $\theta = 90°$ and g = 30nm and (d) $\theta = 90°$ and g = 50nm.

4.6 Summary

This chapter introduced PhC cavities such as the L3 cavity and plasmonic nanoantennas such as BNAs and discussed their characteristics. Most notably, PhC cavities have high Q-factors and are capable of storing light due to their photonic band-gaps and TIR, but they have V_{effs} of the order of cubic wavelength. BNAs on the other hand localize light in small "hot-spots" with V_{eff} three to four orders of magnitude smaller than the cubic wavelength due to LSP. These two devices are the basis of

the hybrid device optimized in chapter 5.

Optimized building blocks for the hybrid device (in air) were then presented, demonstrating their spectral and spatial responses. The optimised L3 cavity has a fundamental resonant mode at 1.54μm and a Q-factor of $\approx$ 37,000 with a V_{eff} of 0.77 $[(\frac{\lambda}{n})^3]$ and $\frac{Q}{V_{eff}}$ of $\approx$ 50,800 $[(\frac{n}{\lambda})^3]$ at the fundamental mode. The optimized BNA has a fundamental resonant mode at 1.54μm and a Q-factor of $\approx$ 25 with a V_{eff} of 3.3×10^{-3} $[(\frac{\lambda}{n})^3]$ and a Q/V_{eff} of $\approx$7,500 $[(\frac{n}{\lambda})^3]$.

Tolerances were calculated for small variations in the design parameters for the L3 cavity bases on a 273nm thick GaAs slab. These results were used by Dr. Mellor when fabricating the PhC cavity (fabrication results presented in chapter 6).

The spectral responses of BNAs of different geometries placed on top of a glass substrate in water was presented, enabling prediction of the trap strength at the gap of each BNA and comparison with experimental data presented in chapter 8.

5

Design of a hybrid photonic-plasmonic cavity for applications in high-throughput single-molecule experiments

The previous chapter introduced photonic crystal (PhC) cavities and nanoplasmonic antennas. It studied their spectral and spatial behaviour and showed that plasmonic nanoantennas such as bowtie nanoantenas (BNAs) have a broad spectral response and are very effective in creating high-intensity, sub-diffraction hot-spots, but they are lossy and inefficient in terms of energy storage. On the other hand, while studying the PhC cavities, it was clear that they have extremely narrow spectral responses and are very effective in storing energy, but they are limited by diffraction in their spatial localization of light.

One of the objectives of this project was to design a device suitable for high-throughput, single-molecule experiments. To obtain this, a hybrid device combining a PhC cavity and a BNA was designed as a building block of a multicomponent platform capable of running multiple single-molecule experiments simultaneously. This building block needs to be energy efficient and have an externally accessible, nanosized hot-spot for single-molecule applications.

This chapter focuses on the design and numerical characterisation of the hybrid photonic-plasmonic device. It consists of a 2D PhC cavity that acts as an energy reservoir and a metallic BNA that confines some of the light into a nano-scale, externally accessible hot-spot on the surface of the planar device. A dielectric spacer layer between the BNA and the PhC controls the energy efficiency of the device and the proportion of the light localised in the hot-spot. A PhC waveguide is coupled to the hybrid device to demonstrate the integration route with photonic integrated circuits.

The chapter begins by providing a quick overview of the existing hybrid photonic-plasmonic devices. The design of the hybrid device proposed during this project follows this. Next, a new figure of merit (FOM) is derived, which ensures the maximum optical energy density in the nanosized, externally accessible hot-spot, given a fixed input power. The optimization of the spacer layer with respect to the new FOM is then presented. This is followed by showing the characteristics of the optimised hybrid device as well as its integration with a PhC waveguide. The chapter concludes with a discussion and comparison between the hybrid device and its building blocks (i.e. the BNA and the L3 PhC cavity).

The optimization of the hybrid device was carried out during a one month visit to the department of engineering at the University of Ferrara (covered by the BESTS scholarship) and in collaboration with Dr. Bellanca at that university.

All simulation results presented in this chapter have been produced by running stable, converegnt 3D FDTD simulations.

5.1 Existing hybrid photonic-plasmonic devices

Combining photonic and plasmonic structures has enabled huge advances in light-matter interactions by creating hybrid devices that benefit from nanometre-scale localization of light enabled by plasmonic phenomena and the high photon lifetime of dielectric photonic structures. In addition to this, the metallic nanoantennas allow light collection and localization over a large bandwidth and k-vector range, much larger than dielectric devices. Controlling the energy flow between the components in a hybrid photonic-plasmonic device has led to a large cache of research advancing the field of optoelectronic circuits. This includes design and fabrication of light sources (lasers) [196,197], waveguides [198–200], response-sensitive filters [201], optical detectors [202] and light-focusing devices that can be used for coupling purposes [203,204]. These devices generally consume less energy and have smaller footprints compared with their commonly used alternatives.

Some hybrid photonic-plasmonic cavities are merely designed to have a high Q/V factor and can be used in a broad range of applications [205–212], from optoelectronic applications such as realization of lasers to life sciences applications such as biosensing [213–215] and optical trapping [100,216]. Figure 5.1 shows published examples of the designs of hybrid photonic-plasmonic devices.

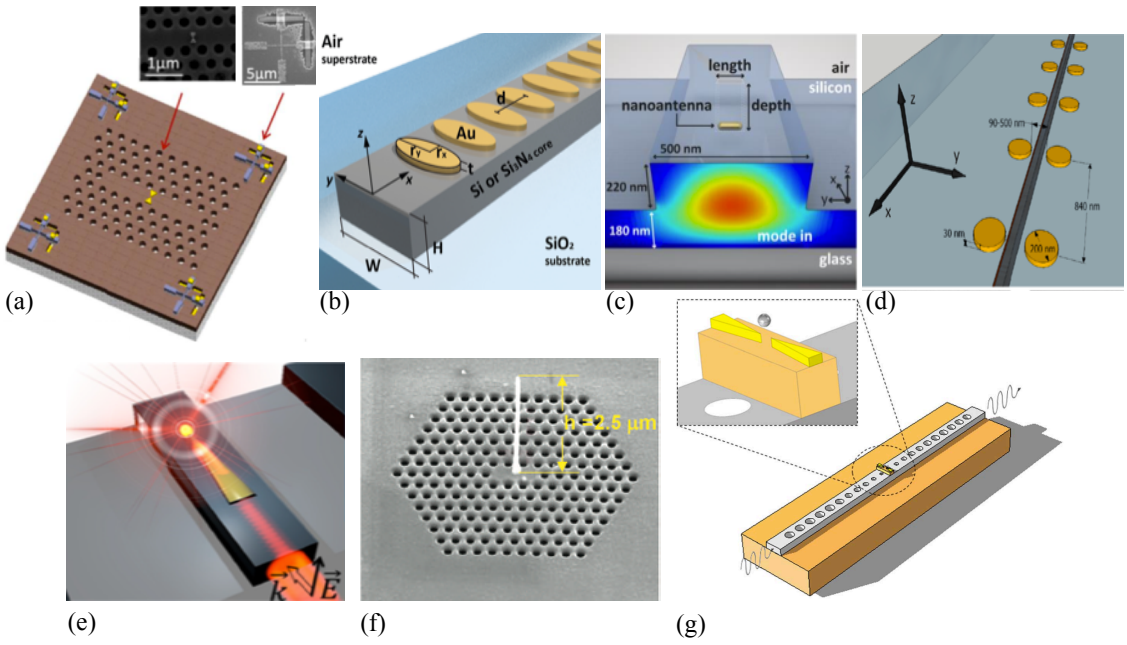


Figure 5.1: Examples of hybrid photonic-plasmonic structures for (a) lasing [197], (b) waveguiding [200], (c) filtering [201], (d) detection [202], (e) on-chip light focusing [204], (f) biosensing [213] and optical trapping [100].

During this project, a novel hybrid device was proposed based on a 2D PhC cavity, a gold BNA and a planar spacer between the two [83,101]. The spacer layer covers the entire top surface of the device. The flat surface and compatibility with fibre optics make it more practical for use in the life sciences. The device is optimized to act as a unit cell of a multicomponent platform for single-molecule high-throughput experiments, maximizing the energy density in the nano-sized BNA gap for a given input power.

5.2 The proposed hybrid device

The device proposed during this project is comprised of a PhC cavity, based on a 275nm thick gallium arsenide (GaAs) slab with a triangular lattice of air holes to

form an air-suspended PhC membrane, a gold BNA with its length tuned to resonate at the fundamental resonant mode of the PhC cavity and a silicon dioxide (SiO_2) layer separating the two. The PhC has a lattice constant of a = 410nm and hole radius of r = 125nm. The L3 cavity is formed by removing three adjacent holes from the PhC structure. The air holes at the ends of the cavity are shifted by 0.2a to increase the Q-factor of the cavity [195]. GaAs was chosen as the slab due to its high refractive index, n, resulting in better confinement of light in the vertical direction compared to other dielectrics in air/water (using total internal reflection). Other materials such as silicon and indium phosphide are also suitable materials for this PhC. The L3 cavity is designed to operate in C-band to be compatible with photonic integrated circuits and common fabrication techniques. The SiO_2 spacer is 75nm thick with the holes of the PhC membrane extending through it to increase the Q-factor of the device by reduction of waveguiding in this layer. The gold BNA consists of two 40nm thick isosceles triangles forming a bowtie shape with a gap of 30nm (the distance between the two tips). The tip full-angle of each triangle, θ, is 30° and the total length of the BNA is 700nm resulting in a resonance in the C-band [217,218]. These dimentions are compatible with current fabrication procedures. The BNA is placed on top of the SiO_2 layer and oriented perpendicular to the longitudinal axis of the L3 cavity (x axis in Fig.5.2a), to couple to the maxima of the fundamental TE mode of the PhC cavity.

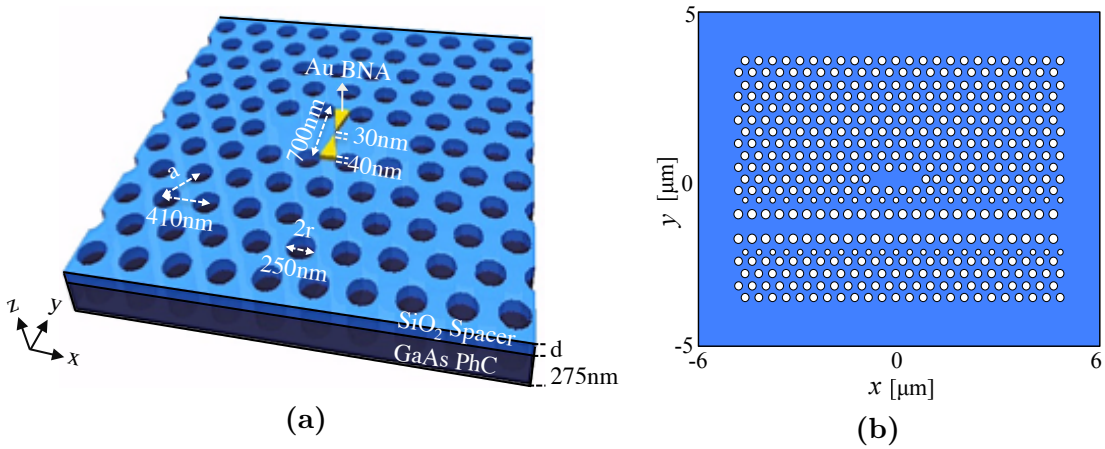


Figure 5.2: (a) Illustration of the proposed hybrid photonic-plasmonic nanoresonator comprised of an L3 PhC cavity (gray), a gold BNA (yellow) and a SiO_2 layer separating the two as well as (b) an illustration of the W1 PhC waveguide combined with an L3 cavity used as a realistic route to excite the hybrid structure realistically.

To demonstrate a configuration allowing a realistic excitation of the structure, a W1 PhC waveguide created by removing a line of holes along the x direction is coupled to the cavity as shown in Fig.5.2b. This waveguide is placed close to the PhC cavity in order to couple the propagating field with the PhC resonator. The waveguide is designed to efficiently couple to the fundamental resonant mode of the cavity while maintaining a high Q-factor for the hybrid structure, as described in S. Malaguti,*et al.* [194]. The radii of the rows of holes immediately adjacent to the waveguide centre were increased from 125nm to 131.2nm. The radii of the second rows of holes adjacent to the waveguide were decreased from 125nm to 90.2nm. These holes were also shifted away from the waveguide by 0.2a.

5.3 Figure of Merit

In order to optimize the hybrid resonator for multiplexed arrays of single-molecule experiments, it is desired that the device achieves the maximum field intensity in the BNA gap for a given input power. This will minimize the energy consumption of the device, allowing multiplexing and the creation of a multicomponent platform. To be able to perform single-molecule experiments, it is important that the hot-spot is externally accessible and nanometres in dimension. Knowing that this hot-spot is created at the BNA gap, its volume is determined by the geometry of the BNA gap and remains minimally changed. Therefore, once the geometry of the BNA is fixed, to optimize the hybrid device, the energy in the externally accessible hot-spot in the BNA gap must be maximized for a given input power. Figure 5.3 illustrates the labelling that is used to refer to different regions of the hybrid device throughout this section.

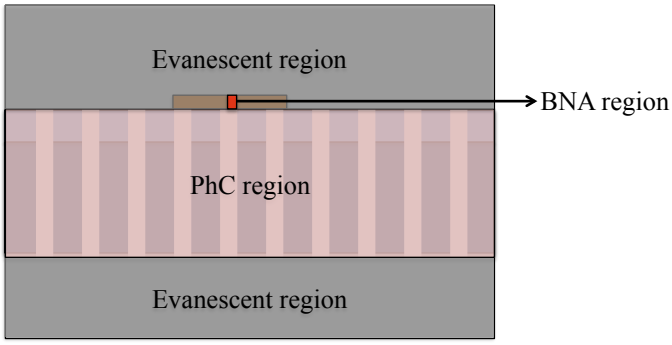


Figure 5.3: Simple illustration of the device in the computational domain (side view) with regions labelled as they will be used during this section.

The energy distribution in the hybrid device can be described as:

$$U_{hybrid} = U_{PhC} + U_{BNA} + U_{evanescent}, \tag{5.3.1}$$

were, U_{hybrid} is the total energy stored in the hybrid device, U_{PhC} is the energy

stored in the PhC region including the spacer layer, U_{BNA} is the energy stored in the externally accessible BNA gap, and $U_{evanescent}$ is the energy stored in the external region excluding the BNA gap and including the BNA itself.

Maximizing the energy in the BNA gap for a give input power leads to the definition of a new figure of merit (FOM),

$$\boxed{FOM = \frac{U_{BNA}}{P_{in}},} \tag{5.3.2}$$

where P_{in} is the input power to the hybrid resonator.

From the definition of Q (refer to the equation 4.1.1):

$$Q = 2\pi f_{opt} \frac{U_{hybrid}}{P_{loss}} \tag{5.3.3}$$

where f_{opt} is the fundamental resonant frequency. Using time-reversal symmetry (i.e. P_{in}=P_{out} when the device is operating at steady state) the input power can be written as:

$$P_{in} = \frac{2\pi f_{opt} U_{hybrid}}{Q}. \tag{5.3.4}$$

Therefore,

$$FOM = \frac{U_{BNA} Q}{2\pi f_{opt} U_{hybrid}}. \tag{5.3.5}$$

Assuming that most of the energy in the device is stored in the PhC region including the spacer layer, the total energy in the device can be approximated to the energy stored in the PhC region. i.e:

$$U_{hybrid} \approx U_{PhC}. \tag{5.3.6}$$

Using the equation 4.1.2 to calculate the energy in the BNA and PhC regions:

$$\frac{U_{BNA}}{U_{hybrid}} \approx \frac{V_{BNA}\ [\epsilon_{BNA}\ E^2_{BNA}]_{max}}{V_{PhC}\ [\epsilon_{PhC}\ E^2_{PhC}]_{max}}, \tag{5.3.7}$$

where V_{BNA}, V_{PhC} are the effective volumes of the BNA gap region and the PhC region and $[\epsilon_{BNA}\ E^2_{BNA}]_{max}$, $[\epsilon_{PhC}\ E^2_{PhC}]_{max}$ are the peak energy densities in the BNA and PhC regions, respectively.

Calculating V_{BNA} and V_{PhC} separately using the method described in equation 4.1.2 is only valid for the hybrid devices in which the field distribution in the BNA gap is minimally perturbed by the PhC and the field distribution in the PhC is minimally perturbed by the BNA. Although both V_{BNA} and V_{PhC} are calculated at the fundamental resonant frequency of the hybrid, they cannot be called "effective mode volume", since they only account for part of the energy of the mode and are not calculated over the entire computational domain.

Once the BNA and PhC cavity designs are fixed, their effective volumes remain nearly constant, so that

$$\frac{U_{BNA}}{U_{hybrid}} \approx \frac{V_{BNA}}{V_{PhC}} R_I, \tag{5.3.8}$$

where R_I is the ratio of the optical intensities near the centres of the BNA gap and the PhC cavity, respectively, where the field in each region reaches a maxima. Thus, the figure of merit becomes:

$$\boxed{FOM \approx \frac{V_{BNA} R_I Q}{2\pi f_{opt} V_{PhC}} \propto R_I Q.} \tag{5.3.9}$$

Thus, for fixed PhC cavity and BNA designs, we need only to optimize the product R_IQ. Equation 5.3.9 also shows that the performance of the device can be improved by starting with a PhC cavity with a high $\frac{Q}{V}$ ratio. Once the designs of the individual components are fixed, the overall structure combining the BNA and PhC cavity can be optimized by maximizing R_IQ.

This new figure of merit represents a significant departure from the use of V_{eff} and $\frac{Q}{V_{eff}}$, which are commonly used to optimize and compare the designs of simple (i.e. non-hybrid) resonators. V_{eff} is normally calculated by dividing the total energy in the resonator by the maximum optical intensity [134]. While this method

eliminates the difficulty of defining the mode boundaries and greatly simplifies the calculation, it systematically underestimates the mode volume of the resonator, by implicitly assuming that the optical intensity in the cavity is the same as the peak intensity. However, applying this method of calculating V_{eff} to a hybrid photonic-plasmonic cavity, is physically misleading and can give V_{eff} an anomalous intensity dependence. This is due to the very high intensity in the plasmonic nanoantenna, which is strongly localized so that only a relatively small percentage of the total energy is stored there. Consequently, V_{eff} for the hybrid resonator often appears to be much smaller than the actual volume in which most of the energy in the device is stored (i.e. the PhC cavity). A misleading value for V_{eff} also affects usefulness of $\frac{Q}{V_{eff}}$, as a measure of how tightly the energy in the structure is confined spatially and spectrally. Furthermore, the use of a $\frac{Q}{V_{eff}}$ for hybrid resonators (such as the one considered here), implicitly assumes that all of the modal energy is located inside the externally accessible gap. Thus, although calculated and presented here for comparison with other work in the field, the values of V_{eff} and $\frac{Q}{V_{eff}}$ should be treated with care.

5.4 Optimisation of the spacer layer

The spacer layer is optimised by changing its thickness and structure. The optimisation of the spacer thickness for the hybrid resonator is shown in Fig. 5.4. When the BNA sits directly on top of the PhC cavity (d = 0 nm), R_I is at its highest, meaning that a large proportion of the energy ($U \propto E^2$) is located in the BNA gap, with a considerable amount of energy still trapped in the slab due to the light cone (Fig. 5.4a). This causes the energy efficiency to be at its lowest, with Q = 817 (Fig.5.4b). Thus, even though the light in the resonator is strongly coupled to the BNA resulting in a high relative intensity, R_I, the absolute optical intensity in the hot-spot is low because the total energy stored in the device is low. When d = 0 the

effective mode volume also has its lowest value of $V_{eff} = 0.059$ ($(\lambda/n)^3$), as shown in Fig. 5.4c, and $\frac{Q}{V_{eff}}$ is 13,850. This is because of the low stored energy and the comparatively high intensity in the BNA gap. As d increases to 150 nm, the energy loss from the BNA decreases and the Q of the resonator increases, reaching a maximum of 26,000 at d = 150 nm (Fig.5.4b). As d increases beyond 150 nm, the SiO_2 layer begins to act like a semi-infinite optical cladding layer and the optical field in the BNA becomes insignificant. At the same time, the Q of the resonator drops - probably because the PhC L3 cavity was optimised for a membrane thickness of 275 nm and the increase in vertical mode width with spacer layer thickness represents an increase in the effective membrane thickness.

Extending the holes of the PhC into the SiO_2 spacer reduces losses due to waveguiding in the spacer, thereby increasing Q (Fig.5.4b). Although $\frac{Q}{V_{eff}}$ is largest for d=150 nm, R_I is low (Fig. 5.4a). The spacer thicknesses which minimizes V_{eff} at d=0 nm or maximizes $\frac{Q}{V_{eff}}$ at d = 150 nm, both lead to suboptimal performance i.e. low values of R_IQ as shown in Fig. 5.4e. In terms of the new FOM, R_IQ, the best performance is obtained for a spacer thickness of d = 75 nm, which maximizes the new figure of merit (FOM $\propto R_IQ \approx$ 35,000). This design provides significant optical intensity enhancement in the externally accessible BNA gap whilst maintaining high optical efficiency or Q. For this design (including the spacer layer with holes drilled into it), the optical intensity at the centre of the BNA gap is 4.3 times higher than that at the centre of the PhC cavity and Q = 8,200. This demonstrates the importance of the new figure of merit and shows that the highest field intensity in the BNA gap for a given input power is obtained with a spacer thickness of 75nm.

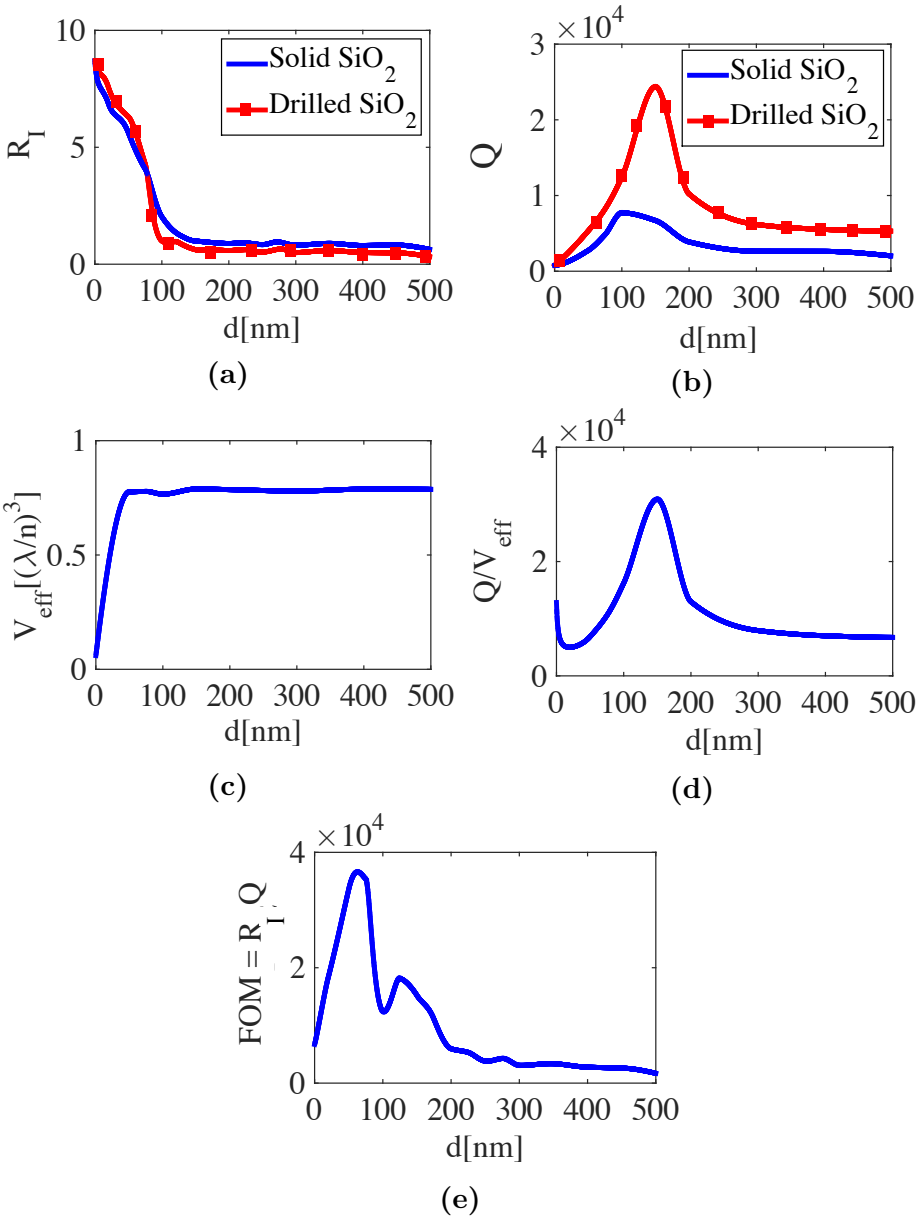


Figure 5.4: Effect of the changing the spacer layer thickness, d, on (a) Q, (b) R_I, (c) V_{eff}, (d) Q/V_{eff} and (e) R_IQ. Figures are produced at the fundamental resonant mode of the structure. Red lines show the response of the device when the spacer layer is solid, and blue lines show the response of the device where the holes of the PhC extend through the spacer layer.

5.5 Characteristics of the optimised hybrid device

5.5.1 Spectral response

The spectral responses of the isolated BNA, isolated L3 PhC cavity and hybrid device are presented in Fig. 5.5. The hybrid device has a spectral response similar in shape to that of the PhC cavity and much sharper than the spectral response of the isolated BNA. Its fundamental resonant mode is at $\lambda_0 = 1.54\mu$m and the second resonant mode is at $\lambda = 1.36\mu$m. The resonant mode of the isolated PhC cavity with odd symmetry at $\lambda = 1.47\mu$m is not present in the hybrid structure because its field distribution has a zero at the centre of the cavity. Thus, it does not get resonantly enhanced by the BNA in the hybrid device. The spectral response of the hybrid structure is evaluated in the PhC cavity as well as in the spacer layer and the BNA gap.

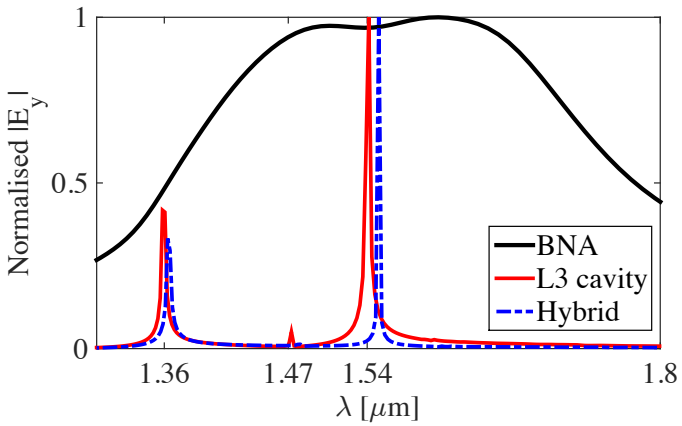


Figure 5.5: Comparison between the spectral responses of the isolated L3 cavity (red curve), the optimized hybrid nanoresonator (blue dashed curve) and the isolated BNA (black curve).

5.5.2 Intensity profiles

Figures 5.6a-d show the optical intensity distribution ($|E_y|^2$) in the xy and yz planes passing through the centre of the device with and without the BNA and Fig. 5.6e shows the optical intensity ($|Ey|^2$) along a vertical line passing through the centre of the structures with and without the BNA when the structure is excited with a point source. The values of intensity throughout the devices are normalized with respect to the intensity at the centre of the PhC cavity. Comparing the optical intensity distributions for the devices with, and without the BNA are presented in Figs. 5.6b,d and Figs. 5.6a,c, respectively. It is clear that the presence of the BNA creates an externally accessible hot-spot in the BNA gap and suppresses the optical field where the metal is located, resulting in high intensity gradients at the BNA gap. This is essential for optical trapping and manipulation experiments. As seen in Fig.5.6e, the optical intensity on top of the structure (at the position of the BNA gap) is approximately 60 times larger when the BNA is present, when excited with a point source located off-centre of the PhC cavity. The plots are produced after the source has fully decayed in the simulation (i.e the results are taken at steady state).

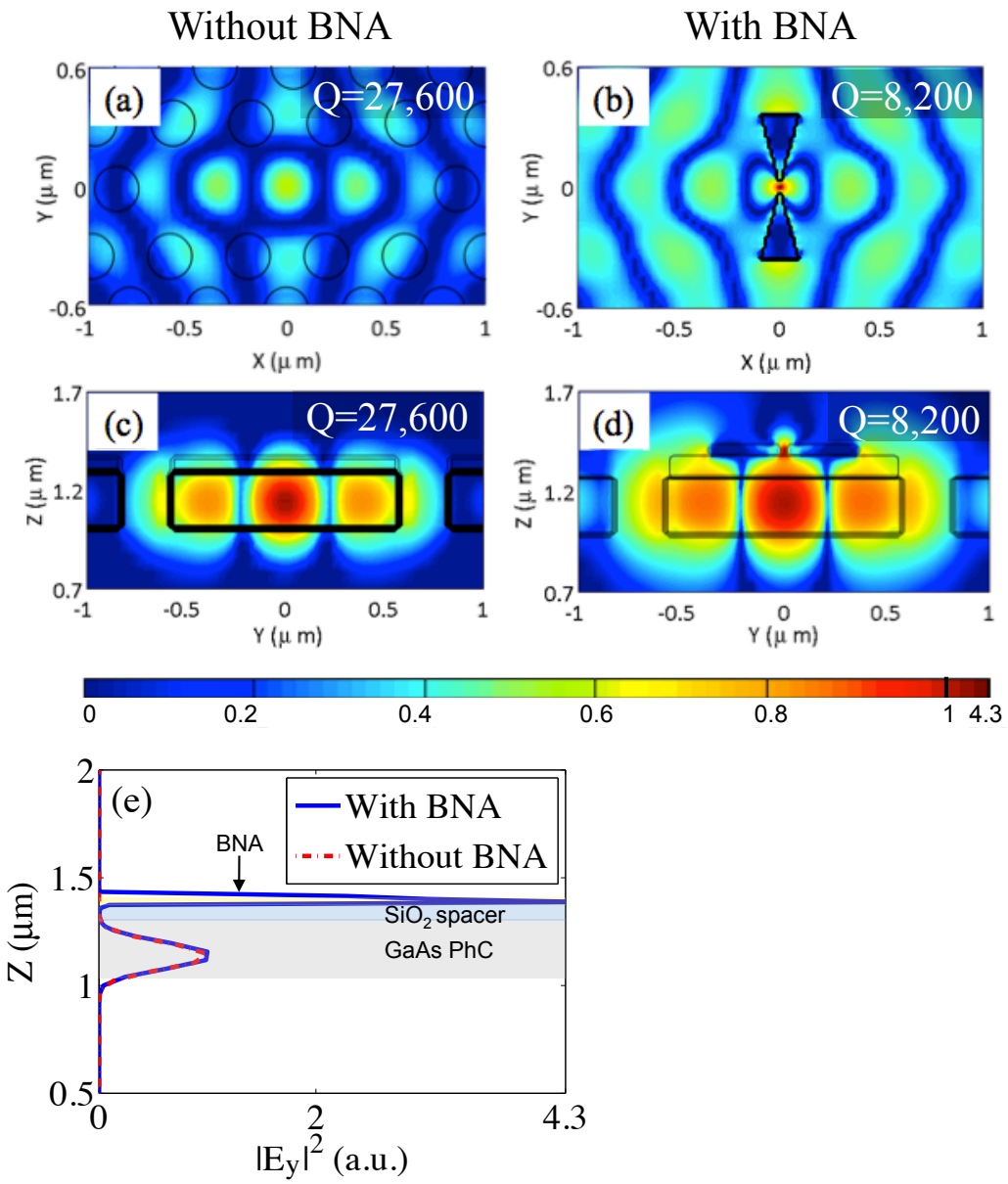


Figure 5.6: Logarithmic plots of the optical intensity ($|E_y|^2$) in the xy plane and positioned on the top surface of the structures (including the 75 nm thick spacer layer) (a) without and (b) with the BNA, and in the yz plane passing through the centre of the structure (c) without and (d) with the BNA when the structure is excited with a point source. (e) Shows the comparison of the optical intensity ($|E_y|^2$) along a vertical line passing through the centre of the structure with (blue) and without (red) the BNA when the structure is excited with a point source.

5.5.3 Coupling the hybrid device to a waveguide

To demonstrate the compatibility of the hybrid device with photonic integrated circuits, this section shows that it is possible to excite the hybrid device using a waveguide.

A W1 waveguide was formed by omitting the fourth row of air holes from the PhC to achieve a good coupling with the cavity and obtain an acceptable quality factor for the hybrid device. The PhC and the PhC cavity remain the same with the lattice constant, a = 410nm. The rows of holes immediately adjacent to the wave-guide (marked as L1 in Fig.5.7) have air holes with a radius of 0.32a and the second rows adjacent to the waveguide (marked as L2 in Fig. 5.7) have a radius of 0.22a. The second rows of air holes adjacent to the waveguide are also shifted away from the waveguide by a length of 0.2a [194]. The holes of the PhC are extended through the SiO_2 layer for the reasons described in the previous sections of this chapter.

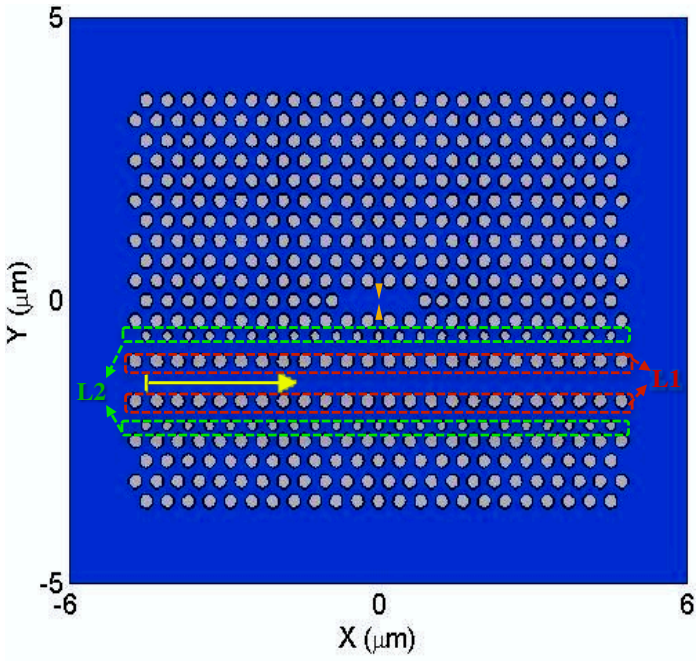


Figure 5.7: Schematic of the hybrid device coupled to a W1 PhC waveguide based on a GaAs membrane. The waveguide is formed by removing the fourth row of air holes below the L3 cavity. The first row of holes immediately adjacent to the waveguide (marked as L1) has been enlarged in radius by a factor of 0.02a. The second rows of holes adjacent to the W1 waveguide (marked as L2) have been reduced in radius by a factor of 0.08a. The second rows of holes adjacent to the waveguide have also been shifted away from the waveguide by 0.2a. The yellow arrows shows the position and direction of the E_y plane source propagating through the waveguide.

To excite the structure via this waveguide, an xz planar source was placed at the beginning of the waveguide (shown by a yellow arrow in Fig. 5.7) generating a TE fundamental mode propagating through the waveguide. Fig. 5.8 shows a plot of the scattering parameter obtained by dividing the optical flux exciting the waveguide by the optical flux propagating through the waveguide close to the source (S_{21} parameter) for the waveguides placed at various distances from the L3 cavity.

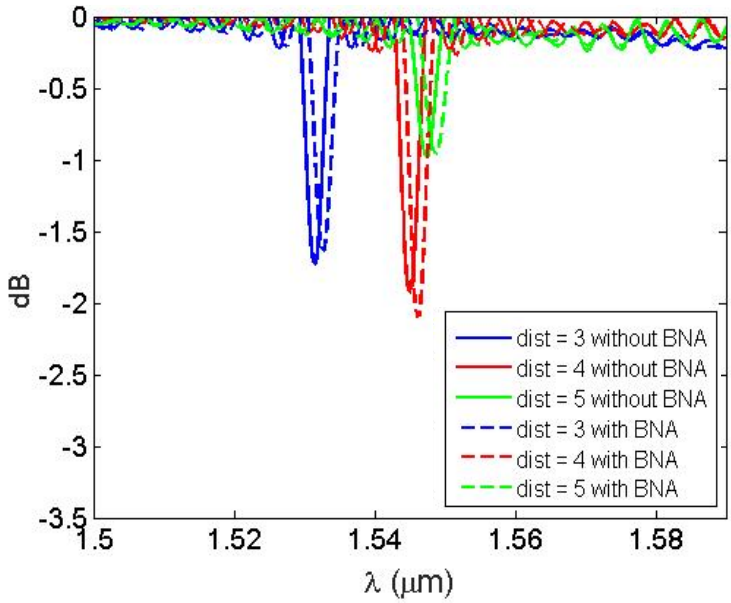


Figure 5.8: Illustration of the S_{21} parameters for the W1 waveguides with distances of 3 (blue), 4 (red) and 5 (green) rows away from the L3 cavity. The solid lines present the S_{21} parameter for The structure without the BNA and the dashed lines present the S_{21} parameters for the structure with the BNA.

The distance of four rows between the PhC cavity and waveguide was chosen as it offers a good coupling between them (PhC cavity and PhC waveguide) as well as maintaining a reasonable quality factor of the hybrid device. The S_{21} parameters of waveguides with distances of 3, 4 and 5 rows from the L3 cavity are illustrated in Fig. 5.8. The S_{21} parameter shows the difference between the light injected into the waveguide and the light exciting the waveguide. A dip in the S_{21} parameter plot shows coupling of light from the waveguide to the L3 cavity at the frequency of the dip. If at the resonance wavelength of the cavity, the light couples more to the cavity from the waveguide, this results in a higher loss at this frequency in the S_{21} parameter and shows a better coupling. The quality factors at the fundamental resonance of the hybrid device excited using a W1 waveguide with 3, 4 and 5 rows between the L3 cavity and the waveguide are presented in Table 5.1. The resonances and quality factors of the device were obtained by taking the Fourier transform (FT)

of the signal at a point probe inside the cavity.

Table 5.1: Fundamental resonance corresponding quality factor for the hybrid device excited via a W1 waveguide with different spacing between the waveguide and L3 cavity with and without the BNA.

# rows between cavity and waveguide	BNA	λ_0	Q
3	absent	1.54	3,400
3	present	1.54	2,500
4	absent	1.55	3,300
4	present	1.55	2,900
5	absent	1.55	6,700
5	present	1.55	4,800

As the distance between the waveguide and the cavity increases, an increase in the Q-factor of the hybrid device can be observed, but a reduction in coupling between the waveguide and the cavity.

When the structure is excited via the W1 waveguide, the shape of the fundamental resonant mode of the device is slightly altered due to the coupling of light between the L3 cavity and waveguide. The shape of the mode near the waveguide also changes as can be seen in Fig. 5.9 where the optical intensity in an xy plane passing the top surface of the BNA (z = 1.415μm) is plotted. Nevertheless, a hotspot is produced in the BNA gap whose intensity is much higher than the optical intensity above the top surface of the hybrid structure in the absence of the BNA. The optical intensity profiles in the xy and xz planes passing through the centre of the cavity are similar to when the structure was excited via a point source inside the PhC cavity. When exciting the structures with and without a BNA through the waveguide, the same excitation power was used. Therefore, the results of these simulations are directly comparable. In this case, similar to when excited with a point source, an externally

accessible hot-spot is created at the BNA gap, as seen in Fig.5.9a. Figure 5.9b shows the optical intensity ($|E_y|^2$) along a vertical line passing through the centre of the structures with and without the BNA. The optical intensity in each simulation is normalised with respect to the power transferred from the waveguide to the hybrid cavity. This is calculated by subtracting the total power entering the waveguide and the total power exciting the waveguide. The optical intensity on top of the structure (at the position of the BNA gap) is 40 times larger when the BNA is present.

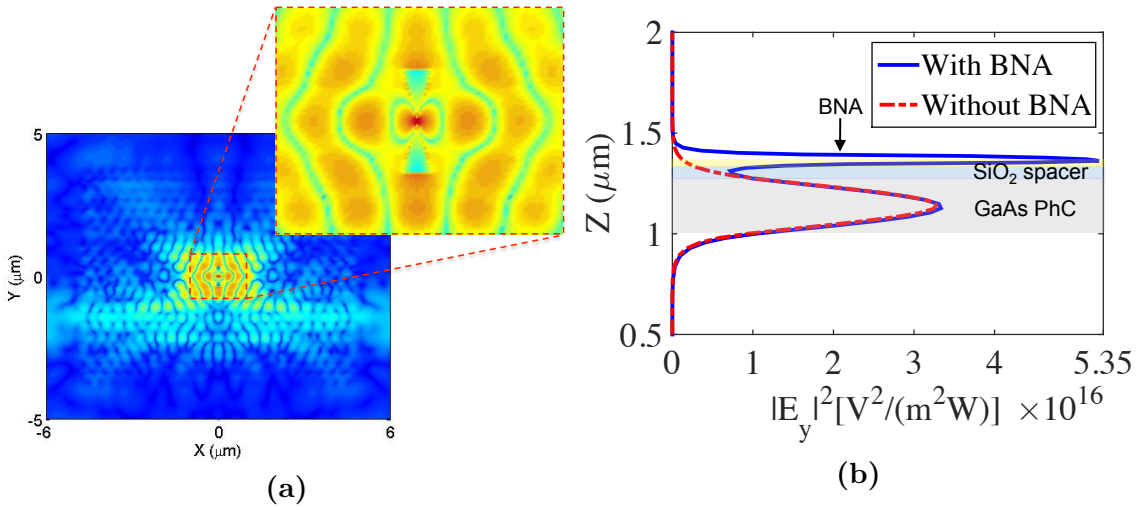


Figure 5.9: (a) Logarithmic plot of the optical intensity ($|E_y|^2$) in the xy plane at the top surface of the structure when the hybrid cavity is excited via a W1 PhC waveguide. (b) The expanded plot shows the optical intensity pattern in the BNA region. (c) A comparison of the optical intensity ($|E_y|^2$) along a vertical line passing through the centre of the structure with (blue) and without (red) the BNA when the structure is excited with a W1 waveguide.

When coupling light into the hybrid device using the W1 waveguide, the S_{21} parameter (forward gain in the optical field) is set to -0.76dB for the fundamental resonant mode of the hybrid device. Thus approximately 17% of the input light to the waveguide couples into a single hybrid device, making it very energy efficient compared to structures comprised of arrays of metallic nanoantennas illuminated vertically, in

which the laser light goes through lossy optics and the light at the BNA gap reaches enhancements up to 10 times the incident intensity. The hybrid device can achieve optical intensities in the BNA gap 60 times higher than the optical intensity on top of the PhC cavity.

5.5.4 The hybrid device in water

Placing the hybrid device in water results in a larger light-cone compared to the case in air, due to the reduction of refractive index difference between the hybrid device and its surroundings. This results in the reduction of Q-factor of the device and a small redshift in the resonant modes. The mode pattern and effective mode volume of the device in water experiences little change. Table 5.2 shows the three major resonant modes of the hybrid device as well as their corresponding Q-factors, effective mode volumes and $\frac{Q}{V_{eff}}$ for the hybrid device with a 175nm thick spacer layer placed in water.

Table 5.2: Major resonances of the hybrid cavity and their corresponding Q-factor, V_{eff} and $\frac{Q}{V_{eff}}$. The hybrid cavity has a 175nm thick spacer layer, placed in water.

Resonance	$\lambda[\mu m]$	Q	V_{eff} $[(\frac{\lambda}{n})^3]$	$\frac{Q}{V_{eff}}$ $[(\frac{n}{\lambda})^3]$
Fundamental	1.59	7,700	0.82	9,400
Second	1.52	700	0.85	800
Third	1.40	1,200	0.79	1,600

Figure 5.10(a) shows the spectral response of the hybrid device in water. Figure 5.10(b) shows the intensity distribution along a vertical line passing the centre of the device, and Fig.5.10(c-d) shows the field patterns in the xz and yz planes passing through the centre of the device. For these simulation a 1μm polystyrene bead

(n=1.57 at 1.5 μm) was also introduced representing a trapped particle. The arrows in the figure show the intensity gradient.

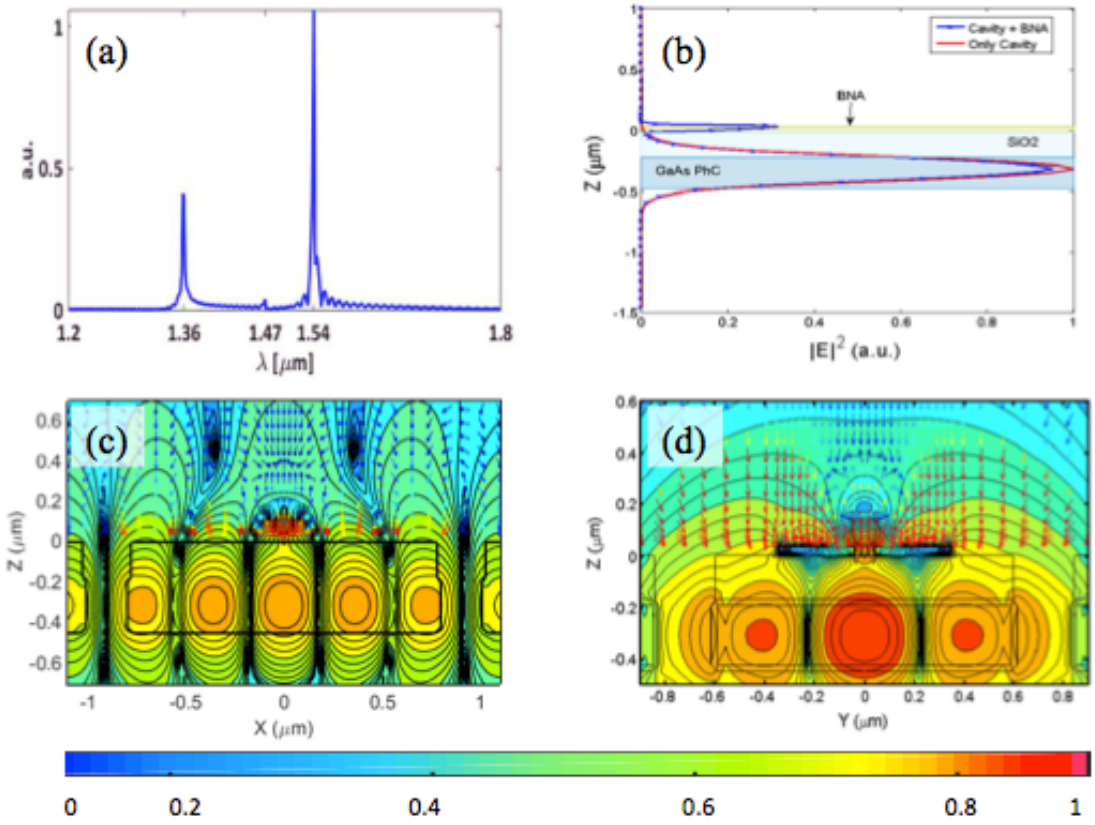


Figure 5.10: (a) Demonstration of the spectral response of the hybrid cavity in water with (b) a comparison of the field intensities across a line passing vertically through the centre of the device with (blue) and without (red) the BNA. The profiles for the fundamental mode of the device with the BNA in zx and zy planes going through the centre of the device are shown in (c-d) respectively.

5.5.5 Overall comparison

Table 5.3 provides a comparison between the characteristics of the hybrid device and its individual components. However, the hybrid structure has a higher Q com-

pared to the isolated BNA and a lower V_{eff} compared to the isolated PhC cavity. It is interesting to note that the isolated PhC cavity has a higher $\frac{Q}{V_{eff}}$ compared to the hybrid structure. The isolated PhC cavity does not provide an externally accessible hot-spot and therefore would not be suitable for studying single-molecule interactions. This is a good example of why the merit of certain devices should not be determined by considering $\frac{Q}{V_{eff}}$alone. R_I and R_IQ are also quoted for the two PhC resonator structures in Table 5.3 for comparison. R_I is simply the ratio of the intensity at the surface to that at the centre of the cavity in these cases.

Table 5.3: Comparison of λ_0, Q, V_{eff}, $\frac{Q}{V_{eff}}$ and R_IQ of the device at different design stages.

Structure	$\lambda_0[\mu m]$	Q	V_{eff} $[(\frac{\lambda}{n})^3]$	R_I	$\frac{Q}{V_{eff}}$ $[(\frac{n}{\lambda})^3]$	R_IQ
Isolated BNA	1.35	25	0.0033	-	7,500	-
Isolated PhC L3	1.54	39,500	0.778	0.65	50,700	25,675
PhC L3 + 75nm SiO_2	1.54	27,600	0.787	0.028	35,000	770
Hybrid device	1.55	8,200	0.777	4.3	10,500	35,000

5.6 K-space and far-field pattern analysis

An important feature taken into account when designing the hybrid device is the vertical emission of the device. This is one of the most important loss mechanisms resulting in the reduction of the Q-factor. The vertical emission of the device at different stages was studied by looking at the k-space and far-field plots obtained as described in section 3.4.

Figure 5.11 shows the k-space plots for isolated BNAs with aperture angles of 30° and 90° (Fig 5.11(a,b)), isolated PhC cavity (Fig 5.11(c)), PhC cavity with a 75nm spacer layer (Fig 5.11(d)), PhC cavity with a 75nm spacer layer and a 30° BNA (Fig 5.11(e)) and PhC cavity with a 75nm spacer layer and a 90° BNA (Fig 5.11(f)). All

devices were simulated in air. The black circle plotted on top of the k-space plots marks the light cone (i.e. $\omega = \frac{ck}{n}$). Therefore the region inside the black circle corresponds to the real k-vectors that emit vertically and the region outside the black circle corresponds to the imaginary k-vectors (i.e. evanescent fields).

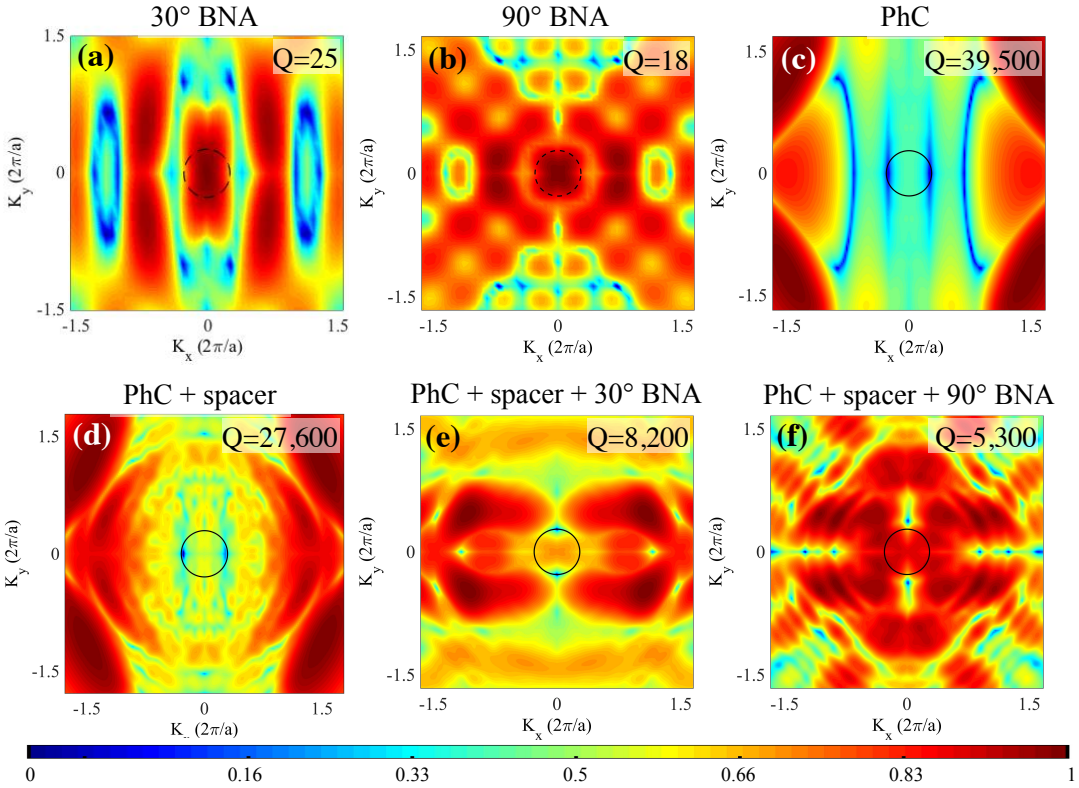


Figure 5.11: Demonstration of k-space plots for (a) the isolated BNA with a 30° aperture angle, (b) the isolated BNA with a 90° aperture angle, (c) isolated L3 PhC cavity, (d) PhC cavity with a 75nm spacer layer, (e) PhC cavity with a 75nm spacer layer and a BNA with a 30° aperture angle and (f) PhC cavity with a 75nm spacer layer and a BNA with a 90° aperture angle. The devices were all simulated in air. The black line marks the light cone (i.e. $\omega = \frac{ck}{n}$). The plots are normalised with respect to their maximum.

As demonstrated in Fig.5.11 both isolated BNAs have a large vertical emission. This is expected from their broad resonance and low Q-factors. The isolated PhC cavity on the other hand, has a very low vertical emission as expected from its

sharp spectral response and high Q-factor. The hybrid devices have a much reduced vertical emission compared to the isolated BNAs and a higher vertical emission compared to the isolated PhC. This is because of the fact that the behaviour of the photons in the device is mostly dictated by the photonic crystal. This was also shown in Fig. 5.5 where it was shown that the hybrid device has a spectral response resembling that of the PhC cavity. Comparing Fig.5.11(e) and Fig.5.11(f), it can be observed that the hybrid device with a 90° aperture angle has greater vertical emission compared to the hybrid device with a 30° aperture angle. This was one of the reasons that the 30° BNA was chosen for the hybrid device as opposed to a 90° BNA. In addition, the 30° BNA had a sharper spectral response and was more suitable for fabrication purposes as it would not fall on the PhC holes.

Figure 5.12 shows the projection of the electric field intensity on a hemisphere with a radius of 1m for z>0 for isolated BNAs with aperture angles of 30° and 90° (Fig 5.12(a,b)), isolated PhC cavity (Fig 5.12(c)), PhC cavity with a 75nm spacer layer (Fig 5.12(d)), PhC cavity with a 75nm spacer layer and a 30° BNA (Fig 5.12(e)) and PhC cavity with a 75nm spacer layer and a 90° BNA (Fig 5.12(f)). Concentric circles show the angle compared to the z-axis.

The far-field patterns, similar to the k-space plots confirm that the combination of the PhC cavity and the BNAs results in the reduction of vertical emission. The far field patterns are also useful for the choice of probe angles when characterising the devices.

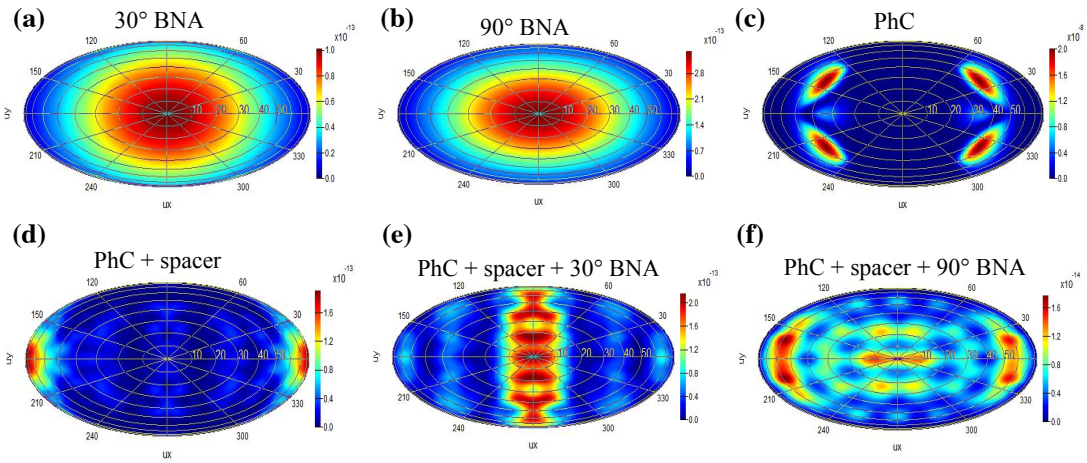


Figure 5.12: Demonstration of far-field electric field intensity patterns projected from a hemisphere with a 1m radius for (a) the isolated BNA with a 30° aperture angle, (b) the isolated BNA with a 90° aperture angle, (c) isolated L3 PhC cavity, (d) PhC cavity with a 75nm spacer layer, (e) PhC cavity with a 75nm spacer layer and a BNA with a 30° aperture angle and (f) PhC cavity with a 75nm spacer layer and a BNA with a 90° aperture angle. The devices were all simulated in air. Concentric circles show the angle compared to the z-axis.

5.7 Discussion

The development of hand-held, application-specific platforms with highly integrated arrays of hybrid optical resonators was an aim of this project. Such platforms would produce patterns of nano-sized optical hot-spots on a smooth surface and be illuminated and interrogated via a hidden network of waveguides. The successful realization of this platform will contribute to advances in many fields, including chemistry, life sciences, personalized medicine and quantum information technology.

The hybrid resonator designed in this chapter represents the key device in this plat-

form and will be used to trap, manipulate and study single-molecules and nanoparticles. They can also be designed to operate at slightly shorter wavelengths (e.g. 800nm-1000nm) to facilitate two-photon fluorescence and imaging in the visible light regime, enabling the use of common dyes and imaging techniques combined with nanoscale site specific excitation and a high signal to noise ratio. The ability of the hybrid resonator to trap on the nanoscale allows individual molecules and nanoparticles to be controlled and studied. The BNA hot-spot in the hybrid device has approximately 40 times higher intensity than the evanescent field at the surface of a conventional PhC cavity. Furthermore, the intensity gradient is as important as the intensity and enters directly into the Maxwell stress tensor describing optical forces. The high intensity in the BNA gap and nanoscale localisation produce very large intensity gradients around the hot-spot - including a positive vertical gradient, which eliminates the force drawing trapped particles down onto the PhC surface and replaces it with an upward force drawing the particles back into the hot-spot. At the same time, when the hybrid resonator is pumped through a waveguide, it only delivers light to the BNA and suppresses the unwanted illumination of the specimen across the rest of the surface. The inclusion of the SiO_2 spacer layer further reduces the surface evanescent field of the waveguides, offering additional control over the trapping and guiding of particles.

Conventional optical manipulation and nanoplasmonic trapping setups are very energy inefficient with most of the light lost passing through the bulk optics or by illuminating a large proportion of the glass substrate rather than just the BNAs. The ability to couple the hybrid resonator to an optical waveguide is a key attribute of this device, which greatly improves its efficiency and allows the unused energy to be harvested by devices downstream. The coupling between the waveguide and the hybrid device can be controlled by adjusting the design of the waveguide and its distance from the cavity to adjust the number of hybrid devices that can be powered and characterized using a single waveguide. Using the W1 waveguide design used

in this structure, about 16% of the input light is coupled into the hybrid cavity, about 2% of which is concentrated in the BNA hot-spot. By properly engineering their waveguide-cavity coupling coefficients, this waveguide could easily support the uniform excitation of four hybrid cavities.

The resonances of the devices can be individually tuned by small changes to the PhC cavity. Thus, light can be selectively delivered to specific resonators by tuning the excitation to the appropriate wavelength - allowing unprecedented control over the optical potential surface of the sample and making it possible to perform many different (or identical) single molecule experiments simultaneously. By facilitating parallel experiments, the platform will reduce the time and effort needed to collect enough data to draw statistically valid conclusions. At the same time, it will reduce the cost, time and complexity of the experiments, while simultaneously increasing experimental control and accuracy. Finally, as a highly integrated, fibre-connected platform, it will be simple and ideal for coupling to micro- and nanofluidic systems for the delivery of the molecules and particles.

5.8 Summary

This chapter focused on the design of a hybrid photonic-plasmonic resonator as the building block of a multicomponent platform for high-throughput, single-molecule experiments. The hybrid device is comprised of an L3 PhC cavity coupled to a BNA. A SiO_2 layer separates the BNA from the PhC cavity. By defining a new FOM that is more appropriate for our target application, the thickness of the spacer layer is optimized to maximize the energy in the BNA gap for a given input power. The device produces an externally accessible hot-spot, whose intensity is 40-60 times larger than that of the evanescent field at the surface of an isolated PhC cavity and at least 4.3 times larger than the intensity at the centre of the PhC cavity. The

optical intensity gradient (often a more important parameter than the optical intensity) created around the hot-spot in the BNA gap will contribute significantly to its trapping performance for nanoparticles. Finally, the hybrid resonator can be excited via a PhC waveguide, greatly improving its energy efficiency and making it compatible with user-friendly fiber-optic technologies. Thus, if successfully fabricated, this hybrid resonator will allow the realization of an integrated platform suitable of conducting a large number of single-molecule experiments simultaneously.

6

Fabrication of devices

The aim of this part of the project was to realize/obtain some of the structures designed and numerically characetrised in chapters 4 and 5. These devices would then be used to design and perform optical trapping experiments. To do this, two separate internal grants (UNICAS fundings 2015) aimed at multi-disciplinary collaborations was applied for, together with Dr. Richard Cousins and Dr. Christopher Mellor of the School of Physics and Astronomy. Both grants were successful. I led the first project aimed at fabricating metallic nanoantennas. Dr. Amanda J. Wright led the second project aimed at gaining experience in photonic crystal fabrication at Nottingham and developing future methods for the fabrication of the hybrid photonic-plasmonic devices. I performed the numerical design and characterization of the devices. Dr. Richard Cousins performed the fabrication of the plasmonic nanoantennas and Dr. Chris Mellor performed fabrication of the photonic crystals. Together these two elements form the basis of the hybrid device.

This chapter begins by presenting the key principles of electron-beam lithography which is needed to pattern nano-scale structures. This is followed by a description of the fabrication process used to realize the nanoplasmonic antennas and lists the nanoantenna dimensions fabricated. Next, the steps for fabricating the photonic/photonic-plasmonic devices are described. The successful steps taken, the

issues tackled and the results obtained in fabrication of the hybrid device follow this. Future steps required for successful fabrication of the hybrid device conclude this chapter.

It is important to note that the fabrication of devices during this project was prior to the commissioning of the University of Nottingham's NanoBeam's EB5 electron beam lithography tool in November 2017. Fabrication of the nanoplasmonic antennas during this project was performed using a converted SEM EBL and was the first successful fabrication of nanoplasmonic antennas at the University of Nottingham,

6.1 Basic principles of electron-beam lithography

Lithography is the process of transferring a pattern from one surface to another [219]. In its ancient form, it was used for imprinting shapes, illustrations and scripts from stamps and seals to clay and wax blocks. Today it is used in a vast range of applications, from production of books and textiles, to the printing of semiconductor devices.

Electron-beam lithography (EBL) is one of the most commonly used lithographic techniques for nanofabrication. It allows direct and projection writing of patterns with sub-10 nm accuracy and is mostly used in areas such as research and product development. This is because EBL is often too expensive and time-consuming for high-volume fabrication. Instead it is regularly used to create precise masks for other lithographic techniques, such as photo-lithography which is widely used for fabricating semiconductor devices [220].

EBL is similar to a scanning electron microscope (SEM) and uses a focused beam of electrons to create patterns in a layer of electron-sensitive material called the resist.

To do this, the sample of interest is first coated with the resist. This is usually done by placing a drop of the resist on the surface of the sample and spinning it to form a thin layer (typically between 10nm to 100 nm) of resist on the sample. The sample is then mounted on a holder in the SEM/EBL chamber and exposed to a focused e-beam.

The e-beam is focused using electrostatic and electromagnetic elements, similar to lenses in optical systems. The e-beam and/or the sample are then moved to draw a pattern in the resist. The length of exposure and pattern of this movement is computer programmed and controlled. This process is called EBL writing. The areas of the resist that have been exposed to the e-beam change in solubility in resist-specific solvents. This allows selective removal of the resist using the solvent, either where exposed to the e-beam (positive resist) or the areas not exposed to the e-beam (negative resist). For positive resist, the e-beam cuts the long chain polymer of the resist into shorter molecules that are soluble in the "developer solution". For the negative resist, the e-beam causes polymerization and permanent linking between the molecules, preventing their dissolution in the developer solution. This process is called resist development. The pattern created in the resist is used as a mask to either etch the sample beneath the resist, or to deposit another layer on top of it. Finally, the remainder of the resist is removed using a second solvent. This process is called lift-off [221]. To have a successful lift-off process, the surface of the structure needs to be clean. Figure 6.1 shows a simple illustration of the EBL method using a positive resist.

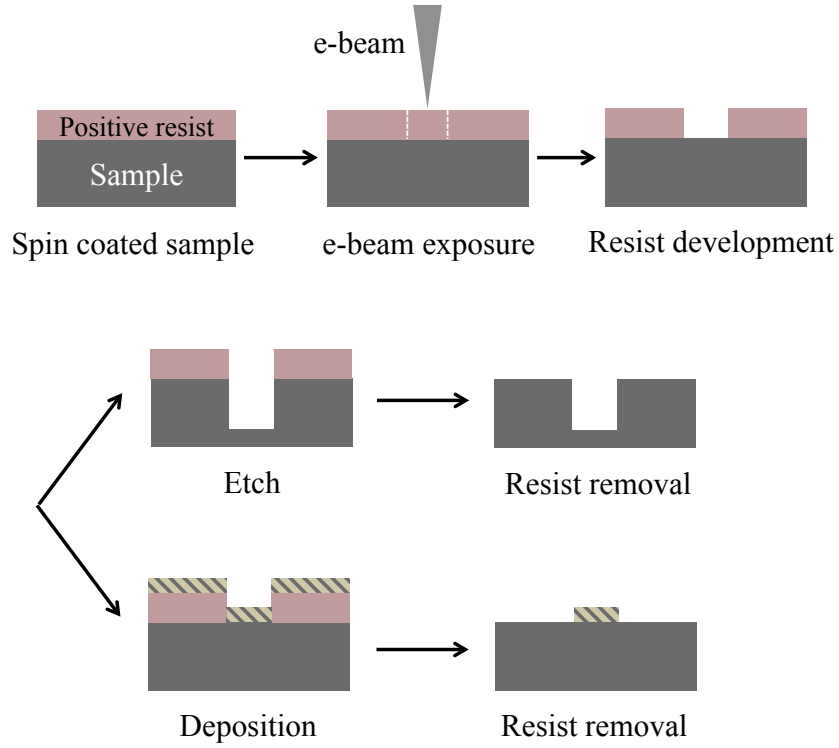


Figure 6.1: Illustration of the EBL method using a positive resist.

Similar to an optical system, when electrons are used to create images, the spot size of the focus of the beam is determined by the wavelength (λ) of the e-beam and the numerical aperture (NA) of the focusing system ($\approx \lambda$ / NA). Although the NA is kept low (typically less than 0.3) to avoid aberrations, the spot size is still very small due to the small wavelengths of the e-beam, typically ranging from 2pm to 150pm depending on the energy of the beam [222].

The limiting factor in the precision of the created pattern is not the spot-size of the focused beam, but the electron scattering in the resist/substrate or the electron-electron repulsion in the beam itself. The electron scattering in the resist or the sample, is caused by the collision of the electrons with the atoms in the sample or the resist. If the electron's path is close to the electron cloud of an atom, its path is altered but still in the same direction (forward scattering). If the electron directly hits the nucleus of an atom in the resist/sample, the electron is scattered backwards

(backward scattering). The combination of electron-electron repulsion effects and scattering effects while writing a pattern using the e-beam, causes the neighbouring material to also be exposed to the beam. These are called the proximity effects [223,224] . In order to create a better pattern, these effects are usually accounted-for by numerical calculations, tailoring the exposure times in the neighbouring material. Still, using the current methods, the practical limit of electron beam lithography is approximately 5nm. In order to have more precise features, techniques such as focused ion beam (FIB) are used in addition to EBL [221,222]. FIB is a technique that uses a focused beam of ions in a setup similar to that of a SEM, to selectively remove particles from the surface of the slab bombarded with the focused ion beam. Lines removed using FIB can be 1-5 nm in width, but FIB, which is frequently performed with Ga ions, also implants ions into the substrate, damaging the device under construction.

6.2 Fabrication of nanoplasmonic antennas

Bowtie nanoantennas (BNA) with varying sizes and separations were designed for nanoplasmonic tweezers in chapter 4 . The BNAs were designed to resonate at 1064 nm to match the wavelength of the laser beam available in the existing optical trapping system (refer to chapter 7 for a description of the existing optical trapping set-up).

Based on the simulation results presented in chapter 4, BNA and cross arrays with varying length, L, gap size, g, tip angle, θ, thickness, d, and periodicity, a were designed for nanoplasmonic trapping experiments. It was desired to investigate the effect of changing each variable on the optical trapping strength for the trapping particles of different sizes. Figure 6.2 illustrates the shape of BNA and cross nanoantennas with their important features marked.

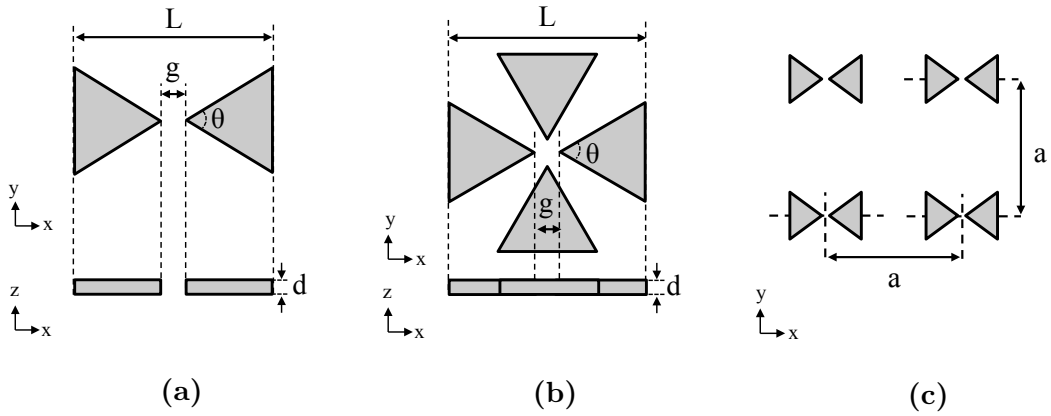


Figure 6.2: Sketch of a BNA nanoantenna, (a) a cross nanoantenna (b) and a BNA array (c). Design parameters, L, gap size, g, tip angle, θ, thickness, d, and periodicity, a, are marked. Dimensions are not to scale.

The goal of the nanoplasmonic antenna fabrication part of this project was to fabricate some of the designed devices, making sure to maintain their sharp tip and uniform structure across the array.

These devices were fabricated on 0.17 mm thick, 25.4mm by 25.4mm glass cover slips using the EBL method. The coverslip dimensions were selected to be compatible with the inverted microscope being used. The devices were fabricated in gold to ensure biocompatibility. The steps taken during the fabrication of the BNA and cross arrays were as follows [225]. For more detail please refer to chapter 5 of reference [225].

1. The cover slip was cleaned in ethyl lactate, acetone, methanol and isopropyl alcohol (IPA) in an ultrasonic bath before being dehydrated on a hot plate.

2. A 170 nm layer of poly methyl methacrylate (PMMA) 495k A5 was spin coated on the glass cover slip (positive resist).

3. The cover slip was then spin coated with a 50 nm layer of specialist conductive

coating (SX AR-PC 5000/90.2, supplied by ALLRESIST GmbH, Strausberg, Germany). This layer was used to stop the charge build-up on the surface and deflection of the e-beam resulting in a non-accurate pattern.

4. The cover slip was soft baked to harden the coating layers.

5. To define the gold nanoantennas, the EBL technique was used with the PMMA layer acting as a positive resist.

6. The sample was then placed in de-ionised water to remove the conductive film, before being chemically developed. This revealed the pattern created by the e-beam.

7. A thermal evaporator evaporating to pressures in the 10^{-7} mbar range was then used to create vacuume around the sample, so that the metal does not react with the environment.

8. A 1-3 nm titanium adhesion layer followed by 50nm of gold was evaporated onto the sample.

9. The sample was then placed in acetone to remove the resist and lift off the excess gold revealing the final nanoantenna structure.

When defining the gold patterns using the EBL method (step 5), the proximity effects caused the tips of the triangles to be over exposed, resulting in rounded tips. A number of different tests were performed to see how the sharp tip of the designed structure can be maintained. Initially the corners of the triangles were removed completely by the e-beam resulting in flat tips in the BNA gap. By indenting the tip of the BNA and adjusting the e-beam dose in this area, sharp points were achieved. This worked well on semi-insulating silicon wafers, but not on the glass slides. Therefore shape correction was used at the tips of the nanoantennas on top of the glass cover slip. Measurements in a SEM showed that the radius of the point

was less than 10 nm.

Figure 6.3 shows an SEM image of a 700nm long, 50nm thick, gold BNA with a 30 nm gap and a 90° tip angle, fabricated using the EBL technique.

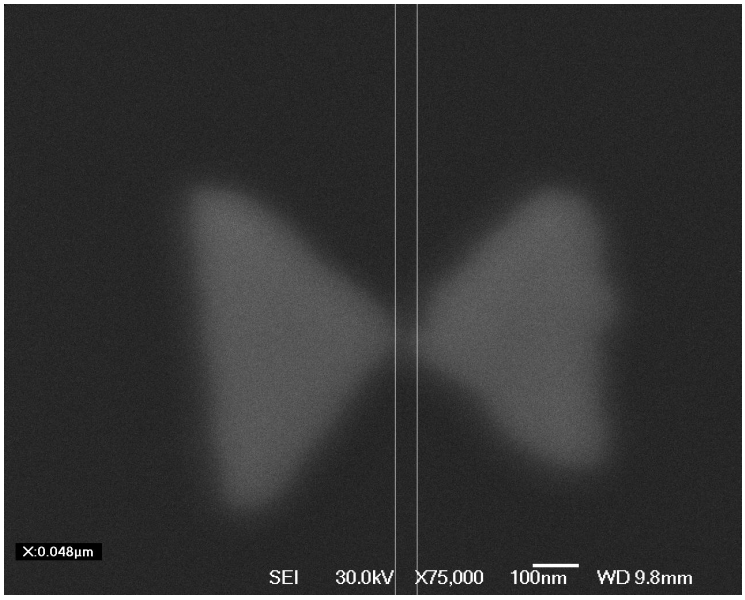
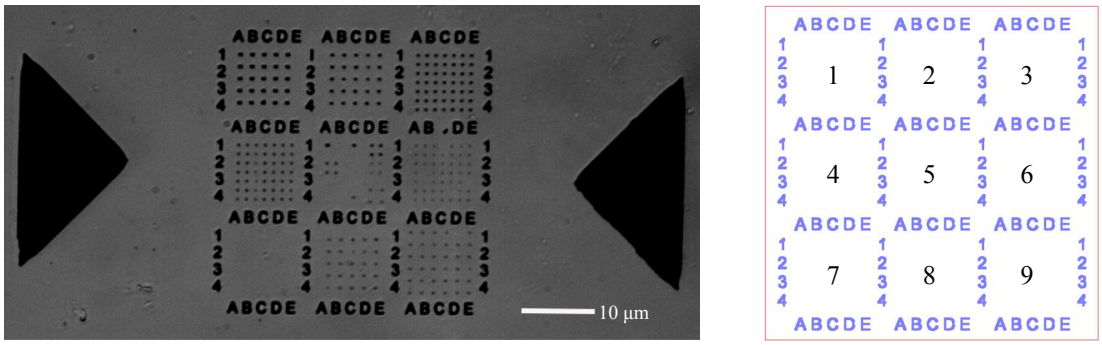


Figure 6.3: SEM image of a 700nm long, 50 nm thick gold BNA with a 30nm gap and a 90° tip angle, fabricated using the electron beam lithography. Supplied courtesy of Dr. Richard Cousins.

In order to locate the arrays when looking under a diffraction limited microscope, arrays of BNAs and crosses were fabricated in 9 by 9 blocks, and marked with letters and numbers. They were positioned at the centre of four 15 μm long markers which are gold triangles pointing toward a block of BNA/cross arrays so that they can be located easily during the optical trapping experiments. Figure 6.4 shows such a block of BNA arrays and two markers pointing towards it.



(a) **(b)**

Figure 6.4: A typical block of BNA arrays (a) and the template for BNA fabrication numbering each section (b).

As can be seen in Fig. 6.4, the structures sometimes lift off during/ prior to the experiment (for example in region 7 in Fig. 6.4a). This could be due to the small sizes of the nanoantennas (most of the lift-off occurred for BNAs that are smaller than 500 nm). This could possibly be prevented by using a thicker adhesion layer between the gold and the glass substrate during the fabrication process. Table 6.1 shows the dimensions of the BNAs in each section of a typical block of BNA arrays, such as the block shown in Figure 6.4a.

Table 6.1: Dimensions of the fabricated BNAs in a typical BNA array block.

Section	L**(nm)**	d**(nm)**	g**(nm)**	θ°	$a(L)$	**BNAs in array**
1	1000	30	50	90	2	5
2	800	30	50	90	2	5
3	700	30	50	90	2	7
4	500	30	50	90	2	7
5	mixture	30	50	mixture	2	-
6	300	30	50	90	2	7
7	100	30	50	90	2	7
8	800	30	50	30	2	5
9	700	30	50	30	2	7

Arrays of varying dimensions were created to study the effect of changing dimensions of the nanoantenna arrays on the strength of the nanoplasmonic optical trap. Table 6.2 lists the dimensions of the BNAs and crosses fabricated for the nanoplasmonic trapping experiments.

Table 6.2: Dimensions of the fabricated BNA and cross arrays.

BNA/cross	L**(nm)**	d**(nm)**	g**(nm)**	θ°	$a(L)$
BNA	150	50	30	9	2
BNA	300	50	30	90	2
BNA	500	50	30	90	2
BNA	700	50	30	90	2
BNA	700	50	30	30	2
BNA	800	50	30	90	2
BNA	700	50	30	30	2
BNA	1000	50	30	90	2
Cross	150	50	30	90	2
Cross	300	50	30	90	2
Cross	500	50	30	90	2
Cross	700	50	30	90	2
Cross	700	50	30	30	2
Cross	800	50	30	90	2
Cross	700	50	30	30	2
Cross	1000	50	30	90	2

6.3 Fabrication of the hybrid device

The hybrid photonic-plasmonic device, that can be used as a building block of a multi-component platform for high-throughput, single molecule experiments was

designed in chapter 4. The devices were designed to resonate around 1550nm so that they can be fabricated using the conventional EBL systems (visible PhCs require lengths that are much smaller) as well as being compatible with the existing equipment in the telecommunication laboratory at Nottingham to perform proof-of-concept experiments. Figure 6.5 shows an illustration of this device suspended in air with its important features marked.

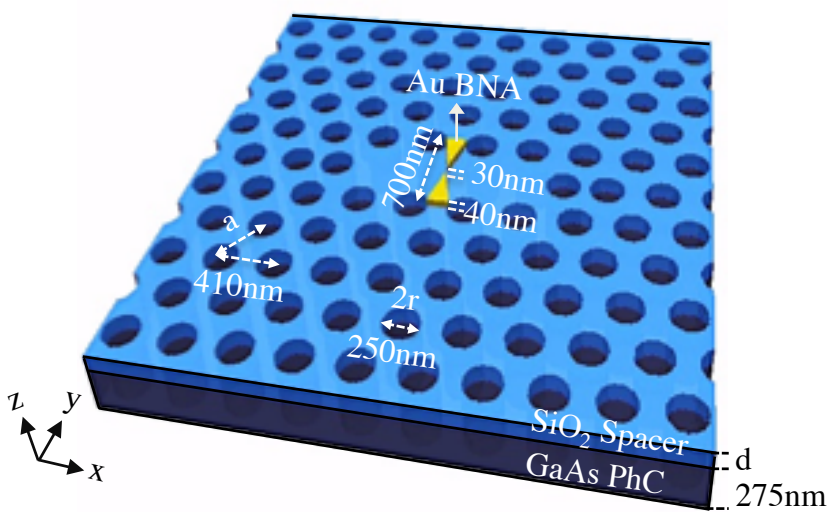


Figure 6.5: Illustration of the designed, air suspended hybrid photonic-plasmonic device comprised of an L3 PhC cavity (grey), a gold BNA (yellow) and a SiO_2 layer separating the two.

The aim of this part of the project was to come up with a route for the fabrication of this device and, where possible, to realise it.

6.3.1 Fabrication method

The fabrication of the hybrid device relies on the EBL method as well as dry and wet etching of the sample to create the PhC membrane. The envisaged steps for the fabrication of this device are described below.

1. Grow epitaxial structure on the GaAs substrate.

2. Spin coat the epitaxial structure with e-beam resist (PMMA) and conductive coating.

3. Create the PhC structure in the e-beam resist using the e-beam exposure.

4. Chemically develop the resist to reveal the PhC pattern.

5. Dry-etch the PhC pattern through the GaAs layer.

6. Remove the resist (lift-off) and the conductive film.

7. Create the BNA on top of the fabricated PhC using the EBL method. This step is the same as the EBL process described in the previous section (refer to section 6.2).

8. Finally, use a wet chemical etch to remove the sacrificial layer beneath the GaAs layer, revealing the PhC membrane. This is done by submerging the structure in water, two times in a row, in IPA and then in methanol. This is followed by drying it by placing it on a hot plate.

Figure 6.6 illustrates the envisaged fabrication process.

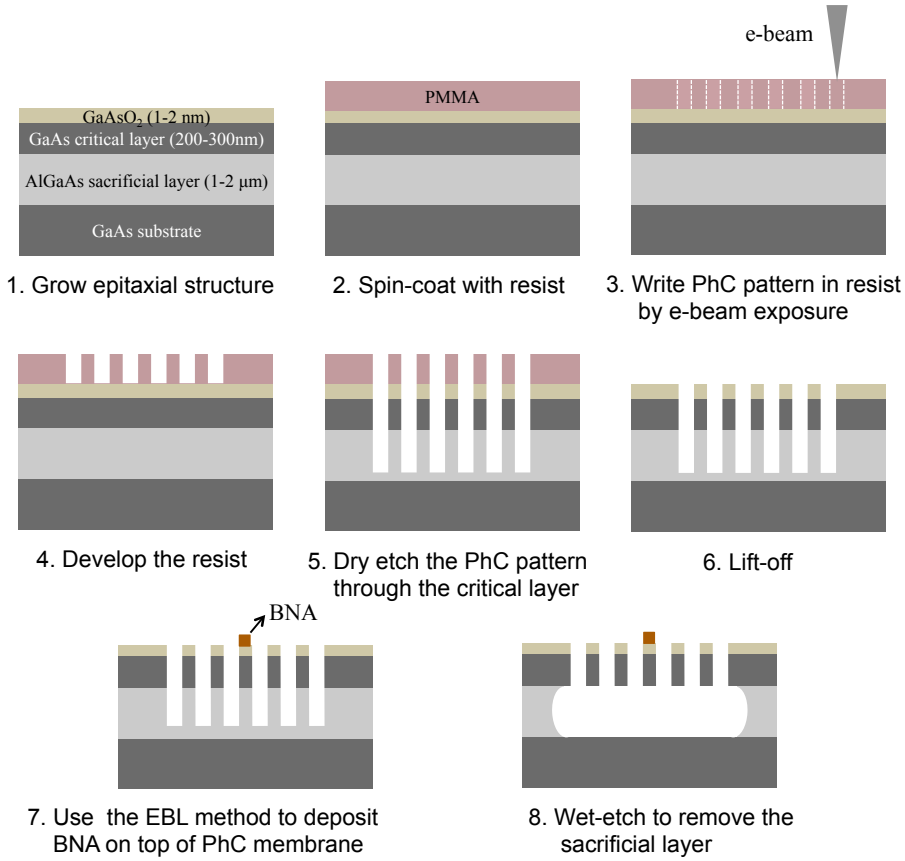


Figure 6.6: Illustration of the envisaged fabrication method for the hybrid photonic-plasmonic device.

6.3.2 Results

First, the epitaxial wafer was successfully grown on a 5cm by 5cm GaAs substrate (step 1 of the described method in section 6.3.1). The wafer thickness was mapped by recording 45 points across the surface of each layer using spectroscopic ellipsometry. Spectroscopic ellipsometry is a non-invasive optical technique that measures the change in the polarization of light, reflected off a film. Analyzing this change in polarization with the help of a model of the layers in the film, provided by the user, gives information about the surface roughness, the thickness of layers in the film and their optical properties [226].

Figure 6.7 shows an illustration of the grown wafer (side-view) as well as the spectroscopic ellipsometry maps showing the thickness across the surface of each layer.

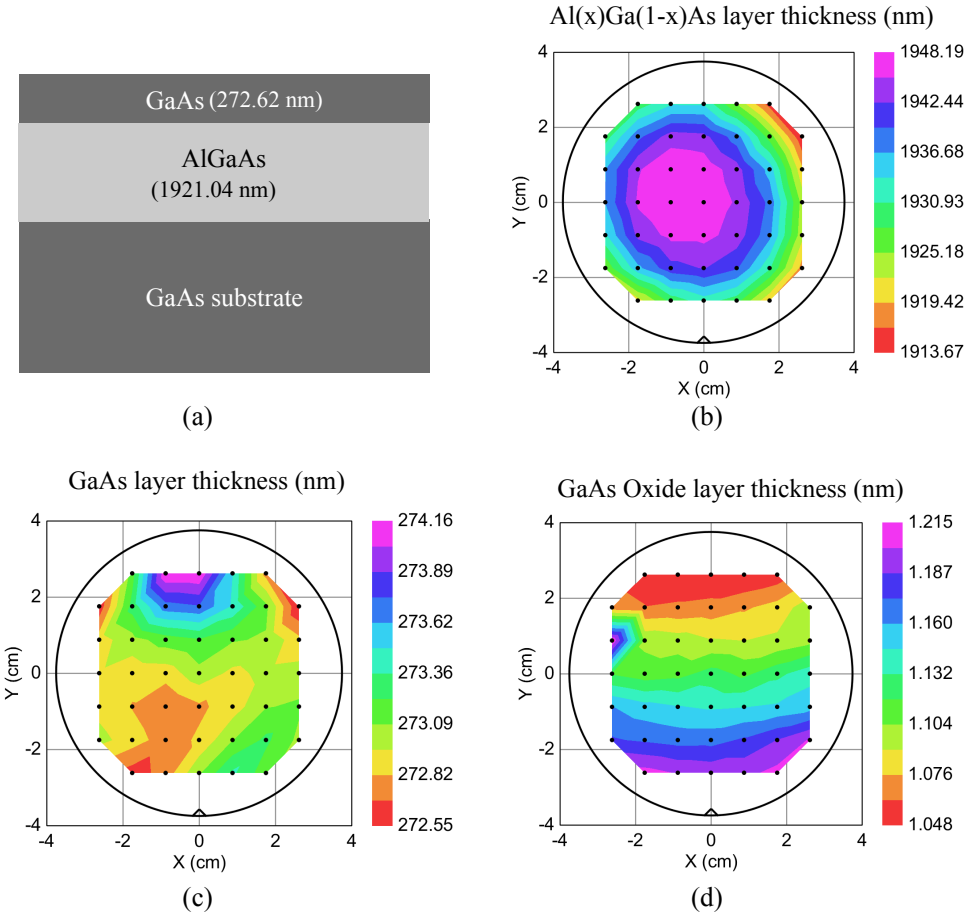


Figure 6.7: (a) Illustration of the wafer layers with mean thicknesses across each layer marked. (b-d) Spectroscopic ellipsometry maps showing the thickness across the surfaces of the AlGaAs, GaAs and $GaAsO_2$ layers. Supplied courtesy of Dr. Richard Cousins.

As seen in Fig. 6.7, the thicknesses of the PhC layers are in good agreement with the designed thicknesses (please refer to section 4.4.3 for the study of the L3 cavity fabrication tolerances, where small variations in PhC slab thickness, oxide thickness and hole diameter are introduced to the PhC and the expected shift in the fundamental resonance and change in its Q-factor are estimated).

Next, the EBL method described in the previous section was used to create the PhC pattern in the GaAs layer (steps 2-6 of the described method in section 6.3.1). Inductively coupled plasma (ICP) etching was used to dry etch the GaAs layer coated with a 200nm thick SiO_2 layer as a hard mask. ICP etching is an etching technique that uses ions to bombard a surface and physically remove the material where the ions contact the surface. It therefore has a better selectivity in terms of the direction of removal of matter compared to a wet etch. Figure 6.8 shows a SEM image of the dry etched SiO_2 covered GaAs layer.

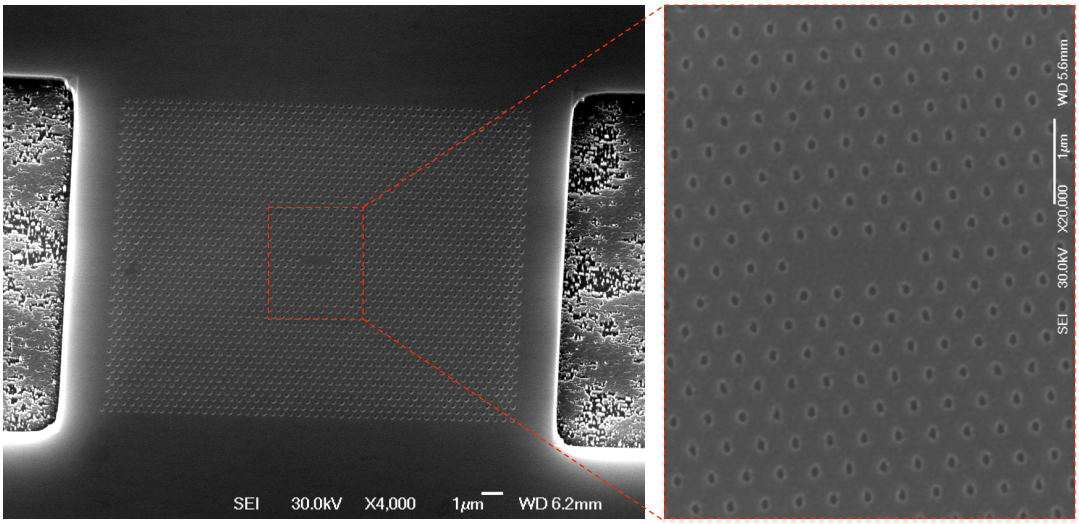


Figure 6.8: SEM image of the dry-etched, SiO_2 covered GaAs layer. Supplied courtesy of Dr. Chris Mellor.

Next, wet-etching was performed with the aim of removing the AlGaAs layer and leaving the SiO_2 covered GaAs layer untouched (step 7 of the described method in section 6.3.1). This was done in two stages. First, orthophosphoric solution was used to remove the Al_2O_3 layer formed at the GaAs/AlGaAs interface and then hydrochloric acid (HCl) was used (in ambient temperature $\approx 22°C$) to etch the AlGaAs and leave GaAs and SiO_2 layers untouched. After this stage, the AlGaAs layer was successfully removed. However, it became apparent that the dry etching of the SiO_2 layer had been incomplete. As a result, the SiO_2 layer had detached

from the GaAs layer.

6.3.3 Future work

The remaining work in this part of the project is to reduce the thickness of the SiO_2 layer to achieve dry etching through the GaAs membrane. This will be followed by forming gold BNAs on top of the created PhC structure.

A new PhD project in our research group is focusing on the fabrication of these hybrid devices. The new student is tasked with learning and performing the current fabrication and characterisation techniques to follow through with the remaining steps in the fabrication of the device. The fabrication process used by Zhang *et al.* [197] can be used to inform the roadmap for the future fabrication efforts.

6.4 Summary

During this PhD, the designed plasmonic nanoantennas were successfully fabricated. These structures were used to perform nanoplasmonic trapping experiments. This will be presented in the next chapters of this thesis. The fabrication of the designed hybrid photonic-plasmonic device unsurprisingly proved more challenging. The fabrication efforts for this part of the project are being continued by a new PhD student.

7

Design and characterization of nanoplasmonic tweezers

Nanoplasmonic tweezers are optical tweezers that take advantage of subwavelength hotspots created when illuminating surfaces with nanometallic features to hold and manipulate micro- and nanoparticles. The mechanisms and applications of nanoplasmonic tweezers have been discussed in chapter 2. The nanoplasmonic tweezer setup in this project is based on conventional optical trapping system which was built prior to the start of this PhD. This chapter describes the changes applied to the conventional optical trapping setup to make it suitable for nanoplasmonic trapping followed by characterizing its features such as the pixel size of an image taken using the system, the laser power and beam size of the focal point and the polarization of the beam. The method of controlling features such as the numerical aperture (NA) of the objective lens and the power at the focal point are also presented. Finally a description of the programs used for measuring the strength of the nanoplasmonic optical traps (both the labview program developed previously for the black and white camera and the labview program that was developed for the Optimos camera during this PhD) is given.

7.1 Experimental setup

The experimental setup of the nanoplasmonic optical trapping system used in this PhD is based on an inverted microscope for conventional optical trapping with the addition of an iris, a half wave plate and a polarizing cube as well as fluorescent filters used to image the fluorescent particles used in our experiments. Figure 7.1 illustrates the schematic diagram of the optical setup used for experiments reported in this chapter and Fig.7.2 shows photographs of the optical setup with the important parts labelled.

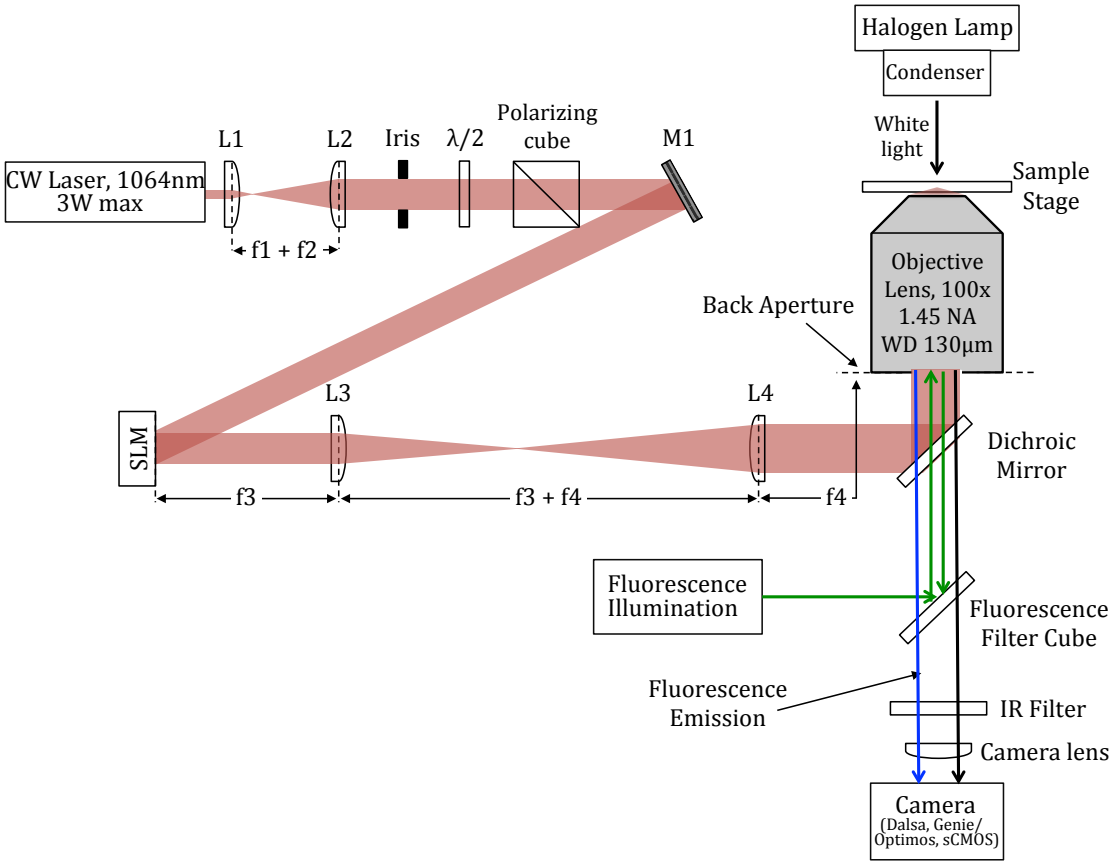
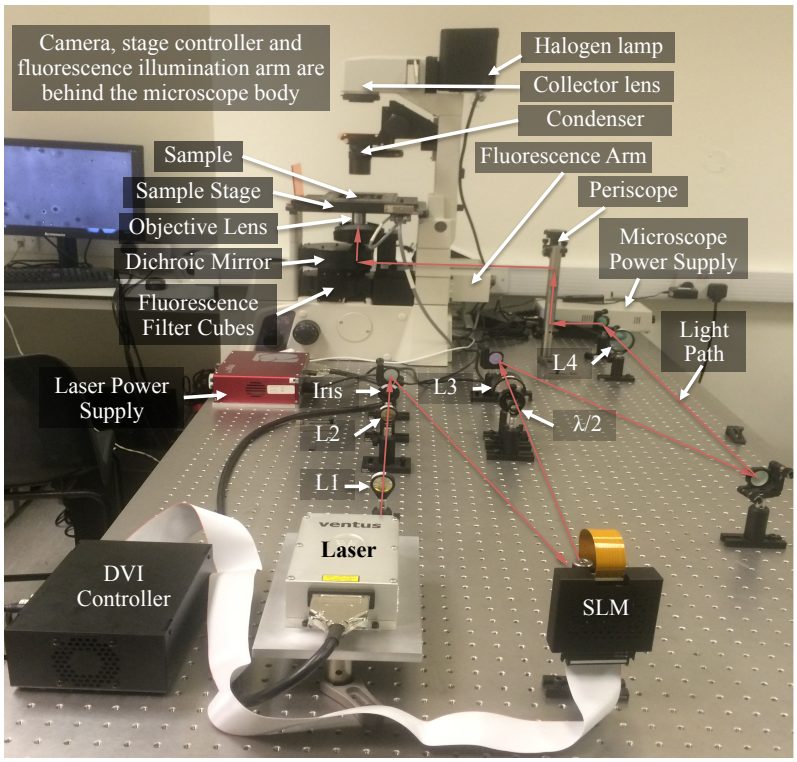
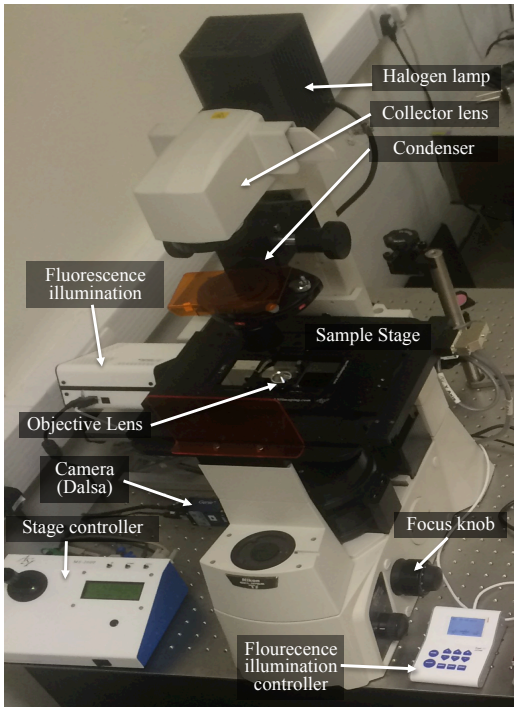


Figure 7.1: Schematic diagram of the optical setup used for nanoplasmonic optical trapping experiments. The focal lengths of lenses, f1 to f4, are 60 mm, 250 mm, 750 mm and 1000 mm respectively. The dimensions are not to scale. L stands for lens, M for mirror, $\frac{\lambda}{2}$ for half-wave plate and SLM for spatial light modulator.



(a)



(b)

Figure 7.2: Photographs of the optical setup used for nanoplasmonic optical trapping experiments with the important devices labelled.

The optical components were mounted on a vibration isolated optical table (Thorlabs, PTR52504) to insulate the optical setup from external mechanical vibrations. The beam height was kept at 10 cm across the table. A continuous wave (CW), diode-pumped solid-state laser (Laser Quantum, Venus), with the wavelength (λ) of 1064nm, maximum power of 3 Watts and beam diameter of 2.35 mm was used to generate the beam of the optical trap.

The laser power supply (Laser Quantum, advanced mpc6000) enables control over the intensity of the beam. The laser beam was fed through a beam expander consisting of two lenses, L1 and L2 with focal lengths, f1 and f2, of 60 mm and 250 mm respectively. L2 is located at a distance of f1 + f2 away from L1 so that the beam is expanded by f2 / f1 which is approximately 4.1. The beam is expanded at this point to overfill the back aperture of the objective lens and allow taking advantage of the high NA of the lens.

The resultant expanded and collimated beam allows the light to overfill the back aperture of the objective lens (Nikon, CFI Plan Apo λ, 100x/1.45 NA, oil immersion, ∞/0.17, WD 0.13mm). This is done to take full advantage of the objective lens for conventional optical trapping purposes. The expanded and collimated light is then fed through an iris that enables the control over the diameter of the light at the back aperture of the high NA lens. This allows the NA of the objective to be reduced from 1.45 (when the iris is kept open) to approximately 0.8 (when the iris diameter is 0.5 mm). This is used to switch from a conventional trapping system to a system that avoids conventional optical trapping of micron-sized particles.

The expanded and collimated beam is fed through a half wave plate ($\frac{\lambda}{2}$) to allow control over the polarization angle of the linearly polarized beam. The objective lens used in our setup is infinity corrected meaning that the image distance is set at infinity, the shape of the focal plane and the image plane are corrected to be flat (not a curved surface) and corrected for chromatic and spherical aberrations for

three visible wavelengths (apochromat).

The expanded beam is then reflected of a spatial light modulator (SLM, from Boulder Nonlinear Systems, XY series, phase and amplitude, 512 × 512 pixels). The SLM can be programmed using the computer to display different diffraction patterns on its surface to change the phase of the beam reflecting off its pixelated surface (square pixels act like mirrors when the SLM is turned off). This can be used to change the position (x, y, and z) of the tightly focused light on the sample plane or to produce multiple optical traps on the sample plane. In the experiments described in this thesis, the SLM is always turned off and acts as a mirror. It is positioned at the focal point of lens L3 away from it, L3 and L4 are positioned at a distance of f3 + f4, and the back aperture of the objective lens is positioned at the focal point of lens L4 creating a 4f system in which the image displayed on the SLM is reverse replicated on the back aperture of the objective lens (conjugate planes).

An inverted microscope body (Nikon, Eclipse Ti-5) is used to provide the illumination and imaging setup of the system. The microscope stage (Applied Scientific Instrumentation, MS-2000) used in the system provides lateral control (x, y) of the position of the sample with micrometre accuracy. It can be controlled manually or computer programmed.

The top illumination is provided by a halogen lamp and fed through a collector lens and a condenser diaphragm before being imaged in transmission by the camera. The fluorescence beam is provided by a controllable broad spectrum LED illumination and is imaged in an 'epi' configuration.

A short pass dichroic mirror (Thorlabs, DMSP805R) positioned in the top turret of the microscope is used to reflect the laser beam towards the microscope stage and transmit the white light illumination and the fluorescent light. The appropriate fluorescence filter cube (Semrock, DA/FI/TR/Cy5-A-000) is used in the bottom turret to reflect the excitation wavelength of the dye used and pass the emission

wavelength to the camera. An IR blocking filter is positioned just before the camera to block any additional 1064nm light from the camera.

7.1.1 Imaging of the sample

The sample is imaged either in bright-field or fluorescence configurations depending on the size of beads being used. When the object to be trapped is larger than 0.5 μm, the sample is imaged in the bright-field configuration and when the trapped object is smaller than 0.5 μm, the sample is imaged in fluorescence configuration. Imaging particles smaller than the diffraction limit (i.e. fluorescent beads and quantum dots used in our experiments) in the fluorescence configuration allows their position to be tracked despite the inability of the optical system to resolve them. Figure 7.3 illustrates the paths for bright-field and fluorescence imaging in our optical setup.

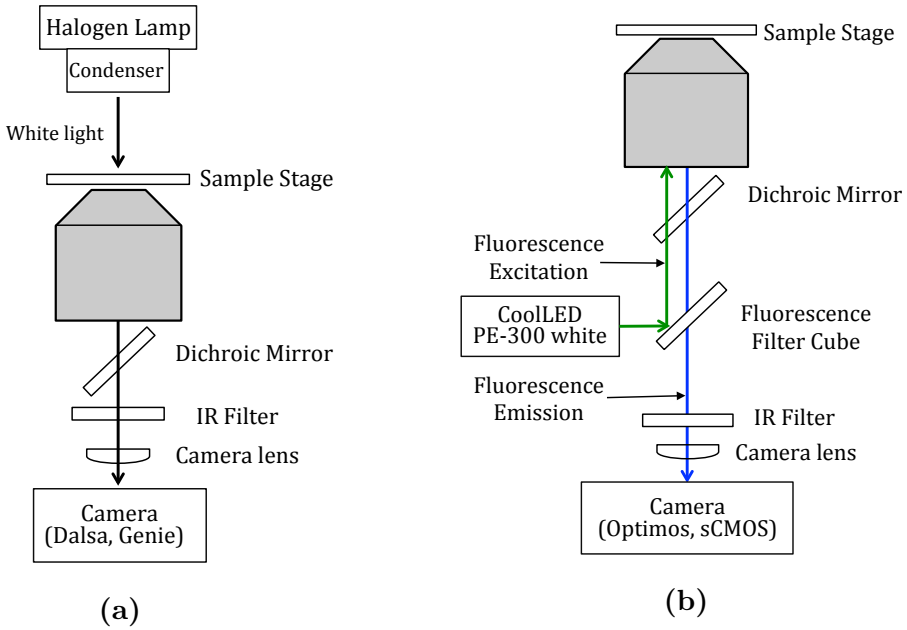


Figure 7.3: Illustration of the bright-field (a), and fluorescence (b) imaging paths in our optical setup.

In bright-field configuration, the white light generated by Nikon D-LH/LC halo-

gen lamp is transmitted through the sample and the objective lens and is then imaged by the 300 fps frame rate when imaging the full field of view, black and white CMOS camera, Dalasa, Gineie HM640. In fluorescence configuration, the excitation beam is generated by a controllable, broad spectrum LED illumination, CoolLED, PE-300-white. The excitation beam goes through a filter cube, Semrock, DA/FI/TR/Cy5-A-000, that includes an exciter filter, an emission filter and a dielectric mirror reflects the excitation wavelength of the fluorescent dyes and transmits their emission to the 100fps, highly sensitive, sCMOS camera, Optimos. An IR blocking filter is positioned just before the camera to block the leaked laser beam from the camera.

7.2 Characterisation of the experimental setup

7.2.1 Image pixel size

The pixel size of the images taken using each camera is calibrated prior to post processing of the experiment results. This is done either by calculating the number of pixels when travelling a fixed distance (using the precision sample stage), or by measuring the size of a known object in terms of pixels. The latter method was used to determine the width of several 2μm beads in terms of pixels in ImageJ. At least 3 measurements were taken and the results were averaged to take into account the variances in the 2 μm bead samples. The standard deviation (SD) of the 2μm bead sample is 0.054μm.

Figure 7.4 shows an image of several 2 μm polystyrene beads imaged with the sCMOS camera.

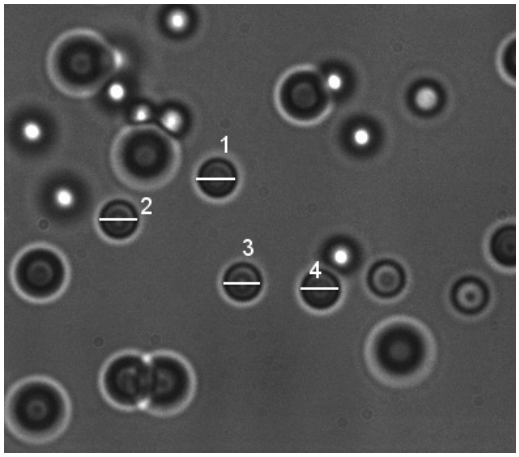


Figure 7.4: An image of polystyrene beads with the diameter of 2μm used to calibrate the pixel size of images taken using the sCMOS and CMOS cameras in our optical set-up.

The measurement of width of the 2μm beads in terms of pixel size resulted in each pixel to be approximately **70 nm** at the focal plane for the CMOS camera (Dalsa, Genie HM640), and approximately **55 nm** at the focal plane for the sCMOS camera (Optimos, sCMOS). The image processing program, ImageJ, was used for analysis of the images in this chapter [227].

7.2.2 Numerical aperture of the objective lens and the focus of the beam

The numerical aperture of an objective lens is a measure of its light collecting capabilities. It marks the largest cone angle in which light can be collected in front of the lens therefore also determines the resolving power of the lens. It is defined as:

$$NA = n \sin(\theta_{max}), \tag{7.2.1}$$

where n is the refractive index of the medium in which the objective lens is immersed and θ_{max} is the half-angle of the maximum cone of light that can be collected by the objective lens [228]. Figure 7.5 shows a simple illustration for an objective lens with collimated light entering its back aperture and focusing at the front focal plane.

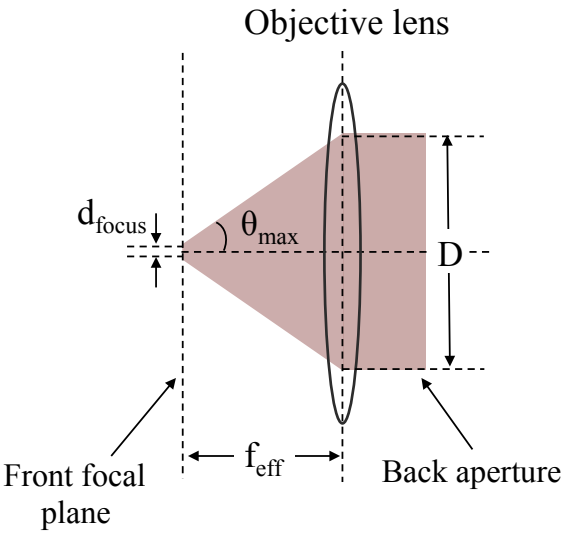


Figure 7.5: Illustration of an objective lens with collimated light input, marking its front focal plane, effective back aperture diameter, D, effective focal length, f_{eff}, half-angle of the maximum light cone, θ_{max}, and diameter of the beam at focus, d_{focus}.

The objective lens that used in the system has a NA of 1.45 and the refractive index of immersion oil is 1.515 [229], therefore the half-angle of the maximum cone is:

$$\theta_{max} = \arcsin(\frac{1.45}{1.515}) \approx 73^{\circ}. \tag{7.2.2}$$

The effective back aperture diameter for the objective lens used in this project was approximately 10 mm. knowing the half-angle of the maximum cone, the effective

focal length, f_{eff}, which marks the distance between the principal plane of the objective lens and the focal plane is calculated from a simple trigonometric ratio (refer to Figure 7.5).

$$f_{eff} = \frac{D}{2\tan(\theta_{max})} \approx \frac{5}{\tan(73.15°)} \approx 1.51[\text{mm}] \tag{7.2.3}$$

Observe that as the effective back aperture diameter, D, decreases, the half-angle of maximum light cone, θ_{max}, decreases and hence the NA of the objective and the resolution of the image decreases.

Figure 7.6 shows the schematic diagram of the main optical components that determine the effective back aperture of the objective lens in our setup. An iris is used in the path of the collimated laser beam in order to reduce the effective back aperture of the objective lens and its effective NA. The effective back aperture diameter in our system is the multiplication of the iris diameter, d_{iris} by the ratio between focal lengths of the lenses L4 and L3 ($L4/L3 = 1.\bar{3}$) when the reflecting surface of the SLM is larger than the area of the beam after it passes through the beam expander.

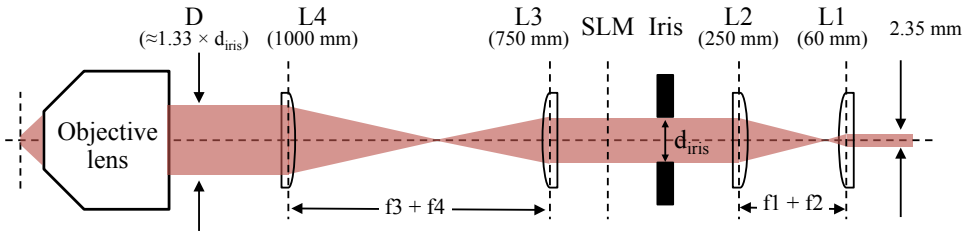


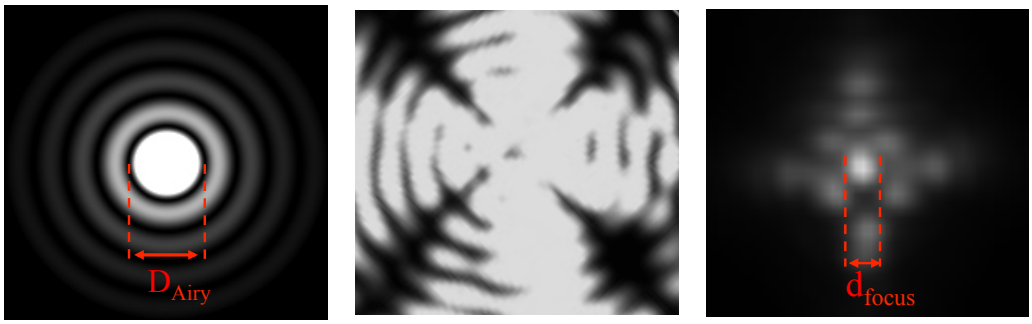
Figure 7.6: Schematic of the optical components changing the effective back aperture of the objective lens.

The diffraction pattern created at the focus of an objective lens, uniformly illuminated at its circular back aperture, namely the Airy disk pattern, is usually used to

measure its resolution. The diameter of the central disk in the Airy disk pattern, D_{Airy} (see Figure 7.7a), depends on the numerical aperture of the objective lens as well as the wavelength of light entering the lens. It is approximated by the Abbe diffraction limit:

$$D_{Airy} = \frac{0.6\ \lambda}{NA}, \tag{7.2.4}$$

where λ is the wavelength of light and NA is the numerical aperture of the objective lens [230]. The diffraction pattern created at the focus of our laser beam is shown in Figures 7.7b and 7.7c. Images are taken with high and low exposure times respectively. The diffraction pattern at the focus of our lens has a cross shape due to the high NA of the objective lens and coma aberration caused by the high curvature of the lenses creating the high NA objective lens.



(a) **(b)** **(c)**

Figure 7.7: (a)Demonstration of the Airy disk diffraction pattern created at the focus of a beam passing through a lens with a circular aperture (reproduced from [228]) and (b) the diffraction pattern created at the focus of the laser beam in the setup used throughout this PhD (reflecting-off the SLM and going through an objective lens with a circular back aperture) when the image is captured with high and (c) low exposure times.

The effect of reducing the iris diameter on the NA of the system is calibrated by imaging the laser beam focused on the cover slip, with iris diameters in the range of 0.5 mm and 12 mm. This is done by looking at the diffraction patterns formed at the focus of the beam, and measuring the diameter of the central disk, d_{focus}, by counting the number of pixels across it. The effective NA of the objective lens for each iris diameter is then estimated using Equation 7.2.4.

Figure 7.8 shows the plot of the optical intensity across a line passing through the centre of the diffraction pattern formed at the focus of the laser beam for iris diameter sizes ranging from 0.5 mm to 12 mm resulting in effective back aperture diameters in the range of 0.66 mm up to 10 mm. Observe that at the iris diameter of 0.5 mm, the diameter of the inner disk in the diffraction pattern is 1320 nm ($\approx$ 24 pixels $\times$ 55 nm) and at the iris diameter of 12 mm (when iris is completely open) the diameter of the inner disk in the diffraction pattern is approximately 770 nm ($\approx$14 $\times$ 55) equivalent to effective NAs of approximately 0.8 and 1.4 respectively.

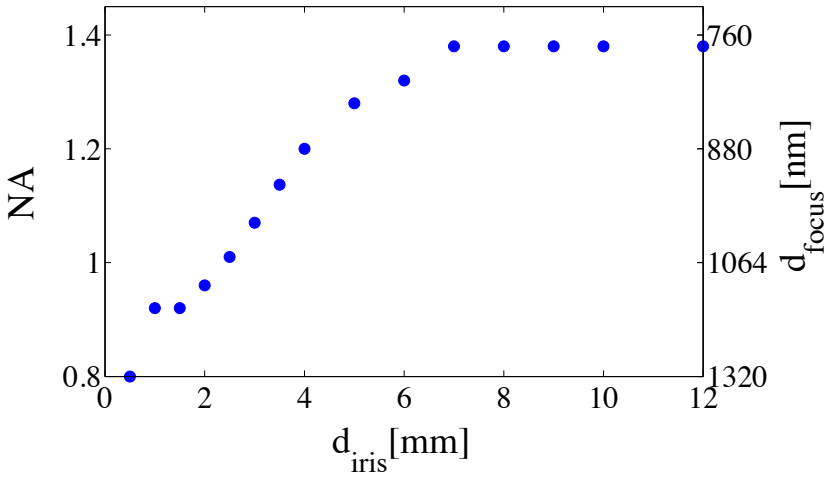


Figure 7.8: Numerical aperture of the objective lens against the iris diameter, d_{iris}, and the effective diameter of the inner disk created at the focal diffraction pattern, d_{focus}.

7.2.3 Polarisation of the beam

In order to take full advantage of the BNAs and crosses during our experiments, the polarization of the vertically polarized laser beam needs to be aligned with the longitudinal axis of the nanoantennas. This is done by rotating the half-wave plate placed in the collimated beam path, until a strong nanoplasmonic trap is observed. Figure 7.9 shows the changes in the shape of the focus of the beam as the half-wave plate is rotated. The images are taken when the objective lens focused on the top coverslip of the sample chamber (refer to section 8.1.2 for description of the sample chamber).

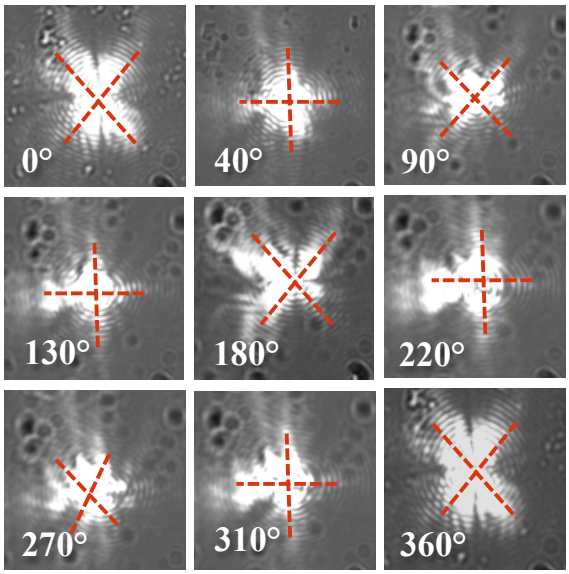


Figure 7.9: Diffraction patterns created at the focus of the objective lens with different angles of rotation applied to the half-wave plate.

It was observed that changing the angle of polarization of the beam modulates the intensity of the beam at the focus of the objective lens with a period of approximately 90°. This might be due to the nonuniform transmission curve of the objective lens across different polarization angles. Therefore the half-wave plate is kept at a constant angle (where the intensity of the beam is maximum and a clear cross shape

at the focus can be seen), and the sample chamber is rotated slightly for fine tuning of the polarization direction of beam for each experiment. As a rule of thumb, when the cross shape formed at the focus of the beam, is aligned with the pointers of the BNA arrays, the BNAs are excited plasmonically by the beam. As the four micron sized gold triangles that point to the array of nanoantennas, are aligned with the axis of the BNAs and crosses (refer to section 6.2), the nanoplasmonic trap strength is high. Figure 7.10 shows such a configuration where the orientation of the cross formed at the focus of the beam is aligned with the direction of the "pointer" triangles pointing towards arrays of BNAs.

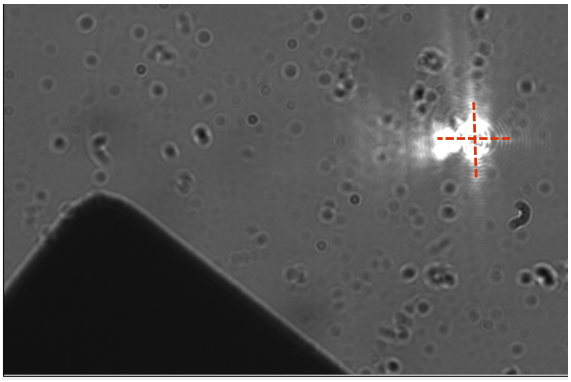


Figure 7.10: An example of a typical configuration of the polarization angle of the focused beam that results in a high nanoplasmonic trap strength for our nanoantenna arrays.

For the nanoplasmonic trapping results presented in this thesis the assumption was made that the dominant polarization of the beam is aligned with the longitudinal axis of the nanoantennas.

7.2.4 Laser power

For calibration of the laser beam in our setup, the power of the beam was measured both after the beam expander and at the back aperture of the objective lens (after

lens L2 and before the objective lens respectively as shown in Figures 7.11 and 7.12). The measurements are made using an infrared optical power meter (Thorlabs, Model D3MM). The power meter is not sensitive for powers below ≈ 0.2 mW.

The power supply in our set-up (Laser Quantum, advanced mpc6000) allows control over the current supplied to the laser diode (0 - 100%). Lasing is observed when the current applied to the laser is approximately 25%. Therefore the power of the beam for input currents in the range of 25% and 100% was calibrated in steps of 5%. This was done three times alternating from stepping up from low to high and stepping down from high to low supplied current. There was not a significant difference between the two. The average of the three measured values for each input current is then reported. The power was not measured directly after the laser itself and at the focus of the objective lens to avoid damage to the power meter due to the high power densities at these locations. Instead, an estimated value of 50% loss through the objective lens and the sample chamber was used [231] to get an the approximation for the laser power at the focus of the beam.

Figure 7.11 shows the laser beam power measured after the beam expander and at the back aperture of the objective as a function of laser current (%) supplied to the laser.

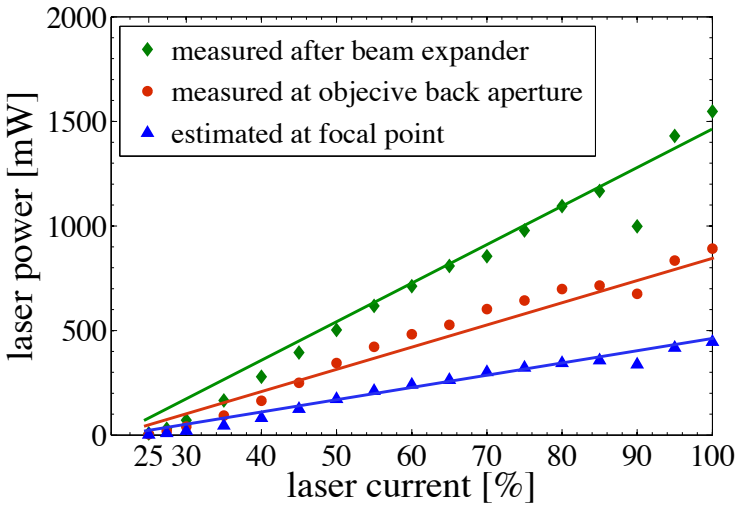


Figure 7.11: Laser power measured after the beam expander (diamond), at the back aperture of the objective lens (circle) and estimated at the focal point (triangle).

A linear increase of laser power with the input current is observed. In our experiments using high laser powers were avoided in order to minimise damage and heating of the sample. The laser was not operated at 90% supplied current because of the unexpectedly low output power at this input current. This is expected to be due to some fault in the internal structure of the laser system.

An iris was implemented at the collimated path of the laser beam to control the NA of the objective lens as described in section 7.2.2. Therefore the laser power is also calibrated as a function of iris diameter. This in small steps (1% supplied laser current) in the range of 25% to 40% since this range was mostly used in nanoplasmonic trapping experiments. For higher powers (input currents of 40% to 100%) the power at the back of the objective lens was calibrated with larger steps in input current (10%). Each measurement was repeated three times and the average of three values were taken before reporting it in this section.

Because the power meter used for taking the measurements, is not sensitive below

powers of 0.2mW (the power meter's readings are unstable), the data points below this value are approximated using the loss rate known from closing the iris. Figure 7.12 shows a plot of measured powers at each input current as a function of iris diameter. The approximated values in each are illustrated with hollow markers.

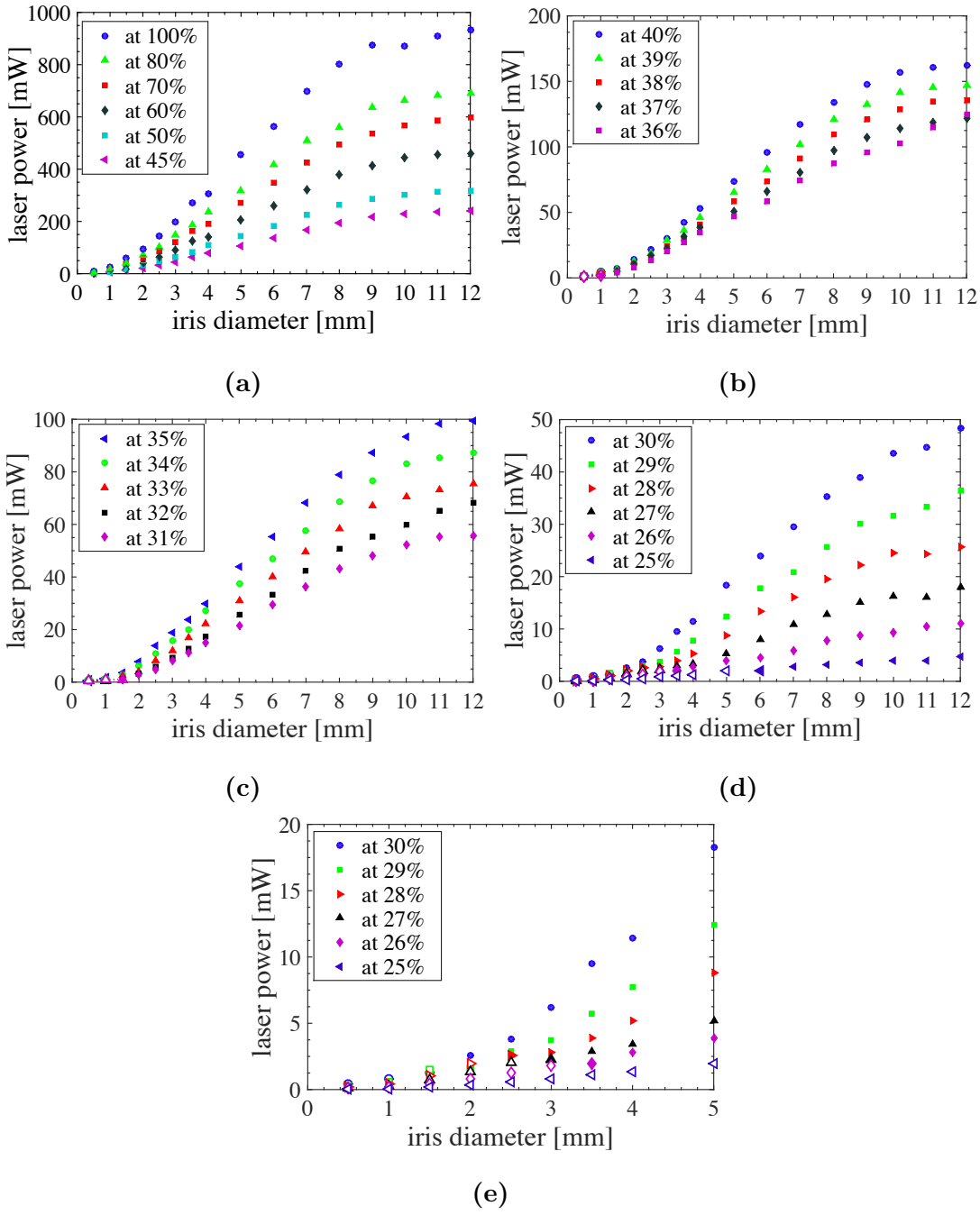


Figure 7.12: Laser power measured at the back aperture of the objective lens as a function of the diameter of the iris placed after the beam expander in the collimated beam path for laser diode input currents between (a) 45% and 100%, (b) 36% and 40%, (c) 31% and 35%, (d) 25% and 30% and (e) 25% and 30% zoomed-in showing the data points clearly.

In the nanoplasmonic trapping experiments presented in this thesis, usually the iris diameter is fixed at 0.5mm to be in the low NA regime and the input current to the laser is between 25% and 40% to avoid damage to the nanoparticles or cause melting and heat-induced gluing of the particles to the BNA. In this regime, the power at the back aperture of the objective lens is in the range between 360μW and 1.2mW and at the focus of the beam in the range between $\approx$ 180μW and 600μW. Effect of changing the laser power on the spot size and intensity profile of the laser beam was not characterised during this project mainly because the spot size was controlled using an iris and the power measurements ensured a linear change in laser power as a function of laser input current. However, this can be characterised for future work.

7.3 Measuring the trap stiffness

In order to quantify the strength of the optical trap in the experiments, a Labview program was used which is based on the equipartition of energy method described in section 2.6.1. The program measured the variance in the lateral position of the trapped particle, $\langle x \rangle^2$ and $\langle y \rangle^2$ and then calculated the spring constant, (or stiffness) of the trap, k_x and k_y.

Calculating the variance of the position of the particle was done by applying a centre of energy (centroid) calculation algorithm to a consecutive sequence of images taken from the particle. To take full advantage of this method, a region of interest (ROI) was defined tightly around the particle, then a user-defined threshold is applied to the image to remove the background noise in the image without changing the edges of the particle. After this, a centroid calculation algorithm which effectively calculates the centre of the shape within the boundaries of ROI was implemented. This method can track the movement of micron-sized particles with nanometre scale precision

[232]. The centroid locations (i.e. x_c and y_c) are calculated using [233]:

$$x_c = \frac{\sum_{x=0}^{W}\sum_{y=0}^{h} xI(x,y)}{\sum_{x=0}^{W}\sum_{y=0}^{h} I(x,y)}, \tag{7.3.1a}$$

$$y_c = \frac{\sum_{x=0}^{W}\sum_{y=0}^{h} yI(x,y)}{\sum_{x=0}^{W}\sum_{y=0}^{h} I(x,y)}, \tag{7.3.1b}$$

where h and W are the height and width of the ROI, x and y are the current positions in x and y directions and $I(x,y)$ is the intensity at point (x,y).

The error in the centroid location calculation is caused by the photon noise at each camera pixel as well as coarse sampling of the spot. For a more complete discussion about errors in the centroid calculation please refer to [234,235]

The program for measuring the optical traps using the black and white (Dalsa) camera was developed prior to the start of this PhD. Using this program one can both view the experiment (live imaging) and specify a region of interest (ROI) around a trapped object and measure the lateral stiffness of the trap.

A flow chart of the existing program is presented in Figure 7.13 and the front panel and block diagram of this program are presented in appendix B.

The program for measuring the lateral trap stiffness using the fluorescence camera (Optimos) was developed during this PhD and is based on the existing program for the black and white camera. Live imaging of the sample for the fluorescence camera is performed in ImageJ. This is due to issues with handles (.dll files in Labview) of this camera for the 32 bit Labview installation. Although live imaging and measuring the trap stiffness with a Labview program is possible for the fluorescence camera, we decided to take movies of the particle in the trap, and import them in a new program to apply threshold and calculate the trap stiffness for conservation of time. To do this, a ROI in ImageJ is defined and an .avi movie of the ROI with the desired

image rate (below the limit of acquisition for the given pixels in the ROI) is saved. The movie is then inputted to the developed Labview program. It converts it to a sequence of images and applies a user defined threshold to each image and calculates the trap stiffness using a similar procedure to the previous program. The front panel and block diagrams of these programs are presented in appendix C.

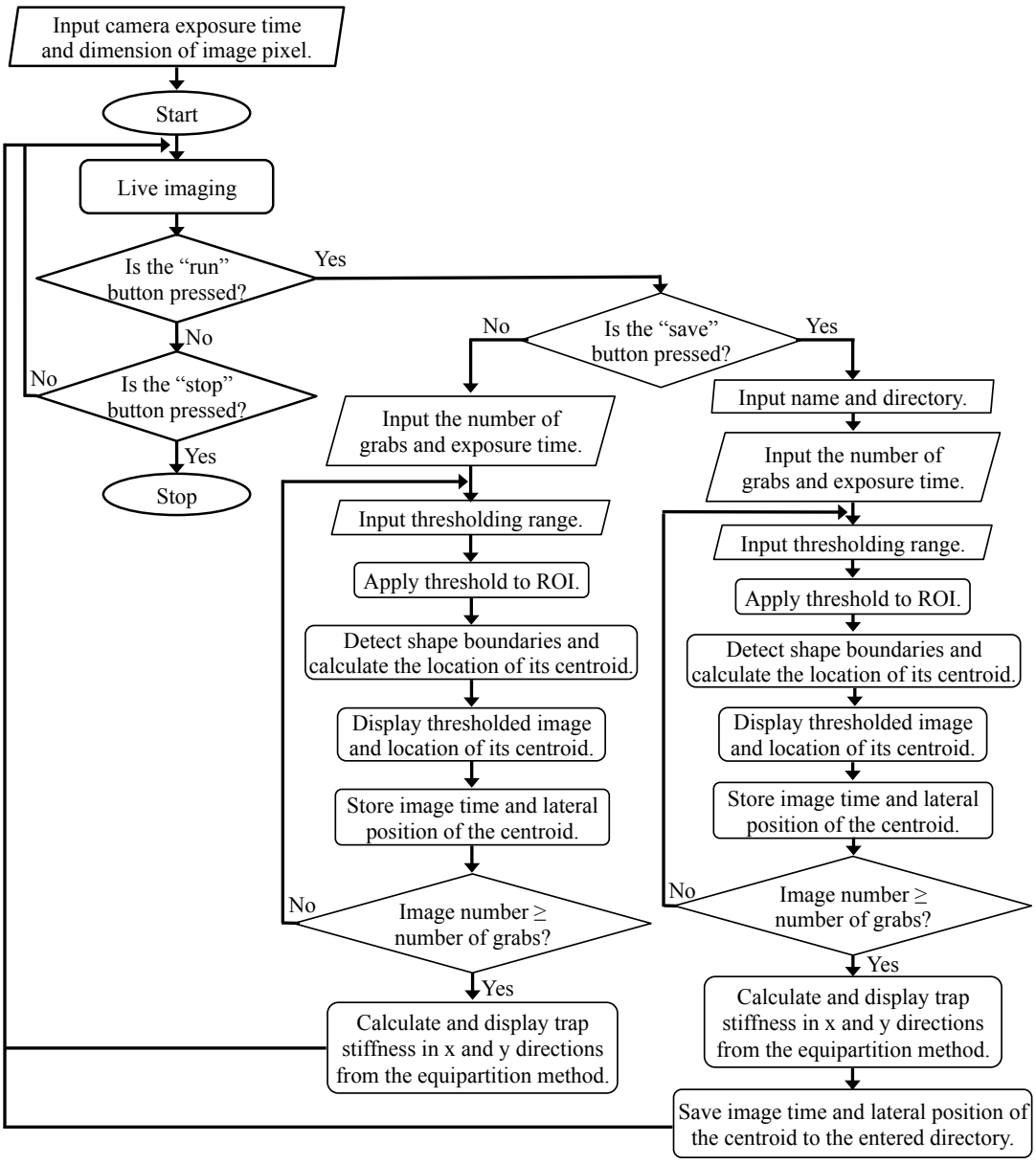


Figure 7.13: Flow chart of the existing labview program used for live imaging of the sample with the black and white camera (Dalsa) and measuring the trap stiffness factor.

The temperature is assumed to be 25°C during the experiments performed during this PhD. This needs to be measured for each experiment for more accuracy, But since the temperature in the laboratory did not vary dramatically and during this PhD, the goal was to look into the relative strengths of the nanoplasmonic and conventional trap, this was overlooked.

8

Optical trapping using nanoplasmonic tweezers

This chapter describes the nanoplasmonic trapping method developed during this PhD as well as presenting measurements that compare conventional far-field traps created at the tight focus of a laser beam, and nanoplasmonic trapping of micro- and nano-sized particles. One of the aims of this chapter is to highlight benefits of nanoplasmonic tweezers compared to conventional tweezers.

The chapter begins by describing the process of preparing the sample solution, creating a sample chamber and cleaning the plasmonic coverslip for reuse. The method for calculating the thickness of the chamber and calculation of depth of focus is discussed briefly. This is followed by explaining the nanoplasmonic trapping method developed during this PhD to increase the speed of experiments for micron sized particles. Conventional and nanoplasmonic trapping of 2μm beads, and 220nm beads are presented along with nanoplasmonic trapping results obtained for 6nm beads. This is followed by presenting the results showing nanoplasmonic traps used for aligning and rotating micron-sized rods follows this. Finally the results presented in this chapter are summarized. The Mycobacteria used to present some of the results in this chapter have been provided by Dr. Andrew Hudson and Dr. Natalie Garton

at the University of Leicester.

8.1 Sample preparation

8.1.1 Sample solution

Nanoplasmonic trapping experiments are performed on 2μm polystyrene beads (Polysciences Inc., 9003-53-6), 220nm dark red fluorescent beads (Life technologies, F8807, λex 660nm /λem 680nm), 6nm quantum dots (Sigma-Aldrich, 753882, carboxylic acid (COOH) functionalized, fluorescence λem 630nm) and rod shaped bacteria (Mycobacterium Smegmatis, 500nm in diameter and 3-5μm in length).

Polystyrene and fluorescent bead samples are prepared by dilution of the beads in a solution of distilled water and sodium dodecyl sulfate (SDS). Usually, 0.25% concentration of SDS in distilled water was used. This is done to prevent sticking of the particles to the gold BNAs. The diluted beads are then placed in an ultrasonic bath for approximately 15 minutes to break up any aggregation in the sample.

Mycobacterium Smegmatis bacteria, is prepared by first streaking the bacteria and then suspending them in Middlebrook broth. The sample is then further diluted in Middlebrook broth (Middlebrook 7H9 broth (BD Biosciences, catalog number: 271310) if necessary.

8.1.2 Sample chamber and cleaning the coverslip

For nanoplasmonic trapping of micro- and nanoparticles, sample chambers are made using a glass slide (0.17mm thick), a glass cover slip patterened with the plasmonic nanoantennas (plasmonic coverslip), sample solution and vacuum grease (Dow

Corning, Z273554 ALDRICH). For conventional optical trapping experiments, the nanoplasmonic cover slip is replaced with an ordinary glass coverslip. The method of assembly of a typical sample chamber is illustrated in Figure 8.1.

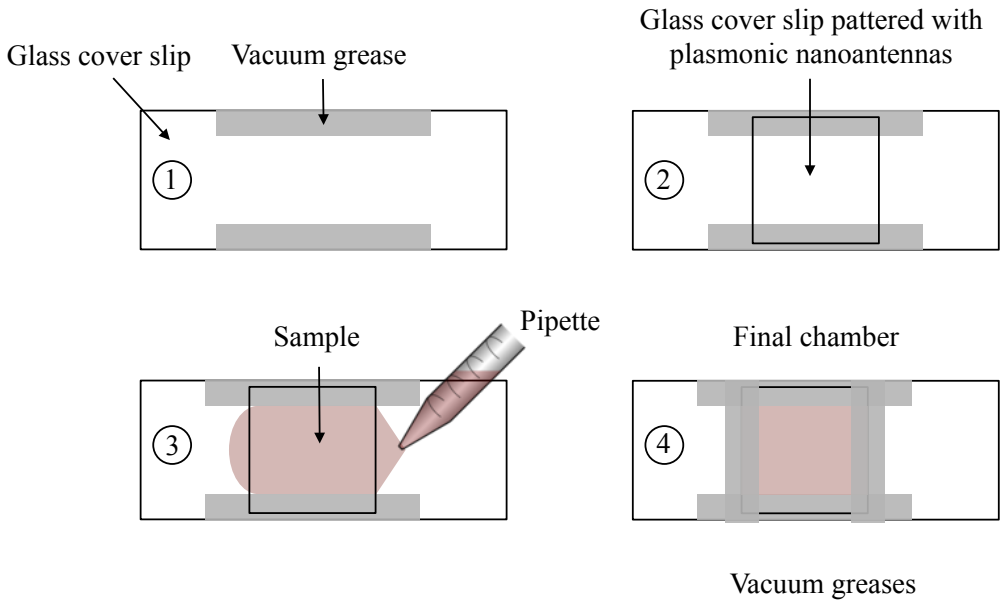


Figure 8.1: Schematic diagram of the preparation method of the sample chamber. Dimensions of the schematic are not to scale.

First, the two sides of the glass were brushed with a thin layer of vacuum grease (Figure 8.1.1). Then the plasmonic coverslip was positioned on top of it. This is done in way that the gold patterns are facing the inside of the chamber. The sides of the coverslip were pressed to fully adhere to the vacuum grease and the bottom glass slide (Figure 8.1.2). A drop of the sample was placed close to the edge of the cover slip (a drop $\approx$ 40μL) and was sucked into the chamber due to van der Waals forces (Figure 8.13). The excess sample solution was then wiped-off using a piece of tissue and the unsealed sides of the cover slip were sealed with a layer of vacuum grease (Figure 8.1.4). It was important that the sample chamber was not too thick (i.e. more than the working distance of the objective lens $\approx$130μm) as nanoplasmonic trapping was be preformed at the top coverslip of the chamber. Figure 8.2 illustrates a typical sample chamber placed on the objective lens.

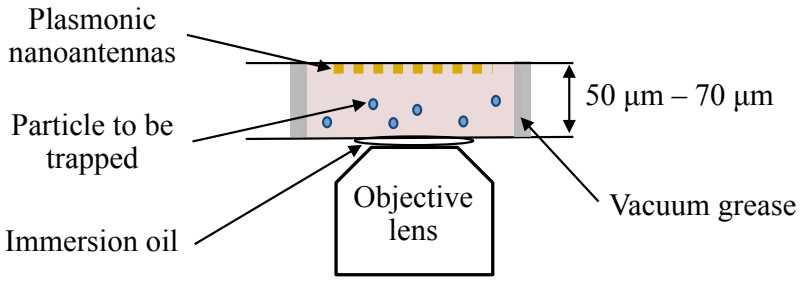


Figure 8.2: Schematic diagram of the sample chamber and objective lens for nanoplasmonic trapping. The dimensions are not to scale.

The plasmonic cover slip is placed on the top surface of the chamber and nanoplasmonic trapping experiments are calibrated in this set-up to avoid gravitational settling of the particles on the BNAs. The sample chamber thickness is usually between 50μm and 70μm. For each experiment reported in this chapter, the sample chamber thickness is measured and reported (refer to section 8.1.3).

The plasmonic cover slips can be cleaned and reused. This is done by gently removing the vacuum grease from the sample chamber (using a Q-tip) avoiding contact with the BNA arrays and placing the plasmonic cover slip submerged in acetone in an ultrasonic bath for 3 to 5 minutes.

8.1.3 Calculation of the thickness of the sample chamber and the depth of focus

The thickness of the sample chamber was measured by imaging the reflections of the laser focus from the first and second cover slips in the sample chamber. The axial movement of the objective lens between the first and second reflections caused by crossing glass-solution and solution-glass interfaces were recorded. Then the axial displacement of the focus of the beam was calculated by the simple geometrical approximation for the focal shift of $\approx n_2/n_1$ based on Snell's law. An illustration

of focal shift caused by changing the medium in which the beam is focused is presented in Fig. 8.3. In experiments presented in this chapter, samples consisting of disperse particles diluted in water were used, therefore the refractive index of the sample was approximated to that of water. Knowing that the refractive index of the immersion oil is ≈ 1.515 and the refractive index of water is ≈1.33, then **1μm** axial movement of the objective lens (in oil) translates into ≈**0.88μm** axial movement of the focal plane in the sample chamber. Reference [236] describes that objectives with high numerical aperture (NA) have relatively larger focal shifts compared to the n2/n1 approximation (≈0.6 versus 0.88). For the purposes of comparison between the results, the simple geometrical approximation for the focal shift is kept as n_2/n_1.

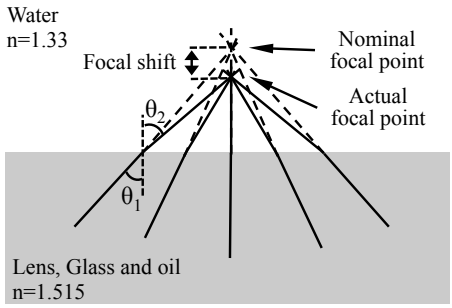


Figure 8.3: Geometrical illustration of the shift in the focal spot as a result of refractive index mismatch between the immersion oil and the water solution.

8.2 Method of nanoplasmonic trapping

Initiating an optical trapping event of an isolated particle using nanoplasmonic traps illuminated under low NA objective lenses usually takes a long time despite large optical trapping forces in close proximity of the plasmonic nanoantennas. This is due to the fact that the sample solutions are prepared to be extremely disperse to avoid multiple particle trapping. In addition, the small features of the plasmonic nanoantennas (tens of nanometeres), mean that the optical trapping forces are only

effective in close proximity of the devices (≈30nm radius of the sharp features of the nanoantennas).

To speed up the trapping procedure and allow flow of different types of particles enabling various experiments such as sensing and manipulation of proteins using plasmonic devices, some research groups take advantage of microfluidic chambers [29,237–239]. They flow a solution with a low concentration of particles across the plasmonic nanoantennas until they reach a single particle trapping incident. In the future it is desired to integrate the existing setup with microfluidic flow and delivery systems (similar to the system presented in reference [237]).

In this PhD, a novel method of nanoplasmonic trapping was developed which takes advantage of the existing conventional optical trapping setup. In this method, particles are initially trapped using a conventional trap (where possible) close to the bottom coverslip, the trap depth is increased by moving the objective lens deeper into the nanoplasmonic coverslip and the particle is brought in close proximity to the BNA or cross arrays. Then the NA of the objective lens is reduced by closing an iris placed in the collimated beam path (refer to Figure 7.1) to switch the conventional trapping which is highly dependent on the high NA to nanoplasmonic trapping which relies on LSP instead. This method increases the experiment speed by removing long waiting periods before a nanoplasmonic trapping incident occurs in hugely dispersed samples [240]. Figure 8.4 illustrates this method. In the cases that the conventional optical trapping of the particles are not possible with the high NA, the number of particles in the solution is increased and the loosely focused laser beam (NA $\approx$ 0.8) is used to illuminated the plasmonic nanoantennas until nanoplasmonic trapping of a single particle is achieved at the hot-spot created by illuminating a nanoantenna. Details of controlling the NA of the objective lens using an iris placed in the collimated beam path is discussed in section 7.2.2.

To check that the particles are optically trapped and not physically stuck to the

BNAs, the laser is turned off. If the particles disperse, then the particles seem to be optically trapped and not mechanically stuck to the BNA. If the particles remain in the same position when the laser in turned off, the measurement was not trusted. This can occur when the particle is physically stuck to the BNA due to high optical intensities at the BNA which can induce heat and cause local melting of the bead. There is also the possibility of laser induced thermal trapping [241,242] of the beads where the thermal gradient can lead to a trapping force. The cooling time of non-metalic beads is relatively slow, therefore if the particles disperse relatively quickly after the illumination is turned off, thermal trapping is ruled out.

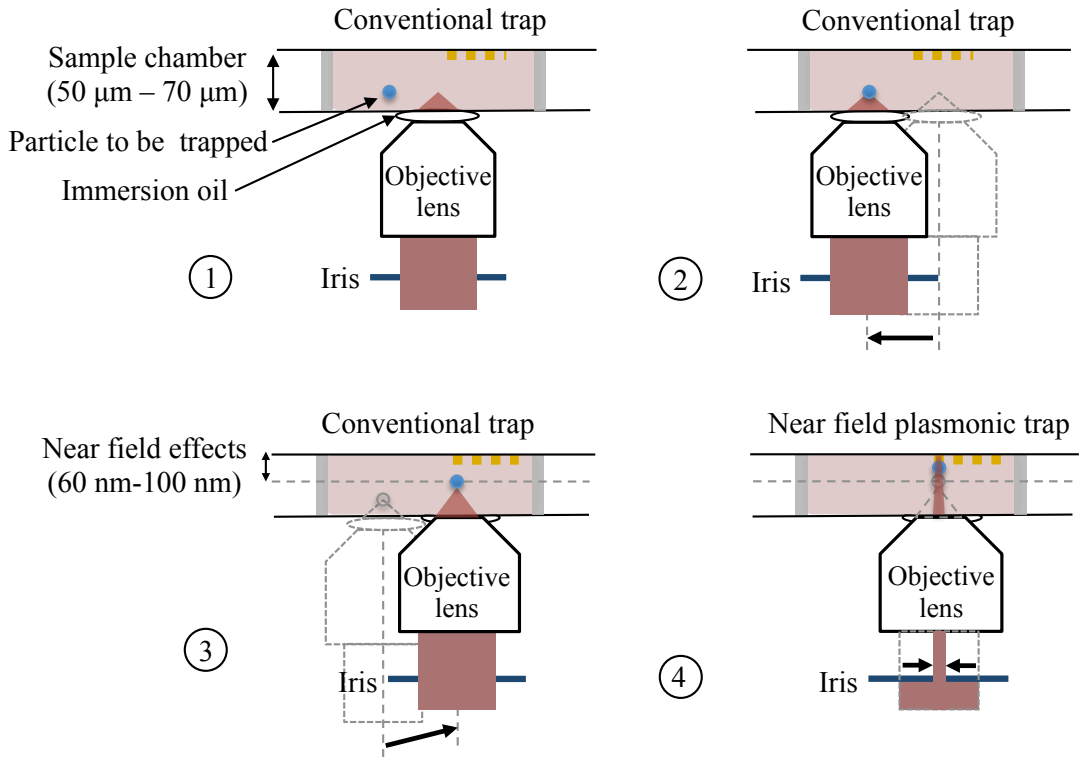


Figure 8.4: Method of placing highly dispersed particles in close proximity of the plasmonic features using a conventional trap and switching to nanoplasmonic traps by reducing the NA of the objective lens. This is done by reducing the diameter of an iris placed in the collimated light path prior to the objective lens. The dimensions are not to scale.

After a single particle is trapped using the nanoplasmonic trap, the trap strength is callibrated by measuring the lateral trap stiffness as described in section 7.3.

8.3 Numerical prediction of trap strength as a function of BNA length

The spectral response of BNAs of various dimensions were studied numerically prior to their fabrication in section 4.5.2. Results presented in this chapter include nanoplasmonic experiments performed using plasmonic coverslips with gold BNA arrays of thickness 50nm, gap size of 30nm, periodicity of 2BNA length and tip angle of 90°. The length of the BNAs used are 500nm, 700nm, 800nm and 1000nm. Figure 8.5 presents the numerical results showing the resonant spectra of the BNAs with these dimensions. The simulations are set-up so that all BNAs are placed on top of glass, and immersed in water. The simulations are performed using the FDTD method and by recording the intensity at a probe in the centre of a single BNA gap excited using a broad spectrum, plane wave (refer to section 4.5.2 for more details). The spectra produced for each BNA is normalised with respect to its maximum.

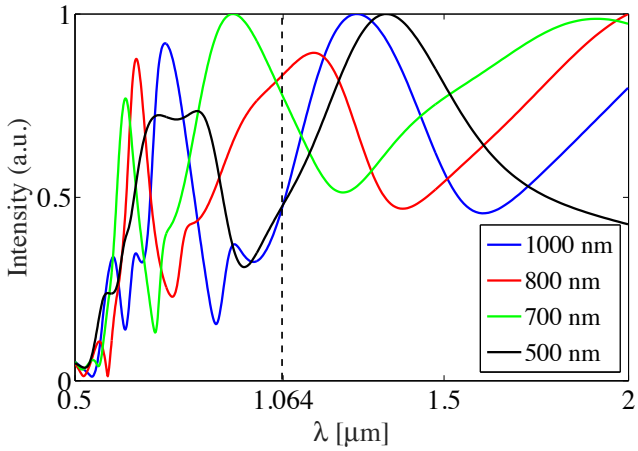


Figure 8.5: Numerical simulation results predicting the behaviour of isolated 50nm thick, gold BNAs with aperture angles of 90° and lengths of 1μm, 800nm, 700nm and 500nm. The BNAs are placed on a glass substrate and are immersed in water. Each spectrum is normalised with respect to its maximum.

Looking at Figure 8.5, all four BNAs have resonances that could be excited at the wavelength of the laser beam used in the optical trapping setup (λ=1064nm). BNAs of length 700nm and 800nm have resonances closer to the laser wavelength compared to the 500nm and 1000nm BNAs. Therefore they should create brighter hot-spots at their gap when illuminated by the laser. The 700nm BNA has a sharper peak compared to the 800nm BNA therefore it should create a slightly brighter hotspot at its gap. The 500nm and 1000nm long BNAs have identical normalised amplitudes at the illumination wavelength of the setup and have similar resonance widths. Therefore the BNAs with lengths 500nm and 1000nm should create hot-spots of similar brightness under the illumination of the laser beam. The 500nm BNA has a slightly wider resonant width therefore the 1000nm BNA should create slightly brighter hotspots compared to the 500nm BNA. The optical traps created by the 700nm BNA should therefore be the strongest of the four, followed by the traps created by the 800nm BNA, the 1000nm BNA and the 500nm BNA.

Figure 8.6 illustrates a prediction of trap strength created at the gap of BNAs

with different lengths. This is based on the expected brightness at the gap when an identical illumination with a wavelength of 1064nm is used. To achieve this prediction, normalized amplitude of the spectra for each BNA at the wavelength of the laser beam (1064nm) was divided by the width of its resonance. This prediction is used throughout this chapter for comparison with experimental results. The width of each spectra is calculated directly from the FFT taken from the intensity probe.

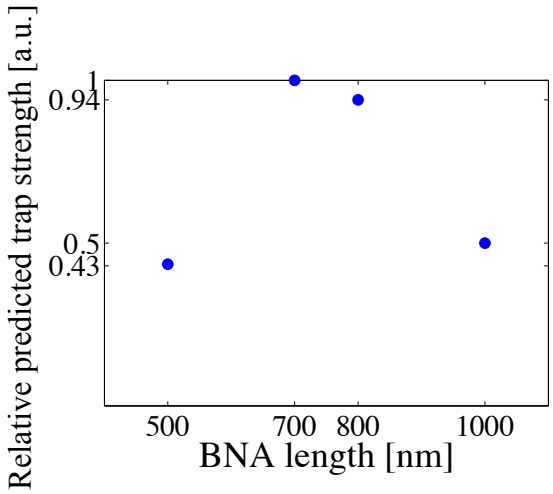


Figure 8.6: Prediction of the trap strength for traps created by illumination of 50nm thick, gold BNAs with aperture angle of 90°, gap size of 30nm and lengths of 500nm, 700nm, 800nm and 1μm. This prediction is achieved by dividing the normalized amplitude of the spectra for each BNA at the wavelength of the laser beam (1064nm) by the width of its resonance.

8.4 Trapping 2μm particles

This section presents results of conventional and nanoplasmonic trapping experiments for 2μm diameter polystyrene beads. The experiments involve measurement of the lateral trap stiffness, k_x and k_y under different conditions. For each k mea-

surement presented, the centroid position fluctuations has been checked in x and y directions to be confident on the validity of presented results. The $x-y$ plots show the variance in the x and y directions and reveal issues with aberration and alignment. For a well aligned conventional optical trap with a Gaussian beam illumination and minimal aberrations, a circular $x-y$ scatter plot is expected. Plots of the fluctuations in position with respect to time, x-t and y-t, show the variation of the particle position over time and can indicate if another bead has fallen into the trap. The lateral trap stiffness, k_x and k_y can also be calculated from these plots using the equipartition method described in section 2.6.1. Figure 8.7 shows typical $x-y$, $x-t$ and $y-t$ plots of the position fluctuations of a 2μm bead trapped using a conventional trap. These plot are based on 50,000 centroid position recordings. Contour lines in the figure show population density at each region.

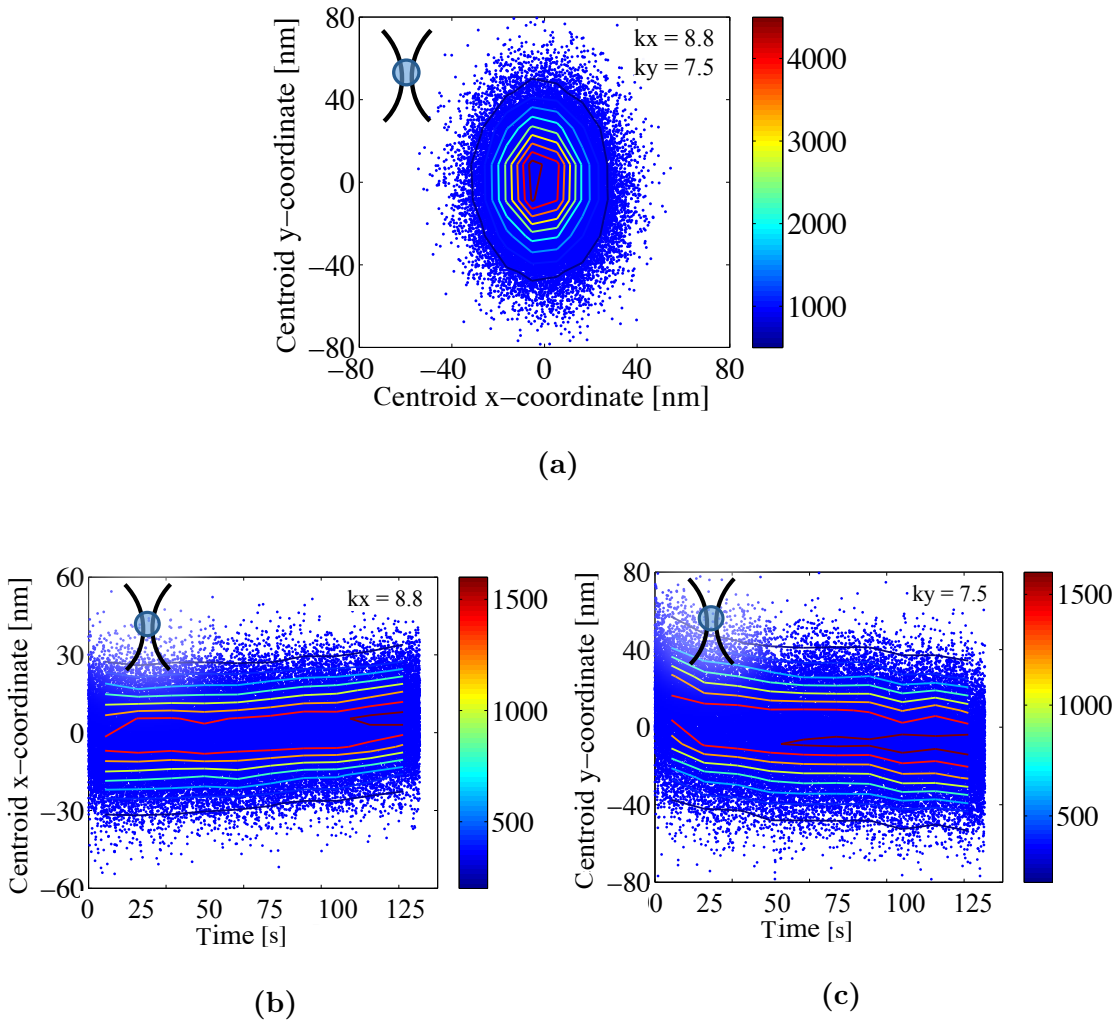


Figure 8.7: x-y (a), x-t (b) and y-t (c) plots of centroid position based on 50,000 images of a 2μm polystyrene bead conventionally trapped with 55% input current to the laser. The iris is kept open for this experiment and the laser power at the focal point is $\approx$ 211.1mW. The contour lines show the population density. The top right insets show lateral trap stiffness in units of pN/μm. The left right insets show that the data is a result of conventional trapping of the beads.

8.4.1 Conventional trapping

8.4.1.1 Trap stiffness as a function of laser power

Figure 8.8 shows a plot of lateral trap stiffness as a function of power at the focus of the beam when conventionally trapping a 2μm polystyrene bead. Each measurement consists of 20,000 position recordings and was repeated three times, each time with a different bead. The error bars account for error originating from the variations in the bead size (coefficient of variance in bead size = 5%). The measurements were taken for input currents to the laser in the range of 27% to 80% corresponding to the power at the focus in the range between 5mW and 345mW. The depth of focus was $\approx 5\mu$m.

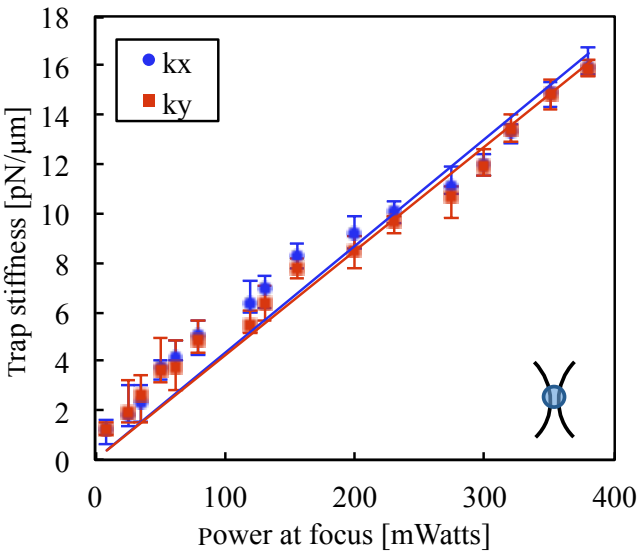


Figure 8.8: Lateral trap stiffness, k_x and k_y (pN/μm), measured as a function of estimated power at the focus of the beam while conventionally trapping 2μm beads at the depth of $\approx$5μm. Error bars show deviation from the mean. The iris is kept open giving an NA of 1.45. The inset indicates that the data is taken using a conventional optical trap.

Figure 8.8 shows that the lateral trap stiffness linearly increases as a function of power at the focus of the beam. This is in accordance with our expectations; as the the gradient force inserted on the particle is proportional to the power of the beam (refer to section 2.3.1.2).

8.4.1.2 Trap stiffness as a function of depth of focus

Figure 8.9 shows the lateral trap stiffness as a function of trap depth. The sample chamber used in this experiment is $\approx 57.2\mu$m thick. The data is measured at the input laser current of 55% (iris is kept open) which corresponds to $\approx$ 110mW at the focus of the beam. Each measurement is repeated 5 times (each time with a different bead) to account for errors. For each data point, the lateral trap stiffness, k_x and k_y, was calculated using the Labview program described in section 7.3. Each measurement is based on 20,000 images of the bead.

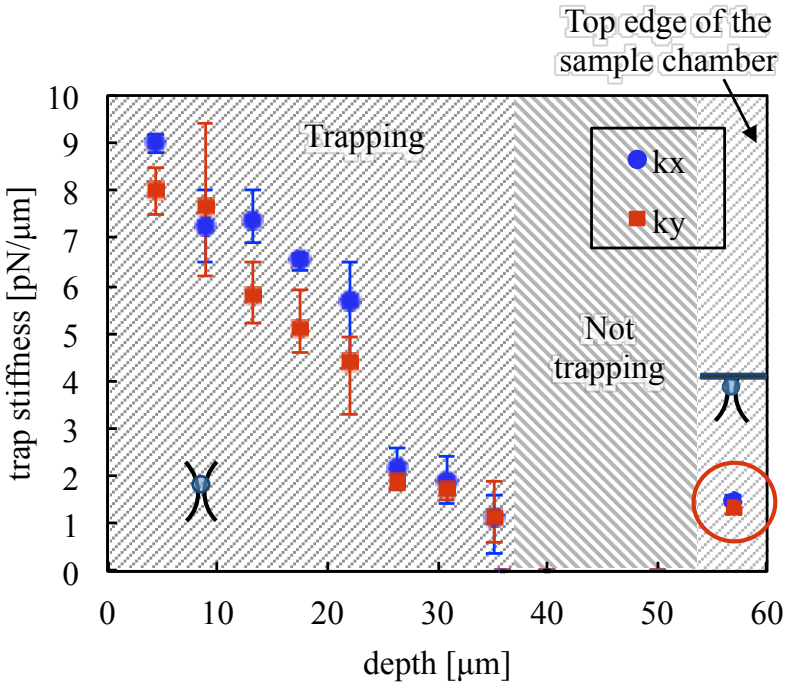


Figure 8.9: Lateral trap stiffness, k_x and k_y, measured as a function of depth of trap. The current supplied to the laser is 55% and iris diameter is 12mm corresponding to the power of ≈110mW at focus of the beam. Error bars indicate deviation from the mean and account for errors. The iris is kept open.

As expected, trap stiffness decreases as the depth of trap increases. This due to increasing spherical aberrations as the depth of focus increases. At this laser power, above the depth of focus of 35μm, the trap is so weak that the particles cannot be immobilised for more than a few seconds. Interestingly, the trap strength increased dramatically at the top cover slip when trapping 2μm polystyrene beads in a thin chamber. The trap is so strong in this case that it pulls multiple particles in the potential well. It is therefore difficult to measure the Brownian motion accurately at this depth. It is expected that this is due to the creation of a nanojets at the surface of the bead creating a strong trap at the top surface of the chamber.

Nanojets are sub-wavelength, high-intensity spots created as a result of resonant scattering of light. This phenomena occurs at the shadow side of micron sized spheres or cylinders (light scattering particles in the Mie regime) when the refractive index difference between the particle and its surrounding is smaller than 2 [243–245]. The position, size and intensity of the nanojet depends on the size of the sphere/cylinder, refractive index of the surroundings and the wavefront and wavelength of illumination. If the refractive index of the surrounding increases, the peak amplitude of the nanojet increases [246].

In the experiments performed using 2μm polystyrene beads, as the bead in the trap gets closer to the top surface of the chamber, the effective refractive difference between the shadow side of the bead and its surroundings reduces dramatically (due to the glass cover slip at the top surface) and creates a strong nanojet resulting in the increased optical trapping force.

8.4.1.3 Control experiment for comparison with nanoplasmonic traps

The lateral trap stiffness for 2μm diameter polystyrene beads is measured when the NA of the objective lens is reduced to approximately 0.8 (iris diameter is 0.5mm), and the focus of the beam is at the top coverslip of the sample chamber (trap depth $\approx 55\mu$m and sample chamber $\approx 60\mu$m thick). Supplied current to the laser is 32% corresponding to an approximate power of 250μW at the focus. This is done to compare the conventional trapping results (assisted with the nanojet effect) and nanoplasmonic results directly. Each measurement is repeated 3 times, each time with a new bead to account for variances in bead size. Each measurement is based on 10,000 position recordings. The average lateral trap stiffnesses are $k_x = \mathbf{0.1\ (pN/\mu m)}$ and $k_y = \mathbf{0.07\ (pN/\mu m)}$ in this configuration. Figure 8.10 shows the position fluctuations in one of the three measurements. This plot is based on 10,000 centroid recordings. Contour lines show population densities at each region. It is

important to note that this mode of trapping is in fact not conventional trapping, but nanojet assisted trapping, as conventional trapping is not possible at low NA and power. Never-the-less it was important to be able to directly compare the strength of the trap at the top coverslip with and without the BNA and under the exact same conditions (i.e. NA and power).

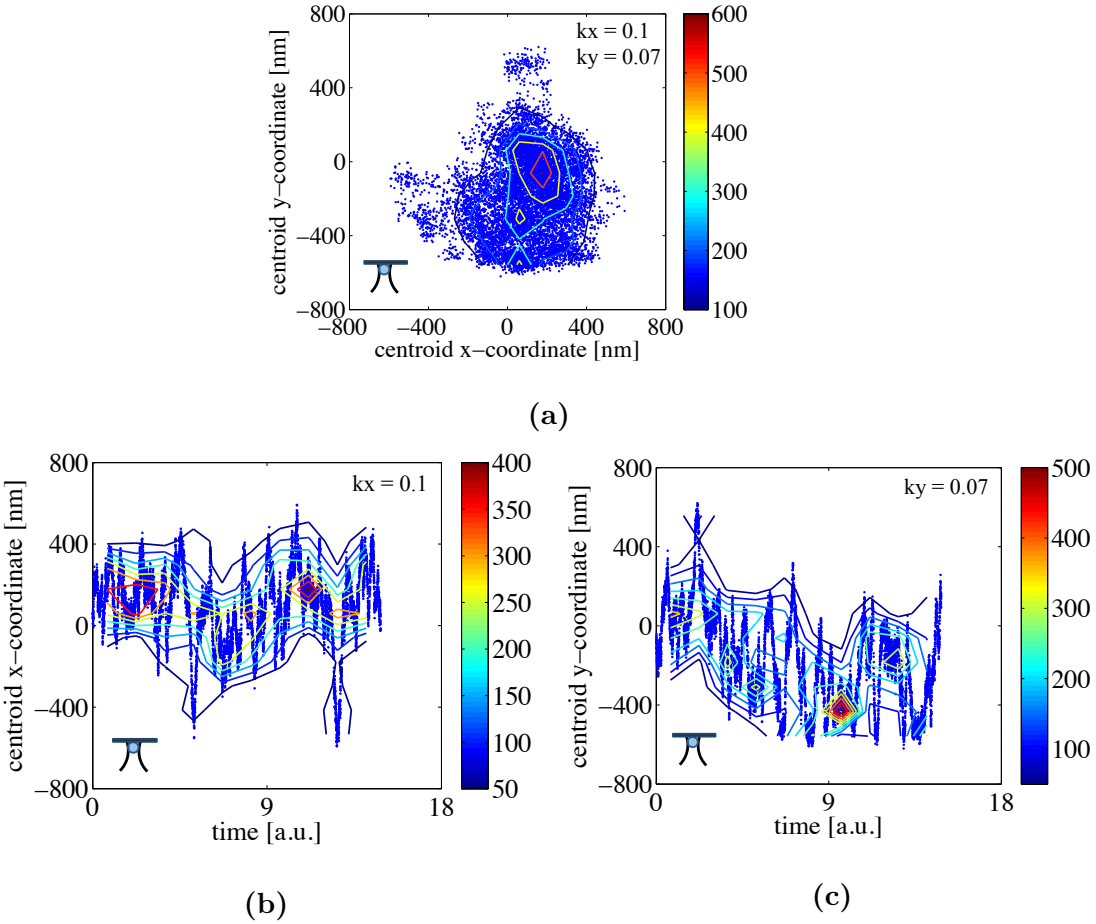


Figure 8.10: $x-y$ (a), $x-t$ (b) and $y-t$ (c) plots of centroid position fluctuations based on 10,000 centroid recordings for a 2μm polystyrene bead trapped with the aid of the nanojet created at the shadow side of the bead at the top surface of the sample chamber. The NA of the objective lens is approximately 0.8 (iris diameter = 0.5 mm) and the power at focus is $\approx$250μW. Contour lines show population density at each region. The top right hand side insets show lateral trap stiffness in units of pN/μm. The bottom left hand side insets indicate optical trapping configuration.

The shape of the $x-y$ scatter plot of the centroid recordings, resembles the shape of the focus of the beam when the iris diameter is 0.5mm shown in Fig. 8.10a.

8.4.2 Nanoplasmonic trapping

The lateral trap stiffness is measured in two main configurations when trapping 2μm polytyrene beads using nanoplasmonic tweezers: 1)when the particle is trapped directly by one BNA and 2) when it is trapped in between four BNAs (focus of the laser is between four BNAs in the BNA array). Figure 8.11 illustrates these two configurations.

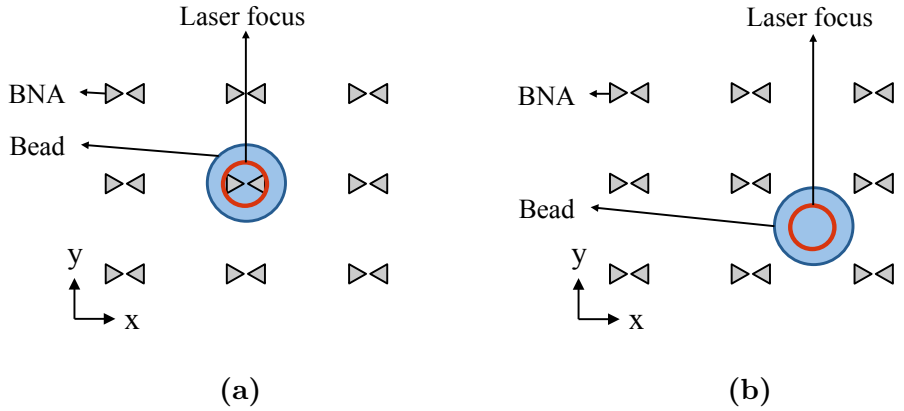


Figure 8.11: Particles are trapped by a single BNA (a) and by the potential field created between four BNAs (b) in a BNA array.

Each trapping experiment is repeated 5 times. Each time the previous trapped particle is driven out of the trap by blocking the beam. The objective lens is then moved down into the sample chamber and the iris is opened to create a conventional trap (NA = 1.45). A new particle (with the same diameter) is trapped with the conventional trap (iris is open) and brought up close to the top coverslip. The iris diameter is then reduced to $\approx$ 0.5mm using the iris placed in the collimated beam path in order to avoid conventional trapping of the particle (NA $\approx$ 0.8). The trap strength is then measured in one of the configurations described above.

8.4.2.1 Bead trapped by illumination of a single BNA

Figure 8.12 shows the lateral trap stiffness as a function of power for nanoplasmonic traps created by illuminating single BNAs of different lengths (500nm, 700nm, 800nm and 1μm). All the BNAs have 90° angles and 30nm gaps. The NA of the objective is approximately 0.8 (iris diameter of 0.5mm corresponding to focus diameter of approximately 1320nm) and the current supplied to the laser is in the range of 30% to 36% resulting in powers at the focus in the range of approximately 170μW to 460μW. The lateral trap stiffness, k_x and k_y, were calculated using the Labview program (described in section 7.3) based on 20,000 position recordings for each measurement. The sample chamber is approximately 60μm thick.

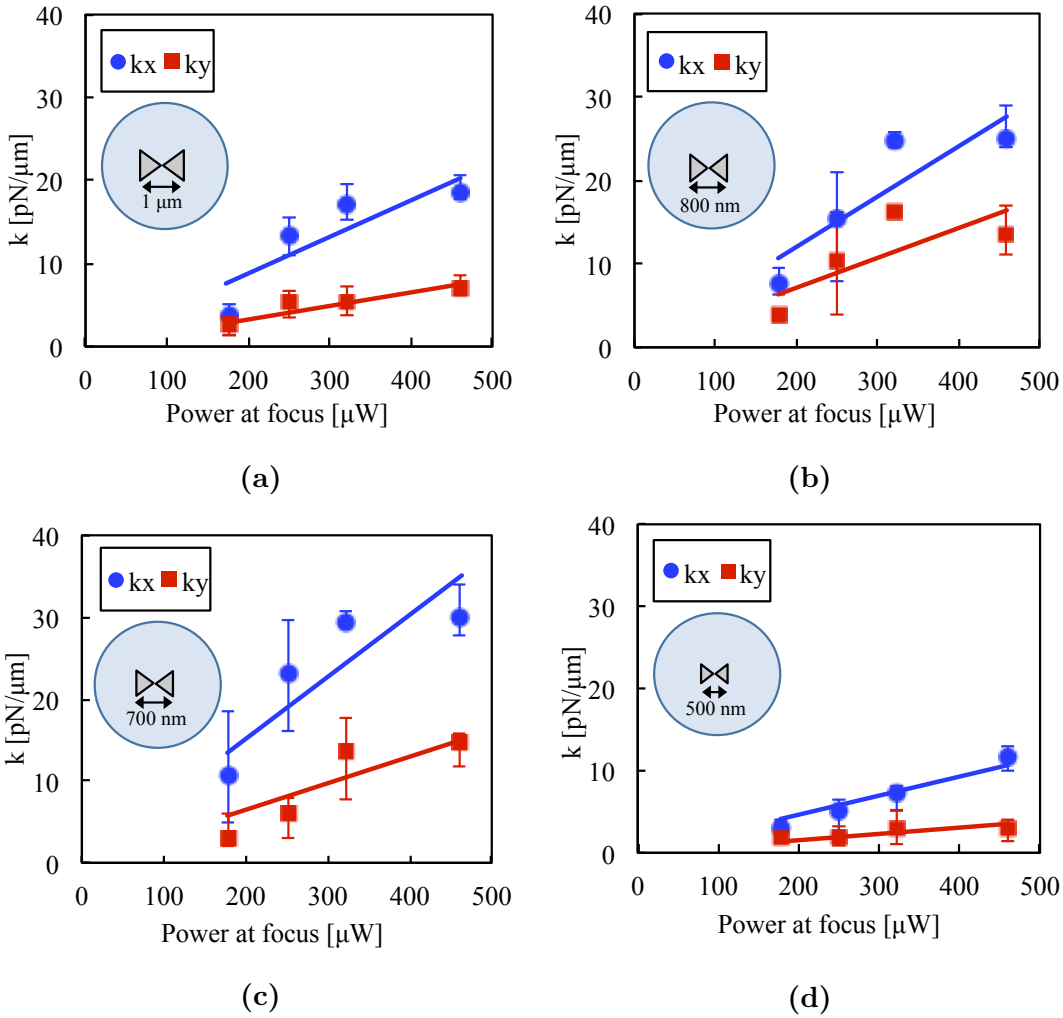


Figure 8.12: Comparison of lateral trap stiffness, kx and ky, as a function of laser power at the focus of the laser beam when 2μm diameter polystyrene beads are trapped by single BNAs with 90° tip angles, 30nm gaps and lengths of 1μm (a), 800nm (b), 700nm (c) and 500nm (d). The longitudinal axis of the BNAs are along x axis. The error bars indicate deviation from the mean and account for errors.

As expected the trap strength increases linearly (linear plot in Fig. 8.12 passing through the origin) as the laser power is increased. The trap strength is much higher when the nanoplasmonic trap is created by illuminating single 700nm long and 800nm long BNAs. This was predicted using simulations as we know that both

of these BNAs are close to resonance at the excitation wavelength as it can be seen in Figure 8.5. Trap stiffness is higher in the x direction due to the shape of the BNAs and polarization of the light exciting them.

Figure 8.13 shows examples of the centroid recordings when the 2μm beads are trapped by single BNAs of lengths 500nm-1μm where the power and NA are kept constant at $\approx$ 250μW and 0.8 respectively. In all cases the nanoplasmonic trap is stronger in the x direction. This is expected since the long axis of BNAs are along the x direction and the illumination polarization is also aligned with the x axis.

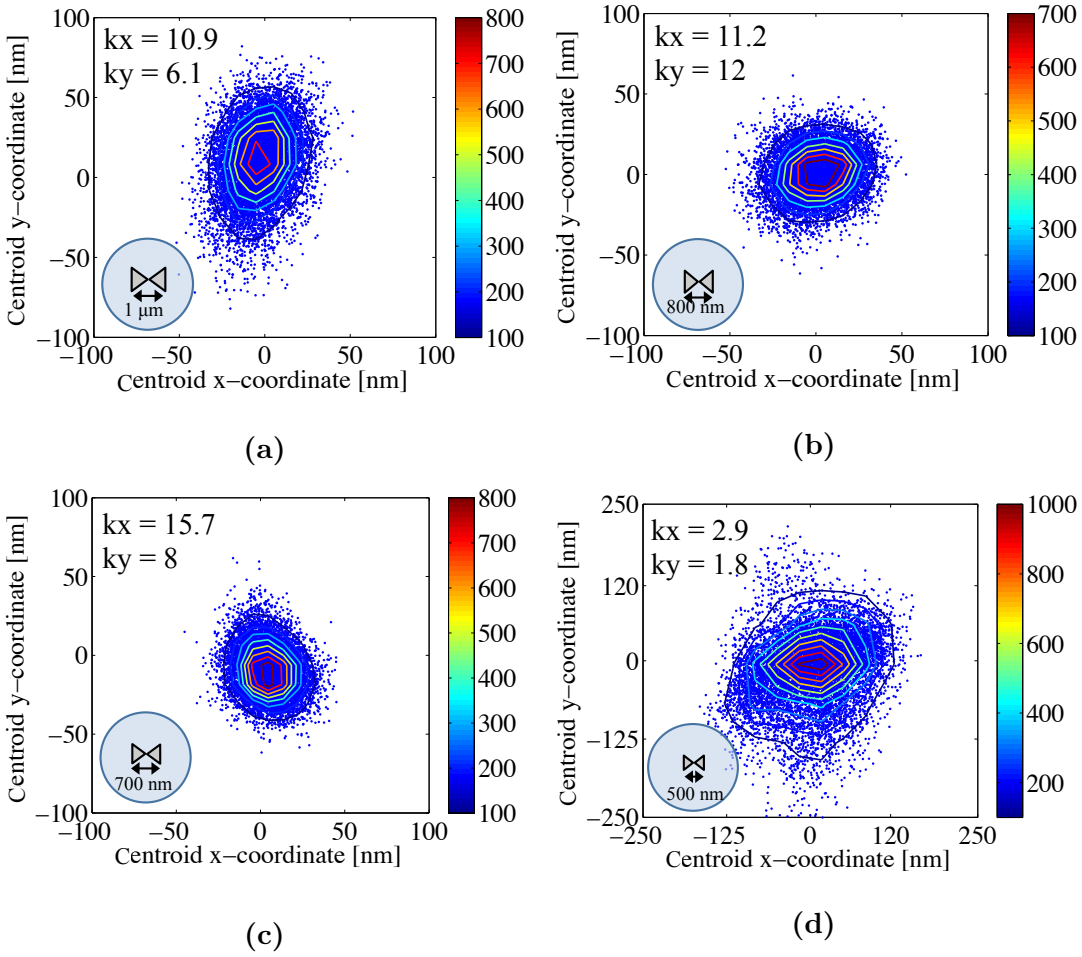


Figure 8.13: Comparison of typical xy scatter plots of centroid position of 2μm polystyrene beads trapped by illuminating single BNAs with input current of 32% and iris diameter of 0.5mm. The BNAs have 90° tip angles, 30nm gaps and lengths of 1μm (a), 800nm (b), 700nm (c) and 500nm (d). The longitudinal axis of the BNAs are along x and the error bars indicate deviation from the mean and account for errors. The insets show lateral trap stiffness in units of pN/μm.

Figure 8.14 compares the trap stiffness measured while trapping 2μm beads by illuminating single BNAs of different lengths against the predicted trap strengths for different BNA lengths. The laser power and NA of the objective lens are kept constant at $\approx$ 250μW and 0.8 respectively. The trend of the numerical models is

followed by the experimental data.

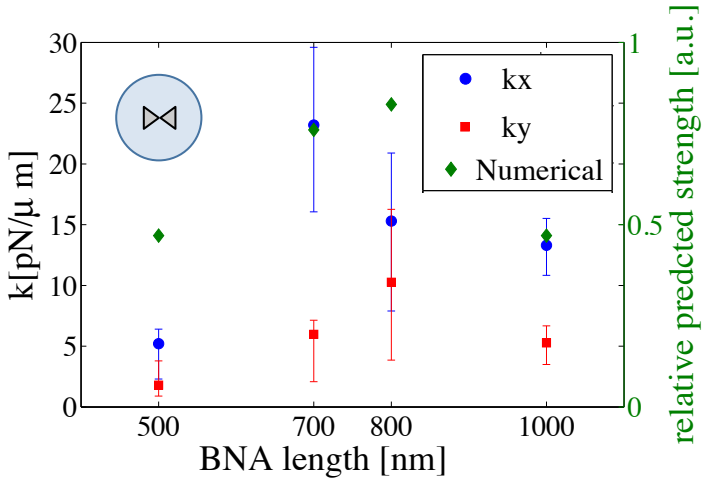


Figure 8.14: Comparison of lateral trap stiffness, k_x and k_y, when 2μm polystyrene beads are trapped by illumination individual BNAs with 90° tip angles, 30nm gaps and lengths of 1μm, 800nm, 700nm and 500nm. The longitudinal axis of the BNAs are along x. The error bars indicate deviation from the mean and account for errors. The green diamonds indicate simulation predictions of relative trap strength.

8.4.2.2 Bead trapped by four BNAs

The trap stiffness is also measured when the focus of the beam is positioned between four BNAs in the BNA array. Figure 8.15 shows the lateral trap stiffness as a function of power for nanoplasmonic traps created between four BNAs of different lengths (500nm, 700nm, 800nm and 1μm). The NA of the objective lens is approximately 0.8 (iris diameter of 0.5mm) and the current supplied to the laser is in the range of 30% to 36% resulting in powers at the focus in the range of $\approx$ 170μW to 460μW. The lateral trap stiffness, k_x and k_y, were calculated using the LaBVIEW program (described in section 7.3) based on 20,000 position recordings for each measurement. All the BNAs have a gap of 30nm and a tip angle of 90 °.

The sample chamber is approximately 60μm thick.

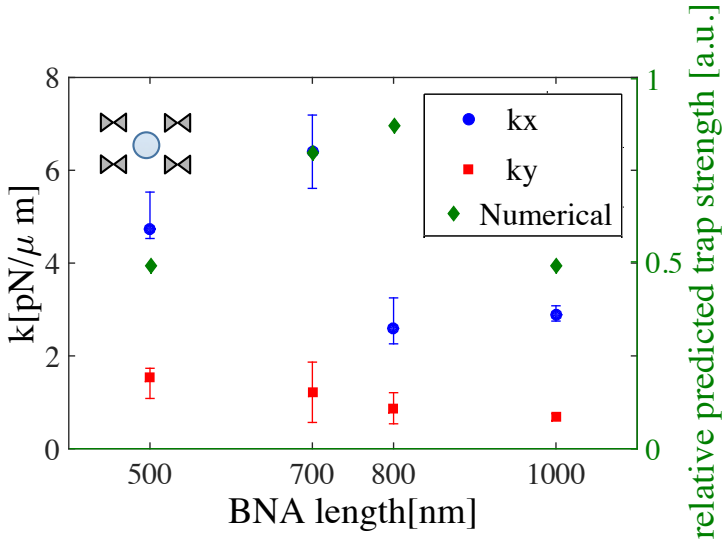


Figure 8.15: Comparison of lateral trap stiffness, kx and ky, when 2μm polystyrene beads are trapped in the near-field between four BNAs with 90° tip angles, 30nm gaps and lengths of 1μm, 800nm, 700nm and 500nm. The longitudinal axis of the BNAs are along x. The error bars indicate deviation from the mean and account for errors caused by differences in the bead size. The green diamonds indicate simulation predictions of trap strength.

The experimental results largely agree with the numerical predictions. However the trap stiffness measured between four 800nm long BNAs has a lower value than predicted. This could be due to larger physical spacing between the particle and hotspots created at the sharp features of the BNAs.

8.4.2.3 Discussion

Table 8.1 compares the trap stiffness measured when 2μm beads are trapped at the top cover slip of the sample chamber assisted by nanojets (labelled as nano-

jet trapping) with the trap stiffness measured when using nanoplasmonic tweezers are created by illuminating single BNAs and illuminating an array of four BNAs of different sizes. The laser power, NA of the objective lens, chamber thickness and depth of focus are kept constant at $\approx 251\mu$W, 0.8, $\approx 60\mu$m and $\approx 59.5\mu$m respectively.

Table 8.1: Comparison of the nano-jet trap stiffness (marked as k_x and k_y) with the trap stiffness of 2μm diameter beads trapped by nanoplasmonic trapping using of BNAs of different lengths. The input current to the laser for all of these measurements are fixed at 32% corresponding to the power at focus of $\approx 251\mu$W.

$\mathbf{L_{BNA[nm]}}$	**Illumination**	$k_{x[\mathbf{pN}/\mu\mathbf{m}]}$	$k_{y[\mathbf{pN}/\mu\mathbf{m}]}$	k_x/k_y	$k_x/kx_{\mathbf{no}BNA}$	$k_y/k_{y\mathbf{no}BNA}$
No BNA	top cover slip	0.1	0.07	1.45	1	1
1000	single BNA	13.3	5.27	2.53	125.3hl	72.2
1000	between BNAs	2.9	0.7	4.14	27.3	9.58
800	single BNA	15.3	10.2	1.49	143	140
800	between BNAs	2.6	0.86	3.02	24.3	11.8
700	single BNA	23.24	5.98	3.88	217	81.9
700	between BNAs	6.4	1.22	5.24	59.9	16.7
500	single BNA	5.2	1.8	2.88	48.73	24.69
500	between BNAs	4.73	1.53	3.09	44.3	21

The maximum of enhancement in trap stiffness (trap stiffness measured for nanoplasmonic tweezer/ trap stiffness measured without BNAs) is achieved when the nanoplasmonic trap was created by illuminating a single 700nm BNA. The nanoplasmonic trap is ≈140 times stronger than the conventional (nanojet assisted) trap in this case. All nanoplasmonic traps created by illuminating a single BNA are stronger than the traps created by illuminating the centre of four BNAs in a BNA array. Never the less, the minimum trap stiffness enhancement achieved is an order of

magnitude. This occurs when the centre of four BNAs in a BNA array of 1μm long BNAs is illuminated. The trap strength enhancement is higher in the x direction compared to the y direction. This is expected as the polarization of the laser beam is aligned with the longitudinal axis of the BNA (along the x direction).

8.5 Trapping 200nm particles

8.5.1 Conventional trapping

Fluorescent beads with diameter of 220nm could be trapped and manipulated using our conventional trapping setup. To be able to have a reliable trap, input currents higher than 80% were needed to be supplied to the laser. The trap was stronger at shallower depths, decreasing in strength as the depth of focus increased as expected due to increasing spherical aberrations. Conventional optical trapping was not observed at depths above 10μm and at the top coverslip of the sample chamber. Figure 8.16 shows that the trap strength reduces as the trap depth increases while conventionally trapping 220nm beads. The input current to the laser was kept constant at 100% translating to a power of $\approx$ 445mW at focus of the beam. The sample chamber thickness was 80μm and the NA of the objective lens was 1.3. The results at each depth are based on 5,000 position recordings taken at 1ms intervals.

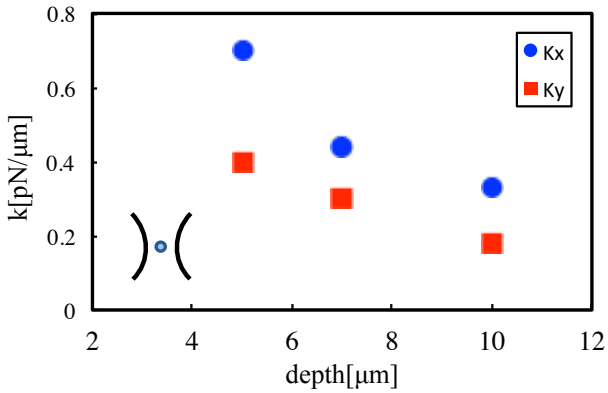


Figure 8.16: Traps stiffness as a function of trap depth for 220nm fluorescent beads. The power at the focus was kept constant at ≈ 445mW and the NA of the objective lens was kept at 1.3. Each datapoint is based on 50,000 centroid location recordings.

Note that for 220nm beads, the method of loading the nanoplasmonic traps using the conventional tweezer was not possible due to the diffraction limit.

8.5.2 Nanoplasmonic trapping

Nanoplasmonic trapping of 220nm beads was most effective when illuminating a single BNA due to the small size of the particle and small features of the hot spots. All results presented in this section are taken when illuminating a single BNA. The NA of the objective lens was reduced to ≈ 0.8.

8.5.2.1 Trap stiffness as a function of laser power

Figure 8.17 shows a plot of lateral trap stiffness as a function of power at the focus of the beam. Each measurement consisted of 20,000 position recordings. One measurement at each power is taken due to the fact that obtaining a single particle trapping incident took considerably longer times compared to when trapping micron

sized particles. When the nanoplasmonic trap was turned on, more than one particle would fall into the trap even at very low concentrations. The concentration of the sample was reduced as described in section 8.1.1 to overcome this issue, but at a certain point diluting the sample further would cause the particles to coagulate. The measurements were taken with an iris diameter of 0.5 mm and laser currents in the range of 25% and 37% resulting in powers at focus in the range of approximately 17μW to 380μW.

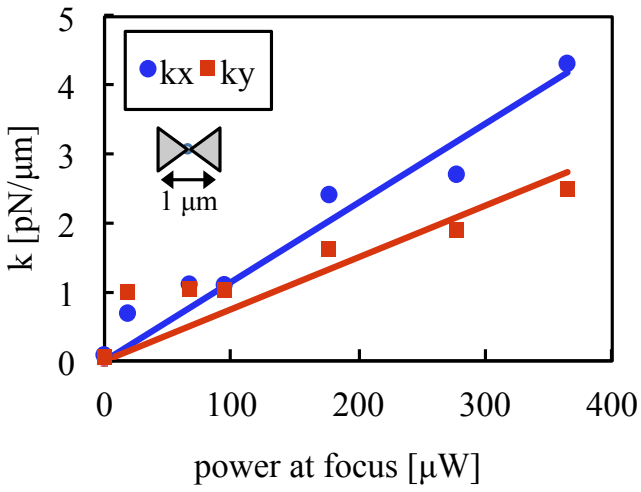


Figure 8.17: Lateral trap stiffness, kx and ky, measured when 220nm flores-cent beads were plasmonically trapped. Particles are trapped by illuminating a 1μm long BNAs with 90° tip angles and gaps of 30nm. Longitudinal axis of the BNAs is in the x direction.

8.5.2.2 Trap stiffness as function of BNA length

Figure 8.18 compares the numerical predictions for relative trap strengths at the centre of BNAs of various lengths with measured trap stiffness (k_x and k_y) of 220nm fluorescent beads. As it can be seen, the experimental data follows the same trend as the numerical simulation results.

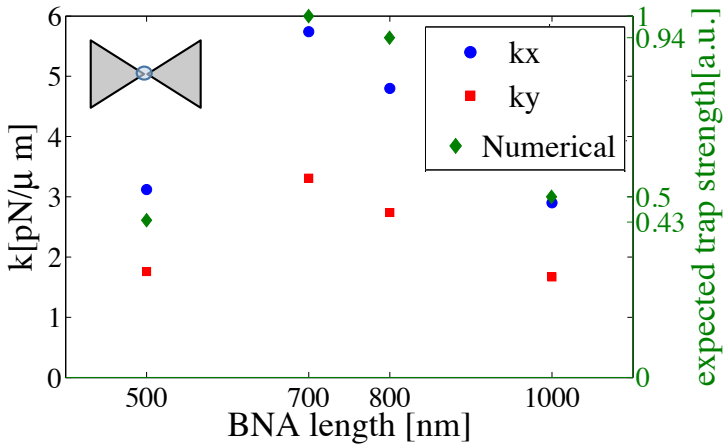


Figure 8.18: Comparison of lateral trap stiffness, k_x and k_y, when 220nm fluorescent beads are trapped by illuminating individual BNAs with 90° tip angles, 30nm gaps and lengths of 1μm, 800nm, 700nm and 500nm. The longitudinal axes of the BNAs are along the x axis. The green diamonds indicate simulation predictions of relative trap strength.

8.6 Trapping 6nm particles

8.6.1 Conventional trapping

Conventional and nano-jets optical trapping of sub 100nm non-metalic beads is not possible due to the diffraction limit of light. The focal spot is large compared to the size of the bead and therefore the bead does not experience a gradient force.

8.6.2 Nanoplasmonic trapping

Nanoplasmonic trapping of 6nm particles was possible, but the particle would appear to undergo a physical change while trapped in the gap of a single BNA. When illuminatiing a single BNA with the laser beam (NA $\approx$ 0.8), the 6nm quantum

dots were pulled towards the BNA gap, and as they entered the gap, they would stop emitting fluorescent photons and would disappear from the image. When the focus of the laser beam was then moved to the BNA gap, a sphere was observed that would increase in diameter when the laser beam would move across it. It is expected that the high energy in the gap of the BNA melted and deformed the quantum dot and glued it at the gap of the BNA. The quantum dot could not be trapped when illuminating the centre of four BNAs. Nanoplasmonic trapping of the quantum dots was possible however when one side of a BNA was illuminated. The quantum dot was therefore trapped at an outer corner of a single BNA where the energy density is lower than the BNA gap. Figure 8.19 illustrates this configuration.

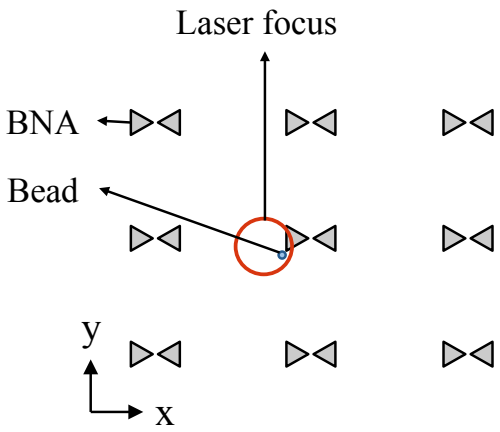


Figure 8.19: Quantum dots with diameters of 6 nm are trapped at an outer corner of a BNA by illuminating the side of a BNA in a BNA array

Figure 8.20 shows the centroid position from 20,000 images for the 6nm QD trapped at an outer corner of a 800nm BNA. The input current to the laser was kept at 25% and the iris diameter was 0.5mm corresponding to the power of $\approx$180μW at the focal point and the NA of $\approx$ 0.8. In this configuration, the lateral trap stiffness was k_x=5.35 pN/μm and k_y=3.1 pN/μm.

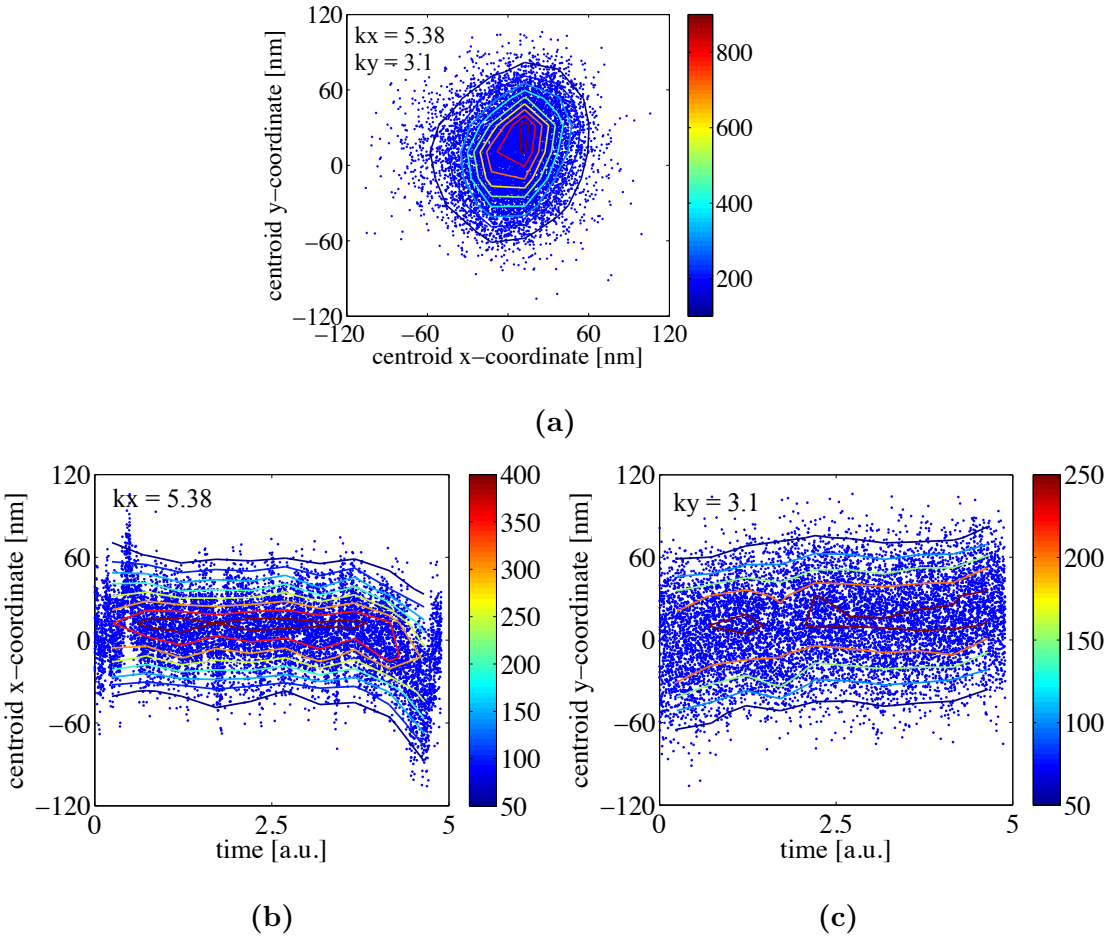


Figure 8.20: x-y (a), x-t (b) and y-t (c) plots of centroid position based on 20,000 images for a 6nm carboxylic acid functionalised QD (COOH) trapped next to a BNA of length 800nm, gap of 30nm and tip angle of 90°. The NA of the objective lens is approximately 0.8 (iris diameter = 0.5 mm) and the approximate power at focus is 17μW. Contour lines show population density at each region. The insets show lateral trap stiffness in units of pN/μm.

8.7 Alignment and rotation of Mycobacteria

When rod shaped micro-particles are trapped using a conventional trap, the rod stands on its end mimicking the incident profile of the beam which is symmetrical

in x and y and elongated in z, along the propagation axis. This can be seen in Fig. 8.21.(a). This limits the application of conventional optical trapping when the user wants to observe changing properties along the length of the object. The aim of this experiment was to demonstrate that nanoplasmonic traps can be used to trap, align and rotate rod shaped particles along their long axis. This is useful for when surface properties of rod shaped bacteria are of interest. For instance if it is desired to perform spectroscopy on a rod shaped bacteria as its surface changes over time. In this experiment, it was also desirable to show that when the polarization of the beam illuminating the plasmonic nanoantennas changes, this results in creation of hotspots along that polarization and causes the rod shaped particle to rotate around the strongest trap created at the focus of the beam. In this experiment, Mycobacterium Smegmatis bacteria, an important model for Mycobacterium Tuberculosis, was used as the rod shaped particle. The particle was $\approx 5\mu$m long and 50nm in diameter. The plasmonic coverslip, consisted of 50nm thick, 700nm long crosses with 30nm gaps between their tips and 30° tip angles.

Figure 8.21 shows the rod shaped particle first trapped under a conventional trap (a). When the focus of the laser beam illuminated the plasmonic coverslip, the rod shaped particle aligned with the longitudinal axis of the antenna that was along the polarization of the beam (b). As the half wave-plate was rotated, rotation of the bacteria was observed (c,d). As expected, the bacteria rotated around the focus of the beam illuminating a cross gap which created the stronger trap compared to the traps created at the edges and gaps of the neighbouring nanoantennas.

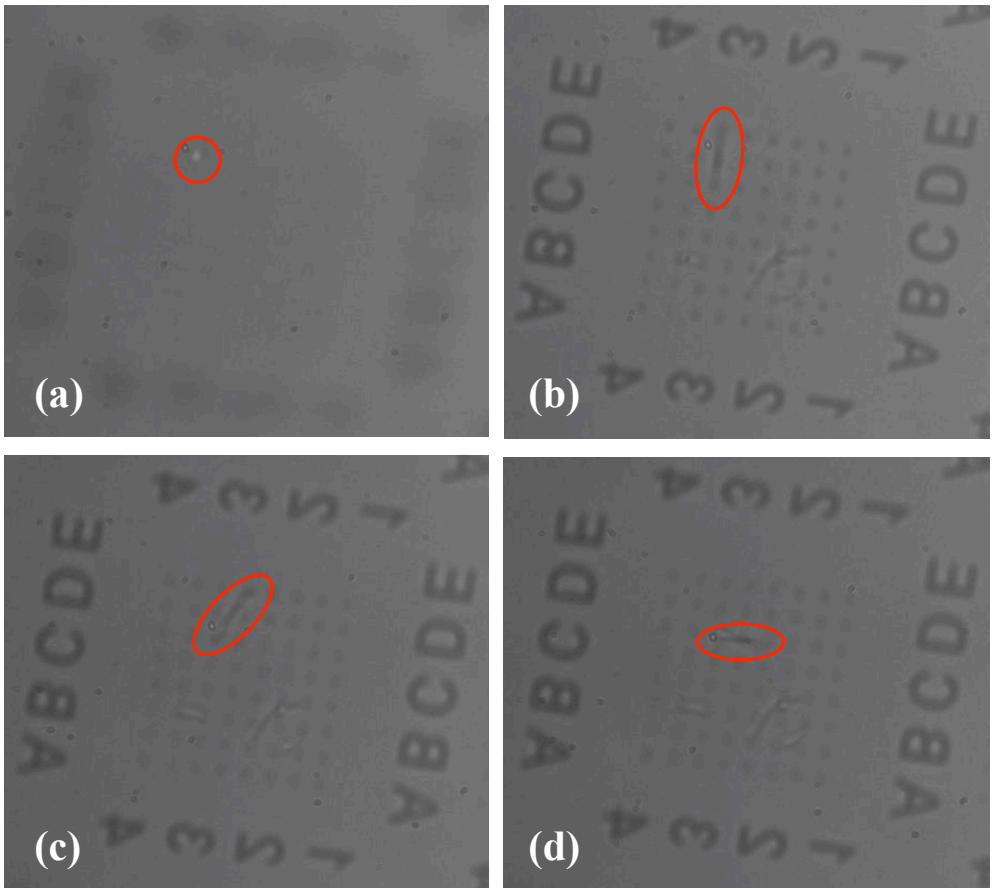


Figure 8.21: (a) Demonstration of conventional optical trapping of 5μm long Mycobacterium Smegmatis. (b)The beam illuminates the surface of the plasmonic cover slip with cross antennas of length 700nm, and the mycrobacterium aligns with the illumination polarization at the hotspots created at the edges of the antennas.(c,d) As the polarization of the beam is altered, the Mycobacterium continues to align with the polarization of the beam and rotates.

It is important to note that the rotation of the bacteria was not smooth and did not include every angle of rotation. This is due to the fluctuations in the transmission of light through the high NA objective lens varying with different polarizations of the laser beam. In practice a smoother rotation could be achieved using a low NA objective lens. A low NA objective lens can be used paired with a plasmonic coverslip with features that allow alignment with larger number of polarization angles. For

example, arrays of 6 - 10 pairs of BNAs/rods centred around a gap, creating a wheel shape or arrays of star shaped nanoantennas with a star shaped hole at their centre can be used to create optical intensity patterns that encourages rotation of rod shaped particles under illumination with rotating polarisations. This effect could be used to create a nanomotors capable of inducing microfluidic effects.

8.8 Summary

In this chapter, first the sample preparation method was described. This was followed by detailing the nanoplasmonic trapping method developed during this PhD. Then conventional optical trapping results obtained from trapping 2μm beads were presented. These results showed that the optical trap strength increases by increasing the power of the laser beam and decreases as the depth of focus of the beam is increased. More interestingly, it was observed that at the top surface of the sample chamber, nanojets can be created due to the size of the spheres being larger than the wavelength of light, and the small effective refractive index difference between the bead and its surroundings. Creation of nano-jets allowed trapping of 2μm beads at the top surface when the NA of the objective lens was reduced to 0.8. At this NA conventional optical trapping is disabled as the gradient force was not strong enough to overcome the scattering force. This was followed by presentation of nanoplasmonic trapping results for 2μm beads. These results revealed a maximum enhancement of $\approx$140 (trapped by a single 700nm BNA) and a minimum enhancement of $\approx$10 (trapped between four 1μm BNAs) compared to nanojet assisted trapping of these beads under low NA illumination at the top of the sample chamber. Nanoplasmonic trapping stiffness was measured at different BNA sizes and agrees with the expected values predicted numerically.

The results for conventional and nanoplasmonic trapping of 220nm beads followed

this. Again the trap strength using a conventional trap increased with the laser power and decreased with the depth of focus. At this particle size, nanojets were not observed since the operation is not in the Mie regime and trapping without BNAs was not possible at the top coverslip. Nanoplasmonic trapping of these particles was measured with respect to the BNA size and results agreed with the numerical predictions. This was followed by a demonstration of nanoplasmonic trapping of 6nm quantum dots. Finally the use of nanoplasmonic trapping for aligning and rotating micron-sized rod shaped particles and the influence of the polarization of light was investigated and demonstrated.

9

Conclusion

The results presented in the previous five chapters are discussed and summarised here. This is followed by a discussion concerning ongoing work and recommendations for future work based on this project.

9.1 Summary and discussions

This project had three main objectives. The first objective was to design a building block which enables the creation of multicomponent platforms that can trap and manipulate multiple nanoparticles simultaneously. Such a device needed to be energy efficient to allow integration and paralellization, and to have a nanoscale, externally accessible "hot-spot", with a high energy density to create near-field optical traps capable of immobilization and manipulation of nanoparticles. This design was achieved numerically by combining an L3 photonic crystal (PhC) resonator and a plasmonic bowtie nanoantenna (BNA) creating a hybrid cavity. In this cavity, the photonic crystal resonator acts as an energy reservoir with high energy storage capacity. It allows integration with photonic integrated circuits and paralellization. The BNA in this hybrid cavity produces a high-intensity, nanoscale "hot-spot", which is externally accessible (unlike the high intensity volume in the PhC slab).

Chapter 4 presented the designs of the building blocks for the hybrid cavity. An L3 PhC resonator design was presented in air and in water with a fundamental resonant mode at 1.54μm to be compatible with photonic integrated circuit technology. The L3 cavity demonstrated a sharp spectral response with a Q-factor of 37,000, effective mode volume of 0.77 $[(\frac{\lambda}{n})^3]$ and $\frac{Q}{V_{eff}}$ of $\approx$ 50,800 $[(\frac{n}{\lambda})^3]$ at the fundamental resonant mode. The BNA demonstrated a wide resonant response with the resonant frequency of the fundamental mode tuned to that of the PhC cavity, a Q-factor of $\approx$ 25 with a V_{eff} of 3.3×10^{-3} $[(\frac{\lambda}{n})^3]$ and a $\frac{Q}{V_{eff}}$ of $\approx$7,500 $[(\frac{n}{\lambda})^3]$. The small mode volume of the BNA enabled near-field trapping of nanometer sized particles. Chapter 4 also presented designs for the fabrication of a PhC cavity based on a 273nm thick GaAs slab and BNAs for nanoplasmonic trapping using the 1064nm laser available in the optical trapping laboratory.

Chapter 5 presented the derivation of a novel figure of merit (FOM) for maximising the optical energy density in the BNA gap for a given input power to the hybrid device. The FOM = QR_I, where R_I is the ratio between intensities at the BNA gap and at the centre of the PhC cavity. This FOM was used to optimise the thickness of the spacer separating the BNA from the PhC cavity. The optimised device has a sharp spectral response, similar to that of the PhC cavity with a Q-factor of 8,200, V_{eff} of 0.77 $[(\frac{\lambda}{n})^3]$, $\frac{Q}{V_{eff}}$ of $\approx$ 50,800 $[(\frac{n}{\lambda})^3]$, R_I of 4.3 and FOM of 3,500. The designed hybrid device has an externally accessible, nanoscale "hot-spot", creating high intensity gradients near the gap, making it ideal for optical trapping and manipulation. The chapter also shows integration of the hybrid cavity to a PhC waveguide, demonstrating its integrability.

The second objective of this project was to realise some of the designed devices so that performing near-field optical trapping experiments would be possible. This was done in collaboration with Dr. Christopher Mellor and Dr. Richard Cousins of the School of Physics and Astronomy at the University of Nottingham.

Chapter 6 presented the results for successful fabrication of the designed BNA and cross plasmonic nanoantennas. The fabricated nanoantennas are based on 50nm thick gold and have different lengths and tip angles. Having gaps as small as 30nm makes them ideal for performing near-field optical trapping of nanoparticles. This chapter also presents the fabrication efforts for realising the designed PhC cavity. The etching process for creating PhC holes faced some difficulties. For example the hard etching of the PhC did not go through to the GaAs layer completely and the adhesion layers used between the SiO_2 mask and the GaAs layer was dissolved by the chemical wash and seeped into the PhC holes. Changing the chemicals used for this process and increasing the e-beam exposure time is likely to rectify these issues.

The third objective of this project was to demonstrate near-field optical trapping of nanoparticles using the fabricated plasmonic devices. This was done by designing a nanotweezer system based on the existing conventional optical trapping setup in the laboratory.

Chapter 7 presented the nanoplasmonic trapping set-up used in this project, reporting the alterations made to transform the conventional optical trapping system to the nanoplasmonic trapping setup. It also presented the calibration of the system and the programs used for measuring the optical trap strength, one of which was developed during this project.

Chapter 8 presented the method of nanoplasmonic trapping developed during this project, explaining the methods used for sample preparation, nanoplasmonic trapping and cleaning of plasmonic cover-slips for re-use. Conventional and nanoplasmonic trapping results for dielectric particles with sizes ranging between 2μm and 6nm were presented and compared. Optical trapping of nanoparticles with diameters below 10nm and aligning and rotating rod-shaped particles were demonstrated using nanoplasmonic tweezers, highlighting the capabilities of nanoplasmonic tweez-

ers, going beyond the capabilities of conventional tweezers.

9.2 Ongoing work

The optimization of the L3 PhC cavity and the hybrid device in water is ongoing. These results will be included in the paper entitled "A hybrid photonic-plasmonic platform for high-throughput single-molecule studies" that is in progress for submission.

Fabrication efforts for realising the designed L3 PhC cavity is ongoing by Dr. Christopher Mellor and Dr. Richard Cousins.

9.3 Recommendations for future work

During this project, a vision has been developed. This vision is to create a hand-held fibre-coupled device, capable of running multiple single-molecule experiments in real time, that can be used in hospitals, laboratories and at home, revolutionising personalized patient care. A building block was designed during this project that will enable high-throughput single-molecule experiments once fabricated. There is still a lot of work that needs to be done for the realization of the device concept. This includes: fabrication of the designed building block, the design and realization of a microfluidic chip, integration with the PhC platform for delivery of the molecules of interest to the "experiment sites" in the platform, the design and fabrication of the electronic circuitry required for the operation of the envisaged device, integration of devices and packaging of the platform integrated with fibre optics.

Going forward with the optimization of the building block, considering an H0 PhC cavity (i.e. a PhC cavity created by shifting the holes slightly away from each other

without removing any holes) to reduce the effective mode volume of the hybrid device is a good starting point. Using other shapes of plasmonic nanoantennas such as two drop-shaped nanoantennas with a small gap between them can reduce the unwanted "hot-spots" at the outer corners of the BNAs and improve trapping at the gap of the nanoantenna.

Moving into the future with the nanoplasmonic trapping and manipulation of particles, an interesting topic to start with would be investigating the thermal effects created by the illumination of nanoplasmonic antennas and how to minimize/harvest them. In order to improve the rotation of rod shaped particles using nanoplamsonic traps, one suggestion is to increase the number of nanoantennas, creating a wheel of BNAs that can be excited by changing the polarisation of light.

Bibliography

[1] C. Joachim, J. Gimzewski, and A. Aviram, "Electronics using hybrid-molecular and mono-molecular devices," *Nature*, vol. 408, no. 6812, p. 541, 2000.

[2] M. C. Leake, "The physics of life: one molecule at a time," *Philosophical Transactions of the Royal Society of London B: Biological Sciences*, vol. 368, no. 1611, 2013.

[3] O. of Basic Energy Sciences (BES), "Scale of things chart kernel description," 2006.

[4] J. Zlatanova and K. van Holde, "Single-molecule biology: what is it and how does it work?," *Molecular cell*, vol. 24, no. 3, pp. 317–329, 2006.

[5] X. Zhuang, "Nano-imaging with STORM," *Nature Photonics*, vol. 3, p. 365, jul 2009.

[6] D. K. Gramotnev and S. I. Bozhevolnyi, "Plasmonics beyond the diffraction limit," *Nature photonics*, vol. 4, no. 2, p. 83, 2010.

[7] B. Huang, M. Bates, and X. Zhuang, "Super-resolution fluorescence microscopy," *Annual review of biochemistry*, vol. 78, pp. 993–1016, 2009.

[8] D. Pohl, "Scanning near-field optical microscopy (snom)," in *Advances in optical and electron microscopy*, vol. 12, pp. 243–312, Elsevier, 1991.

[9] K. C. Neuman and A. Nagy, "Single-molecule force spectroscopy: optical

tweezers, magnetic tweezers and atomic force microscopy," *Nature Methods*, vol. 5, p. 491, may 2008.

[10] I. D. Vlaminck and C. Dekker, "Recent advances in magnetic tweezers," *Annual Review of Biophysics*, vol. 41, no. 1, pp. 453–472, 2012. PMID: 22443989.

[11] A. Ashkin and J. M. Dziedzic, "Optical trapping and manipulation of viruses and bacteria," *Science*, vol. 235, no. 4795, pp. 1517–1520, 1987.

[12] K. C. Neuman and A. Nagy, "Single-molecule force spectroscopy: optical tweezers, magnetic tweezers and atomic force microscopy," *Nature methods*, vol. 5, no. 6, pp. 491–505, 2008.

[13] C. Bustamante, J. C. Macosko, and G. J. Wuite, "Grabbing the cat by the tail: manipulating molecules one by one.," *Nature reviews. Molecular cell biology*, vol. 1, no. 2, pp. 130–136, 2000.

[14] K. C. Neuman and S. M. Block, "Optical trapping," *Review of scientific instruments*, vol. 75, no. 9, pp. 2787–2809, 2004.

[15] D. D. Carlo and L. P. Lee, "Dynamic single-cell analysis for quantitative biology," 2006.

[16] J. D. Joannopoulos, S. G. Johnson, J. N. Winn, and R. D. Meade, *Photonic crystals: molding the flow of light*, ch. Introduction. In [113], 2011.

[17] J. A. Schuller, E. S. Barnard, W. Cai, Y. C. Jun, J. S. White, and M. L. Brongersma, "Plasmonics for extreme light concentration and manipulation," *Nature materials*, vol. 9, no. 3, pp. 193–204, 2010.

[18] J. Gersten and A. Nitzan, "Electromagnetic theory of enhanced raman scattering by molecules adsorbed on rough surfaces," *The Journal of Chemical*

Physics, vol. 73, no. 7, pp. 3023–3037, 1980.

[19] *De cometis liballi tres, author=Ashkin, Arthur, journal=Frankfort, year=1619.*

[20] D. Coulter, *Underestanding!the!FiniteSDifference!TimeSDomain!Method*, 2008 (accessed June 25, 2018).

[21] J. Clerk Maxwell, "On faraday's lines of force," *Transactions of the Cambridge Philosophical Society*, vol. 10, p. 27, 1864.

[22] A. Ashkin, "History of optical trapping and manipulation of small neutral particles, atoms, and molecules," in *Single Molecule Spectroscopy*, pp. 1–31, Springer, 2001.

[23] H. Hora, "Charles townes, how the laser happened: Adventures of a scientist, oxford university press, new york, 1999. 256 pp. isbn: 0-19-5122268-2.-," *Laser and Particle Beams*, vol. 18, no. 1, pp. 151–152, 2000.

[24] A. Ashkin, "Acceleration and trapping of particles by radiation pressure," *Physical Review Letters*, vol. 24, no. 4, p. 156, 1970.

[25] A. Ashkin and J. M. Dziedzic, "Optical levitation by radiation pressure," *Applied Physics Letters*, vol. 19, no. 8, pp. 283–285, 1971.

[26] A. Ashkin, J. M. Dziedzic, J. E. Bjorkholm, and S. Chu, "Observation of a single-beam gradient force optical trap for dielectric particles," *Opt.Lett*, pp. 288–290, 1986.

[27] A. Ashkin, "History of optical trapping and manipulation of small-neutral particle, atoms, and molecules," *IEEE Journal of Selected Topics in Quantum Electronics*, vol. 6, no. 6, pp. 841–856, 2000.

[28] S. Chu, J. E. Bjorkholm, A. Ashkin, and A. Cable, "Experimental observation of optically trapped atoms," *Phys. Rev. Lett.*, vol. 57, pp. 314–317, Jul 1986.

[29] D. G. Grier, "A revolution in optical manipulation.," *Nature*, vol. 424, no. 6950, pp. 810–6, 2003.

[30] N. Malagnino, G. Pesce, A. Sasso, and E. Arimondo, "Measurements of trapping efficiency and stiffness in optical tweezers," *Optics Communications*, vol. 214, no. 1-6, pp. 15–24, 2002.

[31] J. E. Molloy and M. J. Padgett, "Lights, action: optical tweezers," *Contemporary physics*, vol. 43, no. 4, pp. 241–258, 2002.

[32] K. C. Neuman and S. M. Block, "Optical trapping," *Review of Scientific Instruments*, vol. 75, no. 9, pp. 2787–2809, 2004.

[33] S. Reissig, "Determination of the photon force and pressure," in *APS Division of Atomic, Molecular and Optical Physics Meeting Abstracts*, 2004.

[34] E. Fällman and O. Axner, "Design for fully steerable dual-trap optical tweezers," *Applied Optics*, vol. 36, no. 10, pp. 2107–2113, 1997.

[35] N. Simpson, D. McGloin, K. Dholakia, L. Allen, and M. Padgett, "Optical tweezers with increased axial trapping efficiency," *Journal of Modern Optics*, vol. 45, no. 9, pp. 1943–1949, 1998.

[36] J. E. Molloy and M. J. Padgett, "Lights, action: Optical tweezers," *Contemporary Physics*, vol. 43, no. 4, pp. 241–258, 2002.

[37] D. J. Griffiths, *Introduction to electrodynamics; 4th ed.* Boston, MA: Pearson, 2013. Re-published by Cambridge University Press in 2017.

[38] M. Born and E. Wolf, *Principles of optics: electromagnetic theory of propaga-*

tion, interference and diffraction of light. Elsevier, 2013.

[39] J. D. Jackson, *Classical electrodynamics*. Wiley, 1999.

[40] I. C. Lenton, A. B. Stilgoe, H. Rubinsztein-Dunlop, and T. A. Nieminen, "Visual guide to optical tweezers," *European Journal of Physics*, vol. 38, no. 3, p. 034009, 2017.

[41] T. Tlusty, A. Meller, and R. Bar-Ziv, "Optical gradient forces of strongly localized fields," *Physical Review Letters*, vol. 81, no. 8, p. 1738, 1998.

[42] S. LaCavera, *Electromagnetic forces in optical trapping: an overview, MSC Thesis, Department of Electrical and Electrical Engineering, University of Nottingham, UK*, September 2016.

[43] D. S. Bradshaw and D. L. Andrews, "Manipulating particles with light: radiation and gradient forces," *European Journal of Physics*, vol. 38, no. 3, p. 034008, 2017.

[44] A. Radenovic, *Optical Trapping, Ecole Polytechnique Federale De Lausanne*, (accessed July, 2018).

[45] A. Ashkin, J. M. Dziedzic, J. Bjorkholm, and S. Chu, "Observation of a single-beam gradient force optical trap for dielectric particles," *Optics Letters*, vol. 11, no. 5, pp. 288–290, 1986.

[46] M. L. Juan, M. Righini, and R. Quidant, "Plasmon nano-optical tweezers," *Nature Photonics*, vol. 5, no. 6, pp. 349–356, 2011.

[47] J. Happel and H. Brenner, *Low Reynolds number hydrodynamics: with special applications to particulate media*, vol. 1. Springer Science & Business Media, 2012.

[48] M. C. Mullenbroich, *Sensorless Adaptive Optics in Advanced Microscopy Techniques*. PhD thesis, University of Strathclyde, Glasgow, UK, 2012.

[49] Y. Jun, S. K. Tripathy, B. R. Narayanareddy, M. K. Mattson-Hoss, and S. P. Gross, "Calibration of optical tweezers for in vivo force measurements: How do different approaches compare?," *Biophysical Journal*, vol. 107, no. 6, pp. 1474–1484, 2014.

[50] K. Berg-Sørensen and H. Flyvbjerg, "Power spectrum analysis for optical tweezers," *Review of Scientific Instruments*, vol. 75, no. 3, pp. 594–612, 2004.

[51] W. H. Wright, G. Sonek, and M. Berns, "Parametric study of the forces on microspheres held by optical tweezers," *Applied Optics*, vol. 33, no. 9, pp. 1735–1748, 1994.

[52] C. d'Helon, E. Dearden, H. Rubinsztein-Dunlop, and N. Heckenberg, "Measurement of the optical force and trapping range of a single-beam gradient optical trap for micron-sized latex spheres," *Journal of Modern Optics*, vol. 41, no. 3, pp. 595–601, 1994.

[53] W. Singer, S. Bernet, N. Hecker, and M. Ritsch-Marte, "Three-dimensional force calibration of optical tweezers," *Journal of Modern Optics*, vol. 47, no. 14-15, pp. 2921–2931, 2000.

[54] M. J. Lang and S. M. Block, "Resource letter: Lbot-1: Laser-based optical tweezers," *American journal of physics*, vol. 71, no. 3, pp. 201–215, 2003.

[55] F. M. Fazal and S. M. Block, "Optical tweezers study life under tension," *Nature photonics*, vol. 5, no. 6, p. 318, 2011.

[56] A. Ashkin, "Optical trapping and manipulation of neutral particles using lasers," *Proceedings of the National Academy of Sciences*, vol. 94, no. 10,

pp. 4853–4860, 1997.

[57] T. Gustavson, A. Chikkatur, A. Leanhardt, A. Görlitz, S. Gupta, D. Pritchard, and W. Ketterle, "Transport of bose-einstein condensates with optical tweezers," *Physical Review Letters*, vol. 88, no. 2, p. 020401, 2001.

[58] J. Prikulis, F. Svedberg, M. Käll, J. Enger, K. Ramser, M. Goksör, and D. Hanstorp, "Optical spectroscopy of single trapped metal nanoparticles in solution," *Nano Letters*, vol. 4, no. 1, pp. 115–118, 2004.

[59] H. Misawa, N. Kitamura, and H. Masuhara, "Laser manipulation and ablation of a single microcapsule in water," *Journal of the American Chemical Society*, vol. 113, no. 21, pp. 7859–7863, 1991.

[60] M. Dao, C. T. Lim, and S. Suresh, "Mechanics of the human red blood cell deformed by optical tweezers," *Journal of the Mechanics and Physics of Solids*, vol. 51, no. 11-12, pp. 2259–2280, 2003.

[61] S. Rao, Š. Bálint, B. Cossins, V. Guallar, and D. Petrov, "Raman study of mechanically induced oxygenation state transition of red blood cells using optical tweezers," *Biophysical Journal*, vol. 96, no. 1, pp. 209–216, 2009.

[62] S. K. Mohanty, A. Uppal, and P. K. Gupta, "Self-rotation of red blood cells in optical tweezers: prospects for high throughput malaria diagnosis," *Biotechnology Letters*, vol. 26, no. 12, pp. 971–974, 2004.

[63] M. D. Wang, H. Yin, R. Landick, J. Gelles, and S. M. Block, "Stretching dna with optical tweezers," *Biophysical Journal*, vol. 72, no. 3, pp. 1335–1346, 1997.

[64] D. G. Grier, "A revolution in optical manipulation," *Nature*, vol. 424, no. 6950, p. 810, 2003.

[65] A. Ashkin and J. Dziedzic, "Internal cell manipulation using infrared laser traps," *Proceedings of the National Academy of Sciences*, vol. 86, no. 20, pp. 7914–7918, 1989.

[66] K. Svoboda and S. M. Block, "Optical trapping of metallic rayleigh particles," *Optics Letters*, vol. 19, no. 13, pp. 930–932, 1994.

[67] K. Dholakia and P. Reece, "Optical micromanipulation takes hold," *Nano today*, vol. 1, no. 1, pp. 18–27, 2006.

[68] P. Y. Chiou, A. T. Ohta, and M. C. Wu, "Massively parallel manipulation of single cells and microparticles using optical images," *Nature*, vol. 436, no. 7049, p. 370, 2005.

[69] J. E. Curtis, B. A. Koss, and D. G. Grier, "Dynamic holographic optical tweezers," *Optics communications*, vol. 207, no. 1-6, pp. 169–175, 2002.

[70] D. Ganic, X. Gan, M. Gu, M. Hain, S. Somalingam, S. Stankovic, and T. Tschudi, "Generation of doughnut laser beams by use of a liquid-crystal cell with a conversion efficiency near 100%," *Optics Letters*, vol. 27, no. 15, pp. 1351–1353, 2002.

[71] V. Garces-Chavez, D. McGloin, H. Melville, W. Sibbett, and K. Dholakia, "Simultaneous micromanipulation in multiple planes using a self-reconstructing light beam," *Nature*, vol. 419, no. 6903, p. 145, 2002.

[72] S. Kawata and T. Sugiura, "Movement of micrometer-sized particles in the evanescent field of a laser beam," *Optics Letters*, vol. 17, pp. 772–774, Jun 1992.

[73] M. Gu, J.-B. Haumonte, Y. Micheau, J. W. Chon, and X. Gan, "Laser trapping and manipulation under focused evanescent wave illumination," *Applied*

Physics Letters, vol. 84, no. 21, pp. 4236–4238, 2004.

[74] L. Novotny, R. Bian, and X. Xie, "Theory of Nanometric Optical Tweezers," *Physical Review Letters*, vol. 79, no. 4, pp. 645–648, 1997.

[75] C. Girard, D. Dereux, and O. J. F. Martin, "Theoratical analysis of light-inductive forces in scanning probe microscopy," *Physical Review B - Condensed Matter and Materials Physics*, vol. 49, no. 19, pp. 13872–13881, 1994.

[76] A. Dereux, C. Girard, O. Martin, and M. Devel, "Optical binding in scanning probe microscopy," *EPL (Europhysics Letters)*, vol. 26, no. 1, p. 37, 1994.

[77] O. J. F. Martin and C. Girard, "Controlling and tuning strong optical field gradients at a local probe microscope tip apex," *Appl. Phys. Lett.*, vol. 70, no. February, pp. 705–707, 1997.

[78] K. Sasaki, M. Tsukima, and H. Masuhara, "Three-dimensional potential analysis of radiation pressure exerted on a single microparticle," *Applied Physics Letters*, vol. 71, no. 1, pp. 37–39, 1997.

[79] K. Okamoto and S. Kawata, "Radiation force exerted on subwavelength particles near a nanoaperture," *Physical Review Letters*, vol. 83, no. 22, p. 4534, 1999.

[80] P. C. Chaumet, A. Rahmani, and M. Nieto-Vesperinas, "Optical trapping and manipulation of nano-objects with an apertureless probe," *Physical Review Letters*, vol. 88, no. 12, p. 123601, 2002.

[81] M. Nieto-Vesperinas, P. Chaumet, A. Rahmani, *et al.*, "Near-field photonic forces," *Philosophical Transactions-Royal Society of London Series A Mathematical Physical and Engineering Sciences*, pp. 719–738, 2004.

[82] R. Quidant, D. Petrov, and G. Badenes, "Radiation forces on a rayleigh dielectric sphere in a patterned optical near field," *Optics Letters*, vol. 30, no. 9, pp. 1009–1011, 2005.

[83] M. Mossayebi, G. Bellanca, A. Parini, A. Wright, and E. Larkins, "Engineering of hybrid photonic-plasmonic devices for enhanced light-matter interactions," in *Recent Trends in Computational Photonics*, pp. 369–390, Springer, 2017.

[84] A. Rahmani and P. C. Chaumet, "Optical trapping near a photonic crystal," *Optics Express*, vol. 14, no. 13, pp. 6353–6358, 2006.

[85] X. Serey, S. Mandal, and D. Erickson, "Comparison of silicon photonic crystal resonator designs for optical trapping of nanomaterials," *Nanotechnology*, vol. 21, no. 30, p. 305202, 2010.

[86] S. Kawata and T. Tani, "Optically driven mie particles in an evanescent field along a channeled waveguide," *Optics Letters*, vol. 21, no. 21, pp. 1768–1770, 1996.

[87] T. Čižmár, V. Garćs-Chávez, K. Dholakia, and P. Zemánek, "Optical conveyor belt for delivery of submicron objects," *Applied Physics Letters*, vol. 86, no. 17, pp. 1–3, 2005.

[88] A. Grigorenko, N. Roberts, M. Dickinson, and Y. Zhang, "Nanometric optical tweezers based on nanostructured substrates," *Nature Photonics*, vol. 2, no. 6, p. 365, 2008.

[89] M. Righini, P. Ghenuche, S. Cherukulappurath, V. Myroshnychenko, F. J. García de Abajo, and R. Quidant, "Nano-optical trapping of rayleigh particles and escherichia coli bacteria with resonant optical antennas," *Nano Letters*, vol. 9, no. 10, pp. 3387–3391, 2009.

[90] A. Kotnala and R. Gordon, "Quantification of high-efficiency trapping of nanoparticles in a double nanohole optical tweezer," *Nano Letters*, vol. 14, no. 2, pp. 853–856, 2014.

[91] J.-S. Huang and Y.-T. Yang, "Origin and Future of Plasmonic Optical Tweezers," *Nanomaterials*, vol. 5, no. 2, 2015.

[92] A. Krishnan, N. Huang, S.-H. Wu, L. J. Martínez, and M. L. Povinelli, "Enhanced and selective optical trapping in a slot-graphite photonic crystal," *Optics Express*, vol. 24, no. 20, pp. 23271–23279, 2016.

[93] B. J. Roxworthy, K. D. Ko, A. Kumar, K. H. Fung, E. K. Chow, G. L. Liu, N. X. Fang, and K. C. Toussaint Jr, "Application of plasmonic bowtie nanoantenna arrays for optical trapping, stacking, and sorting," *Nano Letters*, vol. 12, no. 2, pp. 796–801, 2012.

[94] Y. Pang and R. Gordon, "Optical trapping of a single protein," *Nano Letters*, vol. 12, no. 1, pp. 402–406, 2011.

[95] M. L. Juan, M. Righini, and R. Quidant, "Plasmon nano-optical tweezers," vol. 5, no. May, 2011.

[96] S. A. Maier, M. L. Brongersma, P. G. Kik, S. Meltzer, A. A. Requicha, and H. A. Atwater, "Plasmonics—a route to nanoscale optical devices," *Advanced materials*, vol. 13, no. 19, pp. 1501–1505, 2001.

[97] M. Righini, G. Volpe, C. Girard, D. Petrov, and R. Quidant, "Surface plasmon optical tweezers: Tunable optical manipulation in the femtonewton range," *Physical Review Letters*, vol. 100, no. 18, pp. 8–11, 2008.

[98] P. Mestres, J. Berthelot, S. S. Aćimović, and R. Quidant, "Unraveling the optomechanical nature of plasmonic trapping," *Light: Science & Applications*,

vol. 5, no. 7, p. e16092, 2016.

[99] J. Berthelot, S. Aćimović, M. Juan, M. Kreuzer, J. Renger, and R. Quidant, "Three-dimensional manipulation with scanning near-field optical nanotweezers," *Nature nanotechnology*, vol. 9, no. 4, pp. 295–299, 2014.

[100] C. Ciminelli, D. Conteduca, F. Dell'Olio, and M. Armenise, "Design of an optical trapping device based on an ultra-high q/v resonant structure," *IEEE Photonics Journal*, vol. 6, no. 6, pp. 1–16, 2014.

[101] M. Mossayebi, A. J. Wright, A. Parini, M. G. Somekh, G. Bellanca, and E. Larkins, "Investigating the use of a hybrid plasmonic–photonic nanoresonator for optical trapping using finite-difference time-domain method," *Optical and Quantum Electronics*, vol. 48, no. 5, p. 275, 2016.

[102] M. L. Juan, R. Gordon, Y. Pang, F. Eftekhari, and R. Quidant, "Self-induced back-action optical trapping of dielectric nanoparticles," *Nature Physics*, vol. 5, no. 12, p. 915, 2009.

[103] P. M. Junque, J. Berthelot, R. Quidant, and S. Acimovic, "Optomechanical plasmonic trapping," in *CLEO: QELS_Fundamental Science*, pp. FM2B–8, Optical Society of America, 2016.

[104] D. Griffiths, *Introduction to Electrodynamics*. Cambridge University Press, 2017.

[105] D. Fleisch, *A Student's Guide to Maxwell's Equations*. Cambridge University Press, 2008.

[106] M. Benson, *Fields, waves and transmission lines*. Springer Science & Business Media, 2012.

[107] H. A. Haus, *Electromagnetic noise and quantum optical measurements*. Springer, 2000.

[108] W. Yu and R. Mittra, "A conformal fdtd algorithm for modeling perfectly conducting objects with curve-shaped surfaces and edges," *Microwave and Optical Technology Letters*, vol. 27, no. 2, pp. 136–138, 2000.

[109] M. O. C. Ware, *Electronic, Optical and Magnetic Properties of Materials*, 2013 (accessed June 8, 2018).

[110] E. I. Markus Zahn and D. Staelin, *Electromagnetics and Applications*, Fall 2005 (accessed June 20, 2018).

[111] A. Taflove and S. C. Hagness, *Computational electrodynamics: the finite-difference time-domain method*. Artech house, 2005.

[112] S. Benkler, *Robust Conformal Subcell Modeling for Electromagnetic Simulations in Time Domain*. PhD thesis, SWISS FEDERAL INSTITUTE OF TECHNOLOGY ZURICH, 2007.

[113] J. D. Joannopoulos, S. G. Johnson, J. N. Winn, and R. D. Meade, *Photonic crystals: molding the flow of light*. Princeton university press, 2011.

[114] U. Andersson, *Time-domain methods for the Maxwell equations*. PhD thesis, Numerisk analys och datalogi, 2001.

[115] M. C. T. Weiland, "Discrete electromagnetism with the finite integration technique," *Progress In Electromagnetics Research*, vol. 32, pp. 65–87, 2001.

[116] C. Christopoulos, *The transmission-line modeling method: TLM*. Oxford University Press, 1995.

[117] D. W. Thomas, A. C. Denton, T. Konefal, T. Benson, C. Christopoulos,

J. Dawson, A. Marvin, S. J. Porter, and P. Sewell, "Model of the electromagnetic fields inside a cuboidal enclosure populated with conducting planes or printed circuit boards," *IEEE Transactions on Electromagnetic Compatibility*, vol. 43, no. 2, pp. 161–169, 2001.

[118] M. Krumpholz, C. Huber, and P. Russer, "A field theoretical comparison of FDTD and TLM," *IEEE Transactions on Microwave Theory and Techniques*, vol. 43, no. 8, pp. 1935–1950, 1995.

[119] B. A. Rahman and A. Agrawal, *Finite element modeling methods for photonics*. Artech House, 2013.

[120] G. Dhatt, E. Lefrançois, and G. Touzot, *Finite element method*. John Wiley & Sons, 2012.

[121] X. C. Wang, *Finite element method*. Tsinghua University Press, Beijing, 2003.

[122] P. Sumithra and D. Thiripurasundari, "Review on computational electromagnetics," *Advanced Electromagnetics*, vol. 6, no. 1, pp. 42–55, 2017.

[123] K. Yee, "Numerical solution of initial boundary value problems involving maxwell's equations in isotropic media," *IEEE Transactions on Antennas and Propagation*, vol. 14, no. 3, pp. 302–307, 1966.

[124] J. B.Schneider, *Underestanding the Finite Difference Time Domain Method*, November 2013 (accessed June 10, 2018).

[125] Y. Hao and R. Mittra, *FDTD Modeling of metamaterials*. 01 2008.

[126] S. Benkler, H. Songoro, N. Chavannes, and N. Kuster, "Robust and fully automated conformal mesh generation for complex conformal fdtd applications," in *Poster Presentation at 2005 IEEE AP-S International Symposium and USNC*,

2005 IEEE AP-S International Symposium and USNC, 2005.

[127] K. L. Shlager and J. B. Schneider, "Comparison of the dispersion properties of several low-dispersion finite-difference time-domain algorithms," *IEEE Trans. Antennas Propagat.*, vol. 51, no. 3, pp. 642–653, 2003.

[128] J.-P. Bérenger, "Perfectly matched layer (pml) for computational electromagnetics," *Synthesis Lectures on Computational Electromagnetics*, vol. 2, no. 1, pp. 1–117, 2007.

[129] S. D. Gedney, "An anisotropic perfectly matched layer-absorbing medium for the truncation of fdtd lattices," *IEEE transactions on Antennas and Propagation*, vol. 44, no. 12, pp. 1630–1639, 1996.

[130] J.-P. Berenger, "Perfectly matched layer for the fdtd solution of wave-structure interaction problems," *IEEE Transactions on Antennas and Propagation*, vol. 44, no. 1, pp. 110–117, 1996.

[131] D. M. Hockanson, "Perfectly matched layers used as absorbing boundaries in a three-dimensional fdtd code," tech. rep., Technical Report, Umr Emc Laboratory.

[132] N. Sukumar and J. Pask, "Classical and enriched finite element formulations for bloch-periodic boundary conditions," *International Journal for Numerical Methods in Engineering*, vol. 77, no. 8, pp. 1121–1138, 2009.

[133] https://kb.lumerical.com/en/index.html?diffractive_optics_cavity_q_calculation.html.

[134] P. T. Kristensen, C. Van Vlack, and S. Hughes, "Generalized effective mode volume for leaky optical cavities," *Optics Letters*, vol. 37, no. 10, pp. 1649–1651, 2012.

[135] M. Toishi, D. Englund, A. Faraon, and J. Vučković, "High-brightness single photon source from a quantum dot in a directional-emission nanocavity," *Optics Express*, vol. 17, no. 17, pp. 14618–14626, 2009.

[136] LumericalSolutions,Inc.http://www.lumerical.com/tcad-products/fdtd/.

[137] https://meep.readthedocs.io/en/latest/.

[138] https://www.paraview.org.

[139] "The Copernicus Project." http://www.copernicusproject.eu, October 2013 (accessed July 19, 2018).

[140] L. Rayleigh, "Xvii. on the maintenance of vibrations by forces of double frequency, and on the propagation of waves through a medium endowed with a periodic structure," *The London, Edinburgh, and Dublin Philosophical Magazine and Journal of Science*, vol. 24, no. 147, pp. 145–159, 1887.

[141] W. H. Bragg, W. L. Bragg, *et al.*, "The reflection of x-rays by crystals," *Proc. R. Soc. Lond. A*, vol. 88, no. 605, pp. 428–438, 1913.

[142] L. Rayleigh, "On the reflection of light from a regularly stratified medium," *Proc. R. Soc. Lond. A*, vol. 93, no. 655, pp. 565–577, 1917.

[143] E. Yablonovitch, "Photonic crystals: What's in a name?," *Optics and Photonics News*, vol. 18, no. 3, pp. 12–13, 2007.

[144] S. John, "Strong localization of photons in certain disordered dielectric superlattices," *Physical Review Letters*, vol. 58, no. 23, p. 2486, 1987.

[145] E. Yablonovitch, "Inhibited spontaneous emission in solid-state physics and electronics," *Physical Review Letters*, vol. 58, no. 20, p. 2059, 1987.

[146] S. Fan, P. R. Villeneuve, R. D. Meade, and J. D. Joannopoulos, "Three-dimensional periodic dielectric structures having photonic bandgaps," Aug. 8 1995. US Patent 5,440,421.

[147] T. F. Krauss and M. Richard, "Photonic crystals in the optical regime—past, present and future," *Progress in Quantum Electronics*, vol. 23, no. 2, pp. 51–96, 1999.

[148] N. Aravantinos-Zafiris, M. Sigalas, M. Kafesaki, and E. Economou, "Phononic crystals and elastodynamics: Some relevant points," *Aip Advances*, vol. 4, no. 12, p. 124203, 2014.

[149] M. L. Cohen and J. R. Chelikowsky, *Electronic structure and optical properties of semiconductors*, vol. 75. Springer Science & Business Media, 2012.

[150] H. Fudouzi, "Tunable structural color in organisms and photonic materials for design of bioinspired materials," *Science and Technology of Advanced Materials*, vol. 12, no. 6, p. 064704, 2011.

[151] B. D. Wilts, K. Michielsen, J. Kuipers, H. De Raedt, and D. G. Stavenga, "Brilliant camouflage: photonic crystals in the diamond weevil, entimus imperialis," *Proceedings of the Royal Society of London B: Biological Sciences*, p. rspb20112651, 2012.

[152] L. Zeng, Y. Yi, C. Hong, J. Liu, N. Feng, X. Duan, L. Kimerling, and B. Alamariu, "Efficiency enhancement in si solar cells by textured photonic crystal back reflector," *Applied Physics Letters*, vol. 89, no. 11, p. 111111, 2006.

[153] S.-Y. Lin, E. Chow, V. Hietala, P. R. Villeneuve, and J. Joannopoulos, "Experimental demonstration of guiding and bending of electromagnetic waves in a photonic crystal," *Science*, vol. 282, no. 5387, pp. 274–276, 1998.

[154] C. Bentham, I. Itskevich, R. Coles, B. Royall, E. Clarke, J. O'Hara, N. Prtljaga, A. Fox, M. Skolnick, and L. Wilson, "On-chip electrically controlled routing of photons from a single quantum dot," *Applied Physics Letters*, vol. 106, no. 22, p. 221101, 2015.

[155] Y. Liu and H. Salemink, "Photonic crystal-based all-optical on-chip sensor," *Optics Express*, vol. 20, no. 18, pp. 19912–19920, 2012.

[156] T. Tanabe, M. Notomi, E. Kuramochi, A. Shinya, and H. Taniyama, "Trapping and delaying photons for one nanosecond in an ultrasmall high-q photonic-crystal nanocavity," *Nature Photonics*, vol. 1, no. 1, p. 49, 2007.

[157] H. Altug, D. Englund, and J. Vuckovic, "Nature phys. 2, 484–488 (2006)," *CrossRef— CAS— Web of Science® Times Cited*, vol. 82.

[158] J. D. Joannopoulos, S. G. Johnson, J. N. Winn, and R. D. Meade, *Photonic Crystals: Molding the Flow of Light (Second Edition)*. Princeton University Press, 2 ed., 2008.

[159] X. Zhang and Z. Liu, "Superlenses to overcome the diffraction limit," *Nature materials*, vol. 7, no. 6, p. 435, 2008.

[160] J. Witzens, M. Loncar, and A. Scherer, "Self-collimation in planar photonic crystals," *IEEE Journal of Selected Topics in Quantum Electronics*, vol. 8, no. 6, pp. 1246–1257, 2002.

[161] C. Luo, S. G. Johnson, J. Joannopoulos, and J. Pendry, "All-angle negative refraction without negative effective index," *Physical Review B*, vol. 65, no. 20, p. 201104, 2002.

[162] B. Gralak, S. Enoch, and G. Tayeb, "Anomalous refractive properties of photonic crystals," *JOSA A*, vol. 17, no. 6, pp. 1012–1020, 2000.

[163] S. G. Johnson and J. D. Joannopoulos, "Introduction to photonic crystals: Bloch's theorem, band diagrams, and gaps (but no defects)," *Photonic Crystal Tutorial*, pp. 1–16, 2003.

[164] A. Yariv and P. Yeh, *Optical waves in crystals*, vol. 5. Wiley New York, 1984.

[165] K. Sakoda, *Optical properties of photonic crystals*, vol. 80. Springer Science & Business Media, 2004.

[166] S. G. Johnson, S. Fan, P. R. Villeneuve, J. D. Joannopoulos, and L. Kolodziejski, "Guided modes in photonic crystal slabs," *Physical Review B*, vol. 60, no. 8, p. 5751, 1999.

[167] T.-I. Weng and G. Guo, "Band structure of honeycomb photonic crystal slabs," *Journal of applied physics*, vol. 99, no. 9, p. 093102, 2006.

[168] E. Kuramochi, M. Notomi, S. Mitsugi, A. Shinya, T. Tanabe, and T. Watanabe, "Ultrahigh-q photonic crystal nanocavities realized by the local width modulation of a line defect," *Applied physics letters*, vol. 88, no. 4, p. 041112, 2006.

[169] X. Xu, T. Tsuboi, T. Chiba, N. Usami, T. Maruizumi, and Y. Shiraki, "Silicon-based current-injected light emitting diodes with ge self-assembled quantum dots embedded in photonic crystal nanocavities," *Optics Express*, vol. 20, no. 13, pp. 14714–14721, 2012.

[170] H.-S. Ee and H.-G. Park, "Ultra-small photonic crystal zero-cell laser cavities," in *Optoelectronic Integrated Circuits XI*, vol. 7219, p. 72190G, International Society for Optics and Photonics, 2009.

[171] M. Notomi, T. Tanabe, A. Shinya, E. Kuramochi, H. Taniyama, S. Mitsugi, and M. Morita, "Nonlinear and adiabatic control of high-q photonic crystal

nanocavities," *Optics Express*, vol. 15, no. 26, pp. 17458–17481, 2007.

[172] E. Kuramochi, H. Taniyama, T. Tanabe, K. Kawasaki, Y.-G. Roh, and M. Notomi, "Ultrahigh-q one-dimensional photonic crystal nanocavities with modulated mode-gap barriers on sio 2 claddings and on air claddings," *Optics Express*, vol. 18, no. 15, pp. 15859–15869, 2010.

[173] M. F. Yanik and S. Fan, "Stopping light all optically," *Physical Review Letters*, vol. 92, no. 8, p. 083901, 2004.

[174] M. Lončar, T. Doll, J. Vučković, and A. Scherer, "Design and fabrication of silicon photonic crystal optical waveguides," *Journal of Lightwave Technology*, vol. 18, no. 10, p. 1402, 2000.

[175] A. Mekis, J. Chen, I. Kurland, S. Fan, P. R. Villeneuve, and J. Joannopoulos, "High transmission through sharp bends in photonic crystal waveguides," *Physical Review Letters*, vol. 77, no. 18, p. 3787, 1996.

[176] D. M. Beggs, T. F. Krauss, K. Kuipers, and T. Kampfrath, "Adiabatic frequency conversion for optical data transfer," *SPIE Newsroom*, pp. x40424–1, 2010.

[177] Q. Zhao, K. Cui, X. Feng, F. Liu, W. Zhang, and Y. Huang, "Low loss sharp photonic crystal waveguide bends," *Optics Communications*, vol. 355, pp. 209–212, 2015.

[178] J.-P. Hugonin, P. Lalanne, T. P. White, and T. F. Krauss, "Coupling into slow-mode photonic crystal waveguides," *Optics Letters*, vol. 32, no. 18, pp. 2638–2640, 2007.

[179] T. F. Krauss, "Slow light in photonic crystal waveguides," *Journal of Physics D: Applied Physics*, vol. 40, no. 9, p. 2666, 2007.

[180] M. Notomi, K. Yamada, A. Shinya, J. Takahashi, C. Takahashi, and I. Yokohama, "Extremely large group-velocity dispersion of line-defect waveguides in photonic crystal slabs," *Physical Review Letters*, vol. 87, no. 25, p. 253902, 2001.

[181] Y. A. Vlasov, M. O'boyle, H. F. Hamann, and S. J. McNab, "Active control of slow light on a chip with photonic crystal waveguides," *Nature*, vol. 438, no. 7064, p. 65, 2005.

[182] S. A. Maier, *Plasmonics: fundamentals and applications*. Springer Science & Business Media, 2007.

[183] D. K. Gramotnev and S. I. Bozhevolnyi, "Nanofocusing of electromagnetic radiation," *Nature Photonics*, vol. 8, no. 1, p. 13, 2014.

[184] M. L. Brongersma and P. G. Kik, *Surface plasmon nanophotonics*, vol. 131. Springer, 2007.

[185] W. Yuming, *Analysis and design of nanoantennas*. PhD thesis, 2010.

[186] N. A. Hatab, C.-H. Hsueh, A. L. Gaddis, S. T. Retterer, J.-H. Li, G. Eres, Z. Zhang, and B. Gu, "Free-standing optical gold bowtie nanoantenna with variable gap size for enhanced raman spectroscopy," *Nano Letters*, vol. 10, no. 12, pp. 4952–4955, 2010.

[187] J. N. Anker, W. P. Hall, O. Lyandres, N. C. Shah, J. Zhao, and R. P. Van Duyne, "Biosensing with plasmonic nanosensors," *Nature materials*, vol. 7, no. 6, pp. 442–453, 2008.

[188] X. Ni, N. K. Emani, A. V. Kildishev, A. Boltasseva, and V. M. Shalaev, "Broadband light bending with plasmonic nanoantennas," *Science*, vol. 335, no. 6067, pp. 427–427, 2012.

[189] S. I. Bozhevolnyi, V. S. Volkov, E. Devaux, J.-Y. Laluet, and T. W. Ebbesen, "Channel plasmon subwavelength waveguide components including interferometers and ring resonators," *Nature*, vol. 440, no. 7083, p. 508, 2006.

[190] V. S. Volkov, S. I. Bozhevolnyi, S. G. Rodrigo, L. Martin-Moreno, F. J. García-Vidal, E. Devaux, and T. W. Ebbesen, "Nanofocusing with channel plasmon polaritons," *Nano Letters*, vol. 9, no. 3, pp. 1278–1282, 2009.

[191] A. Kinkhabwala, Z. Yu, S. Fan, Y. Avlasevich, K. Müllen, and W. Moerner, "Large single-molecule fluorescence enhancements produced by a bowtie nanoantenna," *Nature Photonics*, vol. 3, no. 11, pp. 654–657, 2009.

[192] G. Pellegrini, M. Celebrano, M. Finazzi, and P. Biagioni, "Local field enhancement: comparing self-similar and dimer nanoantennas," *The Journal of Physical Chemistry C*, vol. 120, no. 45, pp. 26021–26024, 2016.

[193] D. Englund, I. Fushman, and J. Vuckovic, "General recipe for designing photonic crystal cavities," *Optics Express*, vol. 13, no. 16, pp. 5961–5975, 2005.

[194] S. Malaguti, G. Bellanca, L. Ottaviano, K. Yvind, S. Combrié, A. De Rossi, and S. Trillo, "Tailored design of wdm filters in bcb embedded phc membranes," *Optical and Quantum Electronics*, vol. 45, no. 4, pp. 329–342, 2013.

[195] C. Sauvan, P. Lalanne, and J.-P. Hugonin, "Slow-wave effect and mode-profile matching in photonic crystal microcavities," *Physical Review B*, vol. 71, no. 16, p. 165118, 2005.

[196] I. Karnadi, J. Son, J.-Y. Kim, H. Jang, S. Lee, K. S. Kim, B. Min, and Y.-H. Lee, "A printed nanobeam laser on a sio2/si substrate for low-threshold continuous-wave operation," *Opt. Express*, vol. 22, pp. 12115–12121, May 2014.

[197] T. Zhang, S. Callard, C. Jamois, C. Chevalier, D. Feng, and A. Belarouci, "Plasmonic-photonic crystal coupled nanolaser," *Nanotechnology*, vol. 25, no. 31, p. 315201, 2014.

[198] S. Mokkapati, D. Saxena, N. Jiang, L. Li, H. H. Tan, and C. Jagadish, "An order of magnitude increase in the quantum efficiency of (al)gaas nanowires using hybrid photonic–plasmonic modes," *Nano Letters*, vol. 15, no. 1, pp. 307–312, 2015. PMID: 25545962.

[199] R. F. Oulton, V. J. Sorger, D. Genov, D. Pile, and X. Zhang, "A hybrid plasmonic waveguide for subwavelength confinement and long-range propagation," *Nature Photonics*, vol. 2, no. 8, pp. 496–500, 2008.

[200] G. Magno, M. Fevrier, P. Gogol, A. Aassime, A. Bondi, R. Mégy, and B. Dagens, "Strong coupling and vortexes assisted slow light in plasmonic chain-SOI waveguide systems," *Scientific Reports*, vol. 7, no. 1, p. 7228, 2017.

[201] M. Castro-Lopez, N. de Sousa, A. Garcia-Martin, F. Y. Gardes, and R. Sapienza, "Scattering of a plasmonic nanoantenna embedded in a silicon waveguide," *Optics Express*, vol. 23, no. 22, pp. 28108–28118, 2015.

[202] A. Casadei, E. F. Pecora, J. Trevino, C. Forestiere, D. Ruffer, E. Russo-Averchi, F. Matteini, G. Tutuncuoglu, M. Heiss, A. Fontcuberta i Morral, *et al.*, "Photonic–plasmonic coupling of gaas single nanowires to optical nanoantennas," *Nano Letters*, vol. 14, no. 5, pp. 2271–2278, 2014.

[203] X. He, L. Yang, and T. Yang, "Optical nanofocusing by tapering coupled photonic-plasmonic waveguides," *Optics Express*, vol. 19, no. 14, pp. 12865–12872, 2011.

[204] Y. Luo, M. Chamanzar, A. Apuzzo, R. Salas-Montiel, K. N. Nguyen, S. Blaize, and A. Adibi, "On-chip hybrid photonic–plasmonic light concentrator for

nanofocusing in an integrated silicon photonics platform," *Nano Letters*, vol. 15, no. 2, pp. 849–856, 2015.

[205] P. Xu and Y. Shi, "High q/v hybrid plasmonic photonic crystal nanobeam cavity: Towards low threshold nanolasers application," *Optics Communications*, vol. 311, pp. 234–238, 2013.

[206] Q. Wang, H. Zhao, X. Du, W. Zhang, M. Qiu, and Q. Li, "Hybrid photonic-plasmonic molecule based on metal/si disks," *Optics Express*, vol. 21, no. 9, pp. 11037–11047, 2013.

[207] X. Yang, A. Ishikawa, X. Yin, and X. Zhang, "Hybrid photonicplasmonic crystal nanocavities," *ACS Nano*, vol. 5, no. 4, pp. 2831–2838, 2011. PMID: 21384850.

[208] M. Barth, S. Schietinger, S. Fischer, J. Becker, N. Nusse, T. Aichele, B. Lochel, C. Sonnichsen, and O. Benson, "Nanoassembled plasmonic-photonic hybrid cavity for tailored light-matter coupling," *Nano Letters*, vol. 10, no. 3, pp. 891–895, 2010.

[209] S. Cui, X. Zhang, T.-l. Liu, J. Lee, D. Bracher, K. Ohno, D. Awschalom, and E. L. Hu, "Hybrid plasmonic photonic crystal cavity for enhancing emission from near-surface nitrogen vacancy centers in diamond," *ACS Photonics*, vol. 2, no. 4, pp. 465–469, 2015.

[210] F. Todisco, M. Esposito, S. Panaro, M. De Giorgi, L. Dominici, D. Ballarini, A. I. Fernández-Domínguez, V. Tasco, M. Cuscunà, A. Passaseo, C. Ciracì, G. Gigli, and D. Sanvitto, "Toward cavity quantum electrodynamics with hybrid photon gap-plasmon states," *ACS Nano*, vol. 10, no. 12, pp. 11360–11368, 2016. PMID: 28024373.

[211] Z. Li, J.-l. Kou, M. Kim, J. O. Lee, and H. Choo, "Highly efficient and tai-

lorable on-chip metal–insulator–metal plasmonic nanofocusing cavity," *ACS Photonics*, vol. 1, no. 10, pp. 944–953, 2014.

[212] A. E. Eter, T. Grosjean, P. Viktorovitch, X. Letartre, T. Benyattou, and F. I. Baida, "Huge light-enhancement by coupling a bowtie nano-antenna's plasmonic resonance to a photonic crystal mode," *Opt. Express*, vol. 22, pp. 14464–14472, Jun 2014.

[213] F. De Angelis, M. Patrini, G. Das, I. Maksymov, M. Galli, L. Businaro, L. C. Andreani, and E. Di Fabrizio, "A hybrid plasmonicphotonic nanodevice for label-free detection of a few molecules," *Nano Letters*, vol. 8, no. 8, pp. 2321–2327, 2008. PMID: 18630973.

[214] A. Bozzola, S. Perotto, and F. De Angelis, "Hybrid plasmonic-photonic whispering gallery mode resonators for sensing: a critical review," *Analyst*, vol. 142, pp. 883–898, 2017.

[215] M. Bahramipanah, S. Dutta-Gupta, B. Abasahl, and O. J. Martin, "Cavity-coupled plasmonic device with enhanced sensitivity and figure-of-merit," *ACS nano*, vol. 9, no. 7, pp. 7621–7633, 2015.

[216] A. E. Eter, N. M. Hameed, F. I. Baida, R. Salut, C. Filiatre, D. Nedeljkovic, E. Atie, S. Bole, and T. Grosjean, "Fiber-integrated optical nano-tweezer based on a bowtie-aperture nano-antenna at the apex of a snom tip," *Opt. Express*, vol. 22, pp. 10072–10080, Apr 2014.

[217] W. Yu-Ming, L. Le-Wei, and L. Bo, "Geometric effects in designing bow-tie nanoantenna for optical resonance investigation," in *Electromagnetic Compatibility (APEMC), 2010 Asia-Pacific Symposium on*, pp. 1108–1111, IEEE, 2010.

[218] H. Chen, A. M. Bhuiya, R. Liu, D. M. Wasserman, and K. C. Toussaint Jr,

"Design, fabrication, and characterization of near-ir gold bowtie nanoantenna arrays," *The Journal of Physical Chemistry C*, vol. 118, no. 35, pp. 20553–20558, 2014.

[219] C. D. C. A. A. Tseng, K. Chen and K. J. Ma, "Electron beam lithography in nanoscale fabrication: recent development," *IEEE Transactions on Electronics Packaging Manufacturing*, vol. 26, no. 2, pp. 141–149, 2003.

[220] M. Mohammad, M. Muhammad, S. Dew, and M. Stepanova, *Nanofabrication: Techniques and Principles*, ch. Fundamentals of Electron Beam Exposure and Development, pp. 11–41. Springer, 2012.

[221] C. Mack, *Fundamental principles of optical lithography: The science of microfabrication*. John Wiley & Sons, 2008.

[222] S. Matsui, "Nanostructure fabrication using electron beam and its application to nanometer devices," in *Handbook of Nanostructured Materials and Nanotechnology*, pp. 555–583, Elsevier, 2000.

[223] T. Chang, "Proximity effect in electron-beam lithography," *Journal of Vacuum Science and Technology*, vol. 12, no. 6, pp. 1271–1275, 1975.

[224] A. A. Tseng, K. Chen, C. D. Chen, and K. J. Ma, "Electron beam lithography in nanoscale fabrication: recent development," *IEEE Transactions on Electronics Packaging Manufacturing*, vol. 26, no. 2, pp. 141–149, 2003.

[225] R. Cousins, *Fabrication and measurement of nanomechanical resonators*. PhD thesis, University of Nottingham, 2017.

[226] H. Fujiwara, *Spectroscopic ellipsometry: principles and applications*. John Wiley & Sons, 2007.

[227] J. Schindelin, I. Arganda-Carreras, E. Frise, V. Kaynig, M. Longair, T. Pietzsch, S. Preibisch, C. Rueden, S. Saalfeld, B. Schmid, *et al.*, "Fiji: an open-source platform for biological-image analysis," *Nature methods*, vol. 9, no. 7, pp. 676–682, 2012.

[228] E. Hecht, *Optics*, ch. 5, pp. 195–215. Addison-Wesley, 4th ed., 1998.

[229] T. J. Fellers and M. W. Davidson, "Coverslip correction." https://www.microscopyu.com/microscopy-basics/coverslip-correction. Accessed: 2017-03-24.

[230] J. S. Silfies and S. A. Schwartz, "The diffraction barrier in optical microscopy." https://www.microscopyu.com/techniques/super-resolution/the-diffraction-barrier-in-optical-microscopy. Accessed: 2017-03-24.

[231] K. Svoboda and S. M. Block, "Biological applications of optical forces," *Annual review of biophysics and biomolecular structure*, vol. 23, no. 1, pp. 247–285, 1994.

[232] J. Gelles, B. J. Schnapp, and M. P. Sheetz, "Tracking kinesin-driven movements with nanometre-scale precision," *Nature*, vol. 331, no. 6155, pp. 450–453, 1988.

[233] B. C. Carter, G. T. Shubeita, and S. P. Gross, "Tracking single particles: a user-friendly quantitative evaluation," *Physical biology*, vol. 2, no. 1, p. 60, 2005.

[234] S. Thomas, T. Fusco, A. Tokovinin, M. Nicolle, V. Michau, and G. Rousset, "Comparison of centroid computation algorithms in a shack–hartmann sensor," *Monthly Notices of the Royal Astronomical Society*, vol. 371, no. 1, pp. 323–336, 2006.

[235] X. Ma, C. Rao, and H. Zheng, "Error analysis of ccd-based point source centroid computation under the background light," *Optics Express*, vol. 17, no. 10, pp. 8525–8541, 2009.

[236] B. P. Bratton and J. W. Shaevitz, "Simple experimental methods for determining the apparent focal shift in a microscope system," *PloS one*, vol. 10, no. 8, p. e0134616, 2015.

[237] L. Huang, S. J. Maerkl, and O. J. F. Martin, "Integration of plasmonic trapping in a microfluidic environment.," *Optics Express*, vol. 17, no. 8, pp. 6018–6024, 2009.

[238] Y. Pang and R. Gordon, "Optical trapping of a single protein," *Nano Letters*, vol. 12, no. 1, pp. 402–406, 2012.

[239] S. Lin and K. B. Crozier, "Trapping-assisted sensing of particles and proteins using on-chip optical microcavities," *ACS Nano*, vol. 7, no. 2, pp. 1725–1730, 2013.

[240] P. Mestres, J. Berthelot, and R. Quidant, "Unravelling the optomechanical nature of plasmonic trapping," *arXiv*, no. November 2015, pp. 1–14, 2015.

[241] J. Chen, H. Cong, F.-C. Loo, Z. Kang, M. Tang, H. Zhang, S.-Y. Wu, S.-K. Kong, and H.-P. Ho, "Thermal gradient induced tweezers for the manipulation of particles and cells," *Scientific reports*, vol. 6, p. 35814, 2016.

[242] H. He, M. Friese, N. Heckenberg, and H. Rubinsztein-Dunlop, "Direct observation of transfer of angular momentum to absorptive particles from a laser beam with a phase singularity," *Physical Review Letters*, vol. 75, no. 5, p. 826, 1995.

[243] G. Gu, J. Song, H. Liang, M. Zhao, Y. Chen, and J. Qu, "Overstepping the

upper refractive index limit to form ultra-narrow photonic nanojets," *Scientific Reports*, vol. 7, no. 1, p. 5635, 2017.

[244] A. A. R. Neves, "Photonic nanojets in optical tweezers," *Journal of Quantitative Spectroscopy and Radiative Transfer*, vol. 162, no. Supplement C, pp. 122 – 132, 2015. Laser-light and Interactions with Particles 2014.

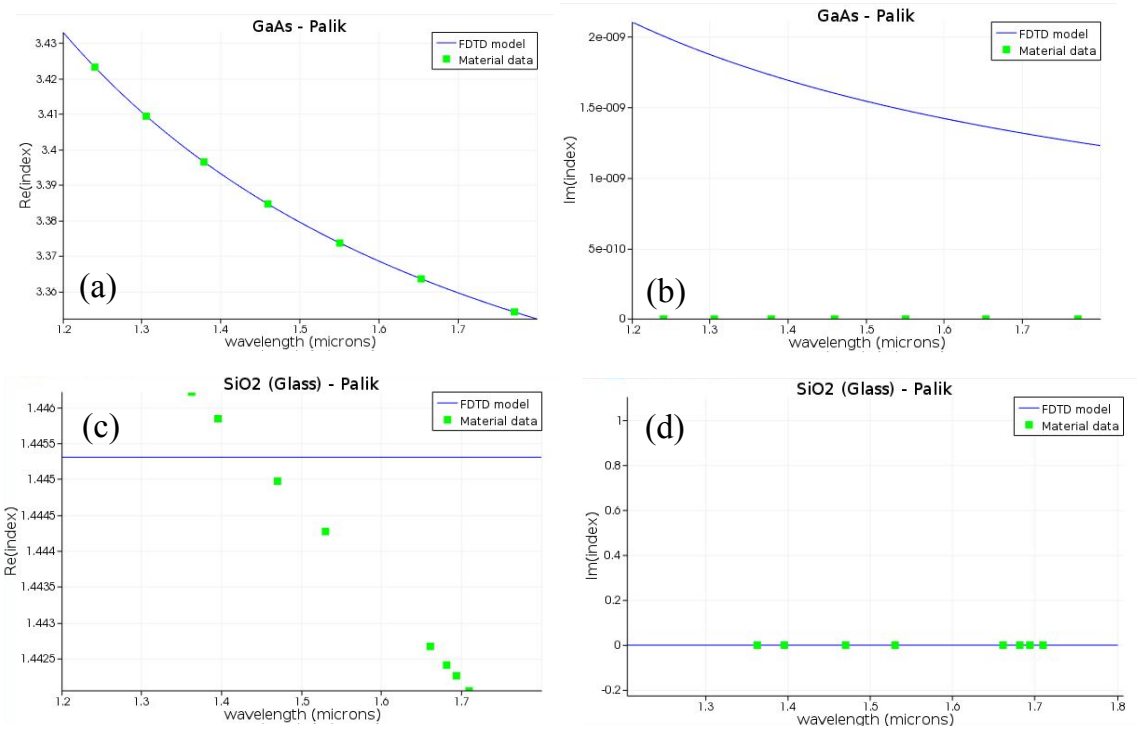
[245] B. S. Luk'yanchuk, R. Paniagua-Domínguez, I. Minin, O. Minin, and Z. Wang, "Refractive index less than two: photonic nanojets yesterday, today and tomorrow[invited]," *Opt. Mater. Express*, vol. 7, pp. 1820–1847, Jun 2017.

[246] H. Ding, L. Dai, and C. Yan, "Properties of the 3d photonic nanojet based on the refractive index of surroundings," *Chin. Opt. Lett.*, vol. 8, pp. 706–708, Jul 2010.

A

Models for representing material used in simulations

Figure A.1 shows the models used for simulating the material behaviour of GaAs, SiO_2, Au and H_2O [136].



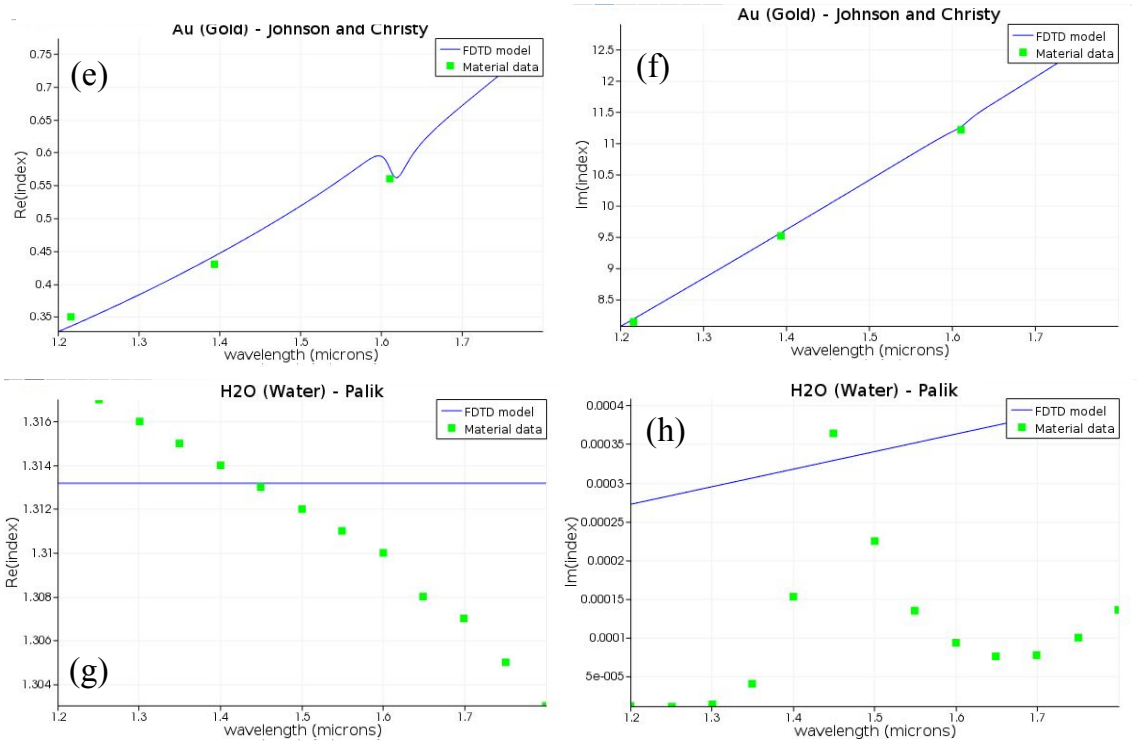


Figure A.1: Plots the material models for (a,b) GaAs, (c,d) SiO_2, (e,f) Au and (g,h) H_2O.

B

Labview program for live imaging and calculating the trap stiffness using the Dalsa camera

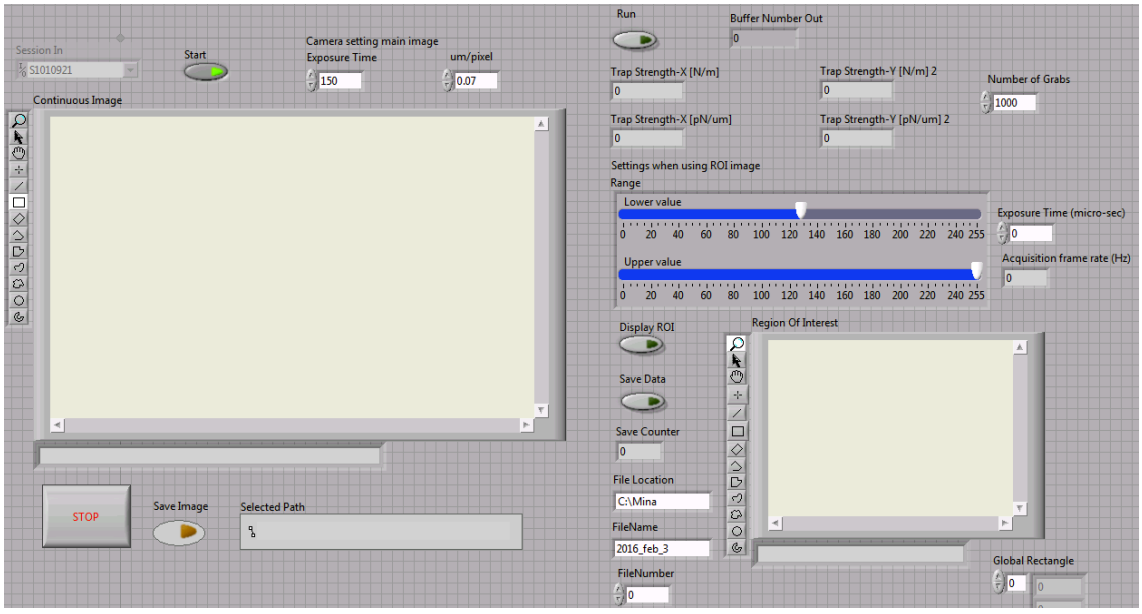


Figure B.1: Front panel of the existing Labview program for live imaging of the sample and calculating the trap stiffness of a particle in trap.

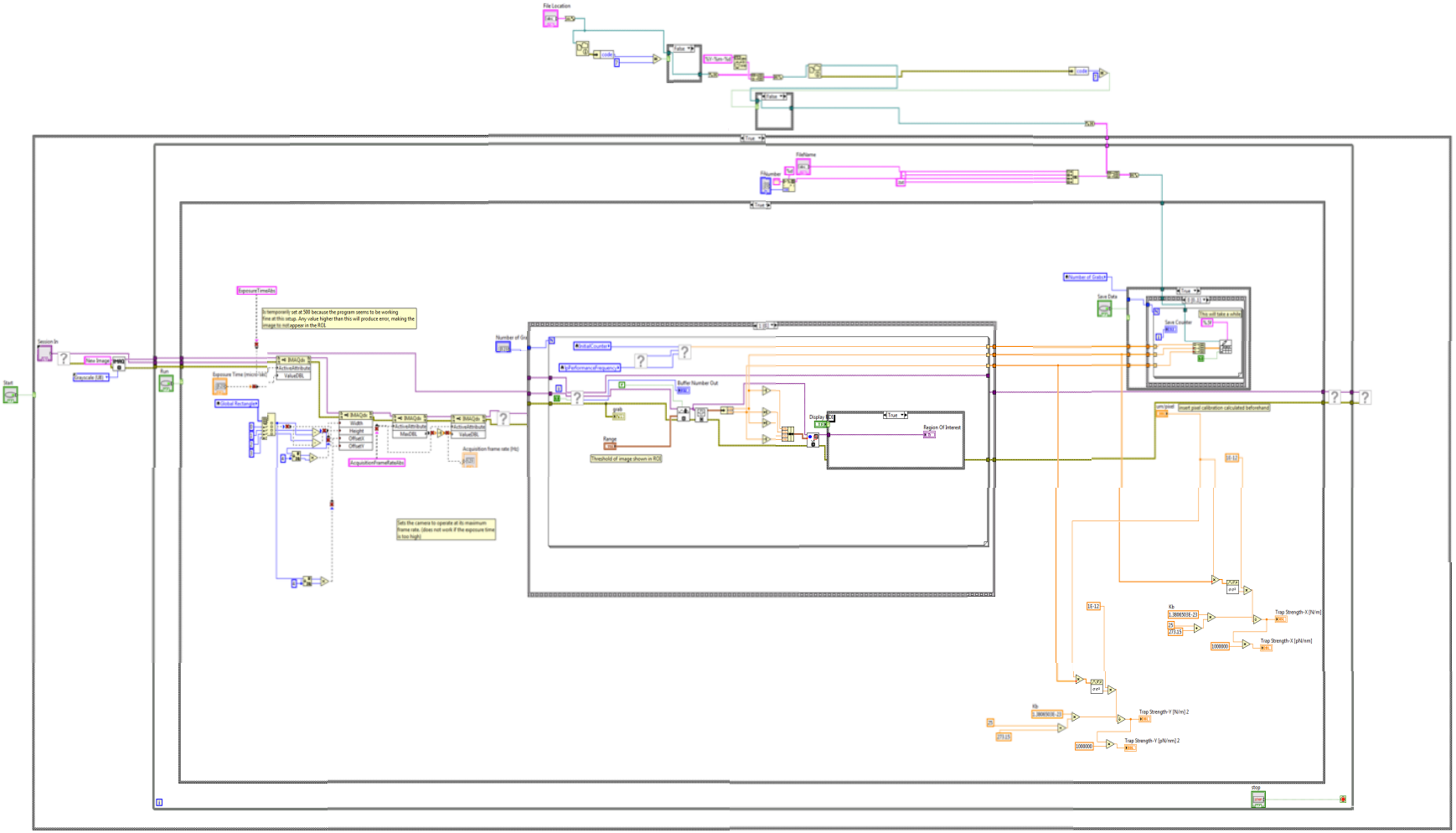


Figure B.2: Block diagram of the existing Labview program for live imaging of the sample and calculating the trap stiffness of a particle in trap.

C

Labview program for calculating the trap stiffness using the Optimos camera

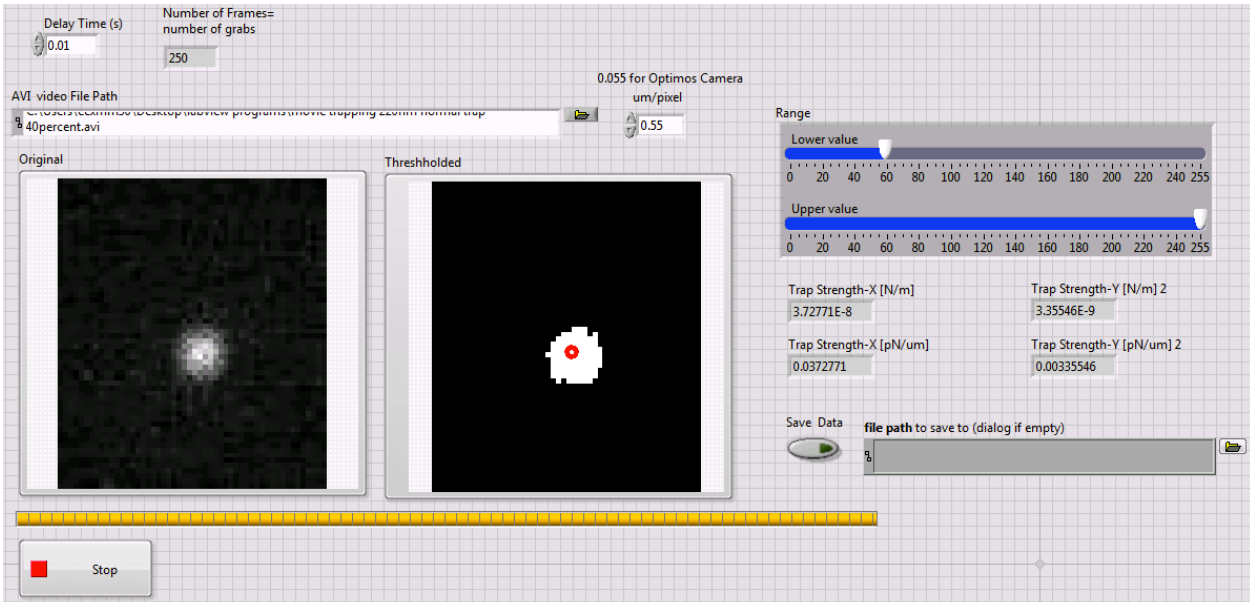


Figure C.1: Front panel of the Labview program developed for calculating the trap stiffness of a particle in trap. The program accepts an .avi movie as an input.

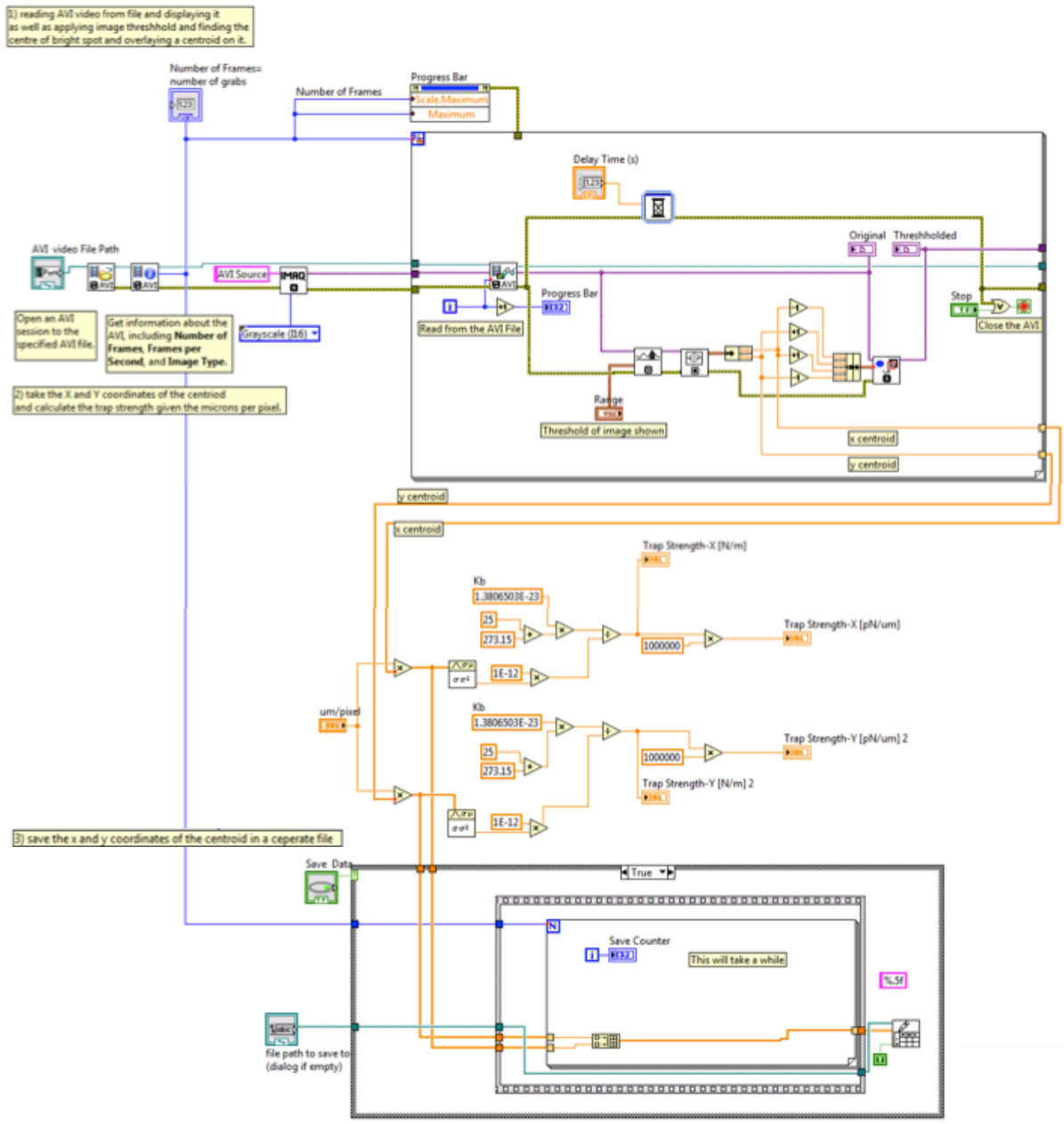


Figure C.2: Block diagram of the Labview program developed for calculating the trap stiffness of a particle in trap. The program accepts an .avi movie as an input.